ACS Partner Journal

PRECISION CHEMISTRY

pubs.acs.org/PrecisionChem

Review

Synergistic and Antisynergistic Intracrystalline Diffusional Influences on Mixture Separations in Fixed-Bed Adsorbers

Rajamani Krishna*

Cite This: *Precis. Chem.* 2023, 1, 83−93

Read Online

ACCESS | Metrics & More | Article Recommendations | Supporting Information

ABSTRACT: Separations of mixtures in fixed-bed adsorbers are influenced by factors such as (1) selectivity of adsorption, S_{ads}, (2) diffusional time constants, $Đ_i/r_c^2$, and (3) diffusion selectivity, $Đ_1/Đ_2$. In synergistic separations, intracrystalline diffusion of guest molecules serves to enhance the selectivities dictated by thermodynamics of mixture adsorption. In antisynergistic separations, intracrystalline diffusion serves to reverse the hierarchy of selectivities dictated by adsorption equilibrium. For both scenarios, the productivities of the desired product in fixed-bed operations are crucially dependent on diffusional time constants, $Đ_i/r_c^2$; these need to be sufficiently low in order for diffusional influences to be effective. Also, the ratio $Đ_1/Đ_2$ should be large enough for manifestation of synergistic or antisynergistic influence. Both synergistic and antisynergistic separations have two common, distinguishing characteristics. Firstly, for transient uptake within crystals, the more mobile component attains supraequilibrium loadings during the initial stages of the transience. Such overshoots, signifying uphill diffusion, are engendered by the cross-coefficients $\Gamma_{ij}(i \neq j)$ of thermodynamic correction factors. Secondly, the component molar loadings, plotted in composition space, follow serpentine equilibration paths. If cross-coefficients are neglected, no overshoots in the loadings of the more mobile component are experienced, and the component loadings follow monotonous equilibration paths. The important takeaway message is that the modeling of mixture separations in fixed-bed adsorbers requires the use of the Maxwell−Stefan equations describing mixture diffusion employing chemical potential gradients as driving forces.

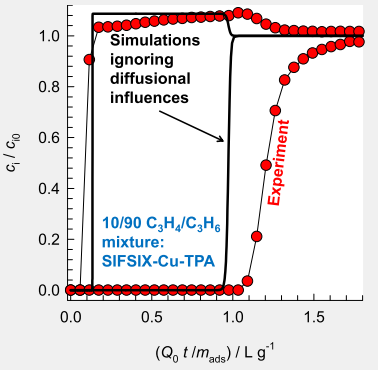

KEYWORDS: *kinetic separations transient uptake, microporous crystalline adsorbents, Maxwell−Stefan equations, thermodynamic coupling, uphill diffusion, transient breakthrough, fixed-bed adsorber*

1. INTRODUCTION

Microporous crystalline porous materials such as metal−organic frameworks (MOFs) and zeolites are finding applications as adsorbents in several different mixture separations of industrial interest. Such separations are commonly conducted in fixed-bed devices in pressure swing adsorption (PSA) processes that are operated in adsorption and desorption phases, operated in a cyclic manner. The separation performance in a fixed-bed adsorber is usually determined by the thermodynamics of mixture adsorption equilibrium, determined in practice using the ideal adsorbed solution theory (IAST).[1,2] The adsorption selectivity for a binary mixture of components 1 and 2 is defined by

$$S_{ads} = \frac{q_1/q_2}{p_1/p_2} \tag{1}$$

where p_1 and p_2 are the partial pressures in the feed mixture; q_1 and q_2 are the component molar loadings in the adsorbed phase. Industrially important examples of such equilibrium-based separations include H_2 purification, production of purified oxygen, and separation of xylene isomers.[3−10]

In several recent developments, the separation performance is additionally influenced by intracrystalline diffusion of guest constituents.[11−13] For production of purified N_2 from air, kinetically driven separations are achieved with carbon molecular sieve (CMS) and LTA-4A zeolite.[6,13−15] For removal of N_2 from natural gas, the use of Ba-ETS-4 allows the selective uptake of N_2 by effective size-exclusion of CH_4.[16,17] For separation of C_2H_4/C_2H_6 mixtures, the crystal structure of UTSA-280 essentially excludes the saturated alkane from the pores.[18] For separation of C_3H_6/C_3H_8 mixtures, the diffusional influence in CHA zeolite and ZIF-8 serves to override the adsorption selectivity that favors propane.[13,19,20]

For separation of C_2H_2/CO_2 mixtures, it is desirable to select MOFs that have adsorption selectivity in favor of CO_2, allowing the desired product C_2H_2 to be recovered, with purities in excess of 99%, in the adsorption cycle in a PSA process scheme. A particularly promising adsorbent is the ultramicroporous Y-bptc in which intracrystalline diffusion also favors CO_2; this

Received: December 7, 2022
Revised: January 30, 2023
Accepted: February 1, 2023
Published: February 16, 2023

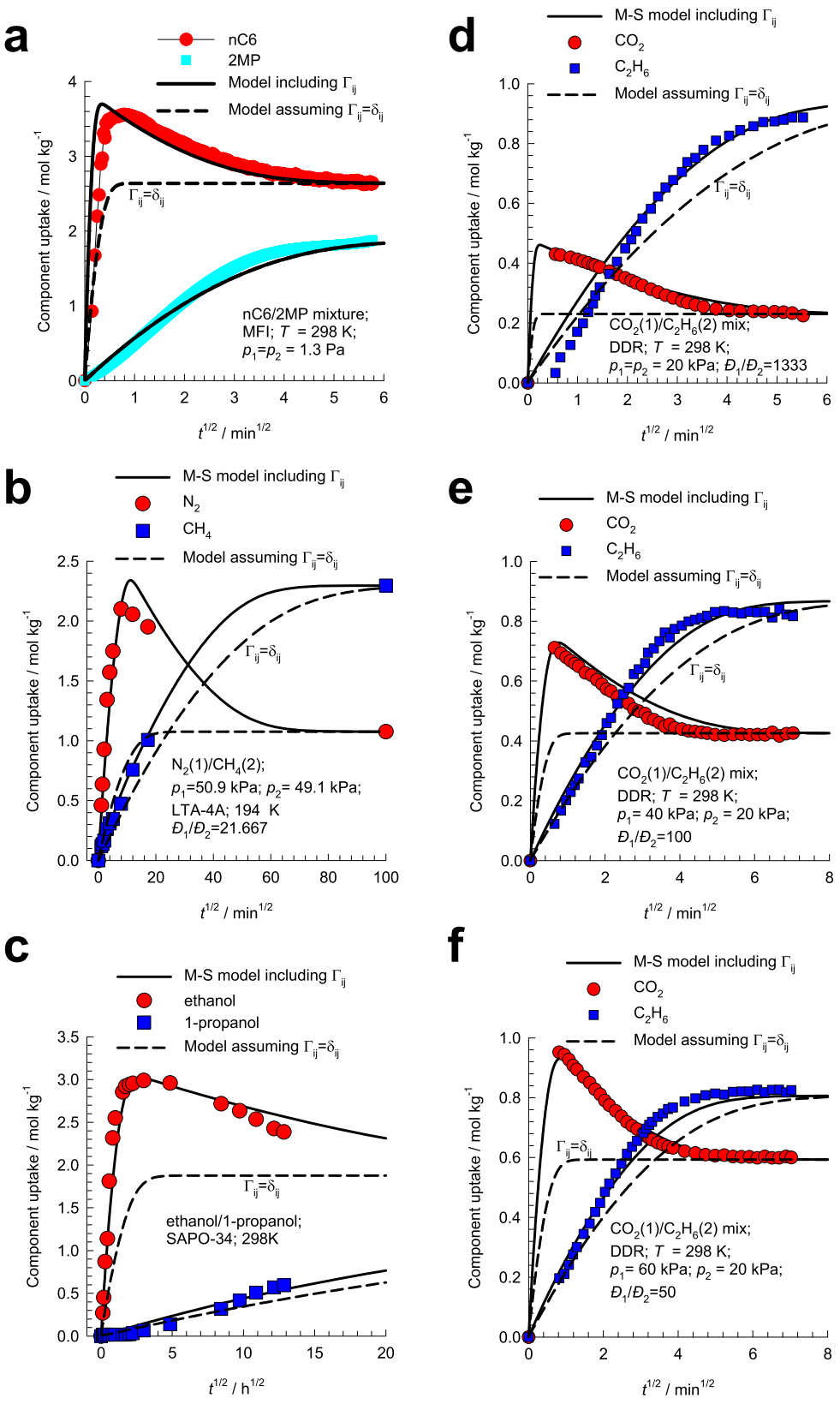

Figure 1. (a) Experimental data on transient uptake of nC6(1)/2MP(2) mixtures in MFI zeolite at 298 K.[27,32] (b) Experimental data on transient uptake of the $N_2(1)/CH_4(2)$ mixture within LTA-4A crystals, exposed to binary gas mixtures at partial pressures p_1 = 50.9 kPa and p_2 = 49.1 kPa at 194 K.[28,33] (c) Experimental data for transient uptake of ethanol/1-propanol mixtures within SAPO-34.[34] (d–f) Experimental data[35,36] for spatial-averaged transient uptake of (d) 1:1 (e) 2:1, and (f) 3:1 $CO_2(1)/C_2H_6(2)$ gas mixtures within crystals of DDR zeolite at 298 K.[32,37] The continuous solid lines are simulations based on eq 5. The dashed lines are the simulations based on eq 7.

https://doi.org/10.1021/prechem.2c00003
Precis. Chem. 2023, 1, 83−93

adsorption/diffusion synergy results in high productivity of purified C_2H_2 (see Figure S26).[21]

The selective capture of propyne from propene is important in the context of preparing polymer-grade propene feedstocks. Jiang et al.[22] report the efficacy of SIFSIX-Cu-TPA (also named as ZNU-2-Si) for this separation task. A particularly interesting feature is that the separation displays synergism between adsorption and diffusion (see Figure S63).

The experimental data on separation of ethanol/1-propanol and ethanol/1-hexanol liquid feed mixtures in a fixed bed packed with SAPO-34, which has the same structural topology as CHA zeolite, shows that the component that is preferentially adsorbed in ethanol.[23,24] The rationalization of these experimental data can be traced to the synergy between adsorption and diffusion, both favoring ethanol (see Figures S23, S24, and S25).[10]

The main objective of this Review is to discuss and underscore the key factors that underlie both synergistic and antisynergistic separations. By detailed analyses of various mixture separations in fixed-bed adsorption devices, we highlight some common characteristics of both synergistic and antisynergistic separations. Such characteristics include transient overshoots in the uptake of the more mobile guest and serpentine equilibration trajectories. The secondary objective is to stress the need to employ the Maxwell−Stefan (M−S) formulation of multicomponent diffusion in which the driving forces for intracrystalline transport of guest species are the corresponding gradients in the chemical potentials.[13,25,26]

The Supporting Information provides (a) the derivation of the M−S equations, (b) computational modeling details of transient mixture uptakes within crystals and adsorber breakthroughs, (c) unary isotherm data fits used for IAST calculations, and (d) guest diffusivities.

2. TRANSIENT OVERSHOOTS IN BINARY MIXTURE UPTAKE

We begin by highlighting an important signature of kinetic separations, either synergistic or antisynergistic, by examining published experimental data sets on transient mixture uptake in adsorbent crystals.

Using infrared microscopy (IRM), Titze et al.[27] have determined the uptake of *n*-hexane (nC6)/2-methylpentane (2MP) mixtures in MFI crystals exposed to an equimolar gas phase mixture at constant total pressure; see Figure 1a. The transient equilibration of nC6 displays a distinct overshoot in its component loading during early stages of the transience; the overshoot is in excess of the final equilibrated loading. The mixture adsorption equilibrium favors the linear isomer (S_{ads} = 1.4).[10] There is synergy between adsorption and diffusion because nC6 has a higher mobility than 2MP, by a factor of 100, within the 5.5 Å sized channels of MFI zeolite (structural details are provided in Figures S6 and S7).

The uptake of $N_2(1)/CH_4(2)$ mixtures in crystallites of LTA-4A zeolite have been reported by Habgood;[28] see Figure 1b.[13,29] The "pencil-like" 4.4 Å × 3.3 Å sized nitrogen molecule hops lengthwise across the 8-ring windows of LTA-4A (structural details are provided in Figure S38).[30] The spherical 3.7 Å methane molecule is constrained in its intercage hopping and has a diffusivity that is significantly lower than that of N_2.[31,32] Due to its higher polarizability, the adsorption strength of CH_4 is higher than that of N_2. At short contact times, the pores of LTA-4A are significantly richer in the more mobile N_2, manifesting in an overshoot in component loading in excess of the final equilibrium value. With the progression of time, the N_2 in the pores is displaced by CH_4 that has a higher adsorption strength.[13,33]

Measurements of the uptake of ethanol/1-propanol mixtures in SAPO-34 zeolite (structural details are provided in Figures S20 and S21) are shown in Figure 1c. The more mobile ethanol exhibits an overshoot during the early stages of the uptake transience.[32,34]

Figure 1d−f shows the experimental uptakes[35,36] of CO_2/C_2H_6 gas mixtures of different compositions within crystals of DDR, a cage-type zeolite (structural details are provided in Figures S29 and S30).[30,37−39] The cross-sectional dimension of CO_2 is smaller than that of C_2H_6,[7] and therefore the intercage hopping rate of CO_2 is significantly higher than that of C_2H_6, by a factor of 100−1000. The mixture adsorption equilibrium favors the saturated alkane due to higher polarizability. During early transience, the more mobile CO_2 attains supraequilibrium loadings.

For elucidation and quantification of the six data sets in Figure 1, we need to solve the set of partial differential equations[13] describing the time derivative of the component molar loadings in a spherical crystallite of radius r_c:

$$\rho\frac{\partial q_i(r,t)}{\partial t} = -\frac{1}{r^2}\frac{\partial}{\partial r}(r^2 N_i) \tag{2}$$

The M−S equation describing the dependence of the intracrystalline fluxes N_i on the gradients of component chemical potentials is[13,25,26]

$$N_i = -\rho Đ_i\frac{q_i}{RT}\frac{\partial \mu_i}{\partial r} \tag{3}$$

The M−S diffusivity $Đ_i$ equals the corresponding diffusivity for a unary system, determined at the same pore occupancy; the diffusivity for any species i in a mixture remains invariant to the choice of the partner species.[40] Other variables in eqs 2 and 3 are described in the Nomenclature section.

We relate the $\partial\mu_i/\partial r$ to the loading gradients $\partial q_i/\partial r$ by defining thermodynamic correction factors Γ_{ij}:

$$\frac{q_i}{RT}\frac{\partial \mu_i}{\partial r} = \sum_{j=1}^{n}\Gamma_{ij}\frac{\partial q_j}{\partial r};\ \Gamma_{ij} = \frac{q_i}{p_i}\frac{\partial p_i}{\partial q_j};\ i, j = 1, 2, ..., n \tag{4}$$

The Γ_{ij} are determinable from the IAST description of the mixture adsorption equilibrium. For binary mixtures, we may combine eqs 3 and 4 to obtain the following explicit expression, using two-dimensional matrix notation, for the intracrystalline fluxes in terms of the gradients in the molar loadings:

$$\begin{pmatrix} N_1 \\ N_2 \end{pmatrix} = -\rho\begin{bmatrix} D_{11} & D_{12} \\ D_{21} & D_{22} \end{bmatrix}\begin{pmatrix} \frac{\partial q_1}{\partial r} \\ \frac{\partial q_2}{\partial r} \end{pmatrix};\ \begin{bmatrix} D_{11} & D_{12} \\ D_{21} & D_{22} \end{bmatrix} = \begin{bmatrix} Đ_1 & 0 \\ 0 & Đ_2 \end{bmatrix}\begin{bmatrix} \Gamma_{11} & \Gamma_{12} \\ \Gamma_{21} & \Gamma_{22} \end{bmatrix} \tag{5}$$

The cross-coefficients Γ_{12} and Γ_{21} cause the flux of species i, N_i, to be influenced by the gradient of the molar loading of the partner species j: $\partial q_j/\partial r$.[13] In order to appreciate the significance of such "coupling" effects, Figure 2 presents calculations of the elements Γ_{ij} for 20/80 $N_2(1)/CH_4(2)$ mixture adsorption in LTA-4A zeolite as a function of the total pressure, p_t. We note

https://doi.org/10.1021/prechem.2c00003
Precis. Chem. 2023, 1, 83−93

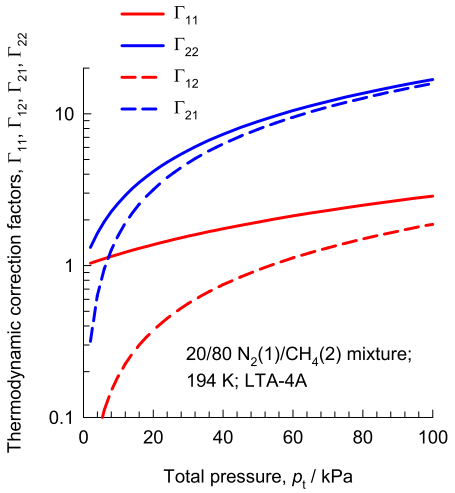

Figure 2. Calculations of the elements Γ_{11}, Γ_{12}, Γ_{21}, and Γ_{22} for 20/80 $N_2(1)/CH_4(2)$ mixture adsorption in LTA-4A zeolite at 194 K.

that the Γ_{12} and Γ_{21} are increasingly significant in relation to the main elements Γ_{11} and Γ_{22} with increasing values of p_t.

The continuous solid black lines in Figure 1 are radial-averaged component loadings

$$\overline{q}_i(t) = \frac{3}{r_c^3}\int_0^{r_c} q_i(r, t)r^2 dr \tag{6}$$

obtained by numerical solution of eqs 2, 5, and 6. For the set of six experiments in Figure 1, the attainment of supraequilibrium loadings by the more mobile guest components are quantitatively portrayed by the M−S diffusion equations. Such overshoots are signatures of the occurrence of uphill diffusion.[29,41]

Additional evidence of uphill diffusion of more mobile partners (component 1) is available for $N_2(1)/CH_4(2)$ uptake in Ba-ETS-4[42] (see Figures S49 and S50), $O_2(1)/N_2(2)$ uptake in LTA-4A zeolite (see Figure S55), C_3H_6/C_3H_8 uptake in CHA zeolite[20] (see Figure S61), C_3H_6/C_3H_8 uptake in ZIF-8[19] (see Figure S62), benzene(1)/ethylbenzene(2) uptake in H-ZSM-5 (see Figure S64a), and benzene(1)/*p*-xylene(2) uptake in H-ZSM-5 (see Figure S64b).[33,43,44]

At low pore occupancies, $\Gamma_{ij} \to \delta_{ij}$, where $\delta_{ij}(i = j) = 1$ and $\delta_{ij}(i \neq j) = 0$ is the Kronecker delta; in this case eq 5 simplifies to yield a set of flux relations that are uncoupled:[45]

$$N_i = -\rho Đ_i \frac{\partial q_i}{\partial r};\ i = 1, 2 \tag{7}$$

The dashed black lines in Figure 1 are simulations based on the simplified eq 7, asserting $\Gamma_{ij} = \delta_{ij}$; we note that this simplification is unable to anticipate the overshoots in the component loadings of the more mobile partners in all six data sets. The first important message to emerge is that thermodynamic coupling influence is of essential importance in kinetic separations, both synergistic and antisynergistic.

3. SERPENTINE EQUILIBRATION TRAJECTORIES

To gain further insights into the characteristics of kinetic separations, we plot the experimentally measured loadings of the more mobile partner, q_1, as a function of the loading of the tardier partner, q_2; see red spherical symbols in Figure 3. In all six cases we note that the component loadings follow serpentine paths to equilibrium. If eq 7 is invoked by asserting $\Gamma_{ij} = \delta_{ij}$, the approach to equilibrium is monotonous in nature, as shown in the dashed black lines in Figure 3.

To obtain further insights, we determine the two eigenvalues λ_1 and λ_2 of the two-dimensional matrix $\begin{bmatrix} D_{11} & D_{12} \\ D_{21} & D_{22} \end{bmatrix} = \begin{bmatrix} Đ_1 & 0 \\ 0 & Đ_2 \end{bmatrix}\begin{bmatrix} \Gamma_{11} & \Gamma_{12} \\ \Gamma_{21} & \Gamma_{22} \end{bmatrix}$. Since component 1 is the more mobile partner, $\lambda_1 > \lambda_2$. The green-colored straight lines in Figure 3 are the trajectories that are followed in the happenstance in which the M−S diffusivities of both species are equal to each other, i.e., $Đ_1 = Đ_2$, and $\lambda_1 = \lambda_2$; the mixtures separations are purely based on mixture adsorption thermodynamics.

The experimentally determined loading trajectories are bounded by the two corresponding eigenvectors. During the early stages of the transience, the equilibration is influenced by the *fast eigenvector* (detailed derivations are provided in the Supporting Information):

$$(q_2 - q_{20}) = e_{12}(q_1 - q_{10})$$

$$e_{12} = \frac{1}{2}\left(-\frac{\Gamma_{11}}{\Gamma_{12}} + \frac{Đ_2}{Đ_1}\frac{\Gamma_{22}}{\Gamma_{12}} + \sqrt{\left(\frac{\Gamma_{11}}{\Gamma_{12}} - \frac{Đ_2}{Đ_1}\frac{\Gamma_{22}}{\Gamma_{12}}\right)^2 + 4\frac{Đ_2}{Đ_1}\frac{\Gamma_{21}}{\Gamma_{12}}}\right) \tag{8}$$

In eq 8, q_{10} and q_{20} are the initial component loadings. The fast eigenvectors are indicated by the straight red lines in Figure 3a−f.

As equilibrium is approached, the equilibration trajectory follows the path dictated by the *slow eigenvector*

$$(q_2 - q_2^*) = e_{22}(q_1 - q_1^*)$$

$$\frac{1}{e_{22}} = \frac{1}{2}\left(\frac{Đ_1}{Đ_2}\frac{\Gamma_{11}}{\Gamma_{21}} - \frac{\Gamma_{22}}{\Gamma_{21}} - \sqrt{\left(\frac{Đ_1}{Đ_2}\frac{\Gamma_{11}}{\Gamma_{21}} - \frac{\Gamma_{22}}{\Gamma_{21}}\right)^2 + 4\frac{Đ_1}{Đ_2}\frac{\Gamma_{12}}{\Gamma_{21}}}\right) \tag{9}$$

In eq 9, q_1^* and q_2^* are the equilibrated loadings; the slow eigenvectors are indicated by the straight blue lines in Figure 3a−f. We note that the slopes of the fast and slow eigenvectors, e_{12} and e_{22}, are dependent on the ratio $Đ_1/Đ_2$. Indeed, it is possible to estimate $Đ_1/Đ_2$ from the tangents to the experimentally measured equilibration paths, along with estimates of Γ_{ij}.

4. ANTISYNERGISTIC SEPARATION OF $N_2(1)/CH_4(2)$ MIXTURES

To meet pipeline specifications (<4% N_2), the selective capture of nitrogen from natural gas streams, primarily containing CH_4, is required in practice because the nitrogen content in several reserves may be as high as 20%.[46] For smaller natural gas reserves, PSA technology is economically preferred to cryogenic distillation because the feed mixtures are available at high pressures.[17,46,47] It is desirable to use adsorbents in PSA units that are selective to N_2 such that CH_4 can be recovered as raffinate in the adsorption cycle. For most known materials,

https://doi.org/10.1021/prechem.2c00003
Precis. Chem. 2023, 1, 83−93

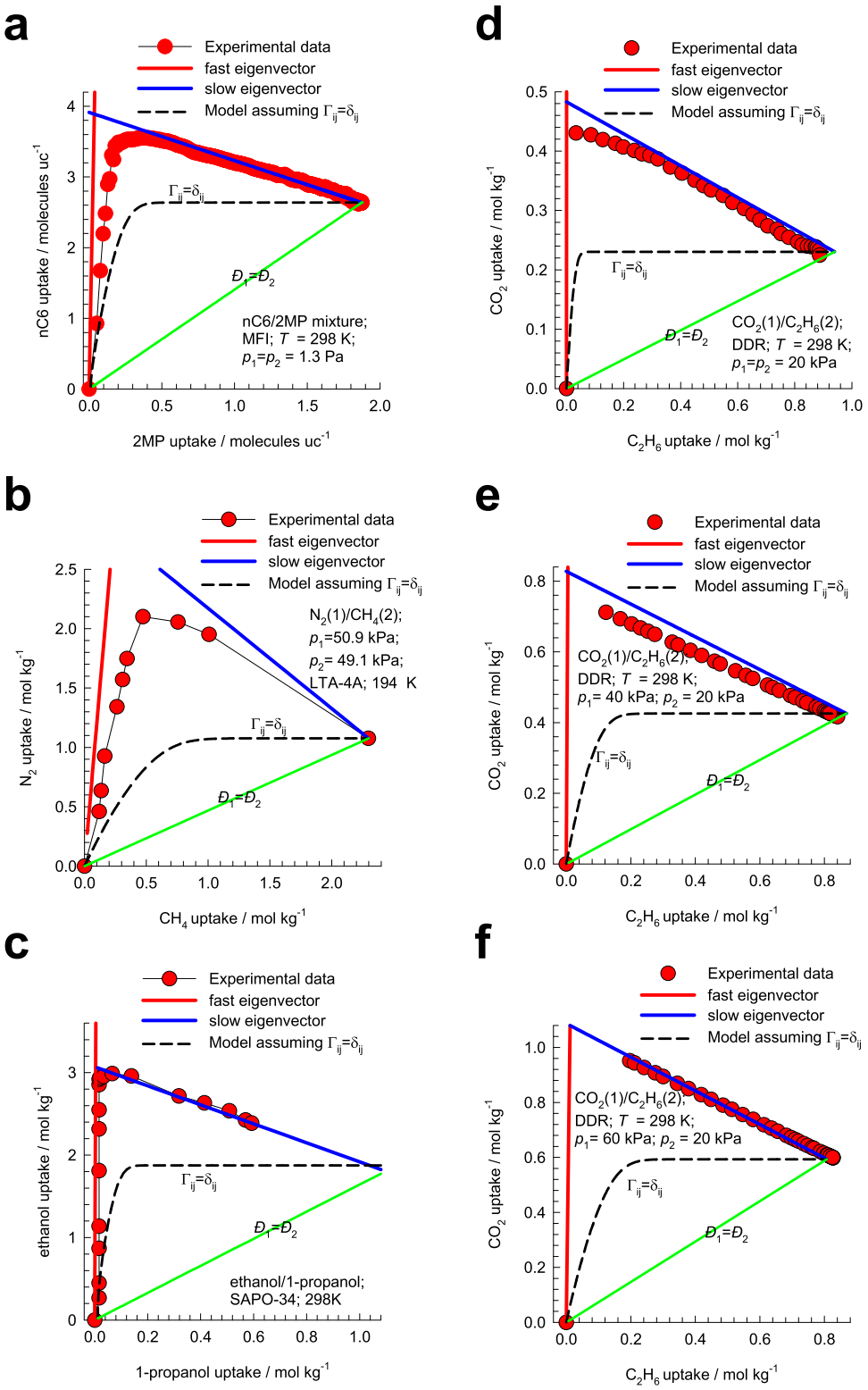

Figure 3. Equilibration trajectories in composition space for (a) nC6(1)/2MP(2) mixtures in MFI zeolite at 298 K, (b) $N_2(1)/CH_4(2)$ mixture in LTA-4A crystals at 194 K, (c) ethanol/1-propanol mixtures in SAPO-34 at 298 K, and (d–f) $CO_2(1)/C_2H_6(2)$ mixtures within crystals of DDR zeolite at 298 K. The red circles represent experimental data on component loadings from Figure 1. The dashed lines are the trajectories based on eq 7. The red lines represent the fast eigenvectors. The blue lines represent the slow eigenvectors. The green lines represent the trajectory followed if $Đ_1 = Đ_2$.

adsorption selectivity for separation of N_2/CH_4 mixtures is in favor of CH_4 due to its higher polarizability.[33]

We analyze separations of 20/80 $N_2(1)/CH_4(2)$ mixtures in a fixed-bed adsorber using LTA-4A zeolite operating at a total pressure of 100 kPa and $T = 194$ K. Figure 4a shows the transient breakthrough simulations for 20/80 $N_2(1)/CH_4(2)$ mixtures through a fixed-bed adsorber packed with LTA-4A crystals operating at 194 K and total pressure $p_t = 100$ kPa. The y-axis is the % CH_4 at the adsorber outlet. The x-axis is Q_0t/m_{ads}, where Q_0 is the volumetric flow rate of the gas mixture at the inlet to the

https://doi.org/10.1021/prechem.2c00003
Precis. Chem. 2023, 1, 83−93

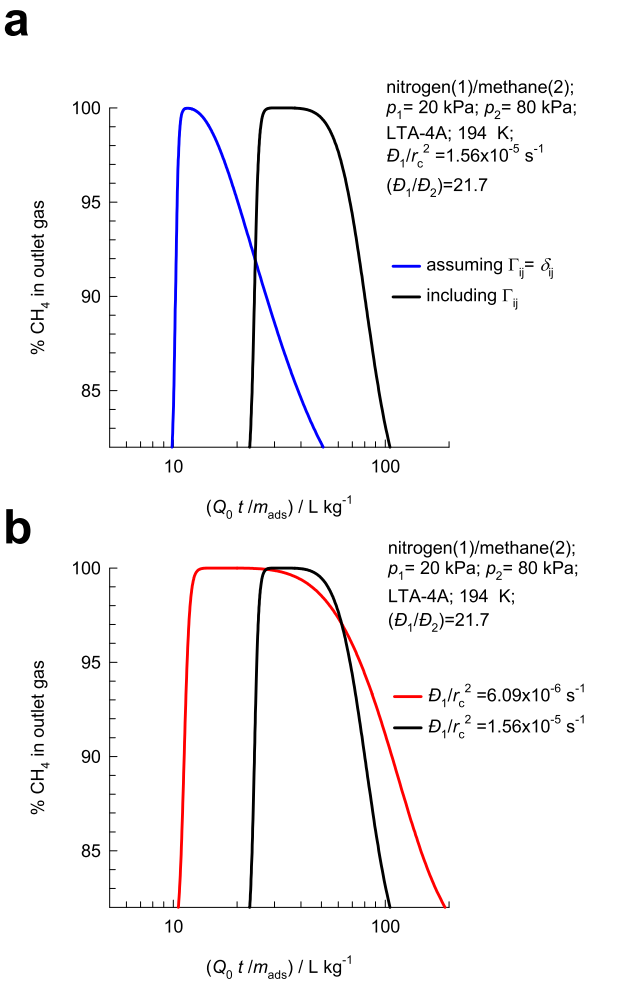

Figure 4. (a, b) Transient breakthrough of the 20/80 $N_2(1)/CH_4(2)$ mixture in a fixed-bed adsorber packed with LTA-4A crystals operating at 194 K and total pressure p_t = 100 kPa. The y-axis is the % CH_4 at the adsorber outlet. The x-axis is Q_0t/m_{ads}, where Q_0 is the volumetric flow rate of the gas mixture at the inlet to the fixed bed at actual temperature and pressure conditions. The black lines are simulations based on eq 5. The blue lines are the simulations based on eq 7. In (a) we maintain $Đ_1/r_c^2 = 1.5 \times 10^{-5}$ s^{-1}; $Đ_1/Đ_2 = 21.7$. In (b) the two simulations include thermodynamic coupling and maintain the ratio $Đ_1/Đ_2 = 21.7$; the black and red lines represent two different severities of diffusional influences: $Đ_1/r_c^2 = 1.56 \times 10^{-5}$ s^{-1}; $Đ_1/r_c^2 = 6.09 \times 10^{-6}$ s^{-1}.

fixed bed at actual temperature and pressure conditions. The continuous black lines are simulations taking due account of intracrystalline diffusion using eq 5, with parameters $Đ_1/r_c^2 = 1.56 \times 10^{-5}$ s^{-1}; $Đ_1/Đ_2 = 21.7$. The blue lines are the simulations based on eq 7. For the target CH_4 purity of say 96%, we can determine the moles of 96%+ pure CH_4 produced from a material balance on the adsorber. Expressed per kilogram of LTA-4A zeolite in the packed bed, the respective productivities are 0.93 and 0.11 mol kg^{-1}, with 96%+ CH_4 purity. Use of the simplified eq 7 asserting $\Gamma_{ij} = \delta_{ij}$ results in a severe underestimation of the CH_4 productivity in the PSA unit.

Having established the importance of including the thermodynamic correction factors in PSA simulations, we proceed to examine the influence of the severity of diffusional limitations. Figure 4b compares the LTA-4A adsorber breakthrough simulations for 20/80 $N_2(1)/CH_4(2)$ mixtures for two different scenarios: $Đ_1/r_c^2 = 1.56 \times 10^{-5}$ s^{-1}; $Đ_1/r_c^2 = 6.09 \times 10^{-6}$ s^{-1}; for both scenarios we maintain $Đ_1/Đ_2 = 21.7$ and include the thermodynamic coupling influences. Expressed per kilogram of zeolite in the packed bed, the respective productivities are 0.93 and 1.62 mol kg^{-1}, with 96%+ CH_4 purity. More severe diffusional limitations, signified by lower values of $Đ_1/r_c^2$, result in higher CH_4 productivity. Indeed, if the diffusional severity is diminished, kinetic separations are not achievable.

A further point to note is that for kinetic separations to be effective with LTA-4A, the operating temperatures need to be below 220 K; see simulations in Figures S44 and S45. In current industrial practice, the adsorbent used is Ba-ETS-4 (also termed CTS-1), which is effective at ambient temperatures; see simulation data in Figures S46−S51.

5. SYNERGISTIC SEPARATION OF NC6(1)/2MP(2) MIXTURES

For hexane isomers, the values of the research octane number (RON) increase with the degree of branching: *n*-hexane (nC6) = 30, 2-methylpentane (2MP) = 74.5, 3-methylpentane (3MP) = 75.5, 2,2-dimethylbutane (22DMB) = 94, and 2,3-dimethylbutane (23DMB) = 105. In the context of octane enhancement of gasoline, branched isomers of hexane are preferred components for inclusion in the high-octane gasoline pool.[33,48,49] There are a number of adsorbents that have potential use in the separation of linear and branched isomers of hexane isomers.[33,50] With the intersecting channel structure of MFI zeolite,[33] the mono- and dibranched isomers locate at the channel intersections that offer more "legroom", whereas the linear nC6 can locate anywhere in straight and zig-zag channels; see computational snapshots in Figure S8 of the Supporting Information.[8,51,52] The hierarchy of adsorption strengths is nC6 > 2MP ≈ 3MP > 22DMB ≈ 23DMB and is governed by entropy effects engendered by differences in molecular configurations and conformations.[8,10,53,54] The intracrystalline diffusivities follow a similar hierarchy: nC6 ≫ 2MP ≈ 3MP > > 22DMB ≈ 23DMB (see Figure S14 of the Supporting Information).[55]

Uphill diffusion of nC6, as evidenced in Figure 1a, is beneficial to the hexane isomer separations in PSA units because the desired raffinate phase in the adsorption cycle will be richer in the branched isomers that have higher RON values. Breakthrough simulations were performed for 50/50 nC6/2MP mixture separations in order to confirm this expectation. Figure 5a plots the dimensionless concentrations at the exit of the adsorber, c_i/c_{i0}, as a function of a modified time parameter defined by Q_0t/m_{ads}. In the three sets of simulations, the ratio $Đ_1/Đ_2 = 100$, as determined from the transient uptake experiments of Titze et al.[27] (cf. Figure 1). Three different values for the diffusional time constants were chosen, $Đ_1/r_c^2 = 1.6 \times 10^{-6}$, 1.0×10^{-5}, and 1.6×10^{-2} s^{-1}, to investigate the varying degrees of diffusional influence. In practice, stronger diffusional influences are achievable for use of larger sized crystals. The comparisons of the separations achieved with different crystal sizes should be on the basis of the parameter Q_0t/m_{ads}. Increasing values of $Đ_1/r_c^2$ signify diminishing influence of intracrystalline transport; indeed, for $Đ_1/r_c^2 \to \infty$, there are no diffusional limitations. We note that with decreasing $Đ_1/r_c^2$, i.e., stronger diffusional influences, the breakthroughs take on a more distended character and 2MP exits the adsorber at earlier times. Figure 5b plots the RON of the product gas mixture exiting the adsorber. With stronger diffusion influences, i.e.. lower values of $Đ_1/r_c^2$, there is a longer time interval during which product gas with RON= 74.5 can be recovered at the exit; these time intervals are indicated by the colored arrows in Figure 5b.

https://doi.org/10.1021/prechem.2c00003
Precis. Chem. 2023, 1, 83−93

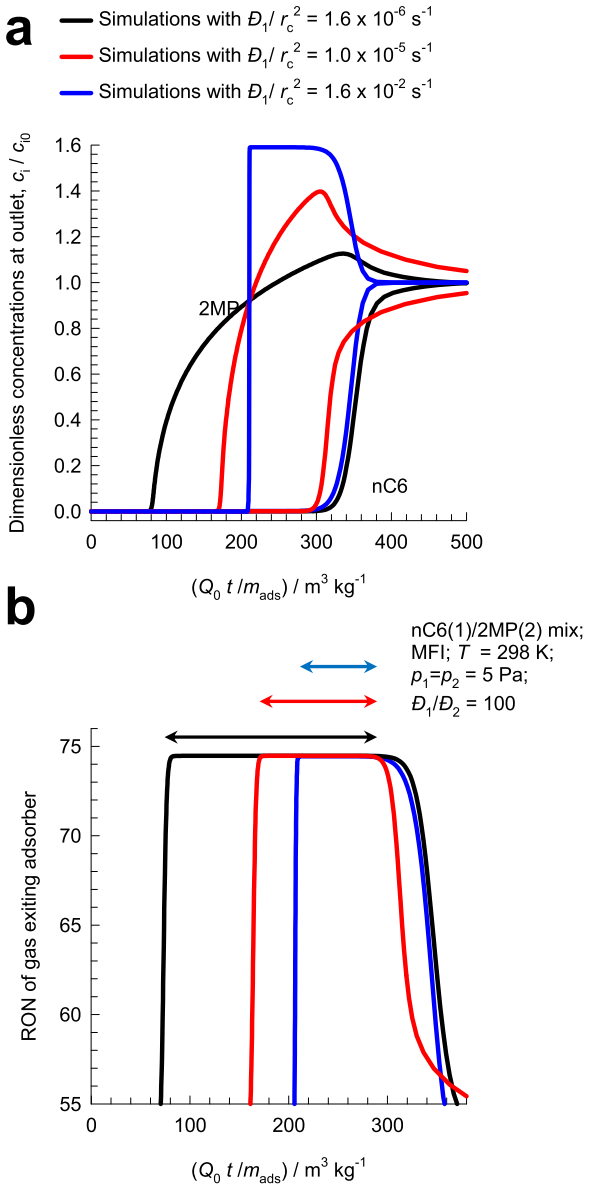

Figure 5. (a) Transient breakthrough for 50/50 nC6(1)/2MP(2) mixtures in MFI zeolite at 298 K and total pressure of 10 Pa. The dimensionless concentrations at the exit of the adsorber, c_i/c_{i0}, are plotted as a function of a modified time parameter defined by Q_0t/m_{ads}. For the three sets of simulations, $Đ_1/r_c^2 = 1.6 \times 10^{-6}$, 1.0×10^{-5}, and 1.6×10^{-2}, s^{-1}, maintaining the ratio $Đ_1/Đ_2 = 100$. (b) RON of a product gas mixture leaving a fixed-bed adsorber packed with MFI zeolite.

The adsorption/diffusion synergy is also effective for the separation of hexane isomers using $Fe_2(BDP)_3$ as the adsorbent;[50] for details see Figures S17−S19 of the Supporting Information.

6. SYNERGISTIC SEPARATION OF C_2H_2(1)/CO_2(2) MIXTURES

The recovery of ethyne (C_2H_2) from mixtures with CO_2 is of industrial importance because C_2H_2 is an important feedstock for chemical synthesis and has wide applications. Due to the closeness of the boiling points, distillation separations need to operate at cryogenic temperatures and high pressures. Adsorption separations are also challenging because both molecules possess zero dipole moments and approximately the same quadrupole moment.[56] The molecular dimensions of C_2H_2 (3.32 Å × 3.34 Å × 5.7 Å) are remarkably close to that of CO_2 (3.18 Å × 3.33 Å × 5.36 Å). Since the desired product C_2H_2 needs to be recovered at high purities, typically >99%, it is preferable to choose adsorbents in which CO_2 is preferentially adsorbed, such that C_2H_2 is recovered as raffinate in the adsorption cycle of PSA operations. MOFs that have adsorption selectivity in favor of CO_2 include ZU-610a,[57] Ce(IV)-MIL-140-4F,[58] and Y-bptc.[21] Of particular interest is the ultra-microporous Y-bptc[21] for which the adsorption selectivity S_{ads} = 3.75, in favor of CO_2. The diffusion selectivity, determined experimentally from unary uptakes,[21] $Đ_2/Đ_1$ = 114, also favors CO_2.

Figure 6a shows transient breakthrough of 50/50 C_2H_2(1)/CO_2(2) mixtures through a fixed-bed adsorber packed with Y-bptc crystals operating at 298 K and total pressure p_t = 100 kPa. The dimensionless concentrations at the exit of the adsorber, c_i/c_{i0}, are plotted as a function of a modified time parameter defined by Q_0t/m_{ads}. For the four sets of simulations we choose $Đ_1/r_c^2$ = 4.25×10^{-6}, 1.18×10^{-5}, 4.72×10^{-5}, and 4.25×10^{-4} s^{-1}, maintaining the ratio $Đ_2/Đ_1$ = 114, as determined experimentally.[21] With lower values of the diffusional constants $Đ_1/r_c^2$, i.e., stronger diffusional influences, the breakthrough of the desired product C_2H_2 occurs earlier, resulting in higher productivity of purified C_2H_2 per kilogram of adsorbent in the bed. In Figure 6b, the productivities of 99%+ pure C_2H_2 are plotted as a function of $Đ_1/r_c^2$. We note that with decreasing $Đ_1/r_c^2$, the C_2H_2 productivities increase from 1.05 to 1.35 mol kg^{-1}.

In the sets of breakthrough simulations in Figure 6c, we maintain $Đ_1/r_c^2$ = 1.18×10^{-5} s^{-1}, with varying ratios of diffusivities of CO_2 to C_2H_2: $Đ_2/Đ_1$ = 200, 114, 50, 10, and 2. We note that with increasing values of $Đ_2/Đ_1$, the C_2H_2 productivities increase from 0.1 to 1.35 mol kg^{-1}; see Figure 6d. We conclude that both $Đ_1/r_c^2$ and $Đ_2/Đ_1$ have a significant impact on the productivities of purified C_2H_2. From the breakthrough experiments of He et al.,[21] for Y-bptc, with $Đ_2/Đ_1$ = 114, the C_2H_2 productivity is calculated to be 1.52 mol kg^{-1}, in reasonable agreement with the simulations.

7. ANTISYNERGISTIC SEPARATION OF CO_2(1)/C_2H_6(2) MIXTURES

The separation of CO_2/C_2H_6 mixtures to produce purified C_2H_6, while capturing CO_2, is relevant in the context of natural gas processing. Due to azeotrope formation, current technologies for CO_2/C_2H_6 separations require use of extractive distillation that is energy demanding. An energy-efficient alternative to extractive distillation is to use PSA technology, drawing inspiration from the antisynergy evidenced in the uptake experiments in Figure 1d−f.

Figure 7 shows the transient breakthrough of 50/50 CO_2(1)/C_2H_6(2) mixtures through a fixed-bed adsorber packed with DDR crystals operating at 298 K and total pressure p_t = 40 kPa. In the two sets of simulations, the ratio $Đ_1/Đ_2$ = 1333, as determined experimentally (cf. Figure 1d). Two different values of the diffusional time constants were chosen: $Đ_1/r_c^2$ = 1.25×10^{-3} and 0.5 s^{-1}. For the case in which diffusional influences are of diminished significance, $Đ_1/r_c^2$ = 0.5 s^{-1}, the separation selectivity favors C_2H_6 because of mixture adsorption equilibrium; in this case CO_2 exits the bed earlier. This is undesirable from the viewpoint of natural gas processing because we need to recover C_2H_6 as raffinate. With significantly stronger diffusional influences, choosing $Đ_1/r_c^2$ = 1.25×10^{-3} s^{-1}, uphill diffusion of CO_2 ensures that it enters the pores

https://doi.org/10.1021/prechem.2c00003
Precis. Chem. 2023, 1, 83−93

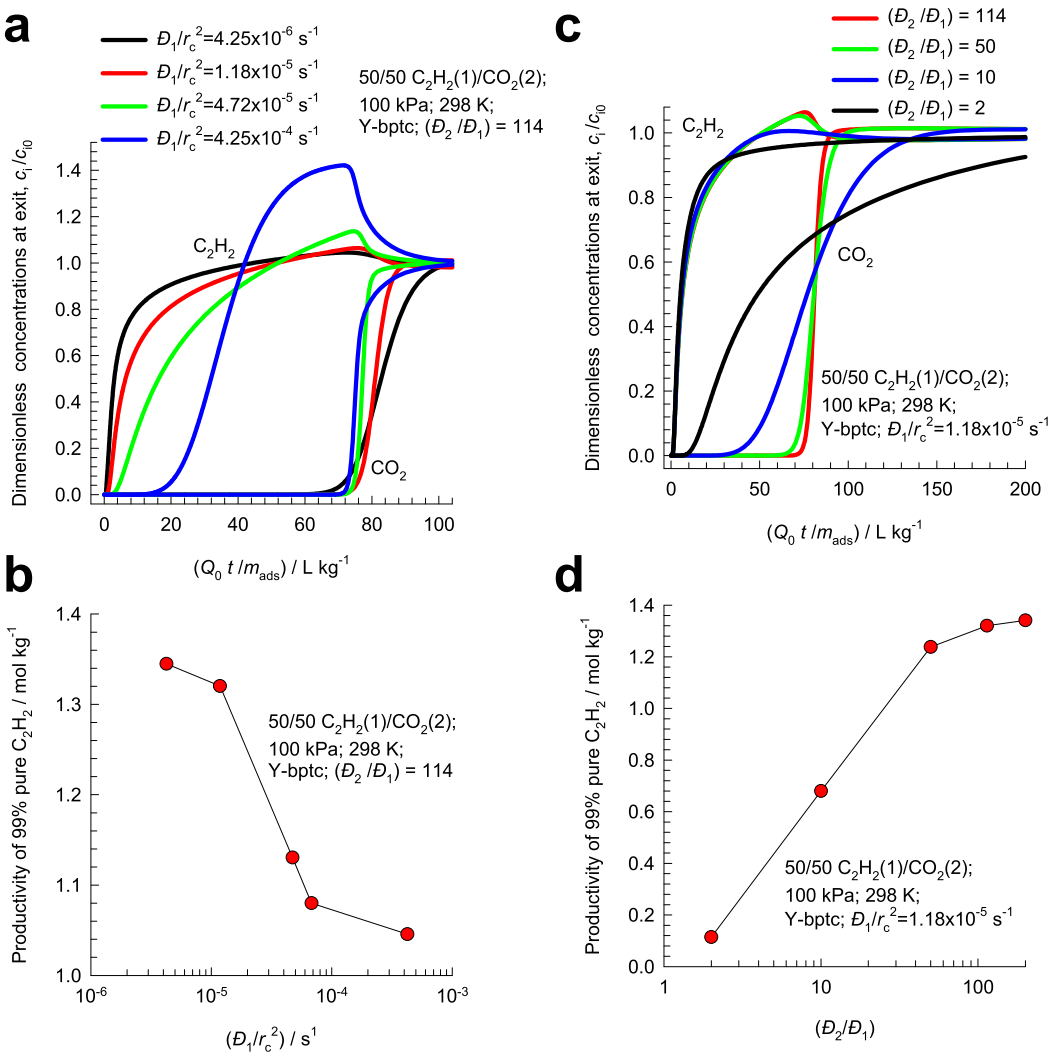

Figure 6. (a–d) Transient breakthrough of 50/50 $C_2H_2(1)/CO_2(2)$ mixtures through a fixed-bed adsorber packed with Y-bptc crystals operating at 298 K and total pressure p_t = 100 kPa. In the sets of simulations in (a, b): $Đ_1/r_c^2$ = 4.25 × 10^{-6}, 1.18 × 10^{-5}, 4.72 × 10^{-5}, and 4.25 × 10^{-4} s^{-1}, maintaining the ratio $Đ_2/Đ_1$ = 114. In the sets of simulations in (c, d): $Đ_1/r_c^2$ = 1.18 × 10^{-5} s^{-1}, and the ratio $Đ_2/Đ_1$ = 200, 114, 50, 10, and 2. In (a, c), the dimensionless concentrations at the exit of the adsorber, c_i/c_{i0}, are plotted as a function of a modified time parameter defined by Q_0t/m_{ads}. In (b, d), the C_2H_2 productivities are plotted as a function of (b) $Đ_1/r_c^2$ and (d) $Đ_2/Đ_1$.

preferentially, while C_2H_6 is rejected into the gas phase as raffinate, as is desired in practice. The stronger antisynergy between adsorption and diffusion serves to reverse the selectivity in favor of CO_2.

8. CONCLUSIONS

On the basis of a detailed and careful examination of a large number of synergistic and antisynergistic mixture separations using microporous crystalline adsorbents, two important conclusions may be drawn.

(1) For transient uptake within crystals, the more mobile component attains supraequilibrium loadings during the initial stages of the transience. For quantification of such overshoots, signifying uphill diffusion, we require the use of the M–S diffusion equations using $\partial\mu_i/\partial r$ as driving forces. The overshoots are engendered by the cross-coefficients $\Gamma_{ij}(i \neq j)$ of the matrix of thermodynamic correction factors. The component molar loadings, plotted in composition space, follow serpentine equilibration paths, which are also attributable to thermodynamic coupling influences. Use of the simplified eq 7 asserting $\Gamma_{ij} = \delta_{ij}$, ignoring thermodynamic coupling, results in monotonous equilibration trajectories without overshoots.

(2) Mixture separations in fixed-bed adsorption devices are influenced by a combination of three separate factors: adsorption selectivity, S_{ads}, diffusional time constants, $Đ_i/r_c^2$, and diffusion selectivity, $Đ_1/Đ_2$. Two different scenarios may be delineated. In synergistic separations, $S_{ads} > 1$; $Đ_1/Đ_2 > 1$, diffusional influences have the potential of enhancing the separation performance. In the second scenario, $S_{ads} > 1$; $Đ_1/Đ_2 < 1$, the antisynergy between adsorption and diffusion may be exploited to reverse the selectivity dictated by mixture adsorption equilibrium. For both scenarios, the productivities of the desired product in fixed-bed operations are crucially dependent on diffusional time constants, $Đ_i/r_c^2$; these need to be sufficiently low in order for diffusional influences to be effective. For synergistic or antisynergistic separations to be effective, the ratio $Đ_1/Đ_2$ should be large

https://doi.org/10.1021/prechem.2c00003
Precis. Chem. 2023, 1, 83–93

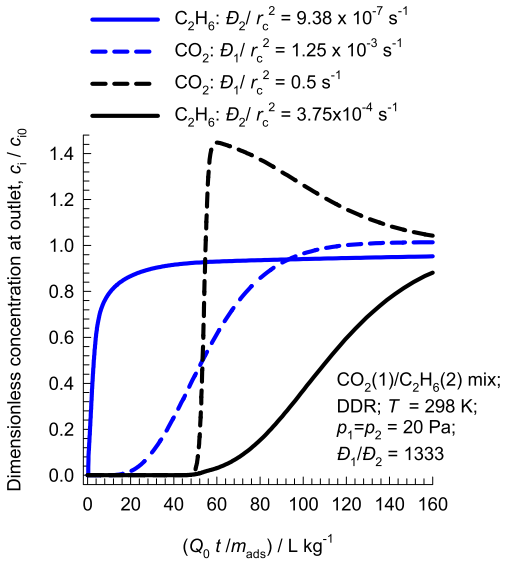

Figure 7. Transient breakthrough of 50/50 $CO_2(1)/C_2H_6(2)$ mixtures through a fixed-bed adsorber packed with DDR crystals operating at 298 K and total pressure p_t = 40 kPa. The dimensionless concentrations at the exit of the adsorber, c_i/c_{i0}, are plotted as a function of a modified time parameter defined by Q_0t/m_{ads}. For the two sets of simulations $Đ_1/r_c^2 = 1.25 \times 10^{-3}$ and 0.5 s^{-1}, maintaining the ratio $Đ_1/Đ_2 = 1333$.

enough, typically by more than one or two orders of magnitude.

■ ASSOCIATED CONTENT

Supporting Information

The Supporting Information is available free of charge at https://pubs.acs.org/doi/10.1021/prechem.2c00003.

Summary of the Maxwell−Stefan theory of diffusion in microporous materials, (b) methodology adopted for numerical solutions to transient uptake within a single crystalline particle, (c) methodology used for transient breakthroughs in fixed-bed adsorbers, and (d) simulation details including input data on unary isotherms and Maxwell−Stefan diffusivities for each case study (PDF)

■ AUTHOR INFORMATION

Corresponding Author

Rajamani Krishna − *Van't Hoff Institute for Molecular Sciences, University of Amsterdam Science Park, 904 1098 XH Amsterdam, The Netherlands;* orcid.org/0000-0002-4784-8530; Email: r.krishna@contact.uva.nl

Complete contact information is available at: https://pubs.acs.org/10.1021/prechem.2c00003

Notes

The author declares no competing financial interest.

■ NOMENCLATURE

Latin Alphabet

c_i molar concentration of species i, mol m^{-3}
c_{i0} molar concentration of species i in the fluid mixture at the inlet, mol m^{-3}
$Đ_i$ Maxwell−Stefan diffusivity for molecule−wall interaction, m^2 s^{-1}
$[D]$ Fick diffusivity matrix, m^2 s^{-1}
m_{ads} mass of adsorbent packed in the fixed bed, kg
n number of species in the mixture, dimensionless
N_i molar flux of species i with respect to the framework, mol m^{-2} s^{-1}
p_i partial pressure of species i in the mixture, Pa
p_t total system pressure, Pa
q_i component molar loading of species i, mol kg^{-1}
$\overline{q}_i$ radial-averaged component loading of species i, mol kg^{-1}
Q_0 volumetric flow rate of gas mixture entering the fixed bed, m^3 s^{-1}
r radial direction coordinate, m
r_c radius of crystallite, m
R gas constant, 8.314 J mol^{-1} K^{-1}
S_{ads} adsorption selectivity, dimensionless
t time, s
T absolute temperature, K

Greek Alphabet

Γ_{ij} thermodynamic factors, dimensionless
δ_{ij} Kronecker delta $\delta_{ij}(i = j) = 1$; $\delta_i(i \neq j) = 0$, dimensionless
λ_i eigenvalues of Fick diffusivity matrix $[D]$, m^2 s^{-1}
μ_i molar chemical potential, J mol^{-1}
ρ framework density, kg m^{-3}

■ REFERENCES

(1) Myers, A. L.; Prausnitz, J. M. Thermodynamics of Mixed Gas Adsorption. *A.I.Ch.E.J.* **1965**, *11*, 121−130.
(2) Krishna, R.; Van Baten, J. M. How Reliable is the Ideal Adsorbed Solution Theory for Estimation of Mixture Separation Selectivities in Microporous Crystalline Adsorbents? *ACS Omega* **2021**, *6*, 15499−15513.
(3) Ruthven, D. M. *Principles of Adsorption and Adsorption Processes*; John Wiley: New York, 1984.
(4) Yang, R. T. *Gas separation by adsorption processes*; Butterworth: Boston, MA, 1987.
(5) Yang, R. T. *Adsorbents: Fundamentals and Applications*; John Wiley & Sons, Inc.: Hoboken, NJ, 2003.
(6) Ruthven, D. M.; Farooq, S.; Knaebel, K. S. *Pressure swing adsorption*; VCH Publishers: New York, 1994.
(7) Krishna, R. Methodologies for Screening and Selection of Crystalline Microporous Materials in Mixture Separations. *Sep. Purif. Technol.* **2018**, *194*, 281−300.
(8) Krishna, R. Screening Metal-Organic Frameworks for Mixture Separations in Fixed-Bed Adsorbers using a Combined Selectivity/Capacity Metric. *RSC Adv.* **2017**, *7*, 35724−35737.
(9) Krishna, R. Methodologies for Evaluation of Metal-Organic Frameworks in Separation Applications. *RSC Adv.* **2015**, *5*, 52269−52295.
(10) Krishna, R. Elucidation and Characterization of Entropy Effects in Mixture Separations with Micro-porous Crystalline Adsorbents. *Sep. Purif. Technol.* **2019**, *215*, 227−241.
(11) Krishna, R.; van Baten, J. M. Investigating the potential of MgMOF-74 membranes for CO_2 capture. *J. Membr. Sci.* **2011**, *377*, 249−260.
(12) Wang, Y.; Zhao, D. Beyond Equilibrium: Metal-Organic Frameworks for Molecular Sieving and Kinetic Gas Separation. *Cryst. Growth Des.* **2017**, *17*, 2291−2308.
(13) Krishna, R. Highlighting the Influence of Thermodynamic Coupling on Kinetic Separations with Microporous Crystalline Materials. *ACS Omega* **2019**, *4*, 3409−3419.
(14) Ruthven, D. M.; Farooq, S. Air Separation by Pressure Swing Adsorption. *Gas Sep. Purif.* **1990**, *4*, 141−148.
(15) Chen, Y. D.; Yang, R. T.; Uawithya, P. Diffusion of oxygen, nitrogen and their mixtures in Carbon Molecular-Sieve. *A.I.Ch.E.J.* **1994**, *40*, 577−585.

(16) Bhadra, S. J. *Methane−Nitrogen Separation by Pressure Swing Adsorption*. Ph.D. Dissertation, National University of Singapore, Singapore, 2007.
(17) Bhadra, S. J.; Farooq, S. Separation of Methane Nitrogen Mixture by Pressure Swing Adsorption for Natural Gas Upgrading. *Ind. Eng. Chem. Res.* **2011**, *50*, 14030−14045.
(18) Lin, R.-B.; Li, L.; Zhou, H.-L.; Wu, H.; He, C.; Li, S.; Krishna, R.; Li, J.; Zhou, W.; Chen, B. Molecular Sieving of Ethylene from Ethane using a Rigid Metal-Organic Framework. *Nature Materials* **2018**, *17*, 1128−1133.
(19) Pimentel, B. R.; Lively, R. P. Propylene Enrichment via Kinetic Vacuum Pressure Swing Adsorption Using ZIF-8 Fiber Sorbents. *ACS Appl. Mater. Interfaces* **2018**, *10*, 36323−36331.
(20) Khalighi, M.; Chen, Y. F.; Farooq, S.; Karimi, I. A.; Jiang, J. W. Propylene/Propane Separation Using SiCHA. *Ind. Eng. Chem. Res.* **2013**, *52*, 3877−3892.
(21) He, C.; Zhang, P.; Wang, Y.; Zhang, Y.; Hu, T.; Li, L.; Li, J. Thermodynamic and kinetic synergetic separation of CO_2/C_2H_2 in an ultramicroporous metal-organic framework. *Sep. Purif. Technol.* **2023**, *304*, 122318.
(22) Jiang, Y.; Wang, L.; Yan, T.; Hu, J.; Sun, W.; Krishna, R.; Wang, D.; Gu, Z.; Liu, D.; Cui, X.; Xing, H.; Zhang, Y. Insights into thermodynamic-kinetic synergistic separation of propyne/propylene in anion pillared cage MOFs with entropy-enthalpy balanced adsorption sites. *Chem. Sci.* **2023**, *14*, 298−309.
(23) Remy, T.; Saint-Remi, J. C.; Singh, R.; Webley, P. A.; Baron, G. V.; Denayer, J. F. M. Adsorption and Separation of C1-C8 Alcohols on SAPO-34. *J. Phys. Chem. C* **2011**, *115*, 8117−8125.
(24) Krishna, R.; van Baten, J. M. Entropy-based Separation of Linear Chain Molecules by Exploiting Differences in the Saturation Capacities in Cage-type Zeolites. *Sep. Purif. Technol.* **2011**, *76*, 325−330.
(25) Krishna, R. Describing the Diffusion of Guest Molecules inside Porous Structures. *J. Phys. Chem. C* **2009**, *113*, 19756−19781.
(26) Krishna, R. Diffusion in Porous Crystalline Materials. *Chem. Soc. Rev.* **2012**, *41*, 3099−3118.
(27) Titze, T.; Chmelik, C.; Kärger, J.; van Baten, J. M.; Krishna, R. Uncommon Synergy Between Adsorption and Diffusion of Hexane Isomer Mixtures in MFI Zeolite Induced by Configurational Entropy Effects. *J. Phys. Chem. C* **2014**, *118*, 2660−2665.
(28) Habgood, H. W. The Kinetics of Molecular Sieve Action. Sorption of Nitrogen-Methane Mixtures by Linde Molecular Sieve 4A. *Canad. J. Chem.* **1958**, *36*, 1384−1397.
(29) Krishna, R. Diffusing Uphill with James Clerk Maxwell and Josef Stefan. *Chem. Eng. Sci.* **2019**, *195*, 851−880.
(30) Krishna, R.; Van Baten, J. M. Investigating the Non-idealities in Adsorption of CO_2-bearing Mixtures in Cation-exchanged Zeolites. *Sep. Purif. Technol.* **2018**, *206*, 208−217.
(31) Krishna, R.; van Baten, J. M. Using Molecular Dynamics Simulations for Elucidation of Molecular Traffic in Ordered Crystalline Microporous Materials. *Microporous Mesoporous Mater.* **2018**, *258*, 151−169.
(32) Krishna, R. Tracing the Origins of Transient Overshoots for Binary Mixture Diffusion in Microporous Crystalline Materials. *Phys. Chem. Chem. Phys.* **2016**, *18*, 15482−15495.
(33) Krishna, R. The Maxwell-Stefan Description of Mixture Diffusion in Nanoporous Crystalline Materials. *Microporous Mesoporous Mater.* **2014**, *185*, 30−50.
(34) Saint-Remi, J. C.; Baron, G. V.; Denayer, J. F. M. Non-Uniform Chain Length Dependent Diffusion of Short 1-Alcohols in SAPO-34 in Liquid Phase. *J. Phys. Chem. C* **2013**, *117*, 9758−9765.
(35) Binder, T.; Lauerer, A.; Chmelik, C.; Haase, J.; Kärger, J.; Ruthven, D. M. Micro-imaging of transient intracrystalline concentration profiles during two-component uptake of light hydrocarbon - carbon dioxide mixtures by DDR-type zeolites. *Ind. Eng. Chem. Res.* **2015**, *54*, 8997−9004.
(36) Lauerer, A.; Binder, T.; Chmelik, C.; Miersemann, E.; Haase, J.; Ruthven, D. M.; Kärger, J. Uphill Diffusion and Overshooting in the Adsorption of Binary Mixtures in Nanoporous Solids. *Nat. Commun.* **2015**, *6*, 7697.
(37) Krishna, R. A Maxwell-Stefan-Glueckauf Description of Transient Mixture Uptake in Microporous Adsorbents. *Sep. Purif. Technol.* **2018**, *191*, 392−399.
(38) Krishna, R.; van Baten, J. M.; Baur, R. Highlighting the Origins and Consequences of Thermodynamic Nonidealities in Mixture Separations using Zeolites and Metal-Organic Frameworks. *Microporous Mesoporous Mater.* **2018**, *267*, 274−292.
(39) Krishna, R.; van Baten, J. M. Influence of Adsorption Thermodynamics on Guest Diffusivities in Nanoporous Crystalline Materials. *Phys. Chem. Chem. Phys.* **2013**, *15*, 7994−8016.
(40) Krishna, R. Occupancy Dependency of Maxwell-Stefan Diffusivities in Ordered Crystalline Microporous Materials. *ACS Omega* **2018**, *3*, 15743−15753.
(41) Krishna, R. Uphill Diffusion in Multicomponent Mixtures. *Chem. Soc. Rev.* **2015**, *44*, 2812−2836.
(42) Majumdar, B.; Bhadra, S. J.; Marathe, R. P.; Farooq, S. Adsorption and Diffusion of Methane and Nitrogen in Barium Exchanged ETS-4. *Ind. Eng. Chem. Res.* **2011**, *50*, 3021−3034.
(43) Niessen, W.; Karge, H. G. Diffusion of *p*-xylene in Single and Binary Systems Investigated by FTIR Spectroscopy. *Microporous Mater.* **1993**, *1*, 1−8.
(44) Karge, H. G. Infrared Spectroscopic Investigation of Diffusion, Co-diffusion and Counter-diffusion of Hydrocarbon Molecules in Zeolites. *C. R. Chim.* **2005**, *8*, 303−319.
(45) Krishna, R.; Li, S.; van Baten, J. M.; Falconer, J. L.; Noble, R. D. Investigation of slowing-down and speeding-up effects in binary mixture permeation across SAPO-34 and MFI membranes. *Sep. Purif. Technol.* **2008**, *60*, 230−236.
(46) Tagliabue, M.; Farrusseng, D.; Valencia, S.; Aguado, S.; Ravon, U.; Rizzo, C.; Corma, A.; Mirodatos, C. Natural gas treating by selective adsorption: Material science and chemical engineering interplay. *Chem. Eng. J.* **2009**, *155*, 553−566.
(47) Jayaraman, A.; Hernandez-Maldonado, A. J.; Yang, R. T.; Chinn, D.; Munson, C. L.; Mohr, D. H. Clinoptilolites for Nitrogen/Methane Separation. *Chem. Eng. Sci.* **2004**, *59*, 2407−2417.
(48) Krishna, R.; van Baten, J. M. Screening of zeolite adsorbents for separation of hexane isomers: A molecular simulation study. *Sep. Purif. Technol.* **2007**, *55*, 246−255.
(49) Dubbeldam, D.; Krishna, R.; Calero, S.; Yazaydın, A. Ö. Computer-Assisted Screening of Ordered Crystalline Nanoporous Adsorbents for Separation of Alkane Isomers. *Angew. Chem. Int. Ed.* **2012**, *51*, 11867−11871.
(50) Herm, Z. R.; Wiers, B. M.; Van Baten, J. M.; Hudson, M. R.; Zajdel, P.; Brown, C. M.; Masciocchi, N.; Krishna, R.; Long, J. R.; Mason, J. A. Separation of Hexane Isomers in a Metal-Organic Framework with Triangular Channels. *Science* **2013**, *340*, 960−964.
(51) Krishna, R.; Smit, B.; Vlugt, T. J. H. Sorption-induced Diffusion-selective Separation of Hydrocarbon Isomers Using Silicalite. *J. Phys. Chem. A* **1998**, *102*, 7727−7730.
(52) Krishna, R.; Baur, R.; Van Baten, J. M. Highlighting Diffusional Coupling Effects in Zeolite Catalyzed Reactions by Combining the Maxwell-Stefan and Langmuir-Hinshelwood Formulations. *React. Chem. Eng.* **2017**, *2*, 324−336.
(53) Krishna, R.; van Baten, J. M. Commensurate-Incommensurate Adsorption and Diffusion in Ordered Crystalline Microporous Materials. *Phys. Chem. Chem. Phys.* **2017**, *19*, 20320−20337.
(54) Vlugt, T. J. H.; Krishna, R.; Smit, B. Molecular Simulations of Adsorption Isotherms for Linear and Branched Alkanes and Their Mixtures in Silicalite. *J. Phys. Chem. B* **1999**, *103*, 1102−1118.
(55) Krishna, R.; Baur, R. Modelling Issues in Zeolite Based Separation Processes. *Sep. Purif. Technol.* **2003**, *33*, 213−254.
(56) Matsuda, R.; Kitaura, R.; Kitagawa, S.; Kubota, Y.; Belosludov, R. V.; Kobayashi, T. C.; Sakamoto, H.; Chiba, T.; Takata, M.; Kawazoe, Y.; Mita, Y. Highly controlled acetylene accommodation in a metal-organic microporous material. *Nature* **2005**, *436*, 238−241.
(57) Cui, J.; Qiu, Z.; Yang, L.; Zhang, Z.; Cui, X.; Xing, H. Kinetic-Sieving of Carbon Dioxide from Acetylene through a Novel Sulfonic Ultramicroporous Material. *Angew. Chem. Int. Ed.* **2022**, *61*, No. e202208756.

https://doi.org/10.1021/prechem.2c00003
Precis. Chem. 2023, 1, 83−93

(58) Zhang, Z.; Peh, S. B.; Krishna, R.; Kang, C.; Chai, K.; Wang, Y.; Shi, D.; Zhao, D. Optimal Pore Chemistry in An Ultramicroporous Metal-Organic Framework for Benchmark Inverse CO_2/C_2H_2 Separation. *Angew. Chem. Int. Ed.* **2021**, *60*, 17198−17204.

https://doi.org/10.1021/prechem.2c00003
Precis. Chem. 2023, 1, 83−93

Supporting Information

Synergistic and Antisynergistic Intra-Crystalline Diffusional Influences on Mixture Separations in Fixed Bed Adsorbers

Rajamani Krishna

Van 't Hoff Institute for Molecular Sciences

University of Amsterdam

Science Park 904

1098 XH Amsterdam, The Netherlands

email: r.krishna@contact.uva.nl

ORCID 0000-0002-4784-8530

Contents

1 The Maxwell-Stefan Diffusion Formulation

Within micro-porous crystalline materials, such as zeolites, and metal-organic frameworks (MOFs), the guest molecules exist in the adsorbed phase. The Maxwell-Stefan (M-S) eqs for *n*-component diffusion in porous materials is applied in the following manner[1-3]

$$
\begin{aligned}
-\frac{\partial \mu_1}{\partial r} &= \frac{RT}{Đ_{12}} x_2 \left(u_1 - u_2\right) + \frac{RT}{Đ_{13}} x_3 \left(u_1 - u_3\right) + \ldots + \frac{RT}{Đ_1}\left(u_1\right) \\
-\frac{\partial \mu_2}{\partial r} &= \frac{RT}{Đ_{21}} x_1 \left(u_2 - u_1\right) + \frac{RT}{Đ_{23}} x_3 \left(u_2 - u_3\right) + \ldots + \frac{RT}{Đ_2}\left(u_2\right) \\
&\cdots\cdots \\
-\frac{\partial \mu_n}{\partial r} &= \frac{RT}{Đ_{n1}} x_1 \left(u_n - u_1\right) + \frac{RT}{Đ_{n2}} x_2 \left(u_n - u_3\right) + \ldots + \frac{RT}{Đ_n}\left(u_n\right)
\end{aligned}
\tag{S1}
$$

The left members of eq (S1) are the negative of the gradients of the chemical potentials, with the units N mol^{-1}; it represents the driving force acting per mole of species 1, 2, 3,..*n*. The u_i represents the velocity of motion of the adsorbate, defined in a reference frame with respect to the framework material. The crystalline framework is considered to be stationary. The term $RT/Đ_i$ is interpreted as the drag or friction coefficient between the guest species *i* and the pore wall. The term $RT/Đ_{ij}$ is interpreted as the friction coefficient for the *i-j* pair of guest molecules. The multiplier $x_i = q_i / q_t$ where q_i is the molar loading of adsorbate, and q_t is the *total* mixture loading $q_t = \sum_{i=1}^{n} q_i$. We expect the friction to be dependent on the number of molecules of *j* relative to that of component *i*.

An important, persuasive, argument for the use of the M-S formulation for mixture diffusion is that the M-S diffusivity $Đ_i$ in mixtures can be estimated using information on the loading dependence of the corresponding unary diffusivity values. Put another way, the M-S diffusivity . $Đ_i$. can be estimated from experimental data on *unary* diffusion in the porous material.

The M-S diffusivity $Đ_{ij}$ has the units m^2 s^{-1} and the physical significance of an *inverse* drag coefficient. The magnitudes of the M-S diffusivities $Đ_{ij}$ do not depend on the choice of the mixture reference velocity because eq (S1) is set up in terms of velocity differences. At the molecular level, the $Đ_{ij}$ reflect how the facility for transport of species *i correlates* with that of species *j*; they are also termed *exchange coefficients*.

The Maxwell-Stefan diffusion formulation (S1) is consistent with the theory of irreversible thermodynamics. The Onsager Reciprocal Relations imply that the M-S pair diffusivities are symmetric

$$Đ_{ij} = Đ_{ji} \tag{S2}$$

We define N_i as the number of moles of species *i* transported per m^2 of crystalline material per second

$$N_i \equiv \rho q_i u_i \tag{S3}$$

where ρ is the framework density with units of kg m^{-3}. Multiplying both sides of eq (S1) by ρq_i, the M-S equations for *n*-component diffusion in zeolites, MOFs, and ZIFs take the form [4-6]

$$-\rho \frac{q_i}{RT}\frac{\partial \mu_i}{\partial r} = \sum_{\substack{j=1 \\ j\neq i}}^{n} \frac{x_j N_i - x_i N_j}{Đ_{ij}} + \frac{N_i}{Đ_i}; \qquad i = 1, 2, ..n \tag{S4}$$

The fluxes N_i in eqs (S4) are defined in terms of the moles transported per m^2 of the *total surface of crystalline material*.

1.1 Thermodynamic correction factors

At thermodynamic equilibrium, the chemical potential of component *i* in the bulk fluid mixture equals the chemical potential of that component in the adsorbed phase. For the bulk fluid phase mixture we have

$$\frac{1}{RT}\frac{\partial \mu_i}{\partial r} = \frac{\partial \ln f_i}{\partial r} = \frac{1}{f_i}\frac{\partial f_i}{\partial r}; \qquad i = 1, 2, ..n \tag{S5}$$

In eq (S5), f_i represent the partial fugacities in the bulk fluid phase mixture. The chemical potential gradients $\partial \mu_i / \partial r$ can be related to the gradients of the molar loadings, q_i, by defining thermodynamic correction factors Γ_{ij}

$$\frac{q_i}{RT}\frac{\partial \mu_i}{\partial r} = \sum_{j=1}^{n} \Gamma_{ij} \frac{\partial q_j}{\partial r}; \quad \Gamma_{ij} = \frac{q_i}{f_i}\frac{\partial f_i}{\partial q_j}; \qquad i, j = 1, ...n \tag{S6}$$

The thermodynamic correction factors Γ_{ij} can be calculated by differentiation of the model describing mixture adsorption equilibrium. Generally speaking, the Ideal Adsorbed Solution Theory (IAST) of Myers and Prausnitz[7] is the preferred method for estimation of mixture adsorption equilibrium.

In some special case, the mixed-gas Langmuir model

$$\frac{q_i}{q_{i,sat}} = \theta_i = \frac{b_i f_i}{1 + \sum_{i=1}^{n} b_i f_i}; \quad i = 1, 2, ...n \tag{S7}$$

may be of adequate accuracy. Analytic differentiation of eq (S7) yields

$$\Gamma_{ij} = \delta_{ij} + \left(\frac{q_{i,sat}}{q_{j,sat}}\right)\left(\frac{\theta_i}{\theta_V}\right); \qquad i, j = 1, 2 \ldots n \tag{S8}$$

where the fractional vacancy θ_V is defined as

$$\theta_V = 1 - \theta_t = 1 - \sum_{i=1}^{n} \theta_i \tag{S9}$$

The elements of the matrix of thermodynamic factors Γ_{ij} can be calculated explicitly from information on the component loadings q_i in the adsorbed phase; this is the persuasive advantage of the use of the mixed-gas Langmuir model. By contrast, the IAST does not allow the calculation of Γ_{ij} explicitly from knowledge on the component loadings q_i in the adsorbed phase; a numerical procedure is required.

In the scenario in which correlation effects are of negligible importance, eqs (S4) simplify to yield

$$N_i = -\rho Đ_i \sum_{j=1}^{n} \Gamma_{ij} \frac{\partial q_j}{\partial r}; \qquad i = 1, 2..n \tag{S10}$$

Furthermore, if thermodynamic correction factors are also ignored, eq (S4) reduces to a set of uncoupled equations

$$N_i = -\rho Đ_i \frac{\partial q_i}{\partial r}; \qquad i = 1, 2..n \tag{S11}$$

Watch also the video presentation titled **Diffusion in Micropores** on YouTube

https://www.youtube.com/@rajamanikrishna250/videos

1.2 M-S formulation for binary mixture diffusion

For binary mixture diffusion inside microporous crystalline materials the Maxwell-Stefan equations (S4) are written

$$\begin{aligned} -\rho\frac{q_1}{RT}\frac{\partial\mu_1}{\partial r} &= \frac{x_2N_1 - x_1N_2}{Đ_{12}} + \frac{N_1}{Đ_1} \\ -\rho\frac{q_2}{RT}\frac{\partial\mu_2}{\partial r} &= \frac{x_1N_2 - x_2N_1}{Đ_{12}} + \frac{N_2}{Đ_2} \end{aligned} \tag{S12}$$

The first members on the right hand side of Eq (S12) are required to quantify slowing-down effects that characterize binary mixture diffusion.[1, 2, 8] There is no experimental technique for direct determination of the exchange coefficients $Đ_{12}$, that quantify molecule-molecule interactions.

In two-dimensional matrix notation, eq (S6) take the form

$$-\begin{pmatrix} \frac{q_1}{RT}\frac{\partial\mu_1}{\partial r} \\ \frac{q_2}{RT}\frac{\partial\mu_2}{\partial r} \end{pmatrix} = [\Gamma]\begin{pmatrix} \frac{\partial q_1}{\partial r} \\ \frac{\partial q_2}{\partial r} \end{pmatrix} \tag{S13}$$

For the mixed-gas Langmuir model, eq (S7), we can derive simple analytic expressions for the four elements of the matrix of thermodynamic factors:[9]

$$\begin{bmatrix} \Gamma_{11} & \Gamma_{12} \\ \Gamma_{21} & \Gamma_{22} \end{bmatrix} = \frac{1}{1-\theta_1-\theta_2}\begin{bmatrix} 1-\theta_2 & \frac{q_{1,sat}}{q_{2,sat}}\theta_1 \\ \frac{q_{2,sat}}{q_{1,sat}}\theta_2 & 1-\theta_1 \end{bmatrix} = \begin{bmatrix} 1+b_1f_1 & \frac{q_{1,sat}}{q_{2,sat}}b_1f_1 \\ \frac{q_{2,sat}}{q_{1,sat}}b_2f_2 & 1+b_2f_2 \end{bmatrix} \tag{S14}$$

where the fractional occupancies, θ_i, are defined by eq (S7).

Let us define the square matrix [B]

$$[B]=\begin{bmatrix} \frac{1}{Đ_1}+\frac{x_2}{Đ_{12}} & -\frac{x_1}{Đ_{12}} \\ -\frac{x_2}{Đ_{12}} & \frac{1}{Đ_2}+\frac{x_1}{Đ_{12}} \end{bmatrix};\quad [B]^{-1}=\frac{1}{1+\frac{x_1Đ_2}{Đ_{12}}+\frac{x_2Đ_1}{Đ_{12}}}\begin{bmatrix} Đ_1\left(1+\frac{x_1Đ_2}{Đ_{12}}\right) & \frac{x_1Đ_1Đ_2}{Đ_{12}} \\ \frac{x_2Đ_1Đ_2}{Đ_{12}} & Đ_2\left(1+\frac{x_2Đ_1}{Đ_{12}}\right) \end{bmatrix} \tag{S15}$$

In proceeding further, it is convenient to define a 2×2 dimensional square matrix $[\Lambda]$:

$$[\Lambda]=\begin{bmatrix} \frac{1}{Đ_1}+\frac{x_2}{Đ_{12}} & -\frac{x_1}{Đ_{12}} \\ -\frac{x_2}{Đ_{12}} & \frac{1}{Đ_2}+\frac{x_1}{Đ_{12}} \end{bmatrix}^{-1}=\frac{1}{1+\frac{x_1Đ_2}{Đ_{12}}+\frac{x_2Đ_1}{Đ_{12}}}\begin{bmatrix} Đ_1\left(1+\frac{x_1Đ_2}{Đ_{12}}\right) & \frac{x_1Đ_1Đ_2}{Đ_{12}} \\ \frac{x_2Đ_1Đ_2}{Đ_{12}} & Đ_2\left(1+\frac{x_2Đ_1}{Đ_{12}}\right) \end{bmatrix} \tag{S16}$$

Eq (S12) can be re-cast into 2-dimensional matrix notation

$$(N)=-\rho[\Lambda][\Gamma]\frac{\partial(q)}{\partial r};$$

$$\begin{pmatrix} N_1 \\ N_2 \end{pmatrix}=-\frac{\rho}{1+\frac{x_1Đ_2}{Đ_{12}}+\frac{x_2Đ_1}{Đ_{12}}}\begin{bmatrix} Đ_1\left(1+\frac{x_1Đ_2}{Đ_{12}}\right) & \frac{x_1Đ_1Đ_2}{Đ_{12}} \\ \frac{x_2Đ_1Đ_2}{Đ_{12}} & Đ_2\left(1+\frac{x_2Đ_1}{Đ_{12}}\right) \end{bmatrix}\begin{bmatrix} \Gamma_{11} & \Gamma_{12} \\ \Gamma_{21} & \Gamma_{22} \end{bmatrix}\begin{pmatrix} \frac{\partial q_1}{\partial r} \\ \frac{\partial q_2}{\partial r} \end{pmatrix} \tag{S17}$$

The elements of $[B]$ can be obtained by inverting the matrix $[\Lambda]$:

$$\begin{bmatrix} B_{11} & B_{12} \\ B_{21} & B_{22} \end{bmatrix}=\begin{bmatrix} \frac{1}{Đ_1}+\frac{x_2}{Đ_{12}} & -\frac{x_1}{Đ_{12}} \\ -\frac{x_2}{Đ_{12}} & \frac{1}{Đ_2}+\frac{x_1}{Đ_{12}} \end{bmatrix}=[\Lambda]^{-1} \tag{S18}$$

A 2×2 dimensional Fick diffusivity matrix $[D]$ is defined as the product of $[\Lambda]$ and the matrix of thermodynamic correction factors $[\Gamma]$:

$$[D]=[B]^{-1}[\Gamma]=\frac{1}{1+\frac{x_1Đ_2}{Đ_{12}}+\frac{x_2Đ_1}{Đ_{12}}}\begin{bmatrix} Đ_1\left(1+\frac{x_1Đ_2}{Đ_{12}}\right) & \frac{x_1Đ_1Đ_2}{Đ_{12}} \\ \frac{x_2Đ_1Đ_2}{Đ_{12}} & Đ_2\left(1+\frac{x_2Đ_1}{Đ_{12}}\right) \end{bmatrix}\begin{bmatrix} \Gamma_{11} & \Gamma_{12} \\ \Gamma_{21} & \Gamma_{22} \end{bmatrix} \tag{S19}$$

$$(N)=-\rho[D]\frac{\partial(q)}{\partial r}$$

1.3 Negligible correlations scenario for M-S diffusivities

For values of $Đ_1/Đ_{12} \to 0$, and $Đ_2/Đ_{12} \to 0$, the contribution of the first right member of M-S Eq (S12) can be ignored and correlations can be considered to be of negligible importance; we derive

$$\frac{Đ_1}{Đ_{12}} \to 0; \quad \frac{Đ_2}{Đ_{12}} \to 0; \quad \begin{bmatrix} \Lambda_{11} & \Lambda_{12} \\ \Lambda_{21} & \Lambda_{22} \end{bmatrix} \to \begin{bmatrix} Đ_1 & 0 \\ 0 & Đ_2 \end{bmatrix}$$
$$\begin{bmatrix} D_{11} & D_{12} \\ D_{21} & D_{22} \end{bmatrix} = \begin{bmatrix} Đ_1 & 0 \\ 0 & Đ_2 \end{bmatrix} \begin{bmatrix} \Gamma_{11} & \Gamma_{12} \\ \Gamma_{21} & \Gamma_{22} \end{bmatrix} \tag{S20}$$
$$\begin{pmatrix} N_1 \\ N_2 \end{pmatrix} = -\rho \begin{bmatrix} D_{11} & D_{12} \\ D_{21} & D_{22} \end{bmatrix} \begin{pmatrix} \frac{\partial q_1}{\partial r} \\ \frac{\partial q_2}{\partial r} \end{pmatrix}$$

Eq (S20) is valid, as a first approximation, for diffusion in cage-type zeolites with 8-ring windows (CHA, LTA, DDR, ERI) and ZIF-8; see earlier publications.[5, 10-16] For all of the guest/host combinations considered in this article, the use of eq (S20) is justified.

When correlation effects are negligible, the diffusional coupling effects are solely traceable to mixture adsorption thermodynamics, embodied in the matrix $[\Gamma]$.

If the mixed-gas Langmuir model is used to describe mixture adsorption equilibrium, the matrix of thermodynamic correction factors is given by Eq (S14). Combining eqs (S14)., and (S20) we obtain the flux expression

$$\begin{pmatrix} N_1 \\ N_2 \end{pmatrix} = -\rho \begin{bmatrix} Đ_1 & 0 \\ 0 & Đ_2 \end{bmatrix} \frac{1}{1-\theta_1-\theta_2} \begin{bmatrix} 1-\theta_2 & \frac{q_{1,sat}}{q_{2,sat}}\theta_1 \\ \frac{q_{2,sat}}{q_{1,sat}}\theta_2 & 1-\theta_1 \end{bmatrix} \begin{pmatrix} \frac{\partial q_1}{\partial r} \\ \frac{\partial q_2}{\partial r} \end{pmatrix} \tag{S21}$$

Eq (S21) is essentially equivalent to the flux relation used by Habgood[17] to model transient overshoots in the loading of N_2 during transient uptake of N_2/CH_4 in LTA-4A zeolite. These flux relations (S21) are also incorporated into the models for describing the transient breakthroughs in fixed bed adsorbers by Ruthven, Farooq, Knaebel, and co-workers.[18-21]

1.4 Ignoring thermodynamic coupling effects

In the Henry regime of adsorption, i.e. at low component loading, thermodynamic correction factors may be adequately described by $\Gamma_{ij} = \delta_{ij}$, the Kronecker delta.

$$\begin{bmatrix} \Gamma_{11} & \Gamma_{12} \\ \Gamma_{21} & \Gamma_{22} \end{bmatrix} = \begin{bmatrix} 1 & 0 \\ 0 & 1 \end{bmatrix}; \quad \begin{pmatrix} N_1 \\ N_2 \end{pmatrix} = -\rho \begin{bmatrix} Đ_1 & 0 \\ 0 & Đ_2 \end{bmatrix} \begin{pmatrix} \dfrac{\partial q_1}{\partial r} \\ \dfrac{\partial q_2}{\partial r} \end{pmatrix} \tag{S22}$$

Indeed, the major objective of this article is to demonstrate the inadequacy of Eq (S22) to model transient mixture uptake in microporous crystals, and transient breakthroughs in fixed bed adsorbers.

1.5 Eigenvalues and Eigenvectors of the Fick Diffusivity Matrix

For future discussions it is necessary to determine the eigenvalues of the Fick diffusivity matrix in Eq (S20); the two eigenvalues λ_1, λ_2 may be determined as follows

$$\begin{aligned}
&\text{trace}\left([D]\right) = Đ_1\Gamma_{11} + Đ_2\Gamma_{22} \\
&|D| = Đ_1\Gamma_{11}Đ_2\Gamma_{22} - Đ_1\Gamma_{12}Đ_2\Gamma_{21} = Đ_1Đ_2|\Gamma| \\
&\text{discriminant}\left([D]\right) = \sqrt{\left(Đ_1\Gamma_{11} + Đ_2\Gamma_{22}\right)^2 - 4Đ_1Đ_2|\Gamma|} \\
&= \sqrt{\left(Đ_1^2\Gamma_{11}^2 + Đ_2^2\Gamma_{22}^2 + 2Đ_1\Gamma_{11}Đ_2\Gamma_{22}\right) - 4Đ_1Đ_2\Gamma_{11}\Gamma_{22} + 4Đ_1Đ_2\Gamma_{12}\Gamma_{21}} \\
&= \sqrt{\left(Đ_1^2\Gamma_{11}^2 + Đ_2^2\Gamma_{22}^2 - 2Đ_1\Gamma_{11}Đ_2\Gamma_{22}\right) + 4Đ_1Đ_2\Gamma_{12}\Gamma_{21}} \\
&= \sqrt{\left(Đ_1\Gamma_{11} - Đ_2\Gamma_{22}\right)^2 + 4Đ_1Đ_2\Gamma_{12}\Gamma_{21}} \\
&\lambda_1 = \frac{Đ_1\Gamma_{11} + Đ_2\Gamma_{22} + \sqrt{\left(Đ_1\Gamma_{11} - Đ_2\Gamma_{22}\right)^2 + 4Đ_1Đ_2\Gamma_{12}\Gamma_{21}}}{2} \\
&\lambda_2 = \frac{Đ_1\Gamma_{11} + Đ_2\Gamma_{22} - \sqrt{\left(Đ_1\Gamma_{11} - Đ_2\Gamma_{22}\right)^2 + 4Đ_1Đ_2\Gamma_{12}\Gamma_{21}}}{2}
\end{aligned} \tag{S23}$$

Let $[P]$ represent the modal matrix of $[D]$; $[P]$ has the property that

$$[P]^{-1}[D][P] = \begin{bmatrix} \lambda_1 & 0 \\ 0 & \lambda_2 \end{bmatrix} \tag{S24}$$

In eq (S24), λ_1 and λ_2 are the eigenvalues of the Fick diffusivity matrix $[D]$. The columns of $[P]$ are the eigenvectors $(e_1)=\begin{pmatrix}1\\ -\dfrac{D_{11}-\lambda_1}{D_{12}}\end{pmatrix}$ c and $(e_2)=\begin{pmatrix}1\\ -\dfrac{D_{21}}{D_{22}-\lambda_2}\end{pmatrix}$ of $[D]$. If $\lambda_1>\lambda_2$, (e_1) is the fast eigenvector, and (e_2) is the slow eigenvector.

$$[P]=[(e_1)(e_2)]=\begin{bmatrix}1 & 1\\ -\dfrac{D_{11}-\lambda_1}{D_{12}} & -\dfrac{D_{21}}{D_{22}-\lambda_2}\end{bmatrix}$$

$$-\frac{D_{11}-\lambda_1}{D_{12}}=-\frac{D_{11}}{D_{12}}+\frac{\lambda_1}{D_{12}}=-\frac{\Gamma_{11}}{\Gamma_{12}}+\frac{\lambda_1}{D_{12}} \qquad \text{(S25)}$$

$$-\frac{D_{22}-\lambda_2}{D_{21}}=-\frac{D_{22}}{D_{21}}+\frac{\lambda_2}{D_{21}}=-\frac{\Gamma_{22}}{\Gamma_{21}}+\frac{\lambda_2}{D_{21}}$$

The elements e_{12}, e_{22} of the two eigenvectors can be determined as follows

$$\frac{\lambda_1}{D_{12}}=\frac{\lambda_1}{Đ_1\Gamma_{12}}=\frac{Đ_1\Gamma_{11}+Đ_2\Gamma_{22}+\sqrt{\left(Đ_1\Gamma_{11}-Đ_2\Gamma_{22}\right)^2+4Đ_1Đ_2\Gamma_{12}\Gamma_{21}}}{2Đ_1\Gamma_{12}}$$

$$=\frac{1}{2}\left(\frac{\Gamma_{11}}{\Gamma_{12}}+\frac{Đ_2}{Đ_1}\frac{\Gamma_{22}}{\Gamma_{12}}+\frac{1}{\Gamma_{12}}\sqrt{\left(\Gamma_{11}-\frac{Đ_2}{Đ_1}\Gamma_{22}\right)^2+4\frac{Đ_2}{Đ_1}\Gamma_{12}\Gamma_{21}}\right) \qquad \text{(S26)}$$

$$e_{12}=-\frac{D_{11}-\lambda_1}{D_{12}}=-\frac{D_{11}}{D_{12}}+\frac{\lambda_1}{D_{12}}=-\frac{\Gamma_{11}}{\Gamma_{12}}+\frac{\lambda_1}{D_{12}}=\frac{1}{2}\left(-\frac{\Gamma_{11}}{\Gamma_{12}}+\frac{Đ_2}{Đ_1}\frac{\Gamma_{22}}{\Gamma_{12}}+\sqrt{\left(\frac{\Gamma_{11}}{\Gamma_{12}}-\frac{Đ_2}{Đ_1}\frac{\Gamma_{22}}{\Gamma_{12}}\right)^2+4\frac{Đ_2}{Đ_1}\frac{\Gamma_{21}}{\Gamma_{12}}}\right)$$

$$\frac{\lambda_2}{D_{21}}=\frac{\lambda_2}{Đ_2\Gamma_{21}}=\frac{Đ_1\Gamma_{11}+Đ_2\Gamma_{22}-\sqrt{\left(Đ_1\Gamma_{11}-Đ_2\Gamma_{22}\right)^2+4Đ_1Đ_2\Gamma_{12}\Gamma_{21}}}{Đ_2\Gamma_{21}}$$

$$=\frac{1}{2}\left(\frac{Đ_1}{Đ_2}\frac{\Gamma_{11}}{\Gamma_{21}}+\frac{\Gamma_{22}}{\Gamma_{21}}-\frac{1}{\Gamma_{21}}\sqrt{\left(\frac{Đ_1}{Đ_2}\Gamma_{11}-\Gamma_{22}\right)^2+4\frac{Đ_1}{Đ_2}\Gamma_{12}\Gamma_{21}}\right) \qquad \text{(S27)}$$

$$\frac{1}{e_{22}}=-\frac{D_{22}-\lambda_2}{D_{21}}=-\frac{D_{22}}{D_{21}}+\frac{\lambda_2}{D_{21}}=-\frac{\Gamma_{22}}{\Gamma_{21}}+\frac{\lambda_2}{D_{21}}=\frac{1}{2}\left(\frac{Đ_1}{Đ_2}\frac{\Gamma_{11}}{\Gamma_{21}}-\frac{\Gamma_{22}}{\Gamma_{21}}-\sqrt{\left(\frac{Đ_1}{Đ_2}\frac{\Gamma_{11}}{\Gamma_{21}}-\frac{\Gamma_{22}}{\Gamma_{21}}\right)^2+4\frac{Đ_1}{Đ_2}\frac{\Gamma_{12}}{\Gamma_{21}}}\right)$$

2 IAST calculations of mixture adsorption equilibrium

2.1 Brief outline of theory

Within microporous crystalline materials such as zeolites and metal-organic frameworks (MOFs), the guest molecules exist in the adsorbed phase. The Gibbs adsorption equation in differential form is

$$Ad\pi = \sum_{i=1}^{n} q_i d\mu_i \tag{S28}$$

The quantity A is the surface area per kg of framework, with units of m^2 per kg of the framework of the crystalline material; q_i is the molar loading of component i in the adsorbed phase with units moles per kg of framework; μ_i is the molar chemical potential of component i. The spreading pressure π has the same units as surface tension, i.e. N m^{-1}.

The chemical potential of any component in the adsorbed phase, μ_i, equals that in the bulk fluid phase. If the partial fugacities in the bulk fluid phase are f_i, we have

$$d\mu_i = RTd \ln f_i \tag{S29}$$

where R is the gas constant (= 8.314 J mol^{-1} K^{-1}).

Briefly, the basic equation of Ideal Adsorbed Solution Theory (IAST) theory of Myers and Prausnitz[7] is the analogue of Raoult's law for vapor-liquid equilibrium, i.e.

$$f_i = P_i^0 x_i; \quad i = 1, 2, ...n \tag{S30}$$

where x_i is the mole fraction in the adsorbed phase

$$x_i = \frac{q_i}{q_1 + q_2 + ...q_n} \tag{S31}$$

and P_i^0 is the pressure for sorption of every component i, which yields the same spreading pressure, π for each of the pure components, as that for the mixture:

$$\frac{\pi A}{RT} = \int_0^{P_1^0} \frac{q_1^0(f)}{f} df = \int_0^{P_2^0} \frac{q_2^0(f)}{f} df = \int_0^{P_3^0} \frac{q_3^0(f)}{f} df = \ldots \tag{S32}$$

where $q_i^0(f)$ is the *pure* component adsorption isotherm. The units of $\frac{\pi A}{RT} \equiv \Phi$, also called the surface potential,[22, 23] are mol kg^{-1}; the surface potential has also been called the adsorption potential in several recent publications.[24-27]

The unary isotherm may be described by say the 1-site Langmuir isotherm

$$q^0(f) = q_{sat} \frac{bf}{1+bf}; \quad \theta = \frac{bf}{1+bf} \tag{S33}$$

where we define the fractional *occupancy* of the adsorbate molecules, $\theta = q^0(f)/q_{sat}$. The superscript 0 is used to emphasize that $q^0(f)$ relates the *pure component* loading to the bulk fluid fugacity. More generally, the unary isotherms may need to be described by, say, the dual-site Langmuir-Freundlich model

$$q^0(f) = q_{A,sat} \frac{b_A f^{\nu_A}}{1+b_A f^{\nu_A}} + q_{B,sat} \frac{b_B f^{\nu_B}}{1+b_B f^{\nu_B}} \tag{S34}$$

Each of the integrals in Eq (S32) can be evaluated analytically:

$$\begin{aligned} \Phi &= \int_{f=0}^{P_i^0} \frac{q^0(f)}{f} df = \frac{q_{A,sat}}{\nu_A} \ln\left(1+b_A\left(P_i^0\right)^{\nu_A}\right) + \frac{q_{B,sat}}{\nu_B} \ln\left(1+b_B\left(P_i^0\right)^{\nu_B}\right) \\ \Phi &= \int_{f=0}^{P_i^0} \frac{q^0(f)}{f} df = \frac{q_{A,sat}}{\nu_A} \ln\left(1+b_A\left(\frac{f_i}{x_i}\right)^{\nu_A}\right) + \frac{q_{B,sat}}{\nu_B} \ln\left(1+b_B\left(\frac{f_i}{x_i}\right)^{\nu_B}\right) \end{aligned} \tag{S35}$$

The right members of eq (S35) is a function of P_i^0. For multicomponent mixture adsorption, each of the equalities on the right side of eq (S32) must be satisfied. These constraints may be solved using a suitable equation solver, to yield the set of values of P_1^0, P_2^0, P_3^0,.. P_n^0, all of which satisfy eq (S32). The corresponding values of the integrals using these as upper limits of integration must yield the same value of the surface potential $\frac{\pi A}{RT} \equiv \Phi$ for each component; this ensures that the obtained solution is the correct one.

The adsorbed phase mole fractions x_i are then determined using eq (S30):

$$x_i = \frac{f_i}{P_i^0}; \quad i = 1, 2, ...n \tag{S36}$$

The applicability of eq (S36) mandates that all of the adsorption sites within the microporous material are equally accessible to each of the guest molecules, implying a homogeneous distribution of guest adsorbates within the pore landscape, with no preferential locations of any guest species. The circumstances in which this mandate is not fulfilled are highlighted in recent works.[25-28]

A further key assumption of the IAST is that the enthalpies and surface areas of the adsorbed molecules do not change upon mixing. If the total mixture loading is q_t, the area covered by the adsorbed mixture is $\frac{A}{q_t}$ with units of m^2 (mole mixture)$^{-1}$. Therefore, the assumption of no surface area change due to mixture adsorption translates as $\frac{A}{q_t} = \frac{Ax_1}{q_1^0\left(P_1^0\right)} + \frac{Ax_2}{q_2^0\left(P_2^0\right)} + \cdots \frac{Ax_n}{q_n^0\left(P_n^0\right)}$; the total mixture loading is $q_t = q_1 + q_2 ... + q_n$ is calculated from

$$\frac{1}{q_t} = \frac{x_1}{q_1^0(P_1^0)} + \frac{x_2}{q_2^0(P_2^0)} + ... + \frac{x_n}{q_n^0(P_n^0)} \tag{S37}$$

in which $q_1^0(P_1^0)$, $q_2^0(P_2^0)$,… $q_n^0(P_n^0)$ are determined from the unary isotherm fits, using the sorption pressures for each component P_1^0, P_2^0, P_3^0,.. P_n^0 that are available from the solutions to eqs (S32), and (S35). The occurrence of molecular clustering and hydrogen bonding should be expected to applicability of eq (S37) because the surface area occupied by a molecular cluster is different from that of each of the un-clustered guest molecules in the adsorbed phase.

The entire set of eqs (S30) to (S37) need to be solved numerically to obtain the loadings, q_i of the individual components in the mixture.

Watch also the presentation titled **The IAST for Mixture Adsorption Equilibrium** on YouTube https://www.youtube.com/@rajamanikrishna250/videos

3 Transient breakthroughs in fixed bed adsorbers

We first analyze the transient uptake of mixtures within a spherical micro-porous crystalline particle. Watch also the presentation titled **Transient Breakthrough Simulations** on YouTube https://www.youtube.com/@rajamanikrishna250/videos

3.1 Transient uptake inside microporous crystals

The radial distribution of molar loadings, q_i, within a spherical crystallite, of radius r_c, is obtained from a solution of a set of differential equations describing the uptake

$$\rho \frac{\partial q_i(r,t)}{\partial t} = -\frac{1}{r^2}\frac{\partial}{\partial r}\left(r^2 N_i\right) \tag{S38}$$

The intra-crystalline fluxes N_i, in turn, are related to the radial gradients in the molar loadings by Eq (S17), or the simplified Eq (S20) for the negligible correlations scenario. At time $t = 0$, i.e. the initial conditions, the molar loadings $q_i(r,0)$ at all locations r within the crystal are uniform (zero loadings). For all times $t \geq 0$, the exterior of the crystal is brought into contact with a bulk gas mixture at partial pressures p_{i0} that is maintained constant till the crystal reaches thermodynamic equilibrium with the surrounding gas mixture. At any time t, the component loadings at the surface of the particle $q_i(r_c,t) = q_i^*$ is in equilibrium with the bulk phase gas mixture with partial pressures p_{i0}. In the general case, the component loadings are calculated using the Ideal Adsorbed Solution Theory (IAST) of Myers and Prausnitz.[7] Alternatively, in some cases, the mixed-gas Langmuir eq (S7) may be of sufficient accuracy. An important advantage of the use of the mixed-gas Langmuir model is that the matrix of the thermodynamic correction factors can be determined explicitly using Eq (S14).

At time t, during the transient approach to thermodynamic equilibrium, the spatial-averaged component loading within the crystallites of radius r_c is calculated using

$$\bar{q}_i(t) = \frac{3}{r_c^3}\int_0^{r_c} q_i(r,t) r^2 dr \tag{S39}$$

Summing eq (S39) over all n species in the mixture allows calculation of the *total average* molar loading of the mixture within the crystallite

$$\bar{q}_t(t,z) = \sum_{i=1}^{n} \bar{q}_i(t,z) \tag{S40}$$

The spatial-averaged $\bar{q}_i(t)$ and $\bar{q}_t(t,z)$ can be compared directly with experimental transient uptake data.

For n-component transient uptake, the set of eqs (S17), (S38), and (S39), and (S40) need to be solved numerically using robust computational techniques. Eqs (S38) are first subjected to finite volume discretization. One of two strategies can be adopted: (a) equi-volume discretization, or (b) equi-distant discretization; see Figure S1. The choice of the discretization scheme used is crucially important in obtaining accurate, converged results. The choice of equi-volume slices is needed when the gradients of the loadings are particularly steep nearer to $r = r_c$. For either strategy, about 20 – 150 slices were employed in the simulations presented in this work, depending on the guest/host combination. Combination of the discretized partial differential equations (S38) along with algebraic equations describing mixture adsorption equilibrium (IAST or mixed-gas Langmuir model), results in a set of differential-algebraic equations (DAEs), which are solved using BESIRK.[29] BESIRK is a sparse matrix solver, based on the semi-implicit Runge-Kutta method originally developed by Michelsen,[30] and extended with the Bulirsch-Stoer extrapolation method.[31] Use of BESIRK improves the numerical solution efficiency in solving the set of DAEs. The evaluation of the sparse Jacobian required in the numerical algorithm is largely based on analytic expressions.[9] Further details of the numerical procedures used in this work, are provided by Krishna and co-workers;[9, 32-34] interested readers are referred to our website that contains the numerical details.[32]

3.2 Analytic solution for binary uptake inside microporous crystals

If the matrix of Fick diffusivities, $[D]=[B]^{-1}[\Gamma]$, defined by either eq (S19), or eq (S20) may be considered to be loading-independent during the entire duration of the equilibration process, it is possible to obtained an analytic solution for the component loading. The analytic solution, derived first by Geddes[35] to describe diffusion inside spherical vapor bubbles on distillation trays, is expressed as

$$\frac{\left(q^*-\bar{q}(t)\right)}{\left(q^*-q_0\right)}=\frac{6}{\pi^2}\sum_{m=1}^{\infty}\frac{\exp(-m^2\pi^2\frac{D}{r_c^2}t)}{m^2};$$
$$\left(q^*-\bar{q}(t)\right)=Q\left(q^*-q_0\right); \tag{S41}$$
$$Q=\frac{6}{\pi^2}\sum_{m=1}^{\infty}\frac{\exp(-m^2\pi^2\frac{D}{r_c^2}t)}{m^2}$$

Eq (S41) hold when (a) the initial loadings at all locations r within the crystal are uniform, i.e. $q(r,0)=q_0$, and (b) for all times $t\geq 0$, the exterior of the crystal is brought into contact with a bulk fluid mixture at a bulk pressure $p(r_c,t)$, and molar loading, q^*, that is maintained constant till the crystal reaches thermodynamic equilibrium with the surrounding fluid mixture.

The matrix generalization of the Geddes model, eq (S41), with the assumption that $[D]$ calculated at the equilibrated loading, say, may be considered to be constant, is discussed in detail in Chapter 5, Example 5.6.1 of Taylor and Krishna [36]; the result is

$$\left(q^*-\bar{q}(t)\right)=[Q]\left(q^*-q_0\right);\quad [Q]\equiv\frac{6}{\pi^2}\sum_{m=1}^{\infty}\frac{1}{m^2}\exp\left[-m^2\pi^2\frac{[D]t}{r_c^2}\right] \tag{S42}$$

In eq (S42), (q_0), (q^*), $\left(\bar{q}(t)\right)$ represent, respectively, the 2-dimensional column matrices of component loadings corresponding to: initial conditions, at final equilibrium, and spatially-averaged values at time *t*.

During the initial transience, the equilibration trajectory is dictated by the fast eigenvector

$$\left(q_2 - q_{20}\right) = -\frac{D_{11} - \lambda_1}{D_{12}}\left(q_1 - q_{10}\right) = e_{12}\left(q_1 - q_{10}\right) \tag{S43}$$

As equilibrium is approached, the equilibration trajectory follows the path dictated by the slow eigenvector

$$\left(q_2 - q_2^*\right) = -\frac{D_{21}}{D_{22} - \lambda_2}\left(q_1 - q_1^*\right) = e_{22}\left(q_1 - q_1^*\right) \tag{S44}$$

In eqs (S42), and (S43) the terms $e_{11} = -\frac{D_{11} - \lambda_1}{D_{12}}; e_{22} = -\frac{D_{21}}{D_{22} - \lambda_2}$ are given by eqs (S26), and (S27).

Pre-multiplying eq by $[P]^{-1}$ we write

$$\begin{aligned}
&[P]^{-1}\left(q^* - \bar{q}(t)\right) = [P]^{-1}[Q][P][P]^{-1}\left(q^* - q_0\right); \\
&[P]^{-1}[Q][P] \equiv \begin{bmatrix} Q_1 & 0 \\ 0 & Q_2 \end{bmatrix}; \\
&Q_1 = \frac{6}{\pi^2}\sum_{m=1}^{\infty}\frac{1}{m^2}\exp\left[-m^2\pi^2\frac{\lambda_1 t}{r_c^2}\right]; \quad Q_2 = \frac{6}{\pi^2}\sum_{m=1}^{\infty}\frac{1}{m^2}\exp\left[-m^2\pi^2\frac{\lambda_2 t}{r_c^2}\right]
\end{aligned} \tag{S45}$$

The theoretical background to eqs (S42), (S43), (S44) and (S45) are provided in Chapter 5, Example 5.6.1 of Taylor and Krishna. [36]

The pseudo-component loadings follow monotonous paths to equilibrium; each pseudo-component relaxes with the corresponding eigenvalues λ_1 and λ_2.

$$\left(qq_i^* - \overline{qq_i}(t)\right) = Q_i\left(qq_i^* - qq_{i0}\right); \quad Q_i = \frac{6}{\pi^2}\sum_{m=1}^{\infty}\frac{1}{m^2}\exp\left[-m^2\pi^2\frac{\lambda_i t}{r_c^2}\right]; \quad i = 1, 2 \tag{S46}$$

3.3 Modelling transient breakthroughs in fixed bed

We describe below the simulation methodology used to perform transient breakthrough calculations for fixed bed adsorbers (see schematics in Figure S1, and Figure S2). The simulation methodology is the same as used in our earlier publications.[4, 6, 37, 38] For an *n*-component gas mixture flowing through a fixed bed maintained under isothermal, isobaric, conditions, the molar concentrations in the gas phase at

any position and instant of time are obtained by solving the following set of partial differential equations for each of the species *i* in the gas mixture[4, 9, 18, 32]

$$-D_{ax}\frac{\partial^2 c_i(t,z)}{\partial z^2}+\frac{\partial c_i(t,z)}{\partial t}+\frac{\partial\left(v(t,z)c_i(t,z)\right)}{\partial z}+\frac{\left(1-\varepsilon\right)}{\varepsilon}\rho\frac{\partial \bar{q}_i(t,z)}{\partial t}=0;\quad i=1,2,...n \tag{S47}$$

In eq (S47), t is the time, z is the distance along the adsorber, ρ is the framework density, ε is the bed voidage, D_{ax} is the axial dispersion coefficient, v is the interstitial gas velocity, and $\bar{q}_i(t,z)$ is the *spatially averaged* molar loading within the crystallites of radius r_c, monitored at position z, and at time t. The time $t = 0$, corresponds to the time at which the feed mixture is injected at the inlet to the fixed bed. Prior to injection of the feed, it is assumed that an inert, non-adsorbing, gas flows through the fixed bed. In this model described by eq (S47), the effects of all mechanisms that contribute to axial mixing are lumped into a single effect axial dispersion coefficient D_{ax}. Ruthven et al.[18] state that more detailed models that include radial dispersion are generally not necessary. They also make the following remark "when mass transfer resistance is significantly greater than axial dispersion, one may neglect the axial dispersion term and assume plug flow". This is the situation that manifests for kinetically controlled separations, the focus of the present article. Consequently, all of the analysis and breakthrough simulations were carried out using the plug flow assumption.

The term $\frac{\partial \bar{q}_i(t,z)}{\partial t}$ in eq (S47) is determined by solving the set of eqs (S38), and (S39), and (S40). At any time t, and position z, the component loadings at the outer surface of the particle $q_i(r_c,t,z)$ is in equilibrium with the bulk phase gas mixture with partial pressures $p_i(t,z)$ in the bulk gas mixture. In the general case, the component loadings $q_i(r_c,t,z)$ are calculated using the Ideal Adsorbed Solution Theory (IAST) of Myers and Prausnitz.[7] Alternatively, in some cases, the mixed-gas Langmuir eq (S7) may be of sufficient accuracy.

The *interstitial* gas velocity is related to the *superficial* gas velocity by

$$v = \frac{u}{\varepsilon} \tag{S48}$$

In all of the simulations reported in this article, the entire bed of crystalline particles is considered to be devoid of adsorbates at time $t = 0$, i.e. we have the initial condition

$$t = 0; \quad q_i(0,z) = 0 \tag{S49}$$

Eq (S49) is relevant to the operation of the transient breakthrough experiments on a laboratory scale, but are not truly reflective of industrial operations.

At time, $t = 0$, the inlet to the adsorber, $z = 0$, is subjected to a step input of the n-component gas mixture and this step input is maintained till the end of the adsorption cycle when steady-state conditions are reached.

$$t \geq 0; \quad p_i(0,t) = p_{i0}; \quad u(0,t) = u_0 \tag{S50}$$

where $u_0 = v_0\varepsilon$ is the superficial gas velocity at the inlet to the adsorber.

Typically, the adsorber length is divided into 100 slices, and each spherical crystallite was discretized into 20 - 150 equi-volume slices. The results thus obtained were confirmed to be of adequate accuracy. Combination of the discretized partial differential equations (PDEs) along with the algebraic equations describing mixture adsorption equilibrium (IAST, or mixed-gas Langmuir model, as appropriate), results in a set of differential-algebraic equations (DAEs), which are solved using BESIRK.[29] BESIRK is a sparse matrix solver, based on the semi-implicit Runge-Kutta method originally developed by Michelsen,[30] and extended with the Bulirsch-Stoer extrapolation method.[31] Use of BESIRK improves the numerical solution efficiency in solving the set of DAEs. The evaluation of the sparse Jacobian required in the numerical algorithm is largely based on analytic expressions.[9] Further details of the numerical procedures used in this work, are provided by Krishna and co-workers;[9, 32-34] interested readers are referred to our website that contains the numerical details.[32]

For all the simulations reported in this article we choose the following: adsorber length, $L = 0.3$ m; cross-sectional area, $A = 1$ m^2; superficial gas velocity in the bed, $u_0 = 0.04$ m s^{-1}; voidage of the packed bed, $\varepsilon = 0.4$. Also, the total pressures is assumed to be constant along the length of the fixed bed. Please

note that since the superficial gas velocity is specified, the specification of the cross-sectional area of the tube, A, is not relevant in the simulation results presented. The total volume of the bed is $V_{bed} = LA$. The volume of zeolite or MOF used in the simulations is $V_{ads} = LA(1-\varepsilon)$ = 0.18 m^3. If ρ is the framework density, the mass of the adsorbent in the bed is $m_{ads} = \rho LA(1-\varepsilon)$ kg. It is important to note that the volume of adsorbent, V_{ads}, includes the pore volume of the adsorbent material. In these breakthrough simulations we use the same volume of adsorbent in the breakthrough apparatus, i.e. (1 - ε) A L = 0.18 m^3 = 180 L.

The transient breakthrough data for the dimensionless concentrations at the exit of the fixed bed, c_i/c_{i0}, are plotted as a function of a modified time parameter defined by

$$\frac{\left(Q_0 = \text{flow rate m}^3\ \text{s}^{-1}\right)\times\left(\text{time in s}\right)}{\left(\text{kg MOF packed in tube}\right)} = \frac{Q_0 t}{m_{ads}} = \text{m}^3\ \text{kg}^{-1}$$
$$= \frac{\left(u_0 \text{A}\right)\times(t)}{(1-\varepsilon)\times\left(L\ \text{m}\right)\times\left(A\ \text{m}^2\right)\times\left(\rho\ \text{kg m}^{-3}\right)} = \frac{u_0 t\varepsilon}{(1-\varepsilon)\varepsilon\times L\times\rho} \qquad \text{(S51)}$$

The theoretical justification for the use of this modified time parameter is the shock-wave model, as described in previous works.[37, 39]

3.4 List of Figures for Transient breakthroughs in fixed bed adsorbers

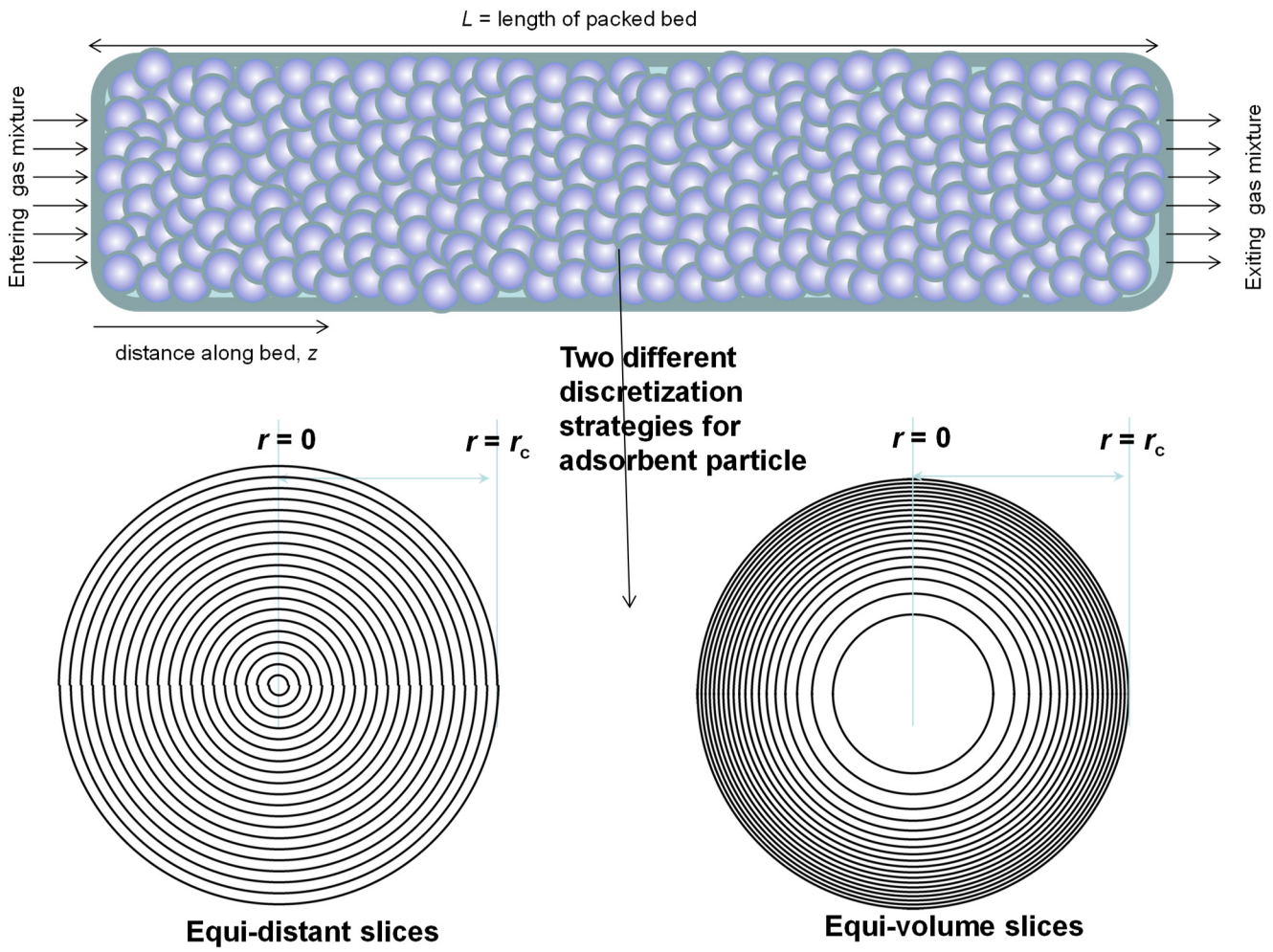

Figure S1. Two different discretization schemes for a single spherical crystallite.

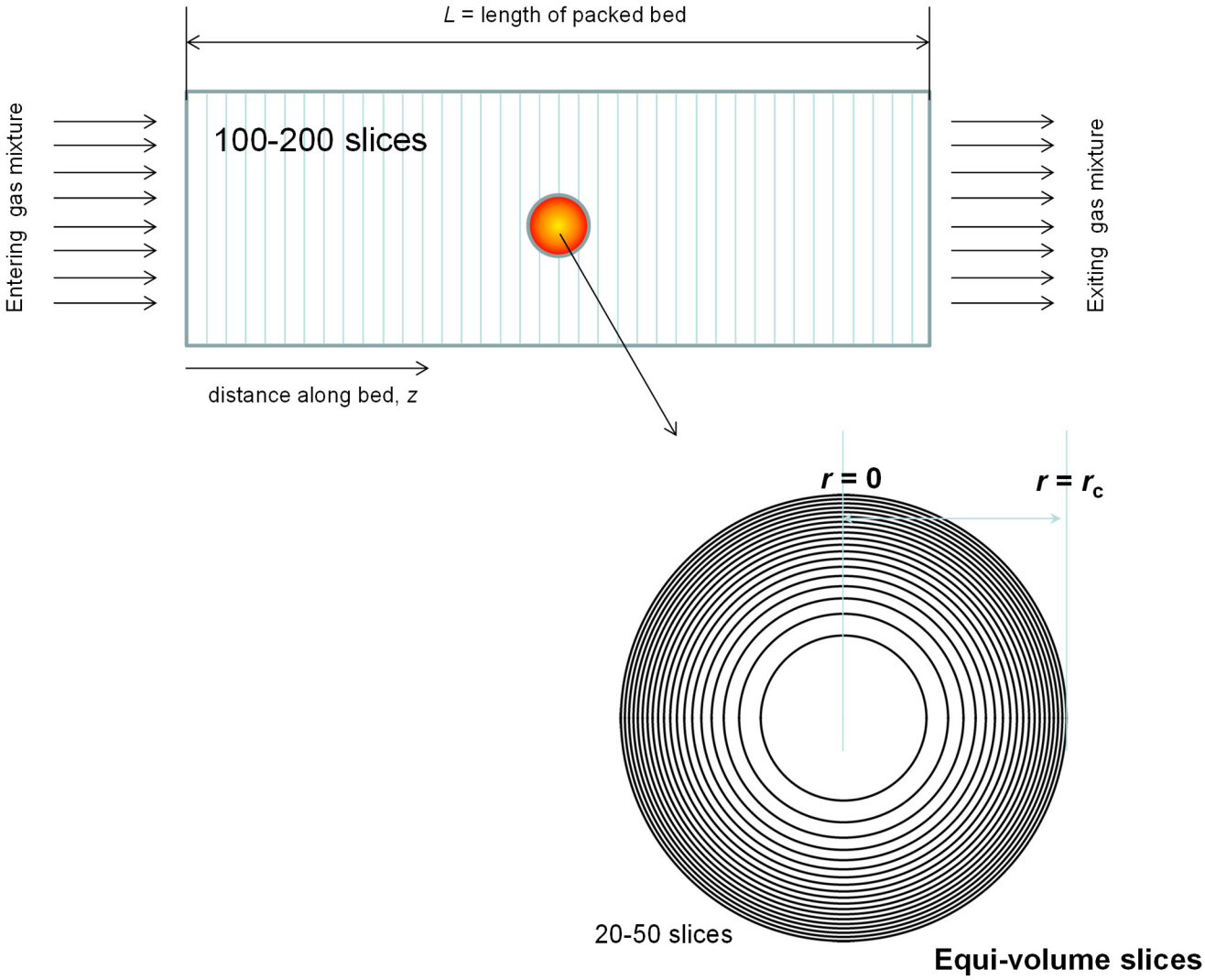

Figure S2. Discretization scheme for fixed bed adsorber.

4 Separation of hexane isomers

4.1 Background on hexane isomers separation

The separation of hexane isomers, n-hexane (nC6), 2-methylpentane (2MP), 3-methylpentane (3MP), 2,2 dimethylbutane (22DMB), and 2,3 dimethylbutane (23DMB) is required for production of high-octane gasoline. The values of the Research Octane Number (RON) increases with the degree of branching; Table S1 lists the Research Octane Numbers (RON) of C6 alkanes.[40] The di-branched isomers (22DMB, 23DMB) have significantly higher RON values than that of the linear isomer (nC6), and mono-branched isomers (2MP, 3MP). The RON values are: nC6 = 30, 2MP = 74.5, 3MP = 75.5, 22DMB = 94, 23DMB = 105. Therefore, di-branched isomers are preferred products for incorporation into the high-octane gasoline pool.[4, 41, 42] Table S1 also lists the boiling points of alkane isomers. Due to the small differences in boiling points, distillation is energy intensive.

Currently, the separation of hexane isomers is performed using LTA-5A zeolite that operates on the principle of molecular sieving; see Figure S3. Linear nC6 can hop from one cage to the adjacent cage through the 4 Å windows of LTA-5A, but branched alkanes are largely excluded. An improved separation scheme, pictured in Figure S4, would require an adsorbent that would separate the di-branched isomers 22DMB and 23DMB from the nC6, 2MP, and 3MP; this would allow the low-RON components to be recycled back to the isomerization reactor. The separation of 22DMB and 23DMB from the remaining isomers is a difficult task because it requires distinguishing molecules on the *degree* of branching; such a separation is not feasible with the currently used LTA-5A. Typically, in such a processing scheme the aim would be to produce a product stream from the separation step with RON value > 92. This requirement of 92+ RON implies that the product stream will contain predominantly the di-branched isomers 22DMB and 23DMB, while allowing a small proportion of 2MP and 3MP to be

incorporated into the product stream. Sharp separations between mono- and di- branched isomers is not a strict requirement.

4.2 Configurational-entropy effects in MFI zeolite

According to a patent granted to Universal Oil Products (UOP) for separation of hexane isomers,[43-45] the desired separation of hexane isomers as portrayed in Figure S4 is achievable with a variety of materials; see the pulse chromatographic separation data as presented in the UOP patents, and reproduced in Figure S5. The UOP patent states:

"The adsorbent may be silicalite, ferrierite, zeolite Beta, MAPO-31, SAPO-31, SAPO-11, zeolite X ion exchanged with alkaline cations, alkaline earth cations, or a mixture thereof, and zeolite Y ion exchanged with alkaline cations…."

Even though a vast number of zeolites are named in the patent, a careful examination of the separation performance of all zeolites[4, 38, 46] reveals the pulse chromatographic separation data in Figure S5 is obtained with MFI (silicalite) zeolite. MFI zeolite (also called silicalite-1) has a topology consisting of a set of intersecting straight channels, and zig-zag (or sinusoidal) channels of approximately 5.5 Å size. The pore landscapes and structural details are provided in Figure S6, and Figure S7. This chromatographic pulse data clearly shows the potential of MFI zeolite to separate a mixture of hexane isomers into three different fractions consisting of linear, mono-branched, and di-branched isomers. The separation relies essentially on configurational entropy effects. Figure S8 shows the computational snapshots for nC6, 2MP, and 22DMB within the intersecting channels of MFI zeolite. The linear nC6 can locate anywhere along the straight and zig-zag channels; the linear isomer is not "configurationally challenged". Mono-branched 2MP and di-branched 22DMB prefer to locate at the intersections of MFI, because these are too bulky to locate within the channels; these branched isomers are subject to a configurational "penalty".

Watch the presentation **Separation of Hexane Isomers** on YouTube

https://www.youtube.com/@rajamanikrishna250/videos

Figure S9a shows the unary isotherms of nC6 and 2MP in MFI zeolite at 300 K. Due to configurational considerations, 2MP molecules prefer to locate at the channel intersections because of the extra "leg room" that is available here. There are four intersection sites per unit cell, and therefore the saturation capacity of 2MP is limited to 4 molecules uc^{-1}, for bulk fugacities ranging to 100 Pa..[46-49] The continuous solid lines are dual-site Langmuir-Freundlich fits; the unary isotherm fit parameters are provided in Table S2. Figure S9b presents CBMC simulations of component loadings of binary 50/50 nC6/2MP mixtures in MFI zeolite at 300 K. At bulk fluid phase fugacities higher than 100 Pa, configurational entropy effects lead to almost total exclusion of 2MP. Figure S9c presents CBMC simulation data on the adsorption selectivity. Figure S9d are the CBMC simulations of the thermodynamic correction factors $\begin{bmatrix} \Gamma_{11} & \Gamma_{12} \\ \Gamma_{21} & \Gamma_{22} \end{bmatrix}$.

Entropy effects in MFI zeolite also manifest for adsorption of nC6/3MP/22DMB mixtures.: n-hexane (nC6), 2-methylpentane (2MP), 3-methylpentane (3MP), 2,2-dimethylbutane (22DMB). Figure S10a shows the unary isotherms, fitted with the dual-site Langmuir-Freundlich model. Figure S10b presents CBMC simulations of component loadings in a ternary equimolar nC6/3MP/22DMB mixture at 433 K as a function of the total hydrocarbons fugacity f_t. The IAST (continuous solids lines) predicts entropy effects in quantitative agreement with CBMC simulations.

Entropy effects also manifest for 5-component nC6/2MP/3MP/22DMB/23DMB mixtures in MFI zeolite. The pure component isotherms are shown in Figure S11a; the continuous solid lines are the unary isotherm fits with the dual-site Langmuir-Freundlich model. Figure S11b presents CBMC simulations of component loadings in a 5-component nC6/2MP/3MP/22DMB/23DMB mixture at 433 K as a function of the total hydrocarbons fugacity f_t.

4.3 Transient nC6/2MP uptake in MFI

The transient uptake of nC6(1)/2MP(2) mixtures in microporous crystals of MFI zeolite, exposed to an equimolar $\left(p_1 = p_2\right)$ gas phase mixture at constant total pressure ($p_t = p_1 + p_2$ = 2.6 Pa) have been reported by Titze et al.;[50] see Figure S12a. The transient equilibration of nC6 displays a pronounced overshoot, achieving supraequilibrium loadings during transient equilibration. Titze et al.[50] have established the validity of the uncoupled M-S eqs (S20) to model intra-crystalline fluxes by detailed consideration of correlation effects. The mixture adsorption equilibrium is determined using the IAST; the unary isotherm data are provided in Table S2. The essential features of the transient uptake on nC6/2MP uptake in MFI zeolite can be adequately captured by the flux equation (S20) taking $Đ_1/r_c^2$ = 0.016 s^{-1}; $Đ_2/r_c^2$ = 1.6×10^{-4} s^{-1} $Đ_1/Đ_2$ = 100.[50] The lower diffusivity of the mono-branched isomer 2MP is due to the severe configurational constraints within 5.5 Å sized channels of MFI. The nC6 overshoot is caused by the significant off-diagonal elements of $\left[\Gamma\right]$; the elements of $\left[\Gamma\right]$ are presented in Figure S9d. At a total pressure $p_t = p_1 + p_2$ = 2.6 Pa, the elements of the $\left[\Gamma\right]$ are $\begin{bmatrix}\Gamma_{11} & \Gamma_{12}\\ \Gamma_{21} & \Gamma_{22}\end{bmatrix} = \begin{bmatrix}4.335 & 2.947\\ 4.051 & 4.438\end{bmatrix}$. The Fick diffusivity matrix is calculated to be $\frac{\begin{bmatrix}D_{11} & D_{12}\\ D_{21} & D_{22}\end{bmatrix}}{r_c^2} = \begin{bmatrix}693.541 & 471.445\\ 6.482 & 7.101\end{bmatrix}\times10^{-4}$ s^{-1}. If we assume $\Gamma_{ij} = \delta_{ij}$, and invoke Eq (S22), the nC6 overshoot disappears; see dashed lines in Figure S12a.[50, 51]

In Figure S12b the component loadings of nC6 and 2MP are plotted in composition space, with 2MP loadings on the *x*-axis. We note that the equilibration trajectory is not monotonous and follows a serpentine trajectory. In order to appreciate the fundamentals that underlie this serpentine trajectory we

plot the two eigenvectors of $[D]$: $(e_1)=\begin{pmatrix}1\\ -\dfrac{D_{11}-\lambda_1}{D_{12}}\end{pmatrix}$ and $(e_2)=\begin{pmatrix}1\\ -\dfrac{D_{21}}{D_{22}-\lambda_2}\end{pmatrix}$ where the two eigenvalues are $\dfrac{\lambda_1}{r_c^2}=697.964\times10^{-4}$ s^{-1}; $\dfrac{\lambda_2}{r_c^2}=2.678\times10^{-4}$ s^{-1}.

During the initial transience, the equilibration trajectory is dictated by the fast eigenvector, indicated by the red line in Figure S12b

$$(q_2-q_{20})=-\frac{D_{11}-\lambda_1}{D_{12}}(q_1-q_{10}) \tag{S52}$$

As equilibrium is approached, the equilibration trajectory follows the path dictated by the slow eigenvector, indicated by the blue line in Figure S12b

$$(q_2-q_2^*)=-\frac{D_{21}}{D_{22}-\lambda_2}(q_1-q_1^*) \tag{S53}$$

The experimental data on the equilibration trajectory lies within the two bounds dictated by eqs (S52), and (S53).

The pseudo-component loadings $[P]^{-1}(q)=(qq)$ follow monotonous paths to equilibrium; each pseudo-component relaxes with the corresponding eigenvalues λ_1 and λ_2.

$$(qq_i^*-\overline{qq_i}(t))=Q_i(qq_i^*-qq_{i0});\quad Q_i=\frac{6}{\pi^2}\sum_{m=1}^{\infty}\frac{1}{m^2}\exp\left[-m^2\pi^2\frac{\lambda_i t}{r_c^2}\right];\quad i=1,2 \tag{S54}$$

The transient equilibration of the pseudo component loadings are plotted in Figure S12c; note that the pseudo loading of 2MP, qq_2 is negative. In pseudo composition space, the pseudo component loadings follow a monotonous approach to equilibrium; see Figure S12d.

4.4 nC6/2MP mixture separations in fixed bed adsorber

Uphill diffusion of nC6 is beneficial to the hexane isomer separations in fixed bed adsorption devices because the desired raffinate phase will be richer in the branched isomers that have high octane numbers. To confirm this expectation, transient breakthrough simulations were performed for separation

50/50 nC6/2MP mixtures at 298 K and total pressure of 10 Pa. Figure S13a plots the dimensionless concentrations at the exit of the adsorber, c_i/c_{i0}, as a function of a modified time parameter defined by $Q_0 t/m_{ads}$. In the three sets of simulations the ratio $Đ_1/Đ_2 = 100$, as determined from the transient uptake experiments of Titze et al.[50] Three different values for the diffusional time constants were chosen $Đ_1/r_c^2 = 1.6\times10^{-6}, 1.0\times10^{-5}, 1.6\times10^{-2}$ s^{-1}, to investigate the varying degrees of diffusional influences. In practice, stronger diffusional influences are achievable for use of larger sized crystals. Increasing values of $Đ_1/r_c^2$ signify diminishing influences of intra-crystalline transport; indeed for $Đ_1/r_c^2 \to \infty$, there are no diffusional limitations. We note that with decreasing $Đ_1/r_c^2$, i.e. stronger diffusional influences, the breakthroughs take on a more distended character and 2MP exits the adsorber at earlier times. Figure S13b plots the RON of the product gas mixture exiting the adsorber. With stronger diffusion influences, i.e. lower values of $Đ_1/r_c^2$, there is a longer time interval during which product gas with RON= 74.5 can be recovered at the exit; these time intervals are indicated by the colored arrows in Figure S13b.

4.5 Separation of nC6/2MP/3MP/22DMB/23DMB mixtures with MFI zeolite

We now examine the influence of thermodynamic coupling on the uptake of 5-component mixtures of hexane isomers nC6/2MP/3MP/22DMB/23DMB in MFI zeolite. Firstly, we get gather some insights in the relative magnitudes of the intra-crystalline diffusivities.

Schuring et al.[52] have reported experimental data on the self-diffusivities of both nC6 and 2MP in nC6/2MP mixtures. These measurements were made at a total loading that is kept nearly constant at 3.5 molecules per unit cell. Their data, that were measured at 433 K shows that *both* self-diffusivities are reduced with increasing loading of 2MP in the mixture; see Figure S14a. The preferential location of 2MP at the intersections causes blocking of molecular traffic in the intersecting channel system of MFI. MD simulations show that such intersection blocking effects also manifest in nC6/22DMB mixtures.[53] We also note that the linear nC6 has a diffusivity that is about an order of magnitude higher than that of

the branched 2MP. MD simulations show that the results such as that in Figure S14a also hold for nC6/22DMB mixtures.[53]

For the transient uptake simulations, we assume $Đ_{nC6}/Đ_{2MP} = 5$.

We now try to get an estimate of the relative values of diffusivities of the branched isomers in MFI. On the basis of the experimental data on diffusivities of hexane isomers reported by Cavalcante and Ruthven[54] and Jolimaître et al,[55] we note that the hierarchy of diffusivities is 2MP ≈ 3MP > > 23DMB > 22DMB; see Arrhenius plots in Figure S14b,c.

The data in Figure S14 implies that inclusion of diffusional considerations will result in sharper separations with MFI between 3MP and 23DMB than is possible on the basis of equilibrium considerations alone. For a conservative evaluation of the separations we assume the ratios of diffusivities as $Đ_{2MP}/Đ_{3MP}$ =1; $Đ_{2MP}/Đ_{22DMB}$ =5; $Đ_{22MB}/Đ_{23DMB}$ =1; these values are also in agreement with those used in the work of Herm et al.[40] By fixing the value of $Đ_{nC6}/r_c^2$, the diffusional characteristics are fully determined. Herm et al.[40] have taken the value of $Đ_{nC6}/r_c^2$ = 0.002 s^{-1} for MFI zeolite.

Figure S15a,b present simulations of transient uptake inside MFI crystal exposed to a gas phase 5-component nC6/2MP/3MP/22DMB/23DMB mixture at a total pressure of 100 kPa and 433 K. The partial pressures of the components in the bulk gas phase at the inlet are $p_1 = p_2 = p_3 = p_4 = p_5 = 20$ kPa. For the uptake simulations that include the influence of thermodynamic coupling, using eq (S10), we note that nC6 shows an overshoot in the uptake during the early stages of the transience. If thermodynamic coupling is ignored and eq (S11) is invoked for determining intra-crystalline fluxes, the nC6 overshoot disappears. The nC6 overshoot signifies uphill diffusion and attainment of supraequilibrium conversions for a brief time span; these phenomena are beneficial to the separation of alkane isomers.

Figure S16a shows the transient breakthrough for 5-component nC6/2MP/3MP/22DMB/23DMB mixture in a fixed bed adsorber packed with MFI (framework density ρ = 1.796 kg L^{-1}) operating at a

total pressure of 100 kPa and 433 K. The partial pressures of the components in the bulk gas phase at the inlet are $p_1 = p_2 = p_3 = p_4 = p_5 = 20$ kPa. Intra-crystalline diffusion effects are taken into account using the input values as in previous work:[4] $Đ_1/r_c^2 = Đ_{nC6}/r_c^2 = 0.002$ s^{-1} ; $Đ_{nC6}/Đ_{2MP} = 5$; $Đ_{2MP}/Đ_{3MP} = 1$, $Đ_{2MP}/Đ_{22DMB} = 5$, $Đ_{22MB}/Đ_{23DMB} = 1$. In the simulations, we choose the mass of the adsorbent in the bed $m_{ads} = 180$ kg, cross-sectional area, A = 1 m^2; superficial gas velocity at the bed inlet, u_0 = 0.04 m s^{-1}; voidage of the packed bed, $\varepsilon = 0.4$. The framework density of MFI is $\rho = 1796$ kg m^{-3}. The length L of the adsorber bed is chosen as $L = \frac{1000}{\rho} \times 0.3 = 0.167002$ m. The CBMC simulated unary isotherms are fitted with the parameters specified in Table S3. The dimensionless concentrations of the component hexanes in the outlet of the fixed bed are plotted against the modified time parameter $\frac{\left(Q_0 = \text{flow rate L s}^{-1}\right) \times \left(\text{time in s}\right)}{\left(\text{kg MFI packed in tube}\right)} = \frac{Q_0 t}{m_{ads}} = \text{L kg}^{-1}$ as the x-axis.

The objective of the separation of hexane isomers is to obtain a raffinate product that has a higher octane number. In Figure S16b, the RON of the mixture exiting the fixed bed is calculated from the pure component RON values in Table S1. The RON calculations are based a linear mixing rule using the mole fractions in the product gas exiting the adsorber; no non-linear mixing rules are applied.

In order to highlight the influence of diffusional limitations on the product RON, Figure S16b presents calculations of the product RON determined from transient breakthrough simulations with five different values of $Đ_1/r_c^2 = 1.39\times10^{-3}, 2\times10^{-3}, 3.13\times10^{-3}, 5.56\times10^{-3}, 1.25\times10^{-2}$ s^{-1}; in these simulations, the ratios $Đ_{nC6}/Đ_{2MP} = 5$; $Đ_{nC6}/Đ_{3MP} = 5$; $Đ_{nC6}/Đ_{22DMB} = 25$; $Đ_{nC6}/Đ_{23DMB} = 25$ were maintained the same. Let us assume a target RON value of the raffinate from the adsorber is 92 RON. From a material balance on the adsorber, we can determine the number of moles of 92 RON+ product that can be recovered. Expressed per kg of MFI zeolite packed in the adsorber, the 92+ RON productivity is plotted in Figure S16c as function of $Đ_1/r_c^2$. We clearly note that with increasing

diffusional influences, due to lowering of the value of $Đ_1/r_c^2$, the 92 RON productivity increases. This is a direct consequence of the adsorption/diffusion synergy.

4.6 Separation of nC6/2MP/3MP/22DMB/23DMB mixtures with $Fe_2(BDP)_3$

Herm et al.[40] report the synthesis of $Fe_2(BDP)_3$ [BDP^{2-} = benzenedipyrazolate] that has 1D channels which are triangular in shape and a pore size of 4.9 Å; see Figure S17. Molecular simulations provide insights into the workings of $Fe_2(BDP)_3$. The linear nC6 can align optimally along the V-shaped gutters, and exert the best van der Waals interaction with the framework. The interactions of the mono- and di-branched isomers are less effective, resulting in considerably lower adsorption strengths. The hierarchy of breakthroughs reported in the transient experiments of Herm [40] is 22DMB, 23DMB, 3MP, 2MP, and nC6 (cf. Figure S18); this hierarchy is dictated by a combination of adsorption strengths (nC6 > > 2MP ≈ 3MP >> 22DMB ≈ 23DMB) and diffusivities (nC6 > 2MP ≈ 3MP > 22DMB ≈ 23DMB). The di-branched isomers 22DMB and 23DMB can be recovered in the early stages of the transient breakthrough in fixed bed adsorbers. The experimentally determined breakthroughs in fixed bed adsorbers displays distended characteristics that is indicative of strong intra-crystalline diffusional limitations within the 4.9 Å channels.

For determining the 92+ RON productivities of $Fe_2(BDP)_3$, we carried out transient breakthrough simulations using experimental data of the unary isotherms of hexane isomers; the isotherm data fits are presented in Table S4. The simulation results are shown in Figure S19a in which the dimensionless concentrations of the hexane isomers exiting the fixed bed are plotted as a function of $\frac{\left(Q_0 = \text{flow rate L s}^{-1} \text{ at STP}\right)\times\left(\text{time in s}\right)}{\left(\text{kg MOF packed in tube}\right)} = \frac{Q_0 t}{m_{ads}} = \text{L kg}^{-1}$ as the *x*-axis. Intra-crystalline diffusion effects are taken into account using the input values as elaborated in previous work:[4] $Đ_{nC6}/r_c^2$ = 0.002 s^{-1}; $Đ_{nC6}/Đ_{2MP}$ =5; $Đ_{nC6}/Đ_{3MP}$ =5; $Đ_{nC6}/Đ_{22DMB}$ =10; $Đ_{nC6}/Đ_{23DMB}$ =10. In the simulations, we choose the mass of the adsorbent in the bed $m_{ads} = 180$ kg, cross-sectional area, A = 1 m^2; superficial gas velocity

at the bed inlet, u_0 = 0.04 m s^{-1}; voidage of the packed bed, ε = 0.4.The framework density of $Fe_2(BDP)_3$ is $\rho = 1145.461$ kg m^{-3}. The length L of the adsorber bed is chosen as $L = \frac{1000}{\rho} \times 0.3 = 0.261903$ m.

The objective of the separation of hexane isomers is to obtain a raffinate product that has a higher octane number. In Figure S19b, the RON of the mixture exiting the fixed bed is calculated from the pure component RON values in Table S1. The RON calculations are based a linear mixing rule using the mole fractions in the product gas exiting the adsorber; no non-linear mixing rules are applied.

In order to highlight the influence of diffusional limitations on the product RON, Figure S19b presents calculations of the product RON determined from transient breakthrough simulations with three different values of $Đ_1/r_c^2 = 2\times10^{-3}, 3.13\times10^{-3}, 5.56\times10^{-3}$ s^{-1}; in these simulations, the ratios $Đ_{nC6}/Đ_{2MP}$ =5; $Đ_{nC6}/Đ_{3MP}$ =5; $Đ_{nC6}/Đ_{22DMB}$ =10; $Đ_{nC6}/Đ_{23DMB}$ =10 were maintained the same. Let us assume a target RON value of the raffinate from the adsorber is 92 RON. From a material balance on the adsorber, we can determine the number of moles of 92 RON+ product that can be recovered. Expressed per kg of $Fe_2(BDP)_3$ packed in the adsorber, the 92+ RON productivity is plotted in Figure S19c as function of $Đ_1/r_c^2$. We clearly note that with increasing diffusional influences, due to lowering of the value of $Đ_1/r_c^2$, the 92 RON productivity increases. This is a direct consequence of the adsorption/diffusion synergy.

4.7 List of Tables for Separation of hexane isomers

Table S1. Research Octane Numbers (RON) and boiling points of C6 alkanes. Information collected from a variety of web sources.

Hexane isomer	Research Octane Number (RON)	Boiling point K
n-hexane (nC6)	30	341.5
2-methyl pentane (2MP)	74.5	333.1
3-methyl pentane (3MP)	75.5	336.5
2,2 dimethyl butane (22DMB)	94	323.15
2,3 dimethyl butane (23DMB)	105	331.2

Table S2. Dual-site Langmuir-Freundlich parameters for pure component isotherms for hexane isomers in MFI at 300 K. This data is from the Supporting Information of Titze et al.[50] The unary isotherm data are fitted with the dual-Langmuir-Freundlich model

$$\Theta = \Theta_{A,sat}\frac{b_A p^{\nu_A}}{1+b_A p^{\nu_A}} + \Theta_{i,B,sat}\frac{b_B p^{\nu_B}}{1+b_B p^{\nu_B}}$$

	Site A			Site B		
	$\frac{\Theta_{A,sat}}{\text{molecules uc}^{-1}}$.	$\frac{b_A}{\text{Pa}^{-\nu_A}}$	ν_A	$\frac{\Theta_{B,sat}}{\text{molecules uc}^{-1}}$	$\frac{b_B}{\text{Pa}^{-\nu_B}}$	ν_B
nC6	6.6	0.7084	0.83	1.4	16.5765	1.5
2MP	4	4.51	1.05	4	7.92×10^{-6}	1.13

Table S3. Dual-site Langmuir-Freundlich parameters for unary hexane isomers at 433 K in MFI zeolite. $\Theta = \Theta_{A,sat}\frac{b_A p^{\nu_A}}{1+b_A p^{\nu_A}} + \Theta_{i,B,sat}\frac{b_B p^{\nu_B}}{1+b_B p^{\nu_B}}$

The fits are based on CBMC simulation data of Krishna and van Baten.[56]

	Site A			Site B		
	$\frac{\Theta_{A,sat}}{\text{molecules uc}^{-1}}$	$\frac{b_A}{\text{Pa}^{-\nu_A}}$	ν_A	$\frac{\Theta_{B,sat}}{\text{molecules uc}^{-1}}$	$\frac{b_B}{\text{Pa}^{-\nu_B}}$	ν_B
nC6	3.2	2.21×10^{-8}	1.6	4.3	7.42×10^{-4}	1
2MP	4	7.85×10^{-4}	1.03			
3MP	4	4.22×10^{-4}	1.02	1	9.88×10^{-7}	1
22DMB	4	2.55×10^{-4}	1.02			
23DMB	4	4.59×10^{-4}	1.02			

Intra-crystalline diffusion effects are taken into account using the input values as in previous work:[4] $Đ_{nC6}/r_c^2 = 0.002$ s^{-1}; $Đ_{2MP}/Đ_{3MP} = 1$; $Đ_{2MP}/Đ_{22DMB} = 5$; $Đ_{22MB}/Đ_{23DMB} = 1$. The transient breakthrough simulations are based on eq (S10) taking due account of thermodynamic coupling effects.[51, 57]

Table S4. Dual-Langmuir-Freundlich parameter fits for $Fe_2(BDP)_3$ based on the experimental data of Herm et al.[40] for isotherms at 403 K, 433 K, and 473 K. These isotherms were fitted with with *T*-dependent parameters

$$q = q_{A,sat}\frac{b_A p^{\nu_A}}{1+b_A p^{\nu_A}} + q_{B,sat}\frac{b_B p^{\nu_B}}{1+b_B p^{\nu_B}}$$

$$b_A = b_{A0}\exp\left(\frac{E_A}{RT}\right);\quad b_B = b_{B0}\exp\left(\frac{E_B}{RT}\right)$$

	Site A				Site B			
	$q_{A,sat}$ mol kg^{-1}	b_{A0} $Pa^{-\nu_i}$	E_A kJ mol^{-1}	ν_A dimensionless	$q_{B,sat}$ mol kg^{-1}	b_{B0} $Pa^{-\nu_i}$	E_B kJ mol^{-1}	ν_B dimensionless
nC6	0.28	2.74×10^{-26}	111	3	1.17	8.86×10^{-13}	73	1.02
2MP	0.78	2.13×10^{-13}	76	1.1	0.63	5.61×10^{-17}	89	1.36
3MP	0.36	4.62×10^{-13}	76	1.1	1.07	1.34×10^{-16}	89	1.36
22DMB	0.53	1.33×10^{-32}	167	2.9	0.94	1.42×10^{-12}	67	1
23DMB	0.61	9.74×10^{-33}	167	2.9	0.92	1.49×10^{-12}	67	1

Intra-crystalline diffusion effects are taken into account using the input values as in previous work:[4] $Đ_{nC6}/r_c^2$ = 0.002 s^{-1}; $Đ_{nC6}/Đ_{2MP}$ =5; $Đ_{nC6}/Đ_{3MP}$ =5; $Đ_{nC6}/Đ_{22DMB}$ =10; $Đ_{nC6}/Đ_{23DMB}$ =10. The transient breakthrough simulations are based on eq (S10) taking due account of thermodynamic coupling effects.[51, 57]

4.8 List of Figures for Separation of hexane isomers

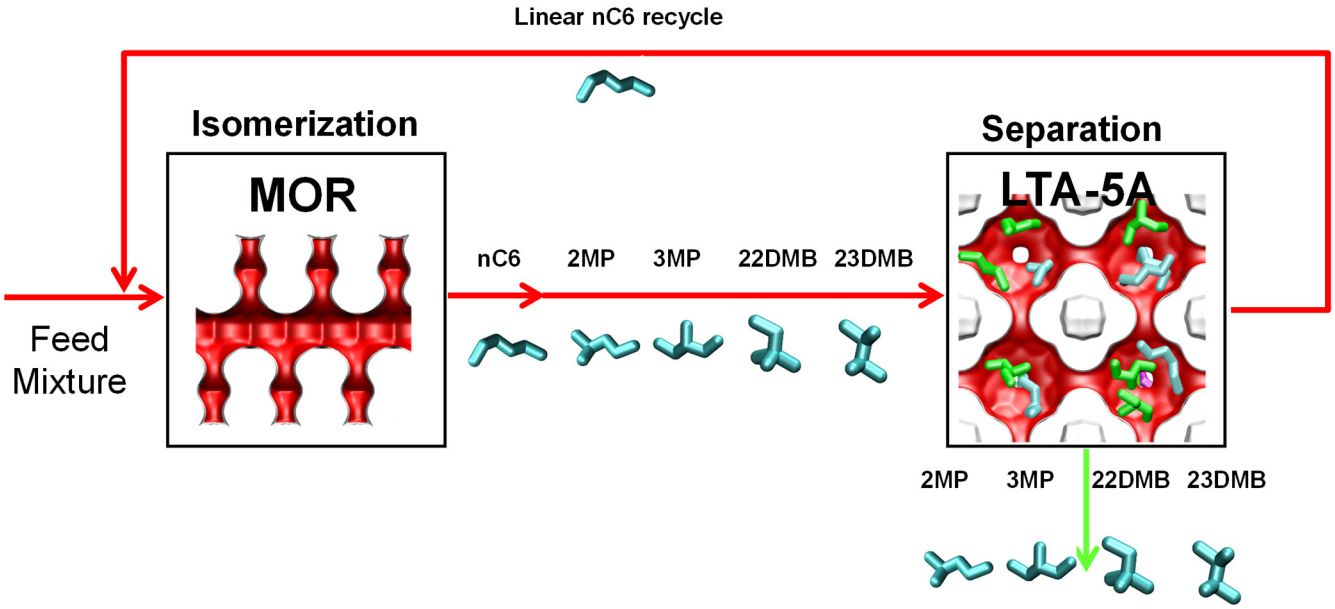

Figure S3. Currently employed processing scheme for nC6 isomerization and subsequent separation step using LTA-5A zeolite.

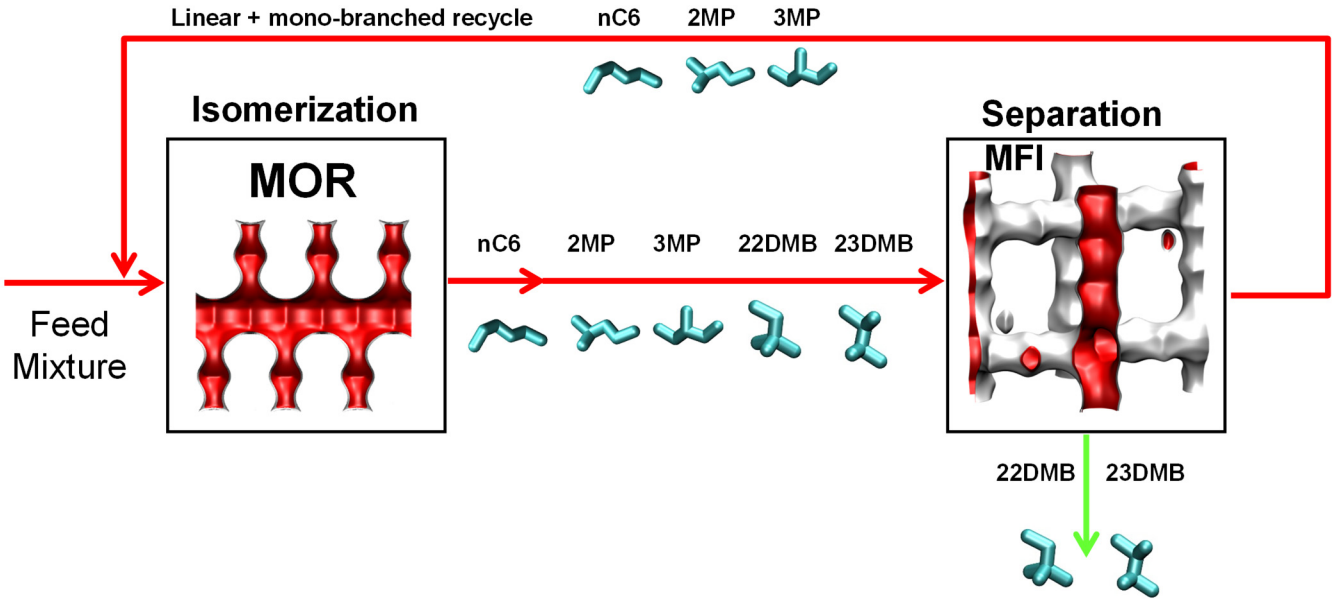

Figure S4. Improved processing scheme for the nC6 isomerization process using MFI zeolite in the separation step.

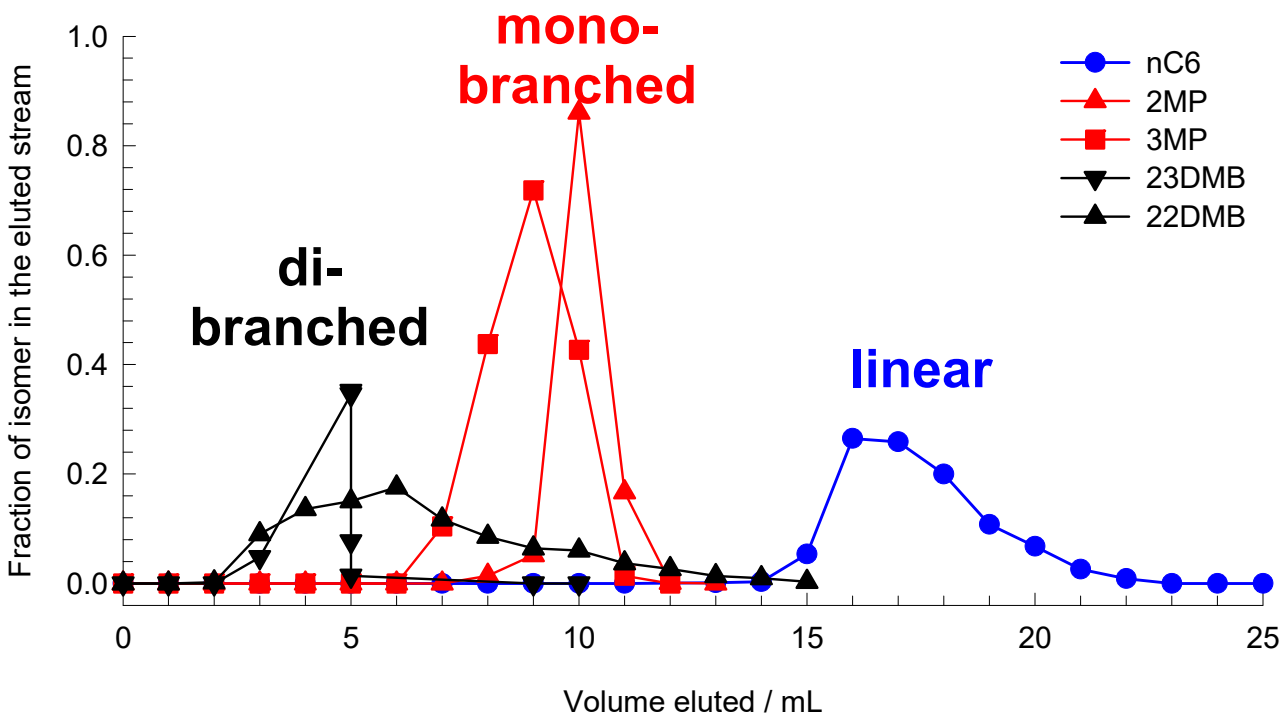

Figure S5 Pulsed chromatographic separation of hexane isomers as reported in the patents assigned to Universal Oil Products (UOP).[43-45]

MFI pore landscape

	MFI
a /Å	20.022
b /Å	19.899
c /Å	13.383
Cell volume / Å^3	5332.025
conversion factor for [molec/uc] to [mol per kg Framework]	0.1734
conversion factor for [molec/uc] to [kmol/m^3]	1.0477
ρ [kg/m3]	1796.386
MW unit cell [g/mol(framework)]	5768.141
ϕ, fractional pore volume	0.297
open space / Å^3/uc	1584.9
Pore volume / cm^3/g	0.165
Surface area /m^2/g	487.0
DeLaunay diameter /Å	5.16

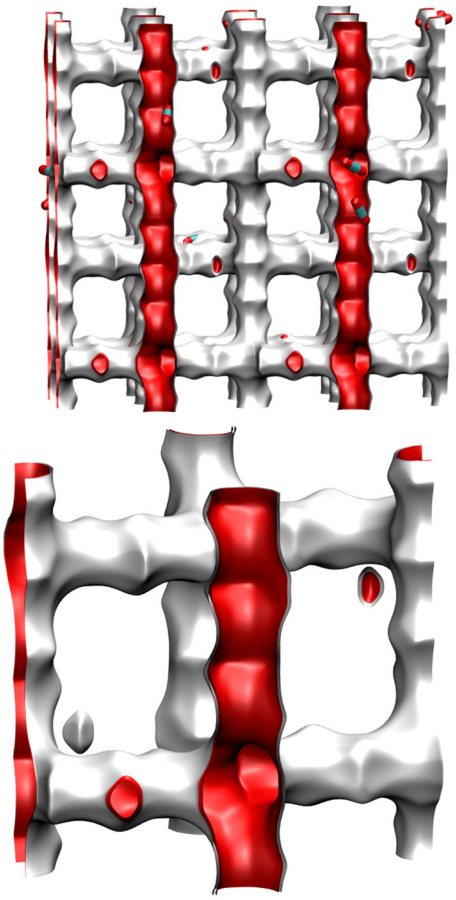

Figure S6. Structural details and pore landscape for MFI zeolite.

10 ring channel of MFI viewed along [100]

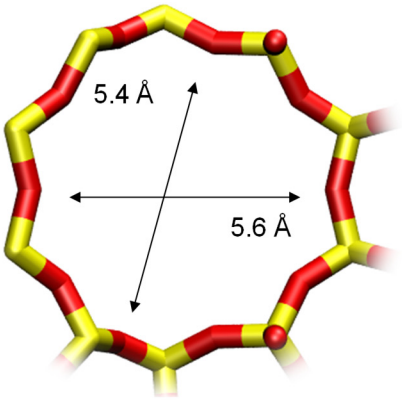

10 ring channel of MFI viewed along [010]

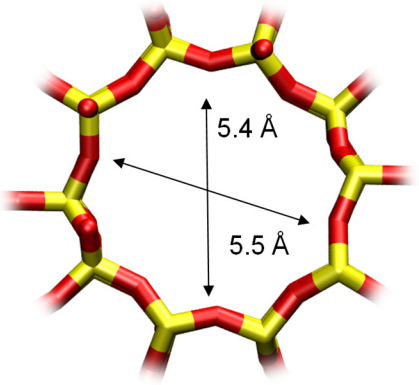

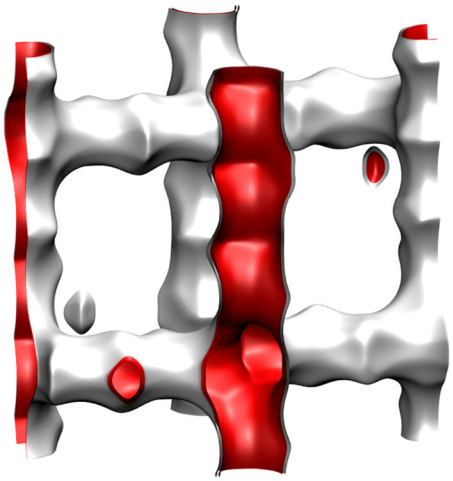

Figure S7. Structural details and pore landscape for MFI zeolite.

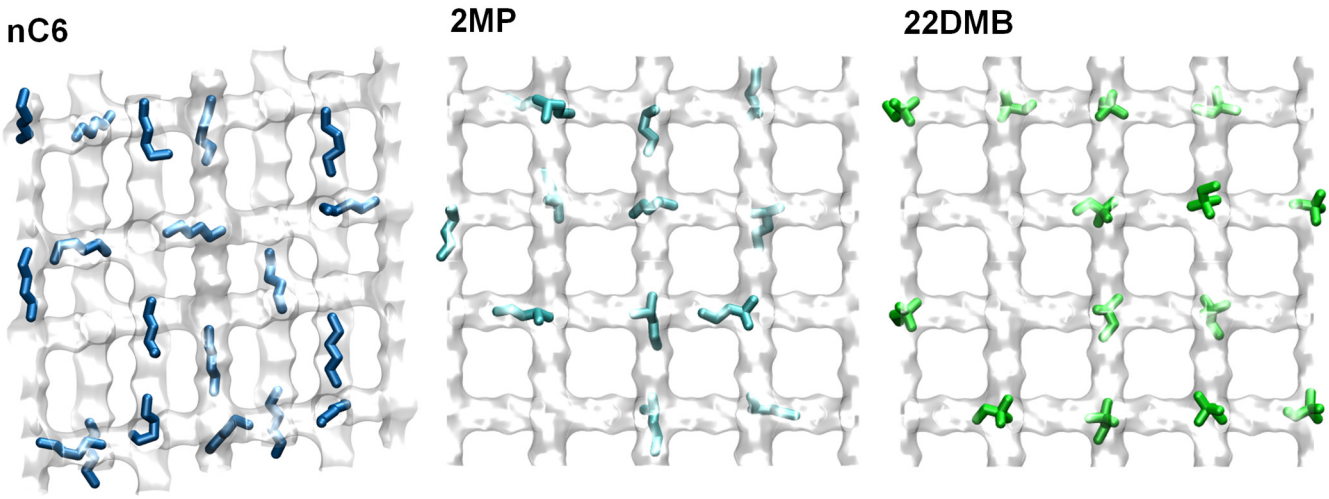

Figure S8. Computational snapshots showing the location of nC6, 2MP, and 22DMB within the intersecting channel topology of MFI zeolite.

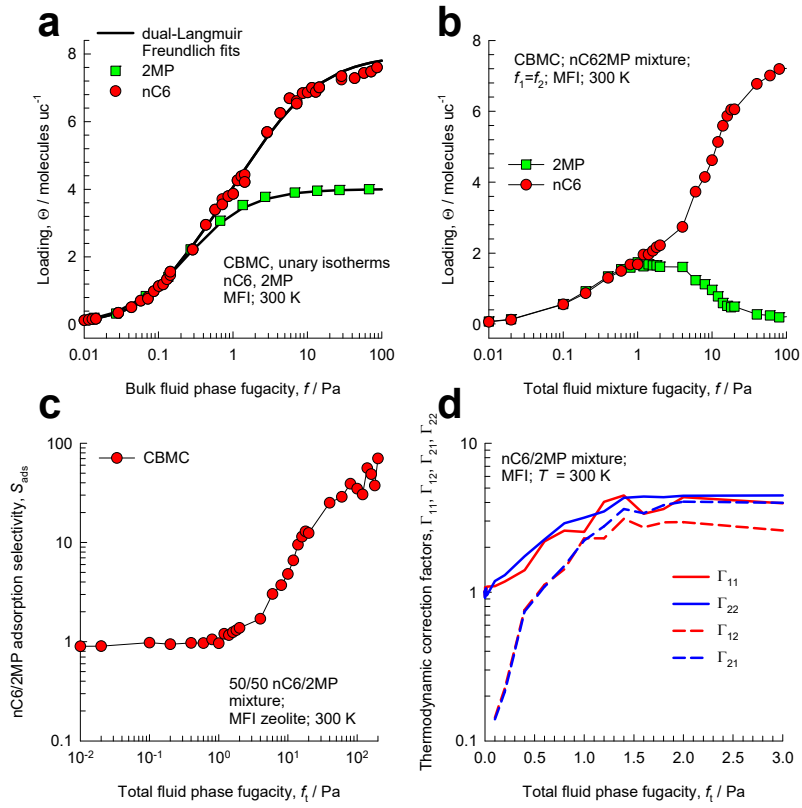

Figure S9. (a) CBMC simulations[50] of unary isotherms of nC6 and 2MP in MFI zeolite at 300 K. The continuous solid lines are dual-site Langmuir-Freundlich fits; the unary isotherm fit parameters are provided in Table S2. (b, c, d) CBMC simulations[50] of (b) component loadings of binary 50/50 nC6/2MP mixtures in MFI zeolite at 300 K, (c) adsorption selectivity, and (d) elements of the matrix of thermodynamic correction factors.

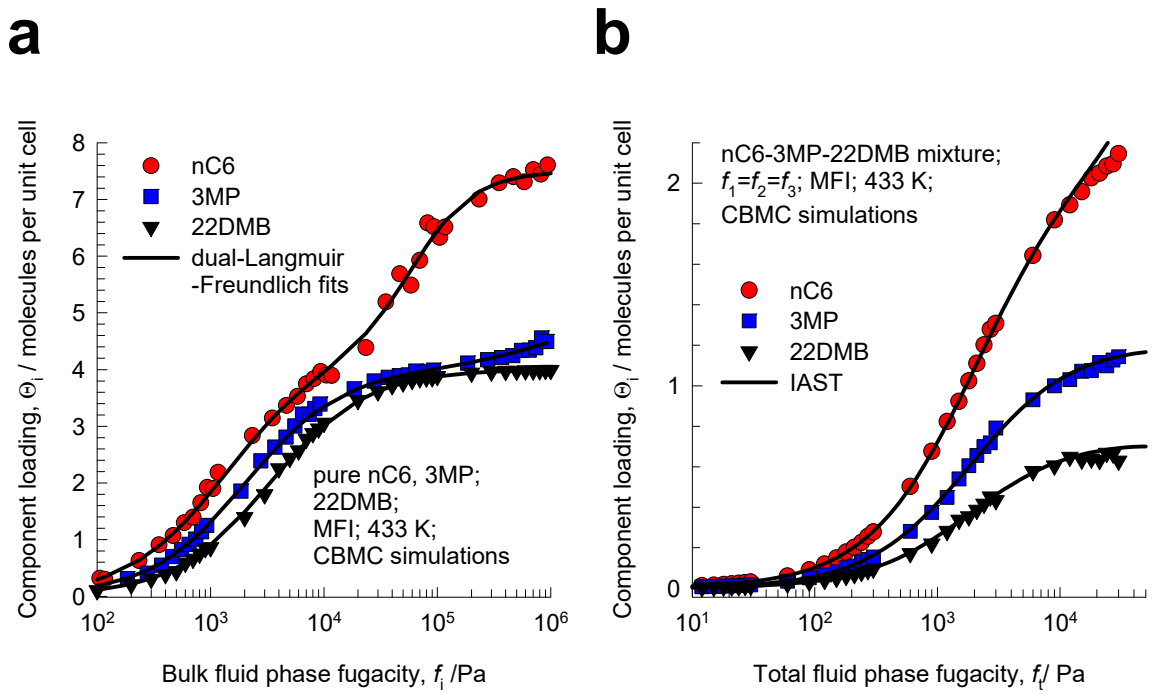

Figure S10. (a) Pure component sorption isotherms for nC6, 3MP and 22DMB in MFI at 433 K. The symbols represent CBMC simulation data.[46, 49, 58] The continuous lines are the fits using the dual-site Langmuir-Freundlich model; the parameter values are specified in Table S3. (b) CBMC simulations (denoted by symbols), of loadings in MFI zeolite at 433 K for equimolar ternary nC6/3MP/22DMB mixture. The continuous solid lines are calculations using IAST.

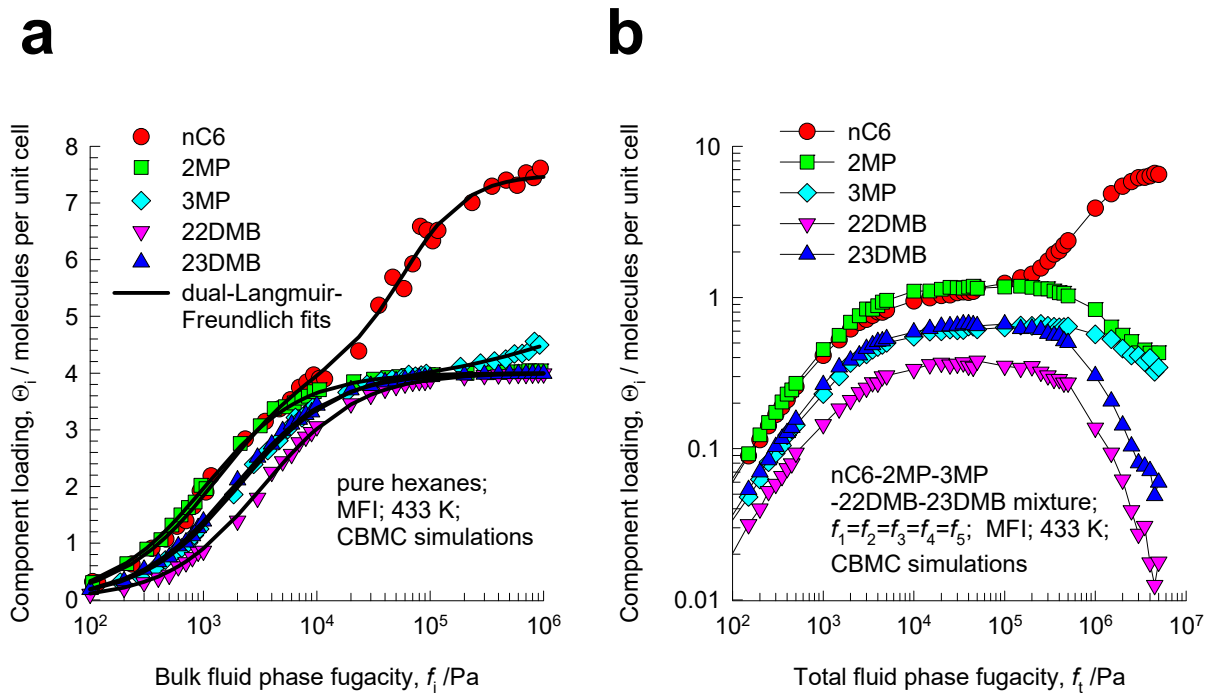

Figure S11. (a) Pure component sorption isotherms for nC6, 2MP, 3MP, 22DMB and 23DMB in MFI at 433 K. The symbols represent CBMC simulation data.[46, 49, 58] The continuous lines are the fits using the dual-site Langmuir-Freundlich model; the parameter values are specified in Table S3. (b) CBMC simulations (denoted by symbols), of loadings in MFI zeolite at 433 K for equimolar 5-component nC6/2MP/3MP/22DMB/23DMB mixture.

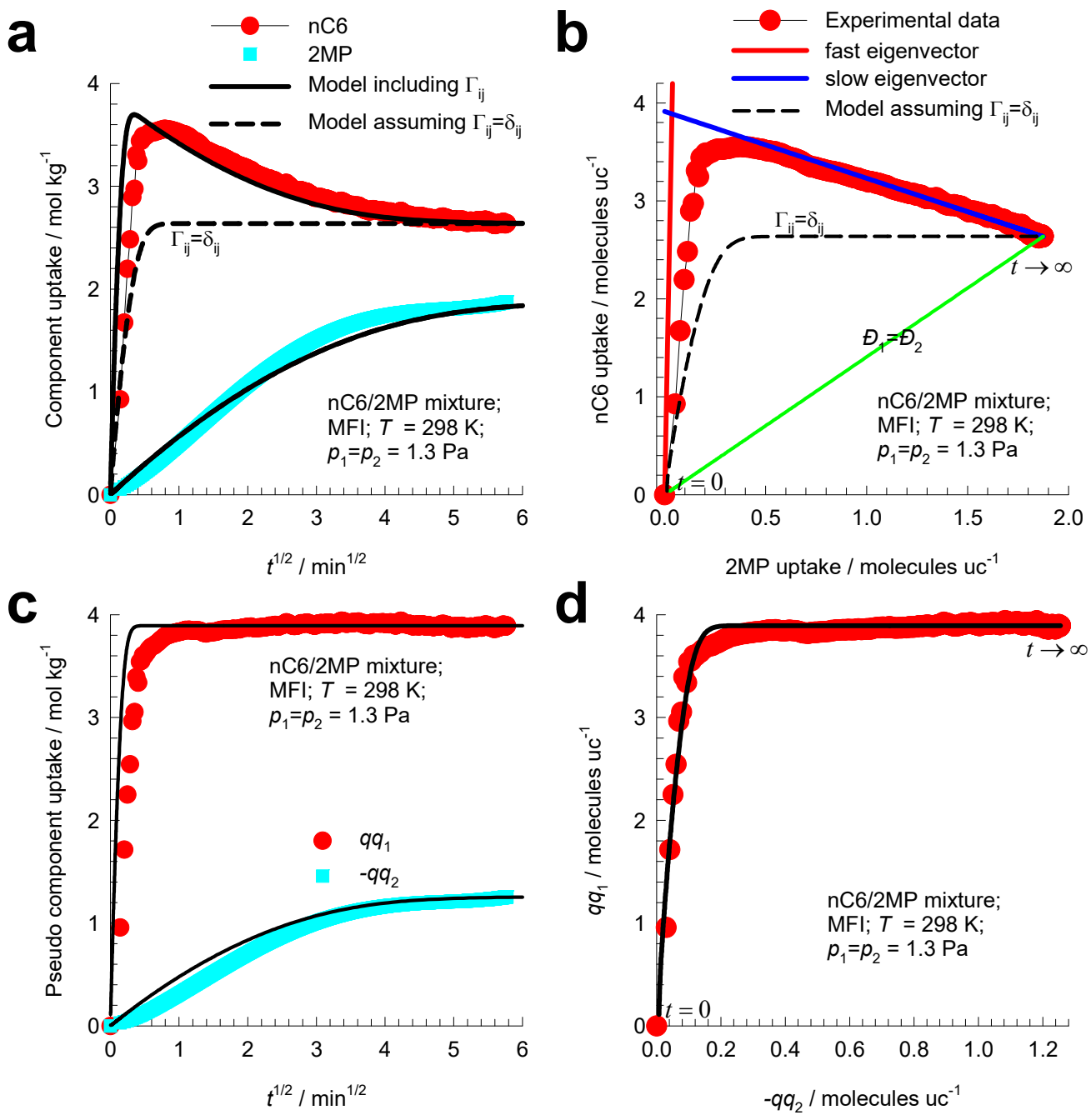

Figure S12. (a) Experimental data of Titze et al.[50] for Run 1 transient uptake of nC6/2MP mixtures in MFI zeolite. Input data simulation of Run 1: $Đ_1/r_c^2$ = 0.016 s^{-1}; $Đ_2/r_c^2$ = 1.6×10^{-4} s^{-1}; = 0 Pa; $t \geq 0$; $p_1(r_c,t) = p_2(r_c,t)$ = 1.3 Pa. The isotherm data are provided in Table S2. (b) component loadings plotted in composition space. (c) Transient equilibration of pseudo component loadings. (d) Pseudo component loadings plotted in composition space.

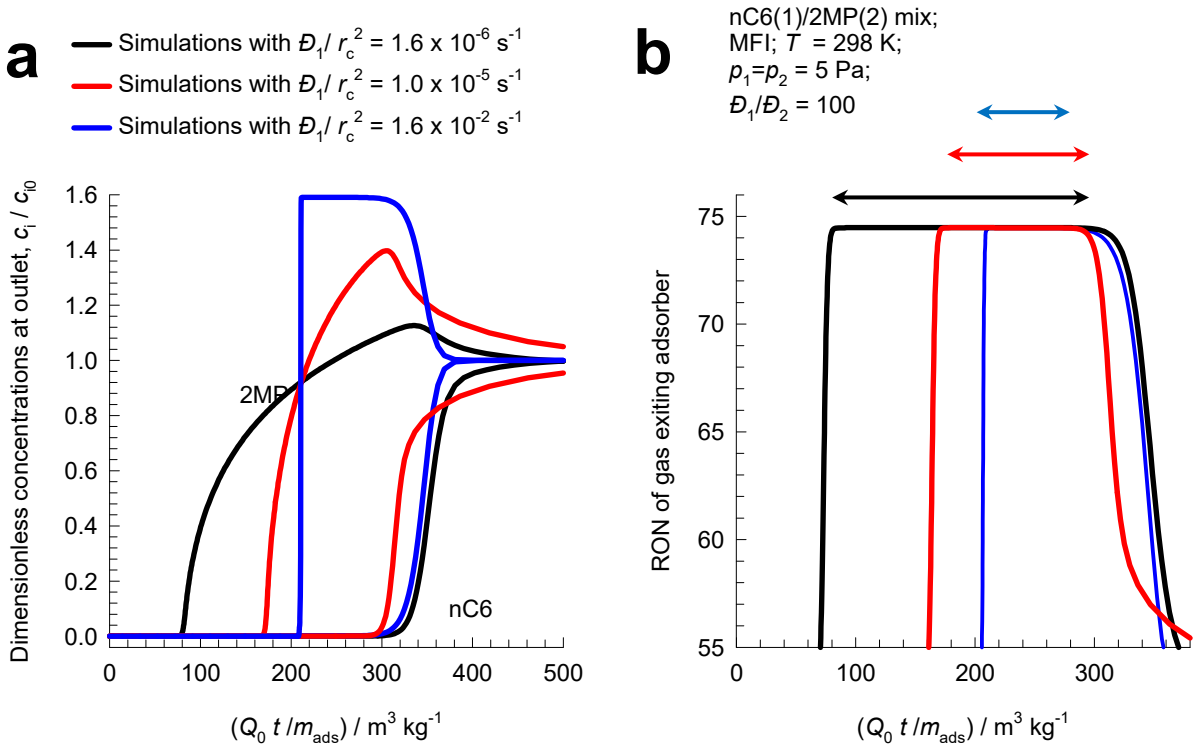

Figure S13. (a) Transient breakthrough for 50/50 nC6(1)/2MP(2) mixtures in MFI zeolite at 298 K and total pressure of 10 Pa. The dimensionless concentrations at the exit of the adsorber, c_i/c_{i0}, are plotted as a function of a modified time parameter defined by $\frac{Q_0 t}{m_{ads}}$.. For the three sets of simulations $Đ_1/r_c^2$ = $1.6\times10^{-6}, 1.0\times10^{-5}, 1.6\times10^{-2}$ s^{-1}, maintaining the ratio $Đ_1/Đ_2 = 100$. (b) RON of product gas mixture leaving fixed bed adsorber packed with MFI zeolite.

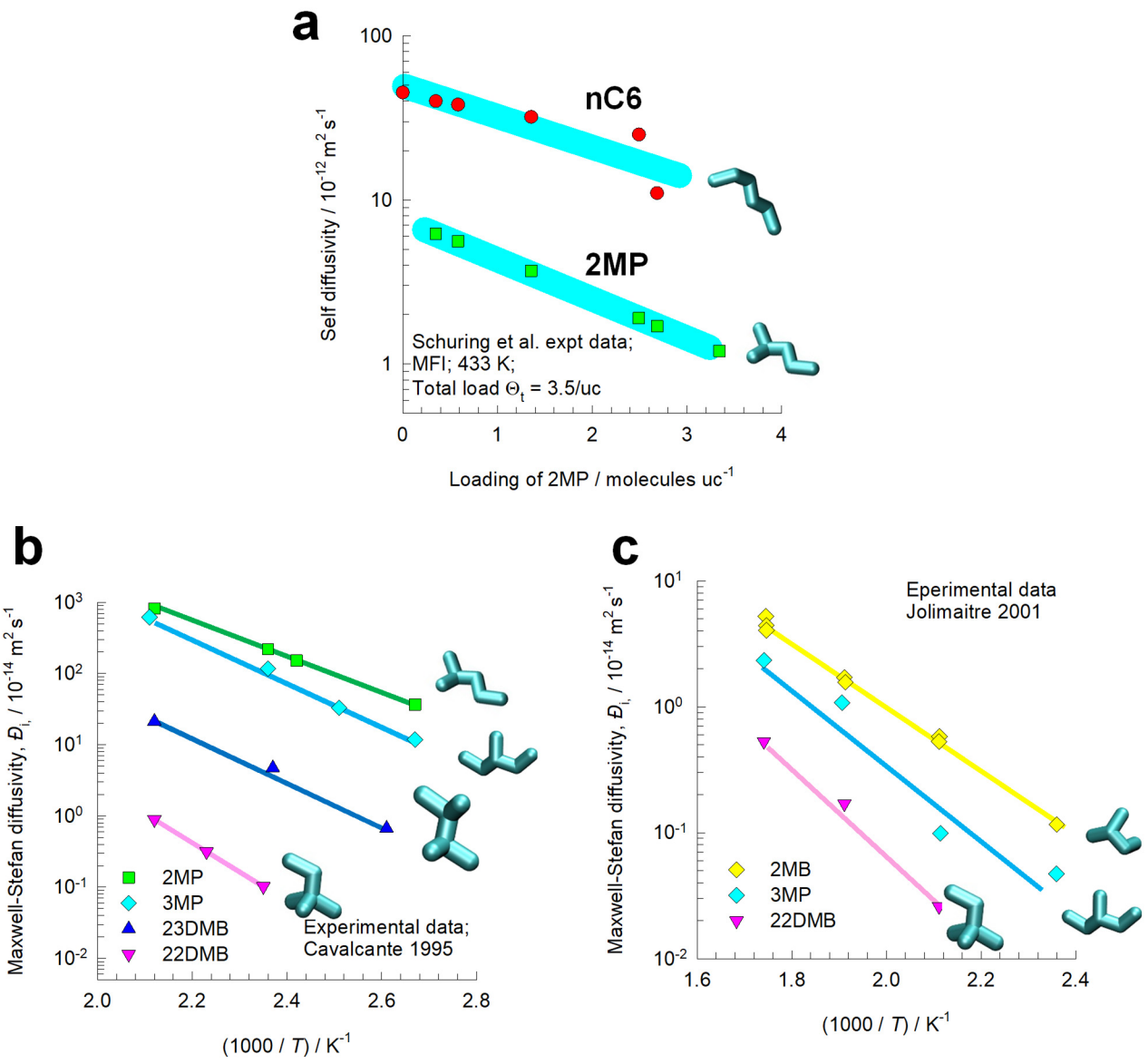

Figure S14. (a) Experimental data[52] on self-diffusivities of nC6 and 2-methylpentane (2MP) as a function of the loading of 2MP, keeping the total loading Θ_t = 3.5/uc. (b, c) Arrhenius plot of diffusivities of 2MB, 2MP, 3MP, 22DMB, and 23DMB in MFI zeolite. The data are re-plotted from the experimental results of (b) Cavalcante and Ruthven,[54] and (c) Jolimaître et al.[55]

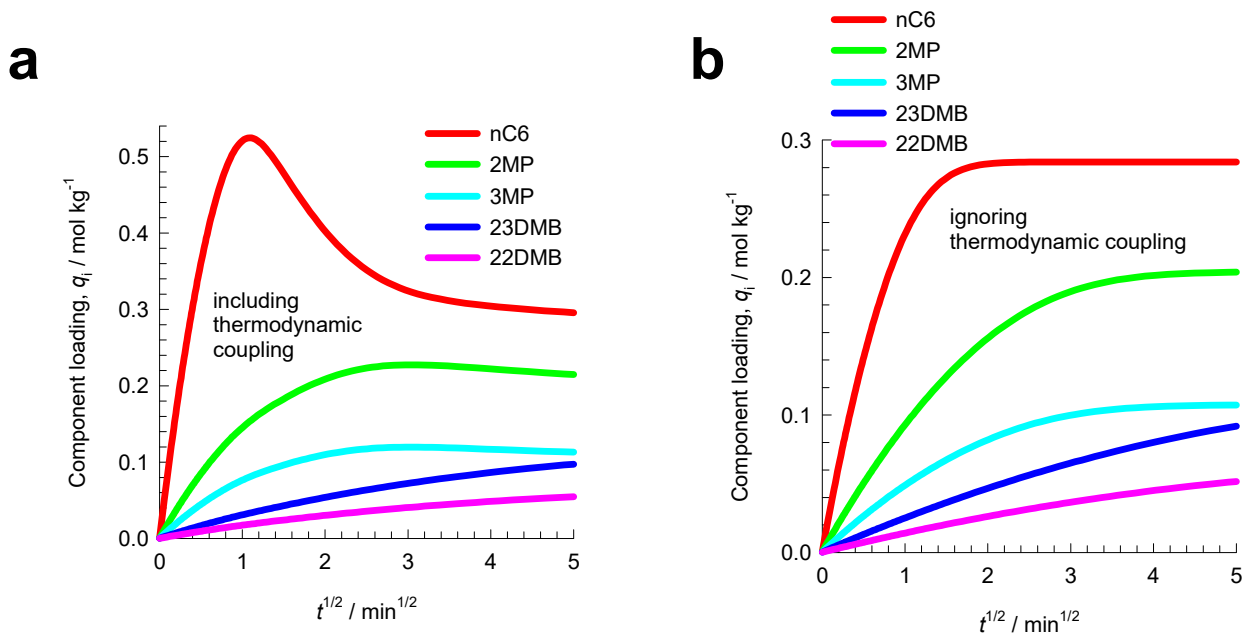

Figure S15. (a, b) Transient uptake inside MFI crystal exposed to a gas phase 5-component nC6/2MP/3MP/22DMB/23DMB mixture at a total pressure of 100 kPa and 433 K. The partial pressures of the components in the bulk gas phase at the inlet are $p_1 = p_2 = p_3 = p_4 = p_5 = 20$ kPa. (a) These uptake simulations include thermodynamic coupling: eq (S10). (b) In these uptake simulations, thermodynamic coupling is ignored: eq (S11). The input data on unary isotherms and M-S diffusivities are provided in Table S3.

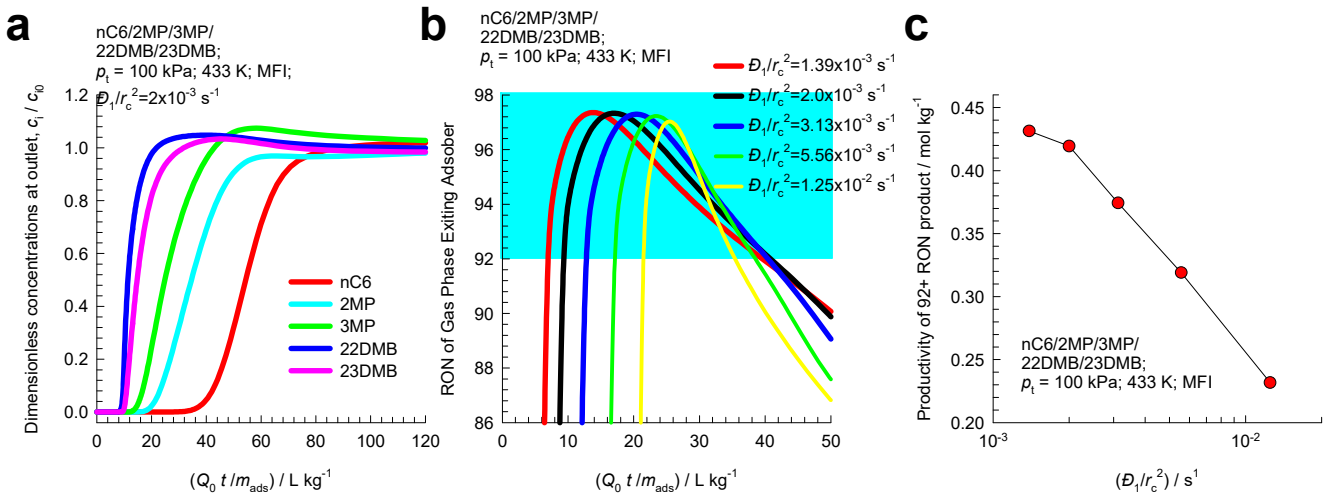

Figure S16. (a) Transient breakthrough characteristics for 5-component nC6/2MP/3MP/22DMB/23DMB mixture in a fixed bed adsorber packed with MFI operating at a total pressure of 100 kPa and 433 K. The partial pressures of the components in the bulk gas phase at the inlet are $p_1 = p_2 = p_3 = p_4 = p_5 = 20$ kPa. (b) RON of the gas mixture exiting the adsorber, plotted as function on $Q_0 t / m_{ads}$, for five different values of $Đ_1 / r_c^2$. (c) 92+ RON productivity of MFI, plotted as function of $Đ_1 / r_c^2$.

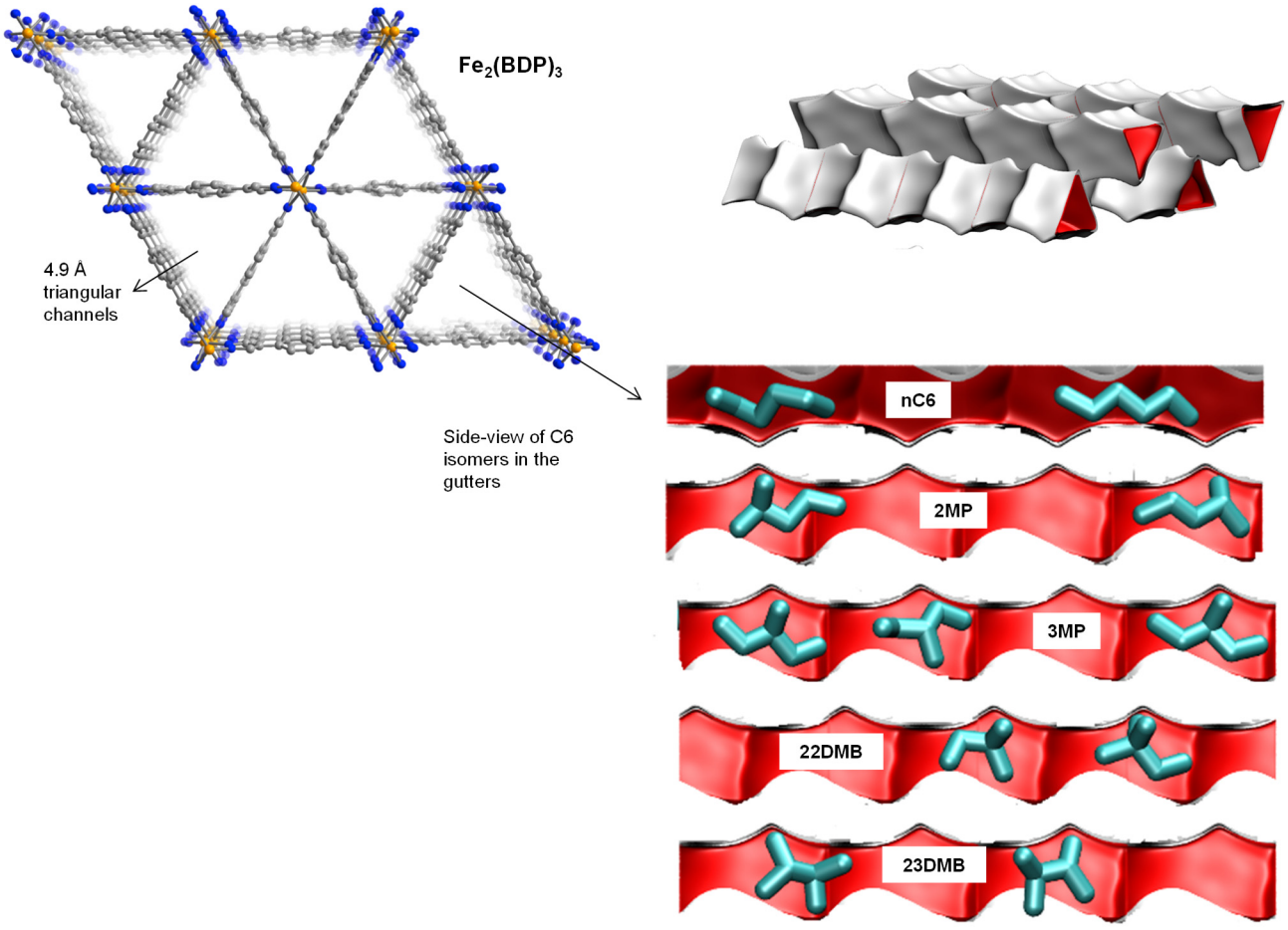

Figure S17. The triangular channel topology of $Fe_2(BDP)_3$.[40] Also shown are computational snapshots (side-on view) of the conformations of nC6, 2MP, 3MP, 22DMB, and 23DMB within the triangular channels.

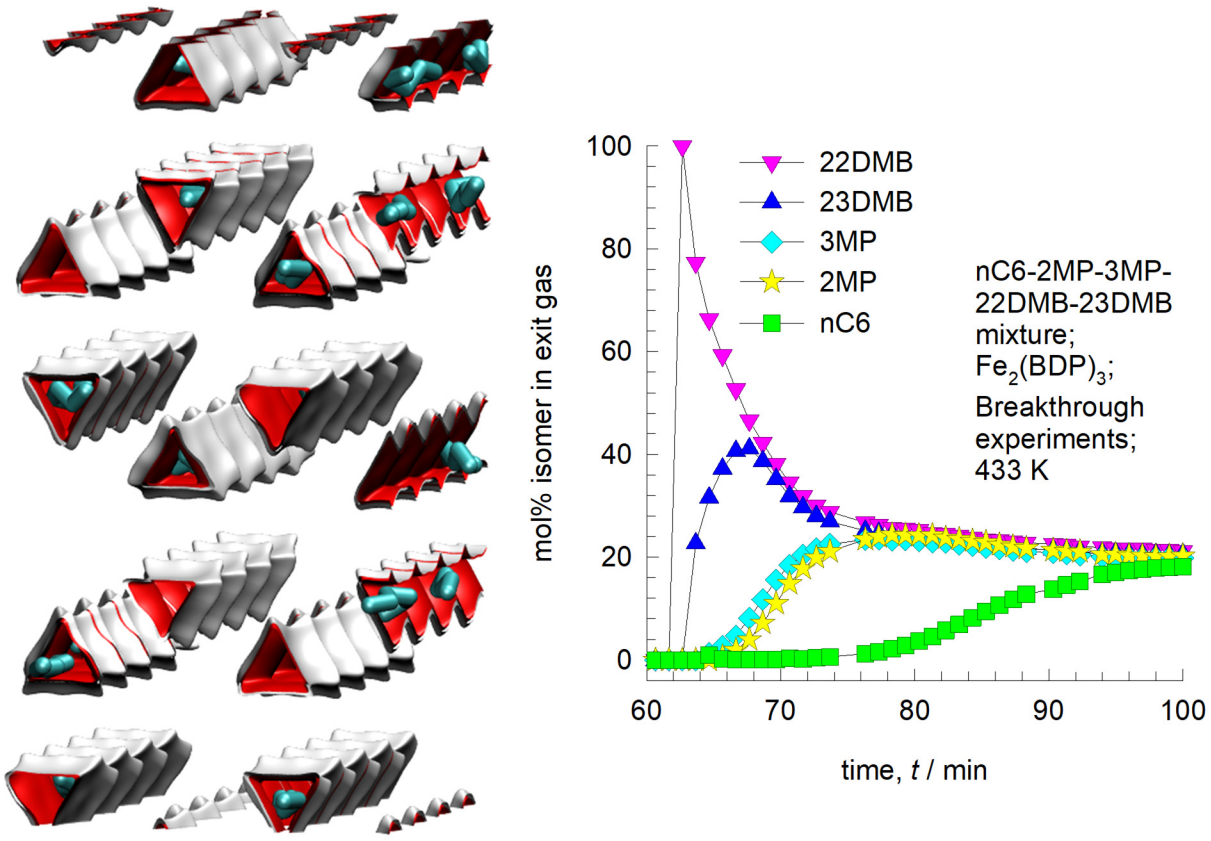

Figure S18. Experimental data on transient breakthrough of hexane isomers in a fixed bed packed with $Fe_2(BDP)_3$.[40]

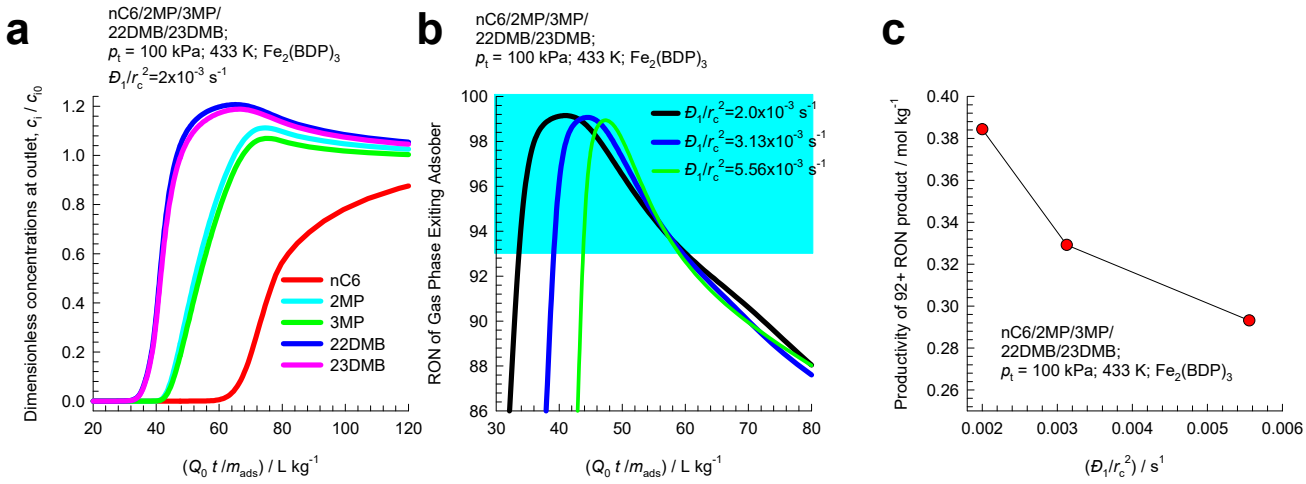

Figure S19. Simulations of breakthrough characteristics for 5-component nC6/2MP/3MP/22DMB/23DMB mixture in a fixed bed adsorber packed with $Fe_2(BDP)_3$, (framework density ρ = 1.145 kg L^{-1}), operating at a total pressure of 100 kPa and 433 K. The partial pressures of the components in the bulk gas phase at the inlet are $p_1 = p_2 = p_3 = p_4 = p_5$ = 20 kPa. (b) RON of the gas mixture exiting the adsorber, plotted as function on $Q_0 t / m_{ads}$, for three different values of $Đ_1 / r_c^2$. (c) 92+ RON productivity of $Fe_2(BDP)_3$, plotted as function of $Đ_1 / r_c^2$.

5 Adsorption/Diffusion of 1-alcohol mixtures in CHA zeolite

Let us examine the adsorption of 1-alcohols in CHA zeolite, which is a cage type zeolite that consists of cages of volume 316 $Å^3$, separated by 3.8 Å × 4.2 Å 8-ring windows. The pore landscapes and structural details of CHA zeolite are provided in Figure S20, and Figure S21.

Watch also the video presentation titled **Exploiting Entropy Effects for Separating Linear Alcohols** on YouTube https://www.youtube.com/@rajamanikrishna250/videos

Figure S22a presents snapshots of the conformations of the 1-alcohols within the cages, at saturation conditions. CBMC simulations of unary 1-alcohols with C atoms in the 1 – 6 range in CHA at 300 K, as reported in the work of Krishna and van Baten,[59] are shown in Figure S22b. The saturation capacities, decreases from 5.4 molecules $cage^{-1}$ for methanol to 1 molecule $cage^{-1}$ for 1-hexanol; see Figure S22c. Except for methanol, the saturation cage capacity has an integer value because 1-alcohol molecules cannot locate at the window regions. For 1-butanol, the cage capacity is restricted to 2 molecules $cage^{-1}$; for 1-hexanol, the cage capacity is 1 molecule $cage^{-1}$.

This difference in the cage capacities can be exploited to separate binary mixtures of linear alcohols. The CBMC simulations for five different binary mixtures: (a) methanol/ethanol, (b) ethanol/1-propanol, (c) ethanol/1-hexanol, (d) 1-butanol/1-pentanol, (e) 1-butanol/1-hexanol, and (f) 1-pentanol/1-hexanol mixtures in CHA at 300 K are shown in Figure S23. The partial fugacities in the bulk fluid phase are taken to be equal, i.e. $f_1=f_2$. In all six cases, we note a tendency for selectivity to reverse in favor of the component with the higher saturation capacity. The shaded regions in Figure S23 indicate that the bulk fluid phase is in the liquid phase for the range of fugacities, f_t. Operations with bulk liquid phase mixtures ensures that the shorter 1-alcohol will be preferentially adsorbed. The dashed lines represent calculations of the IAST; the IAST correctly, and quantitatively, anticipates selectivity reversals for all six mixtures.

Experimental confirmation of the selectivity reversals as evidenced in Figure S23 are available in the experiments reported by Remy et al.[60] for transient breakthroughs of ethanol/propanol, and ethanol/1-hexanol feed mixtures, in the liquid state, in a fixed bed adsorber packed with SAPO-34, that has the same structural topology as CHA; see Figure S24a,b. The component that is eluted first from the adsorber is the alcohol with the longer chain length. The rationalization of these experimental data can be traced to the entropy effects that favor the shorter alcohols under pore saturation conditions. The later elution of the ethanol is due to a combination of (a) entropy effects favoring the adsorption of ethanol, and (b) higher mobility of ethanol. This adsorption diffusion synergy is verified in the experimental data of Saint-Remi et al.[61] for transient uptake of ethanol/1-propanol mixtures within SAPO-34, that is the structural analog of CHA zeolite, are shown in Figure S25. The more mobile ethanol is found to exhibit a pronounced maximum in the uptake transience. The more mobile ethanol is found to exhibit a pronounced maximum during the early stages of the uptake transience.[6, 61]

The essential features of the transient uptake on ethanol/1-propanol uptake in SAPO-34 can be adequately captured by the eq (S20) taking $Đ_1/r_c^2 = 2\times10^{-5}$ s^{-1}; $Đ_1/Đ_2 = 300$. The ethanol overshoot is caused by the significant off-diagonal elements of $[\Gamma]$. If we assume $\Gamma_{ij} = \delta_{ij}$, and invoke eq (S22), the ethanol overshoot disappears; see dashed lines in Figure S25a. The unary isotherm data are provided in Table S5.

In Figure S25b the component loadings of ethanol and 1-propanol are plotted in composition space, with 1-propanol loadings on the *x*-axis. We note that the equilibration trajectory is not monotonous and follows a serpentine trajectory. The serpentine equilibration trajectory is guided and bound by the two eigenvectors, indicated by the straight red and blue lines.

Transient breakthrough simulations for ethanol/1-propanol mixtures in a fixed bed adsorber packed with SAPO-34 are shown in Figure S25c. The partial pressures of the feed mixture are $p_1 = p_2 = 500$ kPa. Two sets of simulations were performed maintaining the ratio $Đ_1/Đ_2 = 300$. For the two sets of simulations $Đ_1/r_c^2 = 0.012, 1.2$ s^{-1}. We note that the separation performance is significantly improved

when the diffusional influences are stronger (indicated by the solid black lines). This demonstrates that synergistic adsorption/diffusion are beneficial to separations. A direct comparison with the breakthrough experiments in Figure S24a is not possible because insufficient information is provided by Saint-Remi et al.[61] on the breakthrough tube dimensions, and operating conditions. There is however a qualitative agreement between experiments and simulations.

5.1 List of Tables for Adsorption/Diffusion of 1-alcohol mixtures in CHA zeolite

Table S5. Dual-site Langmuir-Freundlich parameters for pure ethanol and 1-propanol in CHA at 300 K. The fit parameters are based on the CBMC simulations of pure component isotherms presented in earlier work.[59] Note that the saturation capacities are specified in molecules per cage; multiply these by 1.387 to obtain the values in mol per kg framework.

	Site A			Site B		
	$\frac{\Theta_{A,sat}}{\text{molecules cage}^{-1}}$	$\frac{b_A}{\text{Pa}^{-\nu_A}}$	ν_A	$\frac{\Theta_{B,sat}}{\text{molecules cage}^{-1}}$	$\frac{b_B}{\text{Pa}^{-\nu_B}}$	ν_B
ethanol	2	7.93×10^{-5}	0.87	2	3.6×10^{-3}	1.14
1-propanol	1	1.28×10^{-2}	1.8	1	9.11×10^{-2}	1

5.2 List of Figures for Adsorption/Diffusion of 1-alcohol mixtures in CHA zeolite

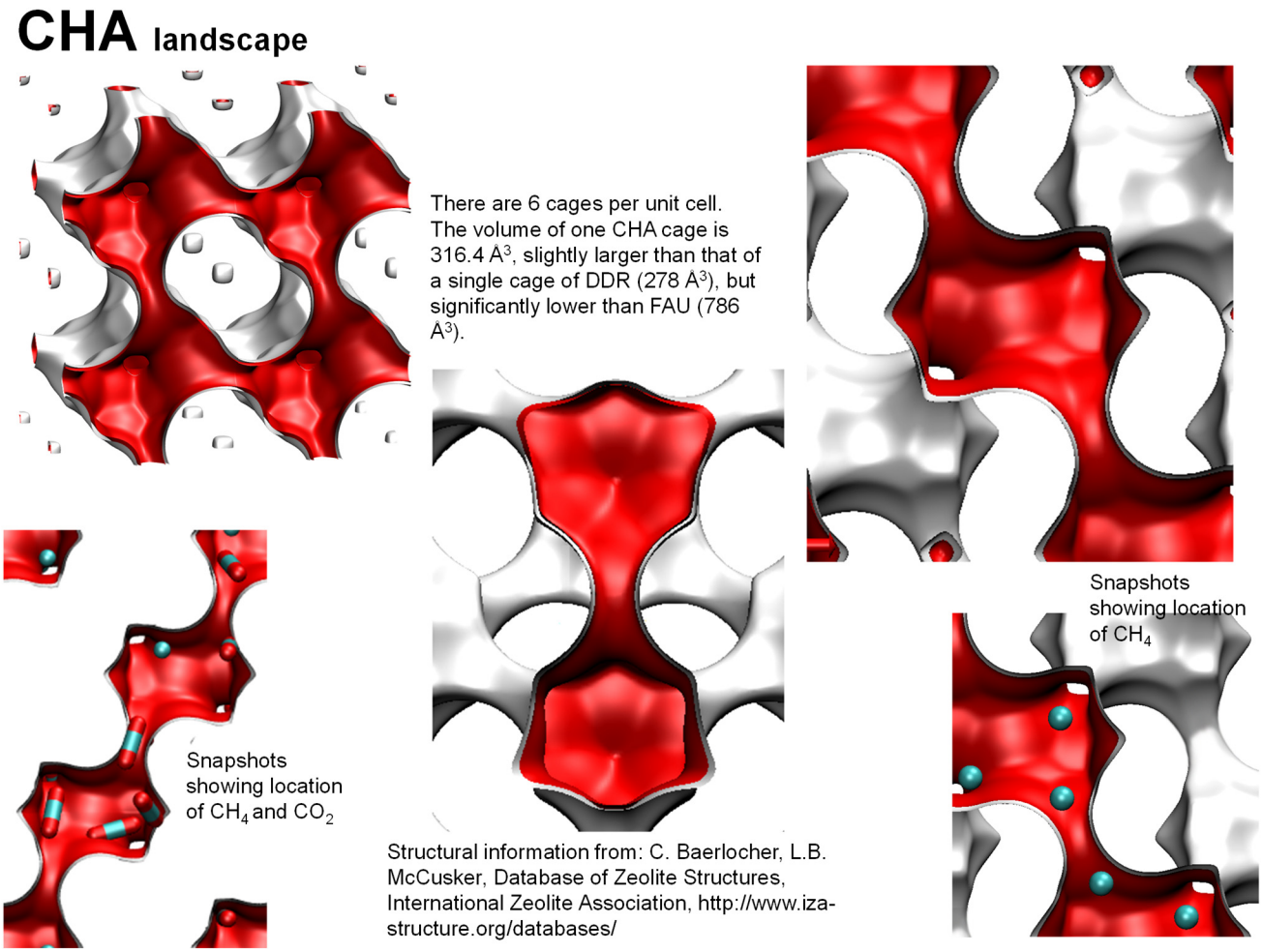

Figure S20. Pore landscapes and structural details for CHA zeolite.

CHA window and pore dimensions

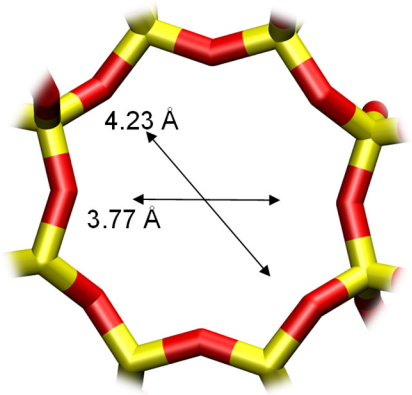

CHA

The window dimensions calculated using the van der Waals diameter of framework atoms = 2.7 Å are indicated above by the arrows.

	CHA
a /Å	15.075
b /Å	23.907
c /Å	13.803
Cell volume / Å^3	4974.574
conversion factor for [molec/uc] to [mol per kg Framework]	0.2312
conversion factor for [molec/uc] to [kmol/m^3]	0.8747
ρ [kg/m3]	1444.1
MW unit cell [g/mol(framework)]	4326.106
ϕ, fractional pore volume	0.382
open space / Å^3/uc	1898.4
Pore volume / cm^3/g	0.264
Surface area /m^2/g	758.0
DeLaunay diameter /Å	3.77

Figure S21. Pore landscapes and structural details for CHA zeolite.

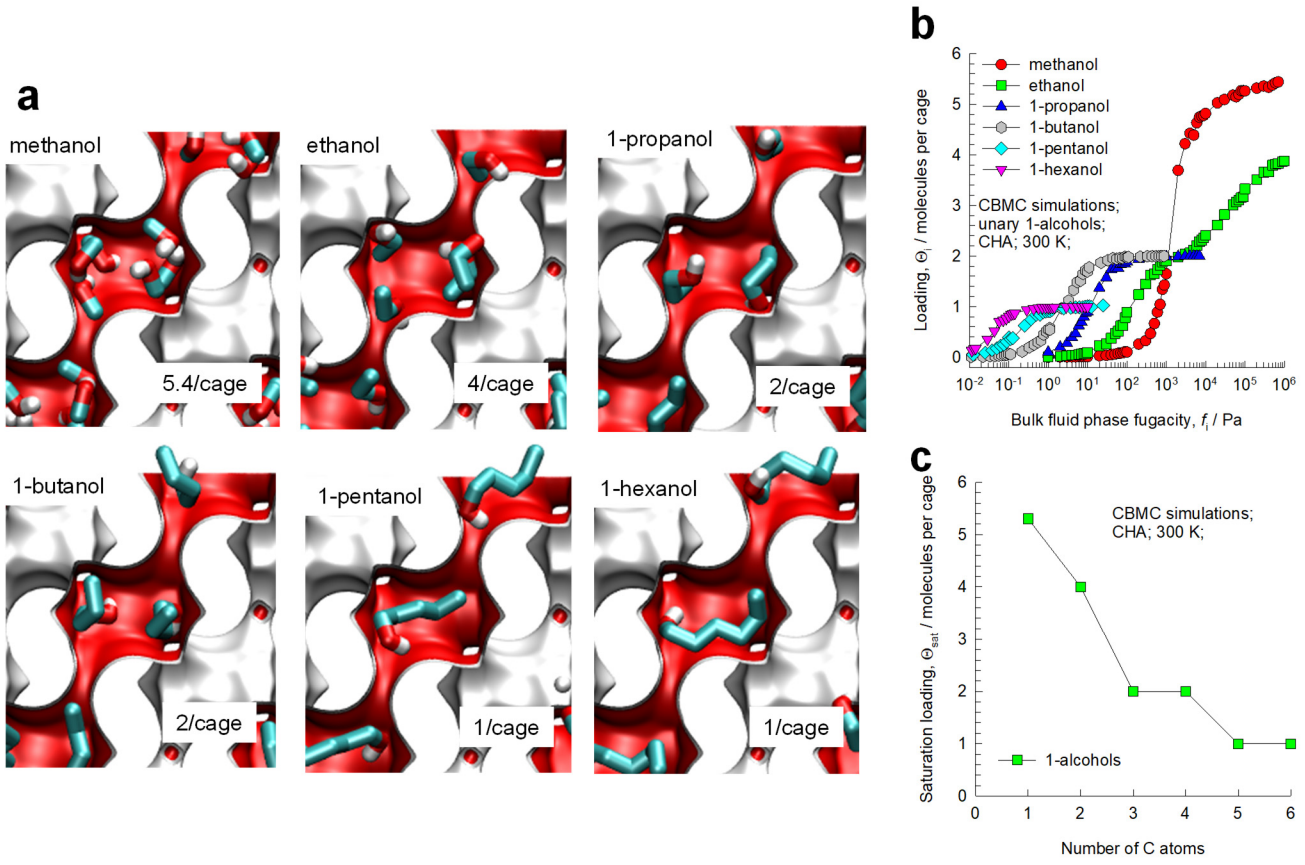

Figure S22. (a) Snapshots showing the conformations of 1-alcohols in CHA at saturation conditions. (b) CBMC simulations[59] of pure component adsorption isotherms for 1-alcohols in CHA at 300 K. (c) Saturation capacities for adsorption of 1-alcohols in CHA at 300 K.

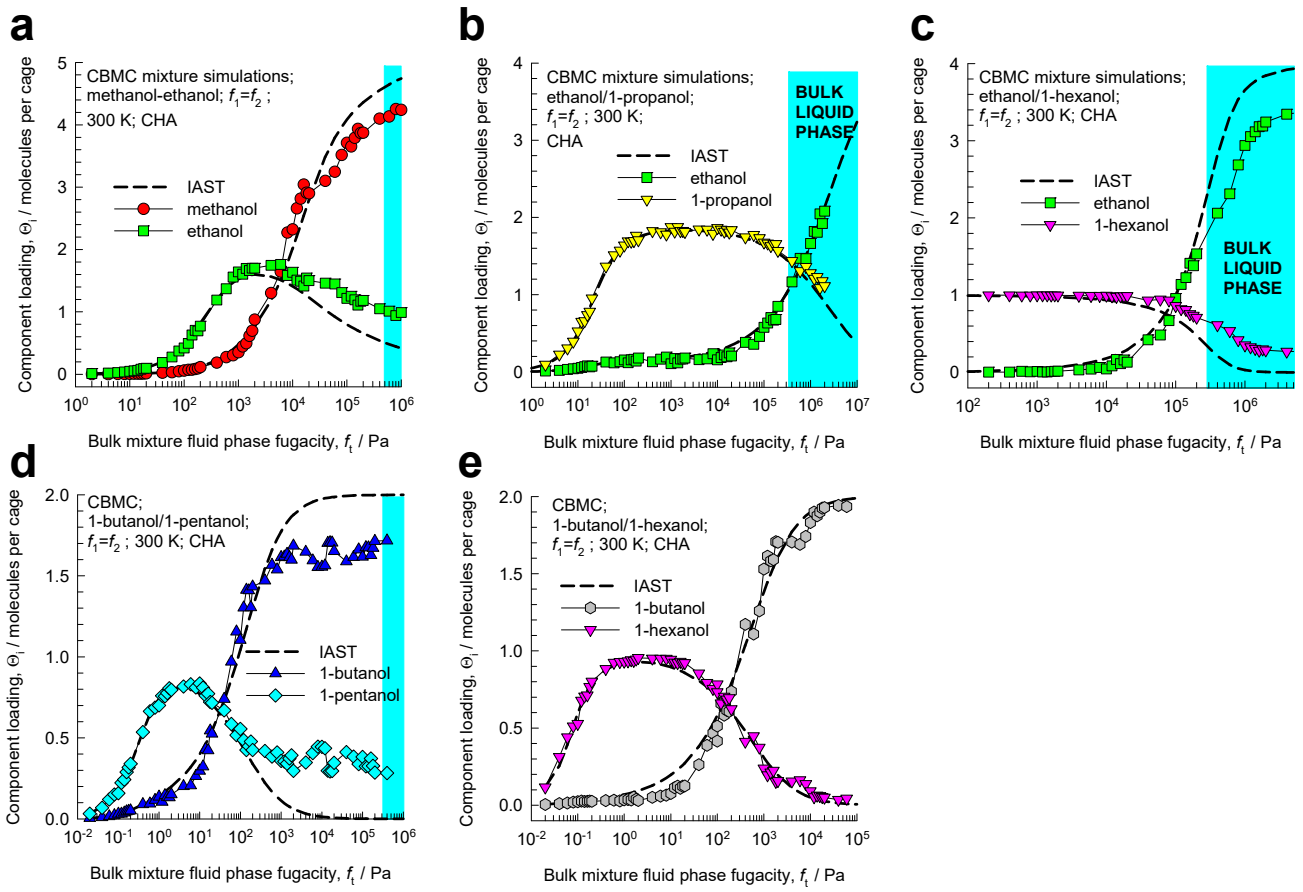

Figure S23. CBMC mixture simulations for (a) methanol/ethanol, (b) ethanol/1-propanol, (c) ethanol/1-hexanol, (d) 1-butanol/1-pentanol, and (e) 1-butanol/1-hexanol mixtures in CHA at 300 K. The partial fugacities in the bulk fluid phase are taken to be equal, i.e. $f_1=f_2$. The dashed lines represent IAST calculations using the unary isotherm data are provided in Table S5. The range of liquid phase operation is indicated by the shaded region; the transition between vapor and liquid bulk phase is determined using the Peng-Robinson equation of state.

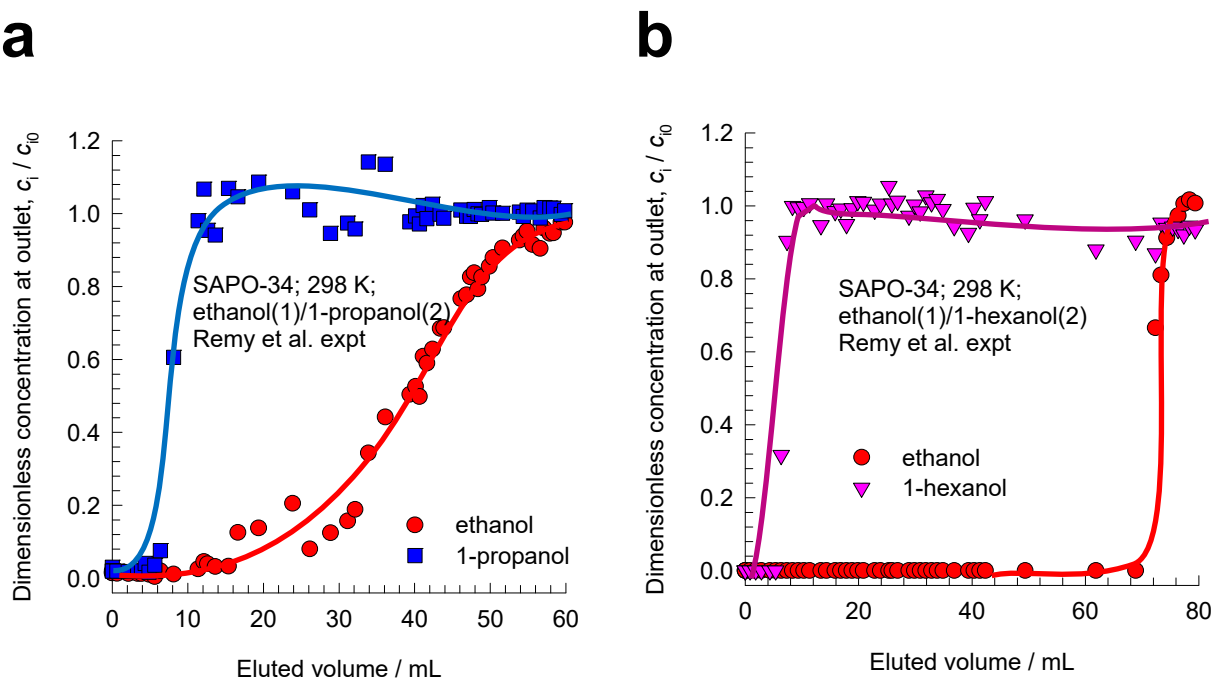

Figure S24. (a, b) Transient breakthrough experimental data of Remy et al.[60] for separation of ethanol/1-propanol and ethanol/1-hexanol liquid mixtures in a fixed bed adsorber packed with SAPO-34.

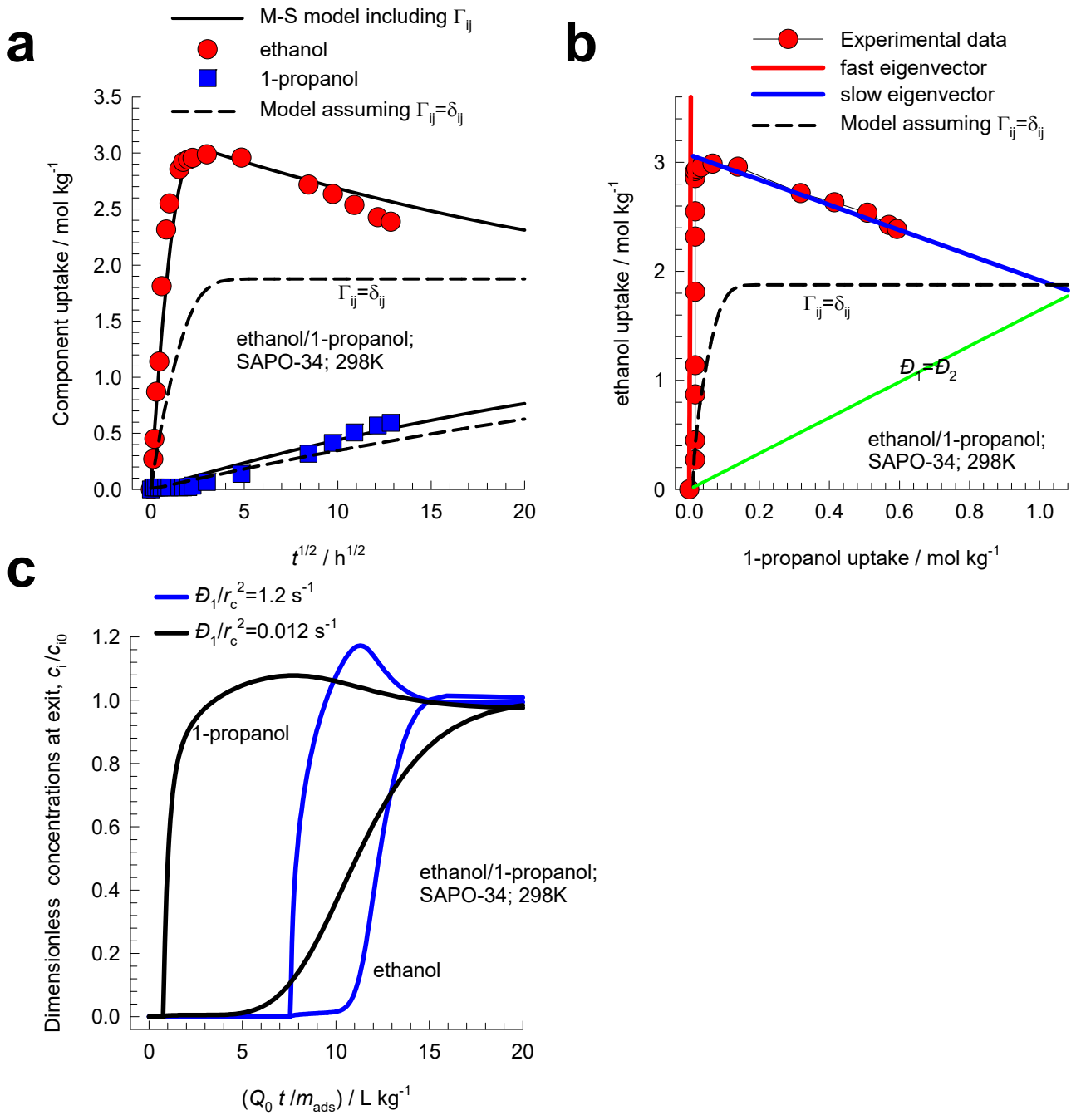

Figure S25. (a, b) Experimental data of Saint-Remi et al.[61] for transient uptake of ethanol/1-propanol mixtures within SAPO-34 (indicated by symbols), that is the structural analog of CHA zeolite. The continuous solid lines are uptake simulations. (c) Transient breakthrough simulations for ethanol/1-propanol liquid mixtures in a fixed bed adsorber packed with SAPO-34.

6 Separation of C_2H_2/CO_2 mixtures

Ethyne (C_2H_2) is an important building block in industrial chemical synthesis and also widely used as a fuel in welding equipment. C_2H_2 is commonly manufactured by the partial combustion of CH_4 or comes from cracking of hydrocarbons. In the reactor product, C_2H_2 co-exists with CO_2. Due to the similarity of molecular sizes and shapes (C_2H_2: 3.32 × 3.34 × 5.7 $Å^3$; CO_2: 3.18 × 3.33 × 5.36 $Å^3$), the separation of C_2H_2/CO_2 mixtures is particularly challenging;[62, 63] both molecules possess zero dipole moments and approximately the same quadrupole moment. Since the boiling points of C_2H_2 (189.3 K) and CO_2 (194.7 K) are close, distillation separations need to operate at cryogenic temperatures and high pressures. For separation of C_2H_2(1)/CO_2(2) mixtures, most of the suggested MOFs such as HOF-3,[64] TIFSIX-2-Cu-i,[65] TIFSIX-2-Ni-i,[66] UTSA-74,[67] FJU-90,[68] FeNi-M'MOF,[69] BSF-3,[70] CPL-1-NH_2,[71] ZNU-1,[72] and Cu^I@UiO-66-$(COOH)_2$[73] and are selective to C_2H_2. Consequently, the desired ethyne product can be recovered in the desorption cycle. MOFs that have adsorption selectivity in favor of CO_2 include ZU-610a, [74] Ce(IV)-MIL-140-4F, [75] and Y-bptc[76]. Figure S26a compares experimental data for transient breakthroughs of 50/50 C_2H_2(1)/CO_2(2) mixtures in ZU-610a, [74] Ce(IV)-MIL-140-4F, [75] and Y-bptc[76] operating at 298 K, and total pressure p_t = 100 kPa. The published experimental data for dimensionless concentrations at the exit of the adsorber, c_i/c_{i0}, are plotted as a function of a modified time parameter defined by $Q_0 t/m_{ads}$. The relative productivity values for pure C_2H_2 are indicated by the length of the arrows. This comparison shows that the best separation performance, in terms of C_2H_2 productivity is afforded by the ultra-microporous Y-bptc;[76] we examine further the good separation performance of this MOF.

The unary isotherm data for the unary guests in Y-bptc are fitted with the 1-site Langmuir parameter fits; the parameters are specified in Table S6.The adsorption selectivity $S_{ads} \approx 3.75$, in favor of CO_2. The experimental data on transient unary uptakes of C_2H_2(1), and CO_2(2) mixtures in Y-bptc as reported in the paper by He et al.[76] at a total pressure is 100 kPa are presented in Figure S26b. We note that CO_2

attains equilibrium more rapidly than C_2H_2. We have synergy between adsorption and diffusion, both favor CO_2. Figure S26c compares the experimental breakthroughs for Y-bptc[76] with simulations ignoring diffusional influences. We note that the experiments show higher productivity for purified C_2H_2 than the simulations ignoring diffusional influences. We now quantify the adsorption-diffusion synergy in Y-bptc.

Figure S27a presents calculations of the elements of the matrix of thermodynamic correction factors as a function of total bulk gas pressure, p_t, calculated using the mixed-gas Langmuir model for 50/50 $C_2H_2(1)/CO_2(2)$ mixtures adsorption in Y-bptc at 298 K. Figure S27b presents calculations of the ratios Γ_{12}/Γ_{11}, Γ_{21}/Γ_{22} as a function of total bulk gas pressure, p_t, These calculations show that the off-diagonal elements are significant fractions of the diagonal elements. Figure S27c shows simulations of the transient uptake of unary guests $C_2H_2(1)$ and $CO_2(2)$ for Y-bptc crystals exposed to bulk gas pressures of 100 kPa. These unary uptake simulations, with $Đ_1/r_c^2 = 4.25\times10^{-6}\,\Gamma_{ij}$ s^{-1}, and with $Đ_2/r_c^2 = 4.85\times10^{-4}$ s^{-1} are in good agreement with the experimental data on unary uptakes presented in Figure S26b. The diffusion selectivity, determined experimentally from unary uptakes,[76] $Đ_2/Đ_1 \approx 114$, also favors CO_2.

Figure S27d presents simulations of transient uptake of 50/50 $C_2H_2(1)/CO_2(2)$ mixtures in Y-bptc crystals operating at 298 K, and total pressure p_t = 100 kPa. We note that there is an overshoot in the loading of the more mobile CO_2 as it approaches equilibrium.

Figure S28a shows transient breakthrough of 50/50 $C_2H_2(1)/CO_2(2)$ mixtures through fixed bed adsorber packed with Y-bptc crystals operating at 298 K, and total pressure p_t = 100 kPa. The dimensionless concentrations at the exit of the adsorber, c_i/c_{i0}, are plotted as a function of a modified time parameter defined by $Q_0 t/m_{ads}$. For the four sets of simulations $Đ_1/r_c^2 = 4.25\times10^{-6}, 1.18\times10^{-5}, 4.72\times10^{-5}, 4.25\times10^{-4}$ s^{-1}, maintaining the ratio $Đ_2/Đ_1 = 114$, as determined experimentally[76]. With lower values of the diffusional constants $Đ_1/r_c^2$, i.e. stronger diffusional

influences, the breakthrough of the desired product C_2H_2 occurs earlier, resulting in higher productivity of purified C_2H_2 per kg of adsorbent in bed. In Figure S28b, the productivities of 99%+pure C_2H_2 is plotted as a function of $Đ_1/r_c^2$. We note that with decreasing $Đ_1/r_c^2$ the C_2H_2 productivities increase from 1.05 to 1.35 mol kg^{-1}.

In the sets of breakthrough simulations in Figure S28c we maintain $Đ_1/r_c^2 = 1.18\times10^{-5}$ s^{-1}, with varying ratios of diffusivities of CO_2 to C_2H_2: $Đ_2/Đ_1 = 200, 114, 50, 10, 2$. We note that with increasing values of $Đ_2/Đ_1$, the C_2H_2 productivities increase from 0.1 to 1.35 mol kg^{-1}; see Figure S28d. We conclude that both $Đ_1/r_c^2$, and $Đ_2/Đ_1$ have a significant impact on the productivities of purified C_2H_2. From the breakthrough experiments of He et al., [76] for Y-bptc, with $Đ_2/Đ_1 = 114$, the C_2H_2 productivity is calculated to be 1.52 mol kg^{-1}, in reasonable agreement with the simulations.

6.1 List of Tables for Separation of C2H2/CO2 mixtures

Table S6. 1-site Langmuir parameters for C_2H_2 and CO_2 in Y-bptc at 298 K. These parameters have been fitted from the data scanned from Figure 2a of He et al.[76]

	$\frac{q_{sat}}{\text{mol kg}^{-1}}$	$\frac{b}{\text{Pa}^{-1}}$
C_2H_2	3.3	6.319E-06
CO_2	3.3	2.374E-05

6.2 List of Figures for Separation of C2H2/CO2 mixtures

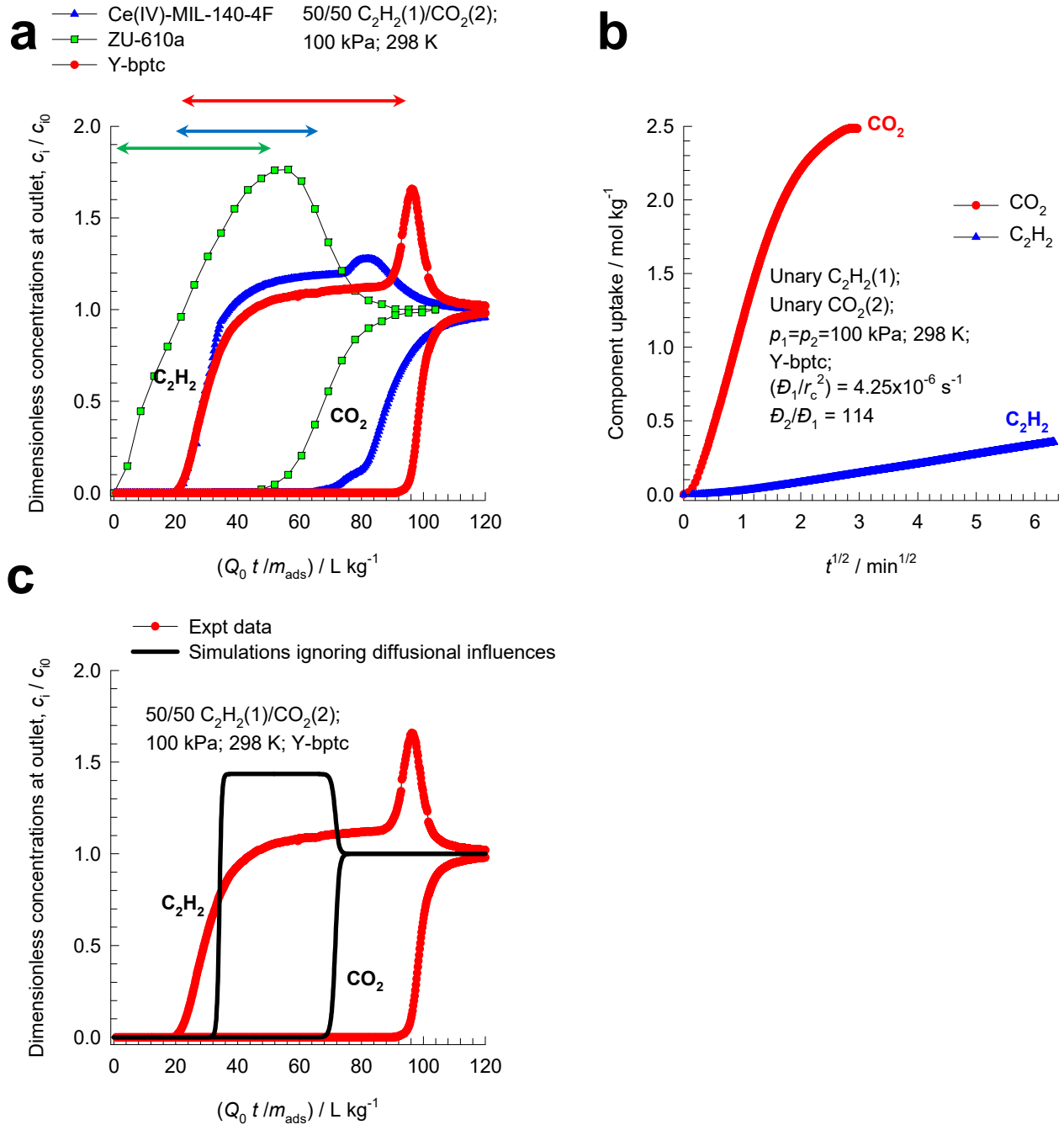

Figure S26. (a) Comparison of experimental data for transient breakthroughs of 50/50 $C_2H_2(1)/CO_2(2)$ mixtures in ZU-610a, [74] Ce(IV)-MIL-140-4F, [75] and Y-bptc[76] operating at 298 K, and total pressure p_t = 100 kPa. The published experimental data for dimensionless concentrations at the exit of the adsorber,

c_i/c_{i0} , are plotted as a function of a modified time parameter defined by $Q_0 t/m_{ads}$. (b) Transient unary uptakes of C_2H_2(1), and CO_2(2) mixtures in Y-bptc; the total pressure is 100 kPa. (c) Comparison of experimental breakthroughs for Y-bptc[76] with simulations ignoring diffusional influences.

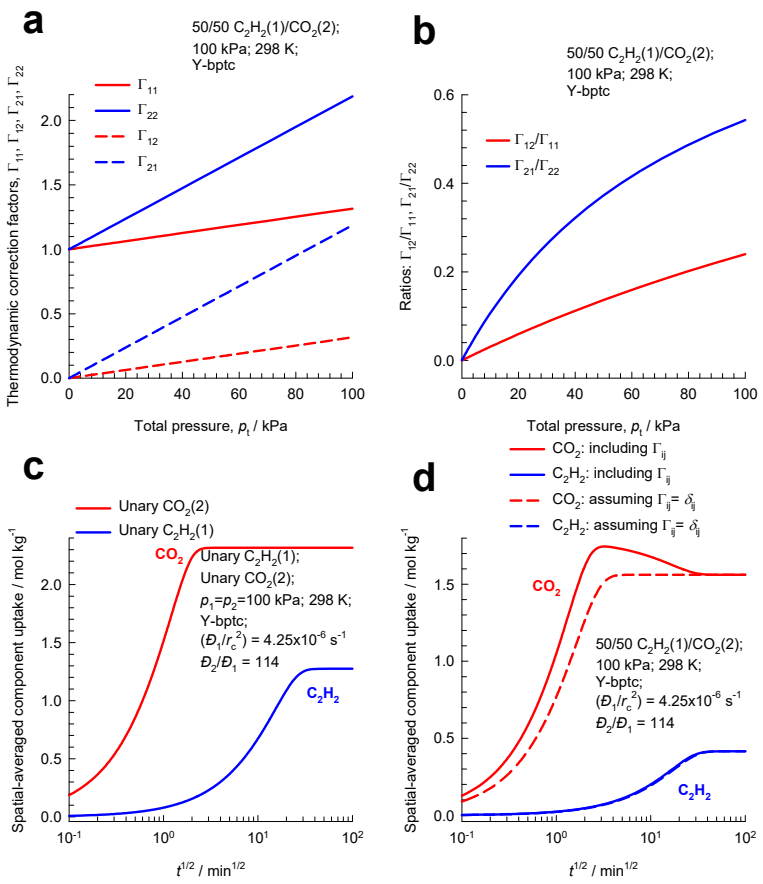

Figure S27. (a) Elements of the matrix of thermodynamic correction factors Γ_{ij} as a function of total bulk gas pressure, p_t, calculated using the mixed-gas Langmuir model for 50/50 $C_2H_2(1)/CO_2(2)$ mixtures adsorption in Y-bptc at 298 K. (b) Calculations of the ratios Γ_{12}/Γ_{11}, Γ_{21}/Γ_{22} as a function of total bulk gas pressure, p_t, (c) Transient uptake of unary guests $C_2H_2(1)$ and $CO_2(2)$ for Y-bptc crystals exposed to bulk gas pressures of 100 kPa for either guests. (d) Transient uptake of 50/50 $C_2H_2(1)/CO_2(2)$ mixtures in Y-bptc crystals operating at 298 K, and total pressure p_t = 100 kPa.

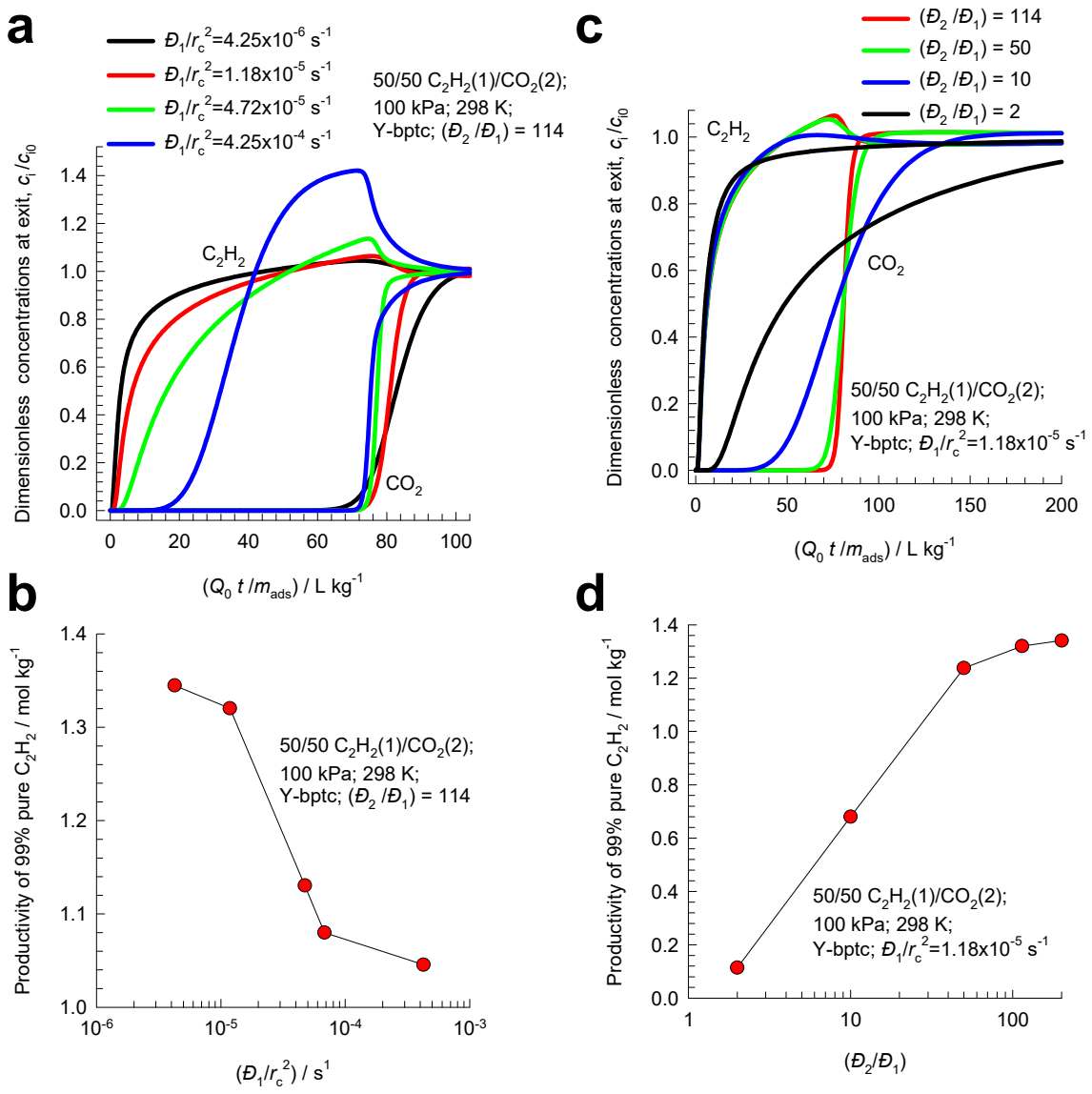

Figure S28. (a, b, c, d) Transient breakthrough of 50/50 $C_2H_2(1)/CO_2(2)$ mixtures through fixed bed adsorber packed with Y-bptc crystals operating at 298 K, and total pressure p_t = 100 kPa. In the sets of simulations in (a, b): $Đ_1/r_c^2 = 4.25\times10^{-6}, 1.18\times10^{-5}, 4.72\times10^{-5}, 4.25\times10^{-4}$ s^{-1}, maintaining the ratio $Đ_2/Đ_1=114$. In the sets of simulations in (c, d): $Đ_1/r_c^2 = 1.18\times10^{-5}$ s^{-1}, and the ratio $Đ_2/Đ_1=200,114,50,10,2$. In (a, c), the dimensionless concentrations at the exit of the adsorber, c_i/c_{i0}, are plotted as a function of a modified time parameter defined by Q_0t/m_{ads}. In (b, d), the C_2H_2 productivities are plotted as a function of (b) $Đ_1/r_c^2$, and (d) $Đ_2/Đ_1$.

7 Separation of CO_2/C_2H_6 mixtures with DDR zeolite

DDR consists of cages of 277.8 Å^3 volume, separated by 3.65 Å × 4.37 Å 8-ring windows; the pore landscapes and structural details are provided in Figure S29, and Figure S30. The guest molecules jump one-at-a-time across the narrow 8-ring windows. Consequently, correlation effects are of negligible importance; the intra-crystalline fluxes N_i, in turn, are related to the radial gradients in the molar loadings by Eq (S20).

Watch also the video presentation titled **Diffusion in DDR Zeolite** on YouTube

https://www.youtube.com/@rajamanikrishna250/videos

7.1 Transient CO_2/C_2H_6 mixture uptake in DDR zeolite

Binder et al.[77] and Lauerer et al.[78] report a set of three mixture uptake experiments with 1:1, 2:1, and 3:1 partial pressure ratios for CO_2 and C_2H_6 in the gas phase.

Experiment 1: 1:1 $CO_2(1)/C_2H_6(2)$ bulk gas mixture at 298 K, p_1 = 20 kPa, p_2 = 20 kPa.

Experiment 2: 2:1 $CO_2(1)/C_2H_6(2)$ bulk gas mixture at 298 K, p_1 = 40 kPa, p_2 = 20 kPa.

Experiment 3: 3:1 $CO_2(1)/C_2H_6(2)$ bulk gas mixture at 298 K, p_1 = 60 kPa, p_2 = 20 kPa.

The data on the unary isotherms of CO_2 and C_2H_6 at 298 K are provided in Figure 36, Chapter 4 of the PhD dissertation of Binder.[79] The unary isotherms for both CO_2, and C_2H_6 can be described adequately by a single-site Langmuir isotherm

$$q_i = \frac{q_{i,sat} b_i p_i}{1 + b_i p_i} \tag{S55}$$

The single-site Langmuir parameters are provided in Table S7. Figure S32a provides a comparison of unary isotherm data with single-site Langmuir fits using the parameters reported in Table S7. The fits are of good accuracy.

Figure 3 of Binder et al.[77] presents IAST calculations for binary mixture adsorption with constant CO_2 partial pressures of p_1 = 20, 40, and 60 kPa for experiments (1), (2), and (3), respectively. The partial pressures of C_2H_6 ethane in the gas phase is varied. The IAST calculations of Binder et al.[77] are shown as symbols in Figure S32b. For the conditions of the Binder/Lauerer experiments,[77, 78] a good prediction of the mixture adsorption equilibrium is also provided by the mixed-gas Langmuir model. To demonstrate this, the calculations using the mixed-gas Langmuir model, eq (S7) are presented as the continuous solid lines in Figure S32b. For the range of experiments, the mixed-gas Langmuir model is in very good agreement with IAST calculations.

Since we have established the accuracy of the mixed-gas Langmuir model to describe CO_2/C_2H_6 mixture adsorption equilibrium in DDR, Figure S32c,d,e presents the calculations using (S8) for the elements of the matrix of thermodynamic correction factors Γ_{ij}, using expressed as a function of total mixture loading, q_t, for (c) 1:1, (d) 2:1, and (e) 3:1 ratios of partial pressures in the gas phase. In these calculations the total gas pressure, p_t, was varied from 1 to 100 kPa. The off-diagonal elements Γ_{12}, and Γ_{21} become increasingly important with increasing loadings. This implies that thermodynamic coupling effects are of particular importance for the uptake of CO_2(1) from CO_2(1)/C_2H_6(2) gas mixtures.

Both of the guest molecules CO_2, and C_2H_6 jump length-wise across the 8-ring windows of DDR zeolite. The cross-sectional dimension of CO_2 is smaller than that of C_2H_6 (see Figure S31), and therefore the intra-crystalline M-S diffusivity of CO2 is significantly higher than that of C_2H_6. The diffusivity input values of $Đ_1/r_c^2$, and $Đ_2/r_c^2$ are taken from earlier work[6]:

Experiment 1: $Đ_1/r_c^2 = 0.125\ \text{s}^{-1}$; $Đ_2/r_c^2 = 9.38\times10^{-5}\ \text{s}^{-1}$; $Đ_1/Đ_2 = 1333$.

Experiment 2: $Đ_1/r_c^2 = 9.375\times10^{-3}\ \text{s}^{-1}$; $Đ_2/r_c^2 = 9.38\times10^{-5}\ \text{s}^{-1}$; $Đ_1/Đ_2 = 100$.

Experiment 3: $Đ_1/r_c^2 = 6.25\times10^{-3}\ \text{s}^{-1}$; $Đ_2/r_c^2 = 1.25\times10^{-4}\ \text{s}^{-1}$; $Đ_1/Đ_2 = 50$.

Figure S33(a,b,c) show the experimental data of Binder et al.[77] and Lauerer et al.[78] (indicated by symbols) for spatial-averaged transient uptake of (a) 20/20 (b) 40/40, and (c) 60/20 CO_2(1)/C_2H_6(2) gas mixtures within crystals of DDR zeolite at 298 K. The continuous solid lines are simulations of the

transient uptake using the flux relations (S20). The Maxwell-Stefan model captures the overshoots in CO_2 loadings with good accuracy for all three cases. The overshoots in the CO_2 uptake signal the phenomenon of uphill diffusion, engendered by thermodynamic coupling.[6, 80] In order to confirm that thermodynamic coupling effects are responsible for the overshoots, we also performed transient uptake in which the thermodynamic correction factors are assumed to be described by $\Gamma_{ij} = \delta_{ij}$, the Kronecker delta. The dashed lines in Figure S33(a,b,c) represent the simulation results based on Eq (S22); with this simplified model, no overshoots in the CO_2 uptake are experienced. An important consequence of thermodynamic coupling effects is that supraequilibrium loadings of CO_2 are realized during the early transience. We now investigate the consequence of thermodynamic coupling and uphill diffusion on CO_2/C_2H_6 mixture separations in a fixed bed adsorber packed with DDR adsorbent.

7.2 Analysis of CO_2/C_2H_6 uptake using eigenvalues and eigenvectors

We now proceed to analyze the three sets of experimental data in more detail in order to gain more fundamental insights.

For 20/20 $CO_2(1)/C_2H_6(2)$ gas mixtures within crystals of DDR zeolite at 298 K, at a total pressure $p_t = p_1 + p_2$ = 40 kPa, the elements of the $[\Gamma]$ are $\begin{bmatrix} \Gamma_{11} & \Gamma_{12} \\ \Gamma_{21} & \Gamma_{22} \end{bmatrix} = \begin{bmatrix} 1.208 & 0.324 \\ 0.849 & 2.32 \end{bmatrix}$. The Fick diffusivity matrix is calculated to be $\frac{\begin{bmatrix} D_{11} & D_{12} \\ D_{21} & D_{22} \end{bmatrix}}{r_c^2} = \begin{bmatrix} 1510 & 404.44 \\ 0.796 & 2.175 \end{bmatrix} \times 10^{-4}$ s^{-1}.

In Figure S34b the component loadings of $CO_2(1)$, and $C_2H_6(2)$ are plotted in composition space, with C_2H_6 loadings on the *x*-axis. We note that the equilibration trajectory is not monotonous and follows a serpentine trajectory. In order to appreciate the fundamentals that underlie this serpentine trajectory we

plot the two eigenvectors of $[D]$: $(e_1)=\begin{pmatrix}1\\ -\dfrac{D_{11}-\lambda_1}{D_{12}}\end{pmatrix}$ and $(e_2)=\begin{pmatrix}1\\ -\dfrac{D_{21}}{D_{22}-\lambda_2}\end{pmatrix}$ where the two eigenvalues are $\dfrac{\lambda_1}{r_c^2}=1510\times10^{-4}$ s^{-1}; $\dfrac{\lambda_2}{r_c^2}=1.962\times10^{-4}$ s^{-1}.

During the initial transience, the equilibration trajectory is dictated by the fast eigenvector, indicated by the red line in Figure S34b

$$\left(q_2-q_{20}\right)=-\frac{D_{11}-\lambda_1}{D_{12}}\left(q_1-q_{10}\right) \tag{S56}$$

As equilibrium is approached, the equilibration trajectory follows the path dictated by the slow eigenvector, indicated by the blue line in Figure S34b

$$\left(q_2-q_2^*\right)=-\frac{D_{21}}{D_{22}-\lambda_2}\left(q_1-q_1^*\right) \tag{S57}$$

The experimental data on the equilibration trajectory lies within the two bounds dictated by the two eigenvectors.

The pseudo-component loadings $[P]^{-1}(q)=(qq)$ follow monotonous paths to equilibrium; each pseudo-component relaxes with the corresponding eigenvalues λ_1 and λ_2.

$$\left(qq_i^*-\overline{qq_i}(t)\right)=Q_i\left(qq_i^*-qq_{i0}\right);\quad Q_i=\frac{6}{\pi^2}\sum_{m=1}^{\infty}\frac{1}{m^2}\exp\left[-m^2\pi^2\frac{\lambda_i t}{r_c^2}\right];\quad i=1,2 \tag{S58}$$

The transient equilibration of the pseudo component loadings are plotted in Figure S34c; note that the pseudo loading of C_2H_6, qq_2 is negative. In pseudo composition space, the pseudo component loadings follow a monotonous approach to equilibrium; see Figure S34d.

Figure S35a,b,c,d presents the corresponding results for 40/20 CO_2(1)/C_2H_6(2) gas mixtures within crystals of DDR zeolite at 298 K, at a total pressure $p_t = p_1 + p_2$ = 60 kPa. The elements of the $[\Gamma]$ are $\begin{bmatrix}\Gamma_{11} & \Gamma_{12}\\ \Gamma_{21} & \Gamma_{22}\end{bmatrix}=\begin{bmatrix}1.416 & 0.647\\ 0.849 & 2.32\end{bmatrix}$. The Fick diffusivity matrix is calculated to be

$\frac{\begin{bmatrix} D_{11} & D_{12} \\ D_{21} & D_{22} \end{bmatrix}}{r_c^2} = \begin{bmatrix} 132.75 & 60.667 \\ 0.796 & 2.175 \end{bmatrix} \times 10^{-4}$ s^{-1}. The two eigenvalues are

$\frac{\lambda_1}{r_c^2} = 133.119 \times 10^{-4}$ s^{-1}; $\frac{\lambda_2}{r_c^2} = 1.806 \times 10^{-4}$ s^{-1}.

Figure S36a,b,c,d presents the corresponding results for 60/20 CO_2(1)/C_2H_6(2) gas mixtures within crystals of DDR zeolite at 298 K, at a total pressure $p_t = p_1 + p_2$ = 80 kPa. The elements of the $[\Gamma]$ are

$\begin{bmatrix} \Gamma_{11} & \Gamma_{12} \\ \Gamma_{21} & \Gamma_{22} \end{bmatrix} = \begin{bmatrix} 1.624 & 0.971 \\ 0.849 & 2.32 \end{bmatrix}$. The Fick diffusivity matrix is calculated to be

$\frac{\begin{bmatrix} D_{11} & D_{12} \\ D_{21} & D_{22} \end{bmatrix}}{r_c^2} = \begin{bmatrix} 101.5 & 60.667 \\ 1.061 & 2.9 \end{bmatrix} \times 10^{-4}$ s^{-1}. The two eigenvalues are

$\frac{\lambda_1}{r_c^2} = 102.148 \times 10^{-4}$ s^{-1}; $\frac{\lambda_2}{r_c^2} = 2.252 \times 10^{-4}$ s^{-1}.

7.3 Separating CO_2/C_2H_6 mixtures in fixed bed adsorber packed with DDR zeolite

The separation of CO_2/C_2H_6 is relevant in the context of natural gas processing. Current technologies for CO_2/C_2H_6 separations use extractive distillation because of CO_2/C_2H_6 azeotrope formation.[81] Another alternative is to combine distillation technology with membrane separations; for this purpose cross-linked polyethylene oxide (XLPEO) membranes have demonstrated to have good separation potential.[3, 82, 83] The Binder/Lauerer uptake experiments suggest the possibility of diffusion-selective purification of ethane by selective removal of CO_2 present as impurities in mixtures with ethane.

To demonstrate the concept of diffusion-selective separations, we carried out transient breakthrough simulations in a fixed bed adsorber packed with crystallites of DDR.

Figure S37a shows the transient breakthrough of 50/50 CO_2(1)/C_2H_6(2) mixtures through fixed bed adsorber packed with DDR crystals operating at 298 K, and total pressure p_t = 40 kPa. In the two sets of simulations the ratio $Đ_1/Đ_2 = 1333$, as determined experimentally in Figure S33a. Two different values

of the diffusional time constants were chosen $Đ_1/r_c^2 = 1.25\times10^{-3}, 0.5$ s^{-1}. For the case in which diffusional influences are of diminished significance, $Đ_1/r_c^2 = 0.5$ s^{-1}, the separation selectivity favors C_2H_6 because of mixture adsorption equilibrium; in this case CO_2 exits the bed earlier. This is undesirable from the viewpoint of natural gas processing because we need to recover C_2H_6 as raffinate. With significantly stronger diffusional influences, choosing $Đ_1/r_c^2 = 1.25\times10^{-3}$ s^{-1}, uphill diffusion of CO_2 ensures that it enters the pores preferentially while C_2H_6 is rejected into the gas phase as raffinate, as is desired in practice. The stronger antisynergy between adsorption and diffusion serves to reverse the selectivity in favor of CO_2.

7.4 Separating CO_2/CH_4 mixtures in fixed bed adsorber packed with DDR zeolite

DDR zeolite is a potent adsorbent for capture of CO_2 from CO_2/CH_4 mixtures. Figure S37b shows the transient breakthrough of 20/80 $CO_2(1)/CH_4(2)$ mixtures through fixed bed adsorber packed with DDR crystals operating at 298 K, and total pressure p_t = 100 kPa. For this separation, there is synergy between adsorption and diffusion; both favor CO_2. In the two sets of simulations the ratio $Đ_1/Đ_2 = 100$. Two different values of the diffusional time constants were chosen $Đ_1/r_c^2 = 2\times10^{-2}, 2$ s^{-1}. In the two sets of simulations the ratio $Đ_1/Đ_2 = 100$. For the case in which diffusional influences are of diminished significance, $Đ_1/r_c^2 = 2$ s^{-1}, the productivity of purified CH_4 is lower.

7.5 Separating $CO_2/C_2H_6/CH_4$ mixtures in fixed bed adsorber packed with DDR zeolite

Figure S37c shows the transient breakthrough of 20/20/60 $CO_2(1)/C_2H_6(2)/CH_4(3)$ mixtures through fixed bed adsorber packed with DDR crystals operating at 298 K, and total pressure p_t = 100 kPa. For separation of this ternary mixture, both synergistic and antisynergistic influences of diffusion are in play. The net result is that both $C_2H_6(2)$, and $CH_4(3)$ can be rejected into the gas phase and recovered during the adsorption cycl.e

7.7 List of Tables for Separation of CO2/C2H6 mixtures with DDR zeolite

Table S7. 1-site Langmuir parameters for CO_2 and C_2H_6 in DDR zeolite at 298 K. These parameters have been fitted from the data scanned from Figure 36, Chapter 4 of the PhD dissertation of Binder.[79] The unary isotherm fit for CH_4 in DDR zeolite at 298 K is based on CBMC simulation data from Krishna and van Baten.[84]

	$\frac{q_{sat}}{\text{mol kg}^{-1}}$	$\frac{b}{\text{Pa}^{-1}}$
CO_2	2.8	1.04E-05
C_2H_6	1.8	6.6E-05
CH_4	2.8	2.0E-06

7.8 List of Figures for Separation of CO2/C2H6 mixtures with DDR zeolite

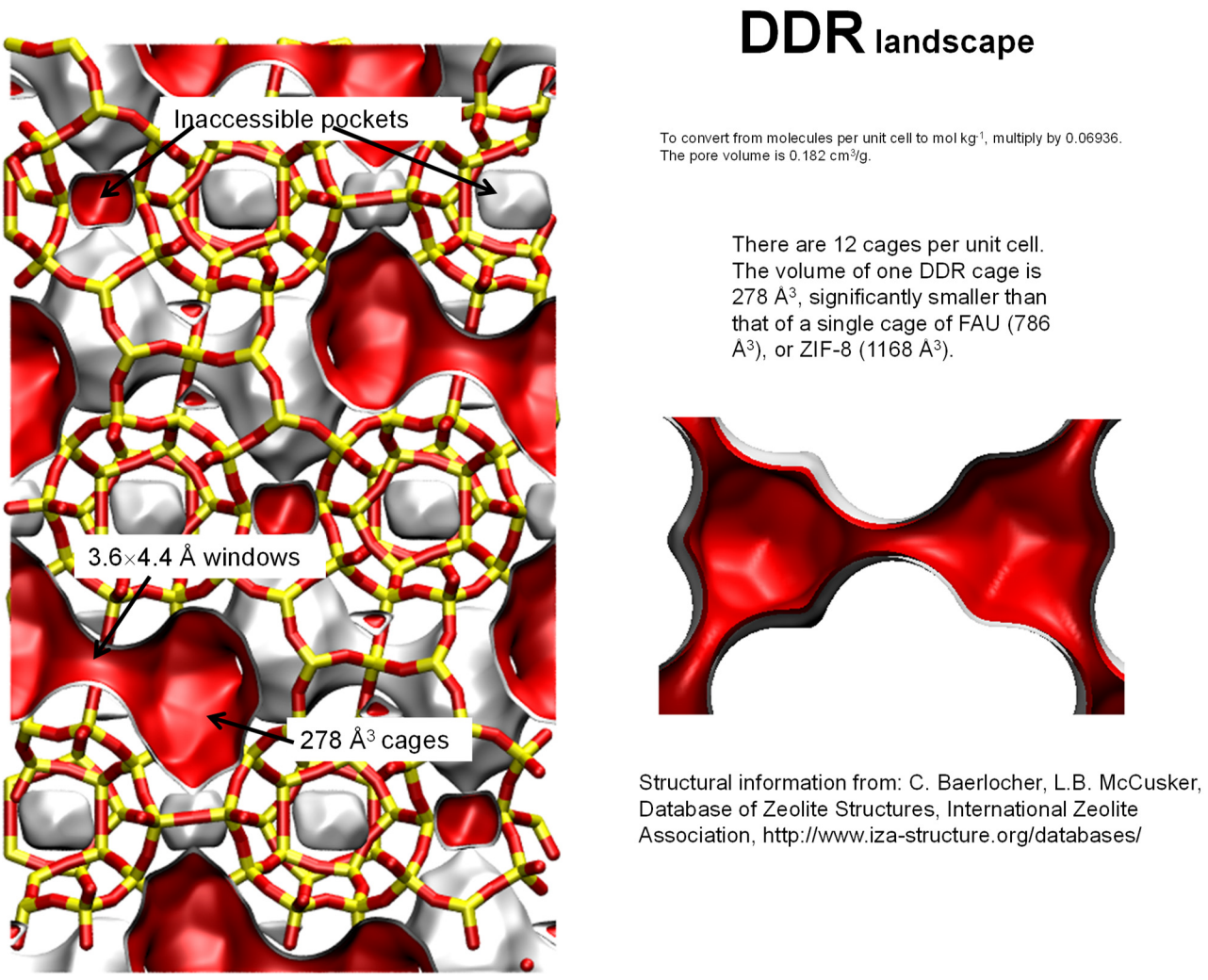

Figure S29. Pore landscape of all-silica DDR zeolite.

DDR window and pore dimensions

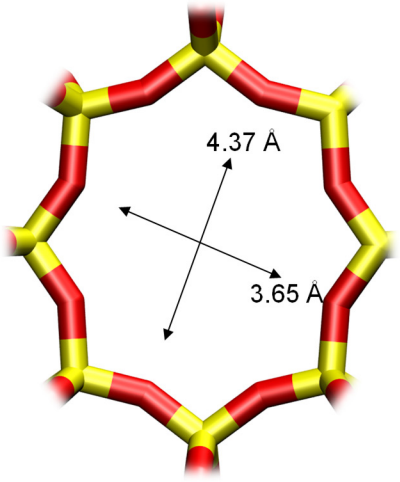

DDR

The window dimensions calculated using the van der Waals diameter of framework atoms = 2.7 Å are indicated above by the arrows.

	DDR
a /Å	24.006
b /Å	13.86
c /Å	40.892
Cell volume / Å^3	13605.72
conversion factor for [molec/uc] to [mol per kg Framework]	0.0693
conversion factor for [molec/uc] to [kmol/m^3]	0.4981
ρ [kg/m3]	1759.991
MW unit cell [g/mol(framework)]	14420.35
ϕ, fractional pore volume	0.245
open space / Å^3/uc	3333.5
Pore volume / cm^3/g	0.139
Surface area /m^2/g	350.0
DeLaunay diameter /Å	3.65

Figure S30. Structural details of all-silica DDR zeolite.

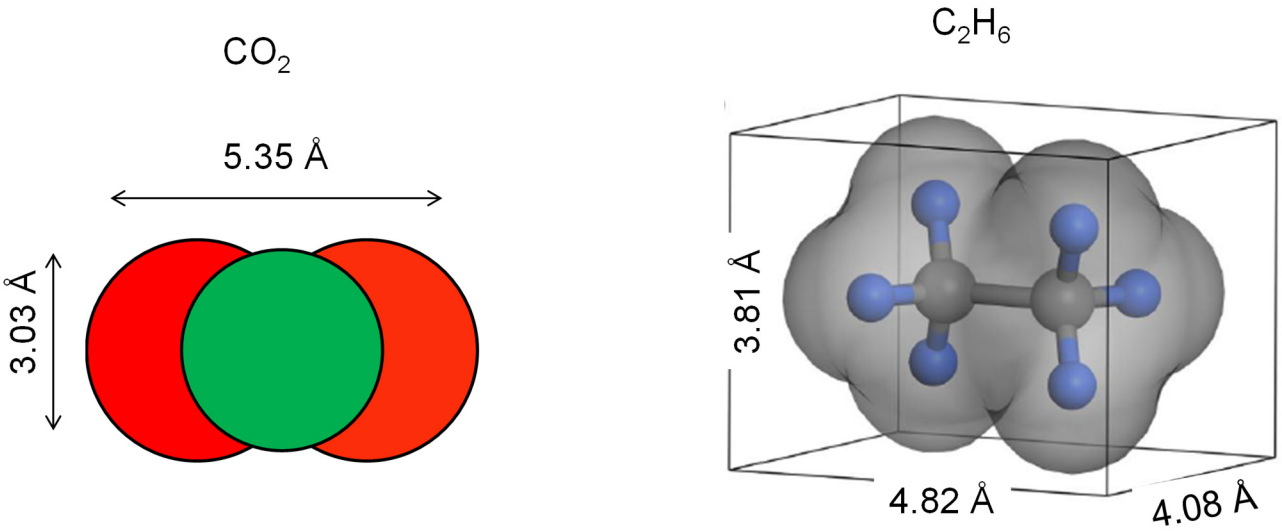

Figure S31. Molecular dimensions of CO_2 and C_2H_6. The molecular dimensions of C_2H_6 are taken from Lin et al.[85]

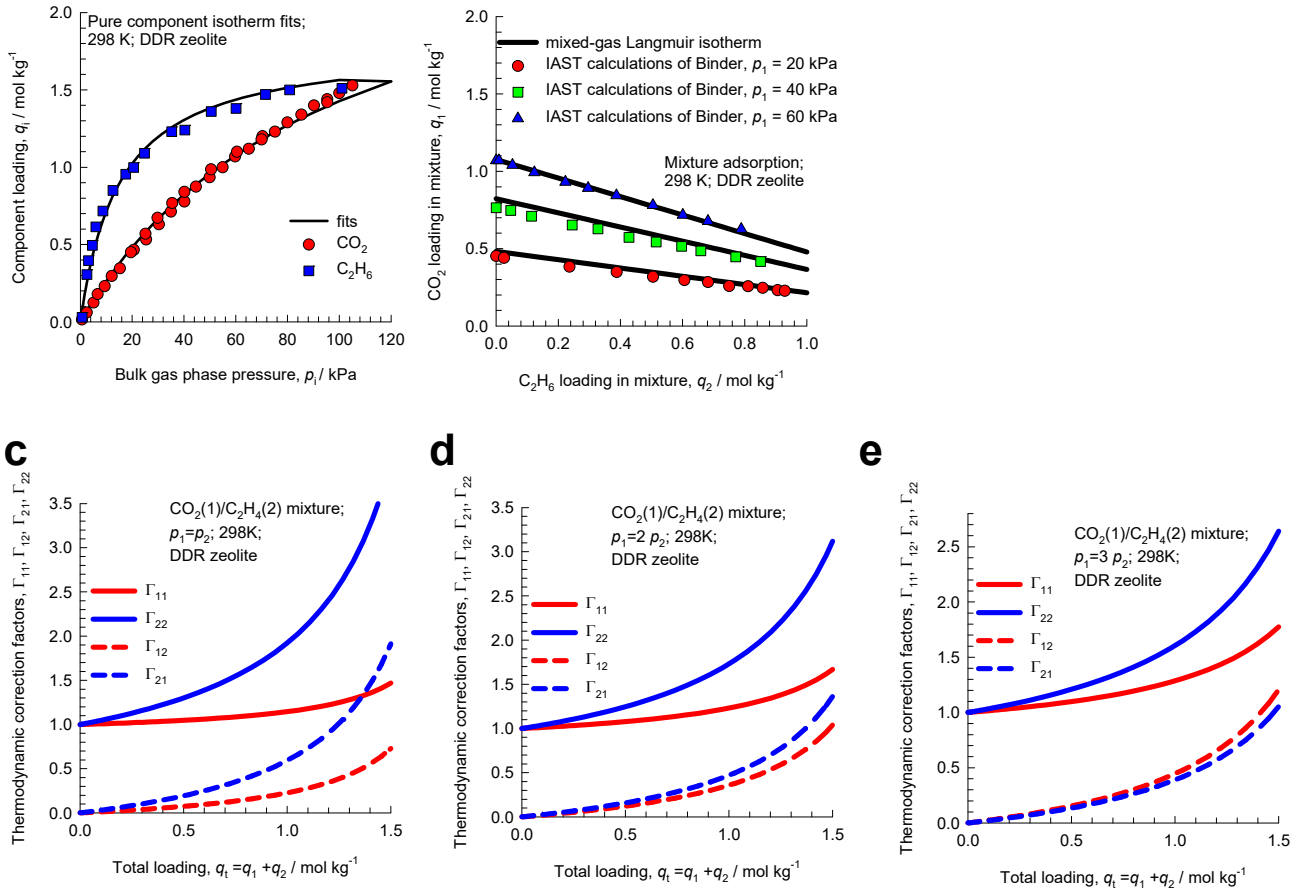

Figure S32. (a) Comparison of unary isotherm data with single-site Langmuir fits using the parameters reported in Table S7. (b) The symbols are scanned from Figure 3 of Binder et al;[77] they represent IAST calculations for binary CO_2 (1)/C_2H_6(2) mixture adsorption in DDR crystals with constant CO_2 partial pressures of p_1 = 20, 40, and 60 kPa for experiments 1, 2, and 3, respectively. The partial pressures of C_2H_6 ethane in the gas phase is varied. The continuous solid lines are our calculations using mixed-gas Langmuir model using the single-site Langmuir parameters reported in in Table S7. (c, d, e) Elements of the matrix of thermodynamic correction factors Γ_{ij} as a function of total mixture loading, q_t, calculated using the mixed-gas Langmuir model for binary CO_2(1)/C_2H_6(2) mixture adsorption in DDR for (c) 20/20 (d) 40/20, and (e) 60/20 ratios of partial pressures in the gas phase.

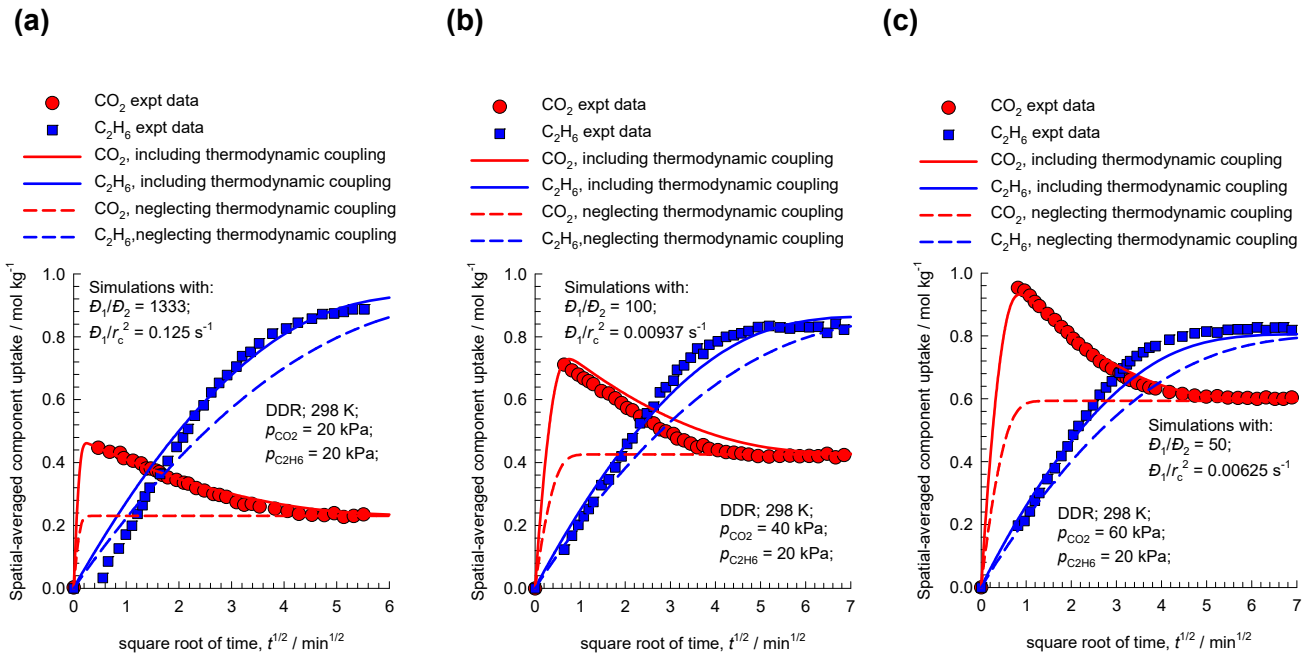

Figure S33. (a, b, c) Experimental data of Binder et al.[77] and Lauerer et al.[78] (indicated by symbols) for spatial-averaged transient uptake of (a) 20/20 (b) 40/20, and (c) 60/20 CO_2(1)/C_2H_6(2) gas mixtures within crystals of DDR zeolite at 298 K. The continuous solid lines are Maxwell-Stefan model simulations based on Eq (S20). The dashed lines are the simulations based on Eq (S22), in which the thermodynamic correction factors are assumed to be described by $\Gamma_{ij} = \delta_{ij}$, the Kronecker delta.

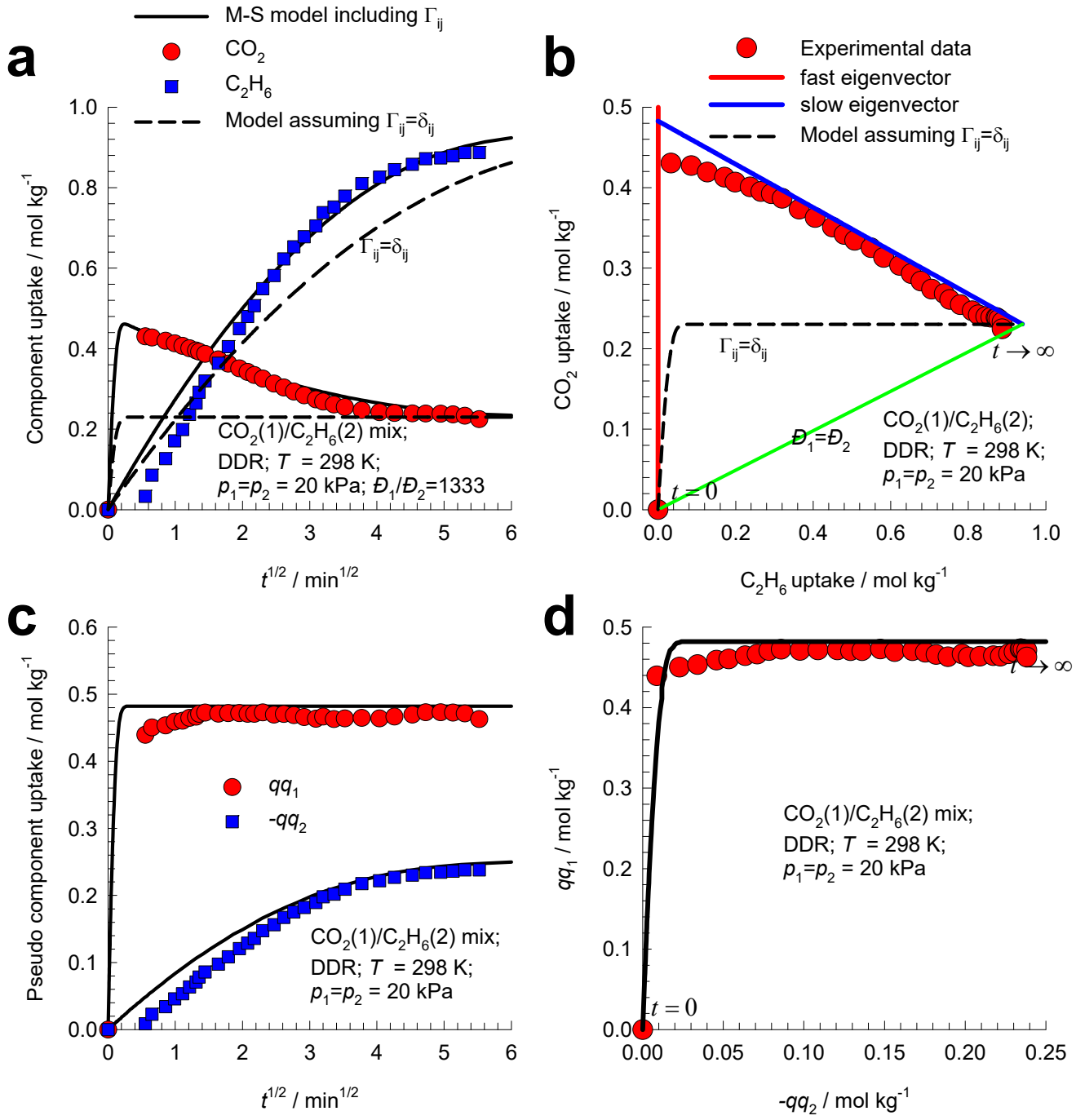

Figure S34. (a) Experimental data of Binder et al.[77] and Lauerer et al.[78] (indicated by symbols) for spatial-averaged transient uptake of 20/20 $CO_2(1)/C_2H_6(2)$ gas mixtures within crystals of DDR zeolite at 298 K. (b) Component loadings plotted in composition space. (c) Transient equilibration of pseudo component loadings. (d) Pseudo component loading plotted in pseudo composition space.

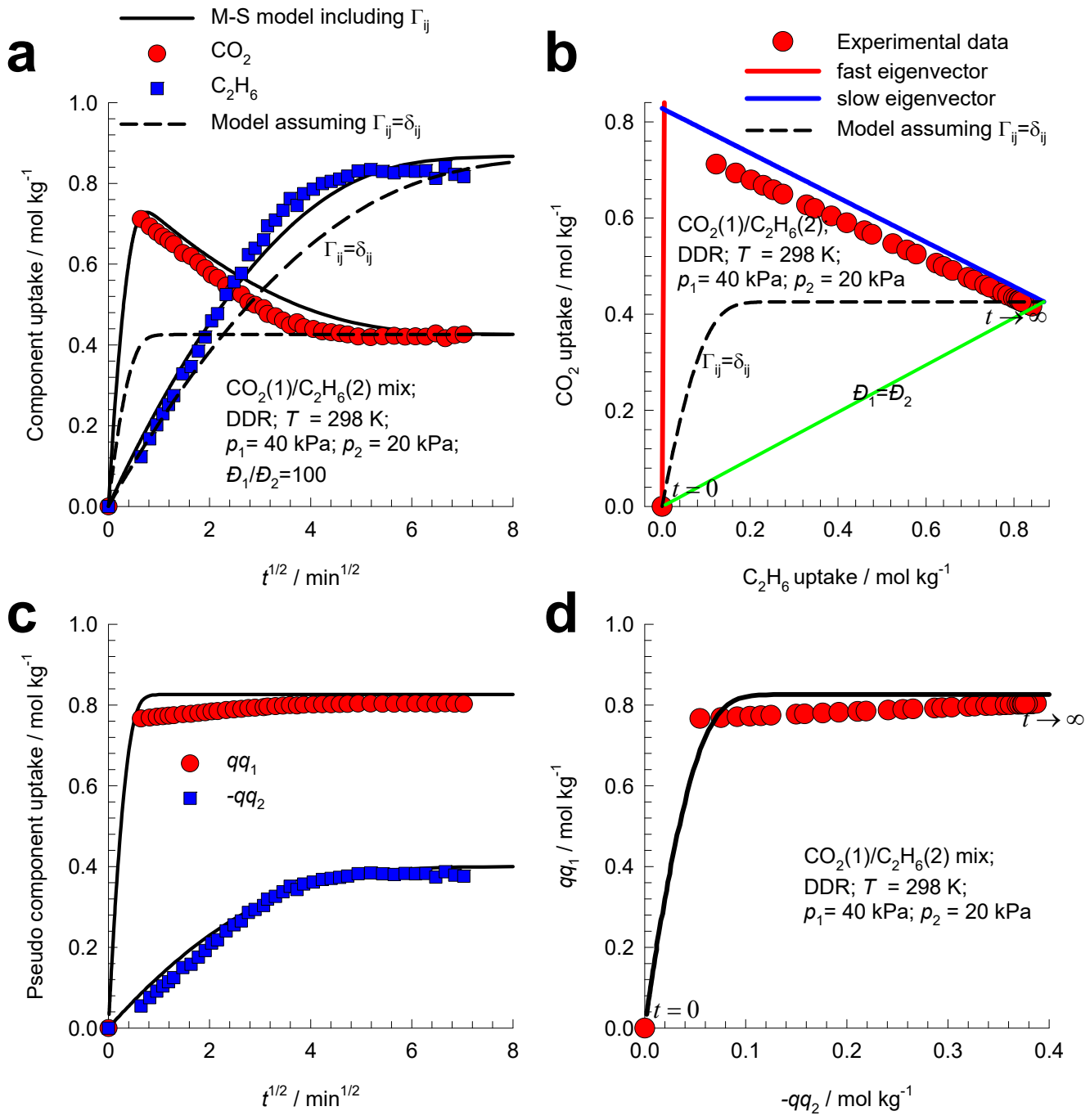

Figure S35. (a) Experimental data of Binder et al.[77] and Lauerer et al.[78] (indicated by symbols) for spatial-averaged transient uptake of 40/20 $CO_2(1)/C_2H_6(2)$ gas mixtures within crystals of DDR zeolite at 298 K. (b) Component loadings plotted in composition space. (c) Transient equilibration of pseudo component loadings. (d) Pseudo component loading plotted in pseudo composition space.

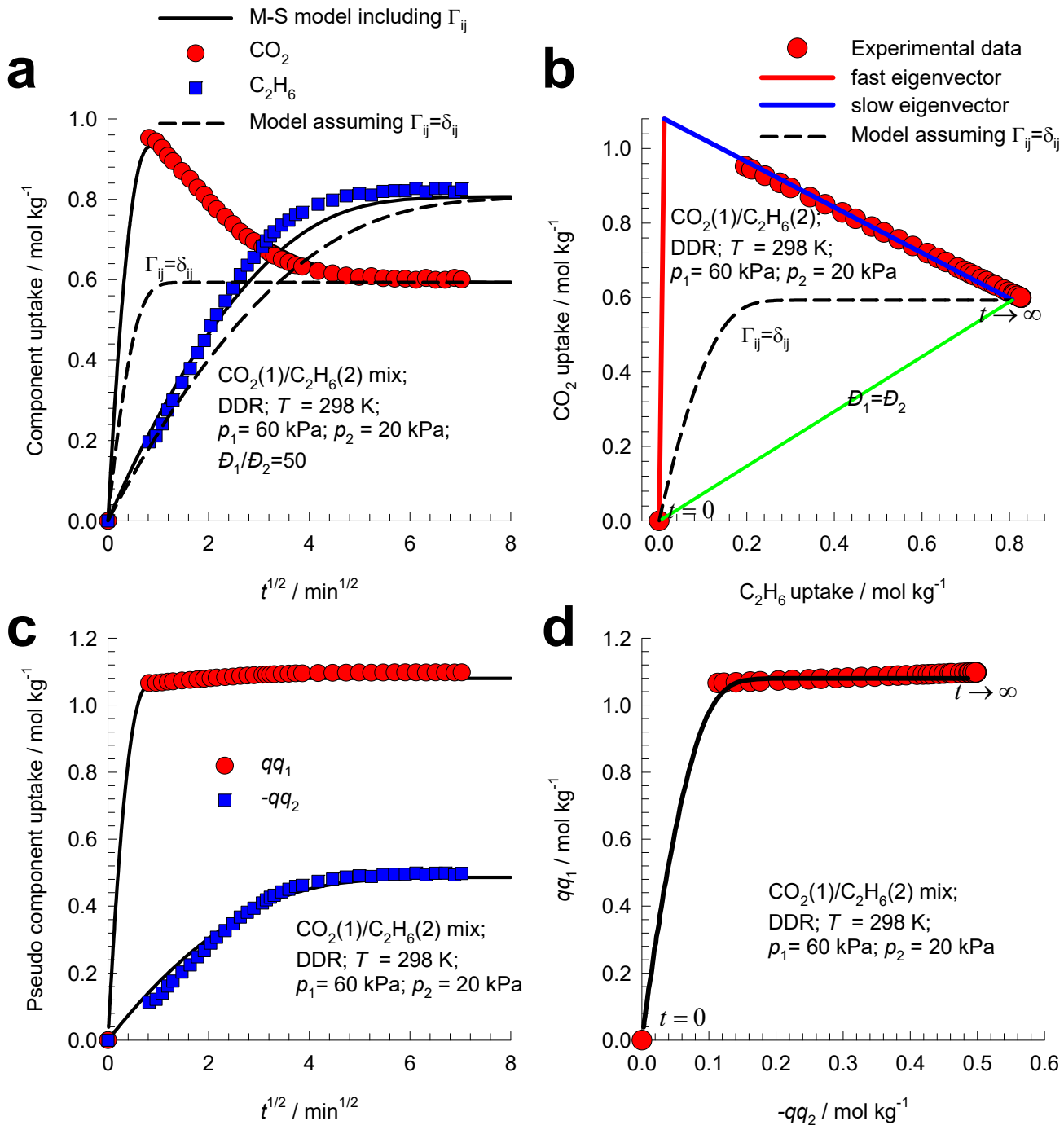

Figure S36. (a) Experimental data of Binder et al.[77] and Lauerer et al.[78] (indicated by symbols) for spatial-averaged transient uptake of 60/20 $CO_2(1)/C_2H_6(2)$ gas mixtures within crystals of DDR zeolite at 298 K. (b) Component loadings plotted in composition space. (c) Transient equilibration of pseudo component loadings. (d) Pseudo component loading plotted in pseudo composition space.

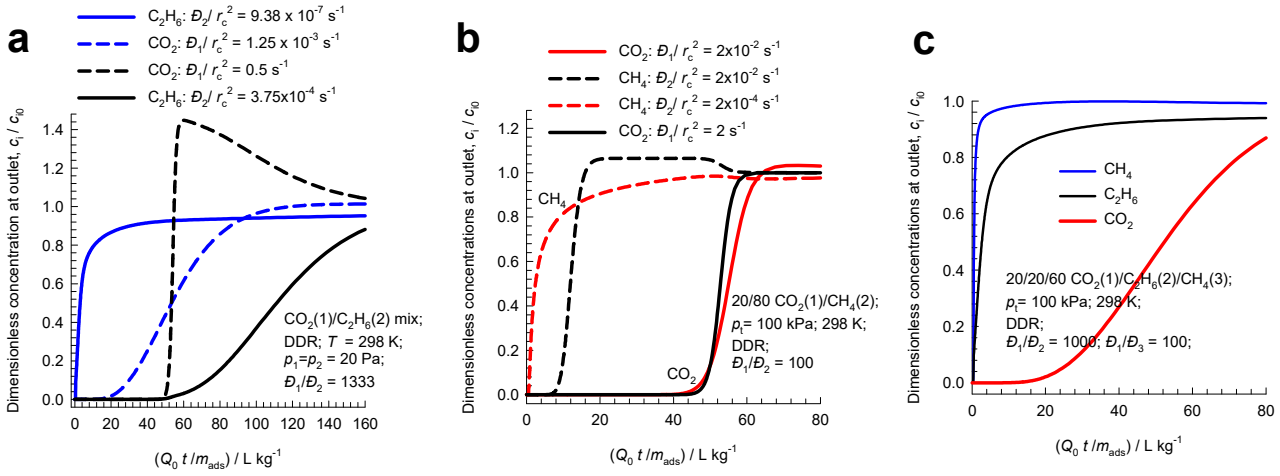

Figure S37. (a) Transient breakthrough of 50/50 CO_2(1)/C_2H_6(2) mixtures through fixed bed adsorber packed with DDR crystals operating at 298 K, and total pressure p_t = 40 kPa. The dimensionless concentrations at the exit of the adsorber, c_i/c_{i0}, are plotted as a function of a modified time parameter defined by $Q_0 t/m_{ads}$. For the two sets of simulations $Đ_1/r_c^2 = 1.25\times10^{-3}, 0.5$ s^{-1}, maintaining the ratio $Đ_1/Đ_2 = 1333$. (b) Transient breakthrough of 20/80 CO_2(1)/CH_4(2) mixtures through fixed bed adsorber packed with DDR crystals operating at 298 K, and total pressure p_t = 100 kPa. (c) Transient breakthrough of 20/20/60 CO_2(1)/ C_2H_6(2)/CH_4(3) mixtures through fixed bed adsorber packed with DDR crystals operating at 298 K, and total pressure p_t = 100 kPa.

8 Nitrogen Capture from Natural Gas Streams

Natural gas reserves often contain up to 20% N_2; reduction to values below 4% is required for meeting pipeline specifications.[86] Cryogenic distillation is the economic choice for large capacity wells but for smaller natural gas reserves, PSA separations become more cost-effective, especially because the feed mixtures are available at high pressures.[86, 87] The adsorbent materials in PSA units need to be selective to N_2, but for most available adsorbents, the adsorption selectivity is in favor of CH_4 due to its higher polarizability.

8.1 N_2/CH_4 separations with LTA-4A zeolite

The earliest study demonstrating the possibility of using LTA-4A zeolite, utilizing diffusion selectivities for separating $N_2(1)/CH_4(2)$ mixtures is contained in the classic paper of Habgood.[17] LTA-4A zeolite (also called 4A or NaA zeolite) contains extra-framework cations (containing 96Si, 96 Al, 96 Na^+ per unit cell; Si/Al=1). LTA-4A zeolite consists of cages of 743 $Å^3$ volume, separated by 4.11 Å × 4.47 Å 8-ring windows. The pore landscape and structural details of LTA-4A zeolite are provided in Figure S38. The Na^+ cations partially block the window sites, leading to low magnitudes of guest diffusivities. The partial blocking of the windows enhances efficacy of kinetic separations, because it significantly enhances the ratio of the diffusivities of mobile and tardier species. Molecules jump one-at-a-time across the windows of LTA-4A. Extensive Molecular Dynamics (MD) simulations have confirmed that correlation effects are of negligible importance for mixture diffusion across cage-type zeolites such as CHA, LTA, DDR, ERI that consist of cages separated by windows in the 3.4 Å – 4.2 Å size range.[1, 2, 8, 16] Consequently, the appropriate flux description is provided by eq (S20).

Habgood[17] performed experimental data on transient uptake of $N_2(1)/CH_4(2)$ mixtures in crystallites of LTA-4A; the data measured at 194 K with partial pressures p_1 =50.9 kPa; p_2 = 49.1 kPa are shown in Figure S39a.The experimental data on the spatial averaged component loadings are plotted as a function of the Fourier number, $Đ_1 t/r_c^2$. Nitrogen is a "pencil-like" molecule (4.4 Å × 3.3 Å) that can hop

length-wise across the narrow windows; see computational snapshots in Figure S40. The "spherical" CH_4 (3.7 Å) is much more severely constrained and has a diffusivity that is 21.7 times lower than that of N_2. The adsorption strength of CH_4, as reflected in the Langmuir "*b*" parameter, is higher than that of N_2 by a factor 2.2; see unary isotherm data fits in Table S8. The $N_2(1)/CH_4(2)$ mixture constitutes a combination of more-mobile-less-strongly-adsorbed-N_2 and tardier-more-strongly-adsorbed-CH_4. During the initial stages of the transient uptake, the pores of LTA-4A are predominantly richer in the more mobile N_2, but this is displaced by the more strongly adsorbed, tardier CH_4 molecules at longer times. This results in an overshoot in the N_2 uptake in both the experimental campaigns.

For video animations of the jumping of nitrogen and methane across the narrow windows of LTA-4A, watch **N2/CH4 Separations with LTA-4A** on YouTube

https://www.youtube.com/@rajamanikrishna250/videos

The black lines in Figure S39a are Maxwell-Stefan model simulations based are simulations based on eq (S21). The Maxwell-Stefan diffusivities used in the simulations are: $Đ_1/r_c^2 = 1.56\times10^{-5}$ s^{-1}; $Đ_1/Đ_2 = 21.7$; these values based on the diffusivity data provided by Habgood.[17] The blue lines are the simulations based on eq (S22), in which the thermodynamic correction factors are assumed to be described by $\Gamma_{ij} = \delta_{ij}$, the Kronecker delta; in this scenario, no N_2 overshoot is experienced. We conclude that the overshoots in the N_2 uptake, that signal the phenomenon of uphill diffusion,[12, 41] is engendered by thermodynamic coupling effects.

Figure S39b is a plot of the transient uptake selectivity, defined by $\frac{\bar{q}_1(t)/\bar{q}_2(t)}{p_{10}/p_{20}}$ as a function of $\sqrt{t}$. As $t \to \infty$, the uptake selectivity will approach the value of the adsorption selectivity $\frac{q_1^*/q_2^*}{p_{10}/p_{20}}$. From the unary Langmuir isotherm parameters in Table S8, we calculate the equilibrium adsorption selectivity $\frac{q_1^*/q_2^*}{p_{10}/p_{20}} = \frac{b_1}{b_2} = 0.451$. Readers should note that the ratio $\frac{b_1}{b_2}$ should be replaced by the ratio of Henry

constants, $\frac{q_{sat,1}}{q_{sat,2}}\frac{b_1}{b_2}$, in case the saturation capacities of components 1 and 2 are unequal. At short contact times, the transient uptake selectivity is strongly in favor of the more mobile nitrogen. If thermodynamic coupling effects are ignored, and the Maxwell-Stefan diffusivities are assumed to be independent of loading, the following simplified expression can be derived for the transient uptake selectivity as the product of the adsorption equilibrium selectivity and the diffusion selectivity[21, 88]

$$\frac{\overline{q}_1(t)/\overline{q}_2(t)}{p_{10}/p_{20}} = \frac{b_1}{b_2}\sqrt{\frac{Đ_1}{Đ_2}} \tag{S59}$$

Readers should note that the ratio $\frac{b_1}{b_2}$ should be replaced by the ratio of Henry constants, $\frac{q_{sat,1}}{q_{sat,2}}\frac{b_1}{b_2}$, in case the saturation capacities of components 1 and 2 are unequal. We note that the uptake selectivity in favor of nitrogen is significantly enhanced due to the influence of Γ_{ij}.

Based on his experimental results for transient uptake, Habgood filed a patent claiming that natural gas could be upgraded by removing the faster diffusing nitrogen using 4A zeolite and a kinetically controlled separation process at sub-ambient temperatures. We now investigate the consequence of thermodynamic coupling and uphill diffusion on N_2(1)/CH_4(2) mixture separations in a fixed bed adsorber packed with LTA-4A adsorbent.

8.2 Analysis of N_2/CH_4 uptake using eigenvalues and eigenvectors

For 40.9/49.1 N_2(1)/CH_4(2) gas mixtures within crystals of LTA-4a zeolite at 194 K, at a total pressure $p_t = p_1 + p_2$ = 100 kPa, the elements of the $[\Gamma]$ are $\begin{bmatrix}\Gamma_{11} & \Gamma_{12}\\ \Gamma_{21} & \Gamma_{22}\end{bmatrix} = \begin{bmatrix}5.785 & 4.785\\ 10.213 & 11.213\end{bmatrix}$. The Fick diffusivity matrix is calculated to be $\frac{\begin{bmatrix}D_{11} & D_{12}\\ D_{21} & D_{22}\end{bmatrix}}{r_c^2} = \begin{bmatrix}90.24 & 74.64\\ 7.353 & 8.073\end{bmatrix}\times 10^{-6}$ s^{-1}.

In Figure S41b the component loadings of N_2(1), and CH_4(2) are plotted in composition space, with CH_4 loadings on the *x*-axis. We note that the equilibration trajectory is not monotonous and follows a

serpentine trajectory. In order to appreciate the fundamentals that underlie this serpentine trajectory we plot the two eigenvectors of $[D]$: $(e_1)=\begin{pmatrix} 1 \\ -\dfrac{D_{11}-\lambda_1}{D_{12}} \end{pmatrix}$ and $(e_2)=\begin{pmatrix} 1 \\ -\dfrac{D_{21}}{D_{22}-\lambda_2} \end{pmatrix}$ where the two eigenvalues are $\dfrac{\lambda_1}{r_c^2}=96.45\times10^{-6}$ s^{-1}; $\dfrac{\lambda_2}{r_c^2}=1.863\times10^{-6}$ s^{-1}.

During the initial transience, the equilibration trajectory is dictated by the fast eigenvector, indicated by the red line in Figure S41b

$$\left(q_2-q_{20}\right)=-\frac{D_{11}-\lambda_1}{D_{12}}\left(q_1-q_{10}\right) \tag{S60}$$

As equilibrium is approached, the equilibration trajectory follows the path dictated by the slow eigenvector, indicated by the blue line in Figure S41b

$$\left(q_2-q_2^*\right)=-\frac{D_{21}}{D_{22}-\lambda_2}\left(q_1-q_1^*\right) \tag{S61}$$

The experimental data on the equilibration trajectory lies within the two bounds dictated by the two eigenvectors.

The pseudo-component loadings $[P]^{-1}(q)=(qq)$ follow monotonous paths to equilibrium; each pseudo-component relaxes with the corresponding eigenvalues λ_1 and λ_2.

$$\left(qq_i^*-\overline{qq_i}(t)\right)=Q_i\left(qq_i^*-qq_{i0}\right);\quad Q_i=\frac{6}{\pi^2}\sum_{m=1}^{\infty}\frac{1}{m^2}\exp\left[-m^2\pi^2\frac{\lambda_i t}{r_c^2}\right];\quad i=1,2 \tag{S62}$$

The transient equilibration of the pseudo component loadings are plotted in Figure S41c; note that the pseudo loading of CH_4, qq_2 is negative. In pseudo composition space, the pseudo component loadings follow a monotonous approach to equilibrium; see Figure S41d.

8.3 Influence of temperature on kinetic N_2/CH_4 separations

The experimental data and simulations presented in the foregoing section was for a temperature of 194 K. We know examine the influence of increasing temperature on separations of 20/80 $N_2(1)/CH_4(2)$

mixtures using LTA-4A. The unary isotherm data at 194 K and 273 K from the paper by Habgood, [17] combined with the unary isotherm data of Wilkins and Rajendran,[89] measured at 303 K, 323 K, and 343 K were fitted with the temperature-dependent 1-site Langmuir model $q = \frac{q_{sat} bp}{1 + b_A p}; \quad b = b_0 \exp\left(\frac{E}{RT}\right)$. The fit parameters are provided in Table S9. The goodness of the combined fits is demonstrated in Figure S44 in which the component loadings are plotted against the surface potential $\Phi \equiv \frac{\pi A}{RT} = \int_{f=0}^{P} \frac{q(f)}{f} df = q_{sat} \ln(1 + bP)$; for details of the concept of surface potential refer to Krishna and van Baten.[84]

The diffusivity data for N_2(1) and CH_4(2) in LTA-4A are reported by Habgood[17] and Wilkins and Rajendran,[89] for a range of temperatures; the combined data set may be fitted with $Đ_1/r_c^2 = A_1 \exp(-E_1/RT); \quad Đ_2/r_c^2 = A_2 \exp(-E_2/RT)$ with $A_1 = 38.15$ s^{-1}; $E_1 = 20.86$ kJ mol^{-1} for N_2 and $A_2 = 6.418$ s^{-1}; $E_2 = 22.93$ kJ mol^{-1} for CH_4.

With the *T*-dependent fits of unary isotherms, and diffusivities we can determine (a) adsorption selectivity, $\frac{b_1}{b_2}$, (b) diffusion selectivity, $\frac{Đ_1}{Đ_2}$, and (c) kinetic selectivity, $\frac{b_1}{b_2}\sqrt{\frac{Đ_1}{Đ_2}}$. These data are plotted in Figure S45 (see left *y*-axis values). We note that all three selectivities decrease, albeit slightly with increasing temperatures. Also plotted on the right *y*-axes in Figure S45 are the values of $Đ_1/r_c^2$. We note there is a significant increase in $Đ_1/r_c^2$ with increasing *T*, implying that the severity of diffusion influences diminishes at higher temperature. Indeed, kinetic separations with LTA-4A are not realizable at temperatures in excess of about 220 K.

Another material that affords kinetic separations of N_2(1)/CH_4(2) mixtures Ba-RPZ (= Ba exchanged reduced pore Zorite); the unary data on isotherms and diffusivities are presented by Wilkins and Rajendran.[89] The unary isotherm data of Wilkins and Rajendran,[89] measured at three different temperatures may be fitted with the temperature-dependent 1-site Langmuir model

$q = \frac{q_{sat} bp}{1 + b_A p}$; $b = b_0 \exp\left(\frac{E}{RT}\right)$. The fit parameters are provided in Table S10. The goodness of the combined fits is demonstrated in Figure S46 in which the component loadings are plotted against the surface potential $\Phi \equiv \frac{\pi A}{RT} = \int_{f=0}^{P} \frac{q(f)}{f} df = q_{sat} \ln(1 + bP)$; for details of the concept of surface potential refer to Krishna and van Baten.[84]

The diffusivity data for N_2(1) and CH_4(2) in Ba-RPZ are reported by Wilkins and Rajendran,[89] for a range of temperatures; the data set were fitted with $Đ_1/r_c^2 = A_1 \exp(-E_1/RT)$; $Đ_2/r_c^2 = A_2 \exp(-E_2/RT)$ with $A_1 = 536.6$ s^{-1}; $E_1 = 25.77$ kJ mol^{-1} for N_2 and $A_2 = 4.498$ s^{-1}; $E_2 = 30.46$ kJ mol^{-1} for CH_4.

With the *T*-dependent fits of unary isotherms, and diffusivities we can determine (a) adsorption selectivity, $\frac{b_1}{b_2}$, (b) diffusion selectivity, $\frac{Đ_1}{Đ_2}$, and (c) kinetic selectivity, $\frac{b_1}{b_2}\sqrt{\frac{Đ_1}{Đ_2}}$. These data are plotted in Figure S47 (see left *y*-axis values). We note that all three selectivities decrease with increasing temperatures. Also plotted on the right *y*-axes in Figure S47b are the values of $Đ_1/r_c^2$. We note there is a significant increase in $Đ_1/r_c^2$ with increasing *T*, implying that the severity of diffusion influences diminishes at higher temperature. Kinetic separations with Ba-RPZ are not realizable at temperatures in excess of about 273 K.

Figure S48a shows the transient uptake of 20/80 N_2(1)/CH_4(2) mixture in Ba-RPZ crystals operating at 273 K, and total pressure p_t = 100 kPa. The overshoot in the N_2 loading signifies uphill diffusion. In Figure S48b, the component loadings plotted in composition space. The serpentine equilibration trajectory determined using the Maxwell-Stefan diffusion model (solid black lines) is dictated by the fast and slow eigenvectors, as indicated, respectively, by the red and blue lines.

Watch also **N2/CH4 Separations with Ba-RPZ** on YouTube

https://www.youtube.com/@rajamanikrishna250/videos

8.4 Separation of N_2/CH_4 mixtures in fixed bed adsorber

Let us analyze the separations of 20/80 N_2(1)/CH_4(2) mixtures in a fixed bed adsorber using LTA-4A zeolite operating at a total pressure of 100 kPa, and T = 194 K. Figure S42a presents calculations of the elements of the matrix of thermodynamic correction factors Γ_{ij} as a function of total bulk gas pressure, p_t, calculated using the mixed-gas Langmuir model for 20/80 N_2(1)/CH_4(2) mixtures in LTA-4A zeolite at 194 K. Figure S42b presents calculations of the ratios $\Gamma_{12}/\Gamma_{11}, \Gamma_{21}/\Gamma_{22}$ as a function of total bulk gas pressure, p_t, Thermodynamic coupling effects are of significant importance, and therefore should be expected to influence transient breakthroughs in fixed-bed adsorbers.

Figure S43a show the transient breakthrough simulations for 20/80 N_2(1)/CH_4(2) mixtures through fixed bed adsorber packed with LTA-4A crystals operating at 194 K, and total pressure p_t = 100 kPa. The y-axis is the % CH_4 at the adsorber outlet. The x-axis is $Q_0 t/m_{ads}$, where Q_0 is the volumetric flow rate of the gas mixture at the inlet to the fixed bed at actual temperature and pressure conditions. The continuous black lines are simulations taking due account of intra-crystalline diffusion using eq (S21) with parameters: $Đ_1/r_c^2 = 1.56\times10^{-5}$ s^{-1}; $Đ_1/Đ_2 = 21.7$. The blue lines are the corresponding simulations based on eq (S22), in which the thermodynamic correction factors are assumed to be described by $\Gamma_{ij} = \delta_{ij}$, the Kronecker delta. For the target CH_4 purity of say 96% we can determine the moles of 96%+ pure CH_4 produced from a material balance on the adsorber. Expressed per kg of LTA-4A zeolite in the packed bed, the respective productivities are 0.93 and 0.11 mol kg^{-1}, with 96%+ purity. Ignoring thermodynamic coupling effects severely underestimates the CH_4 productivity

Having estΓ_{12}/Γ_{11}, Γ_{21}/Γ_{22} ablished the importance of including the thermodynamic correction factors in PSA simulations, we proceed to examine the influence of the severity of diffusional limitations. Figure S43b compares the transient breakthrough simulations for 20/80 N_2(1)/CH_4(2) mixtures through fixed bed adsorber packed with LTA-4A for two different scenarios:

$Đ_1/r_c^2 = 1.56\times10^{-5}$ s^{-1}; $Đ_1/r_c^2 = 6.09\times10^{-6}$ s^{-1}; for both scenarios we maintain $Đ_1/Đ_2 = 21.7$, and include the thermodynamic coupling influences. Expressed per kg of LTA-4A zeolite in the packed bed, the respective productivities are 0.93 and 1.62 mol kg^{-1} mol kg^{-1}, with 96%+ purity. More severe diffusional limitations, signified by lower value of $Đ_1/r_c^2$ results in higher CH_4 productivity. Indeed, if the diffusional severity is diminished, kinetic separations are not achievable.

In Figure S43c,d the same sets of data in Figure S43a,b are plotted using the dimensionless concentrations in the gas phase exiting the adsorber, c_i/c_{i0}, as *y*-axes.

8.5 N_2/CH_4 separations with Ba-ETS-4

Ba-ETS-4 (ETS = Engelhard Titano-silicate; ETS-4 is also named as CTS-1 = Contracted Titano Silicate -1) with pore size ≈ 3.7 Å effectively exclude the spherical CH_4 molecule (3.7 Å) while allowing entry for the pencil-like nitrogen molecule (4.4 Å × 3.3 Å).[17, 86, 88, 90, 91] The process background is described in detail by Bhadra and Farooq.[86, 92]

Watch also **N2/CH4 Separations with Ba-ETS-4** on YouTube

https://www.youtube.com/@rajamanikrishna250/videos

The transient uptake data of Majumdar et al.[88] for Ba-ETS-4 are shown in Figure S49a,b for (a) 10/90, and (b) 50/50 mixtures show overshoots in the uptake of the more mobile N_2. To confirm these overshoots, we performed transient uptake simulations using the isotherm parameters reported in the thesis of Bhadra;[92] see Table S11. Figure S50a,b presents simulation of transient uptake of 20/80 N_2(1)/CH_4(2) mixture inside crystallite of Ba-ETS-4. The input data on isotherms are taken from Table 3.2 of the PhD thesis of Bhadra.[92] The Maxwell-Stefan diffusivities used in the simulations are: $Đ_1/r_c^2 = 2.8\times10^{-2}$ s^{-1}; $Đ_2/Đ_2 = 4180$, The surrounding bulk gas mixture is at 283 K, and total pressure p_t = 1 MPa. The *x*-axes represent the Fourier number $Đ_1 t/r_c^2$. The black lines are simulations based on eq (S21). The blue lines are the simulations based on eq (S22), in which the thermodynamic correction factors are described by $\Gamma_{ij} = \delta_{ij}$, the Kronecker delta. Inclusion of thermodynamic coupling effects

causes uphill diffusion of N_2, resulting in significantly enhanced N_2/CH_4 uptake selectivities during the early stages of transience.

Let us analyze the separations of 20/80 $N_2(1)/CH_4(2)$ mixture in fixed bed adsorber packed with Ba-ETS-4, operating at 283 K, and total pressure p_t = 1 MPa. Figure S51a,b presents simulation results for transient breakthroughs; the black lines are simulations based on eq (S21). The blue lines are the simulations based on eq (S22) in which the thermodynamic correction factors are assumed to be described by $\Gamma_{ij} = \delta_{ij}$, the Kronecker delta. For the target CH_4 purity of say 96% we can determine the moles of 96%+ pure CH_4 produced from a material balance on the adsorber. Expressed per kg of Ba-ETS-4 in the packed bed, the respective productivities are 3.06 and 1.11 mol kg^{-1}. Ignoring thermodynamic coupling effects severely underestimates the CH_4 productivity.

8.6 List of Tables for Nitrogen Capture from Natural Gas Streams

Table S8. 1-site Langmuir parameters for N_2 and CH_4 in LTA-4A zeolite at 194 K. These parameters have been fitted from the isotherm data scanned from the paper by Habgood[17]

	$\frac{q_{sat}}{\text{mol kg}^{-1}}$	$\frac{b}{\text{Pa}^{-1}}$
N_2	3.6	9.403E-05
CH_4	3.6	2.084E-04

Table S9. Temperature-dependent 1-site Langmuir parameter fits for N_2 and CH_4 in LTA-4A zeolite. $q = \frac{q_{sat} b p}{1 + b_A p}; \quad b = b_0 \exp\left(\frac{E}{RT}\right)$. These parameters have been fitted from the isotherm data at 194 K and 273 K from the paper by Habgood,[17] combined with the unary isotherm data of Wilkins and Rajendran,[89] measured at 303 K, 323 K, and 343 K. For CH_4, the Configurational-Bias Monte Carlo (CBMC) data are also included in the fits.

	$\frac{q_{sat}}{\text{mol kg}^{-1}}$	$\frac{b_0}{\text{Pa}^{-1}}$	$\frac{E}{\text{kJ mol}^{-1}}$
N_2	3.6	4.101E-10	19.9
CH_4	3.6	8.145E-10	20

Table S10. Temperature-dependent 1-site Langmuir parameter fits for N_2 and CH_4 in Ba-RPZ.

$q = \frac{q_{sat} b p}{1 + b_A p}; \quad b = b_0 \exp\left(\frac{E}{RT}\right)$. These parameters have been fitted using the unary isotherm data of Wilkins and Rajendran,[89] measured at three different temperatures.

	Site A		
	$\frac{q_{sat}}{\text{mol kg}^{-1}}$	$\frac{b_0}{\text{Pa}^{-1}}$	$\frac{E}{\text{kJ mol}^{-1}}$
N_2	0.8	5.125E-10	25.5
CH_4	0.8	5.309E-09	22.2

Table S11. Langmuir parameters for adsorption of CH_4, and N_2 in Ba-ETS-4 at 283.15 K. The isotherm parameters are taken from Table 3 of Majumdar et al.[88], and Table 3.2 of the Ph.D. dissertation of Bhadra.[92] The cited parameters are converted to the units that are consistent with the other data presented in our article. For conversion purposes, we use the framework density for BaETS-4 of 1720 kg m^{-3}.

	$\frac{q_{sat}}{\text{mol kg}^{-1}}$	$\frac{b}{\text{Pa}^{-1}}$
N_2	1.4	9.02E-06
CH_4	0.5	9.339E-06

8.7 List of Figures for Nitrogen Capture from Natural Gas Streams

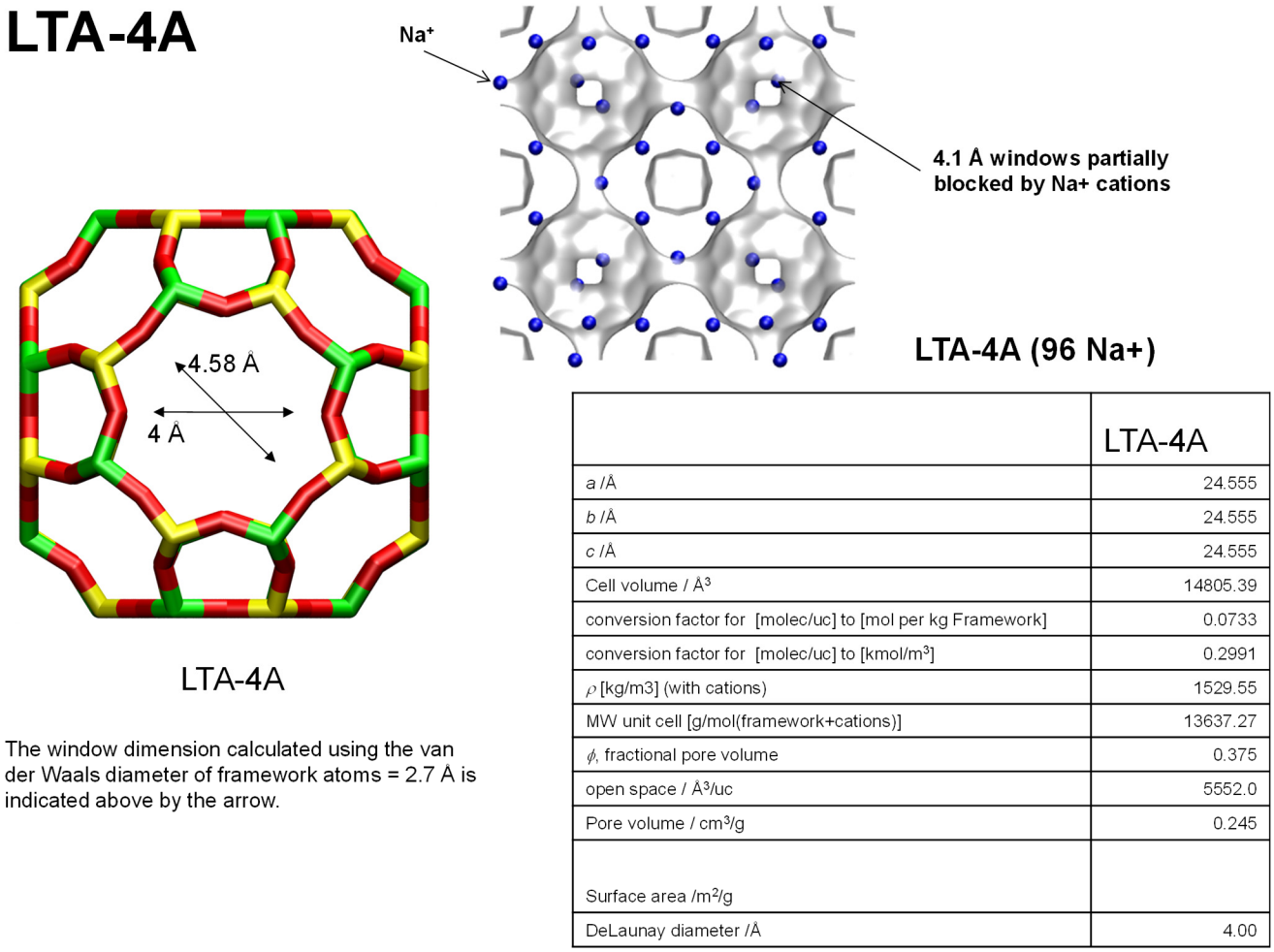

The window dimension calculated using the van der Waals diameter of framework atoms = 2.7 Å is indicated above by the arrow.

	LTA-4A
a /Å	24.555
b /Å	24.555
c /Å	24.555
Cell volume / Å^3	14805.39
conversion factor for [molec/uc] to [mol per kg Framework]	0.0733
conversion factor for [molec/uc] to [kmol/m^3]	0.2991
ρ [kg/m3] (with cations)	1529.55
MW unit cell [g/mol(framework+cations)]	13637.27
ϕ, fractional pore volume	0.375
open space / Å^3/uc	5552.0
Pore volume / cm^3/g	0.245
Surface area /m^2/g	
DeLaunay diameter /Å	4.00

Figure S38. Structural details of LTA-4A zeolite.

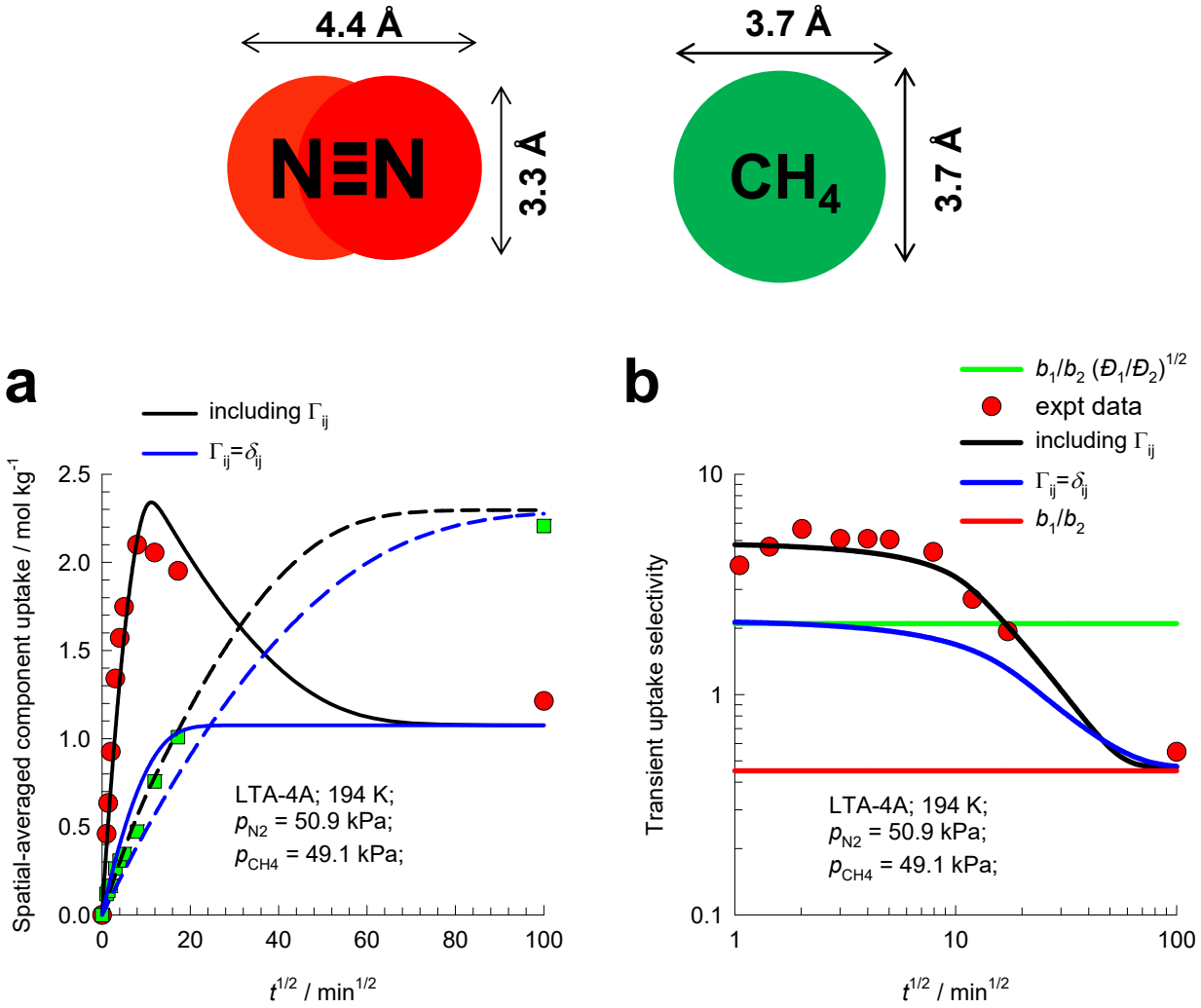

Figure S39. (a, b) Experimental data of Habgood[17] on transient uptakes of N_2(1)/CH_4(2) mixture within LTA-4A crystals, exposed to binary gas mixtures at partial pressures p_1 =50.9 kPa; p_2 = 49.1 kPa. The unary isotherms are provided in Table S8. The black lines are simulations based on eq (S21). The blue lines are the simulations based on eq (S22) in which the thermodynamic correction factors are assumed to be described by $\Gamma_{ij} = \delta_{ij}$, the Kronecker delta.

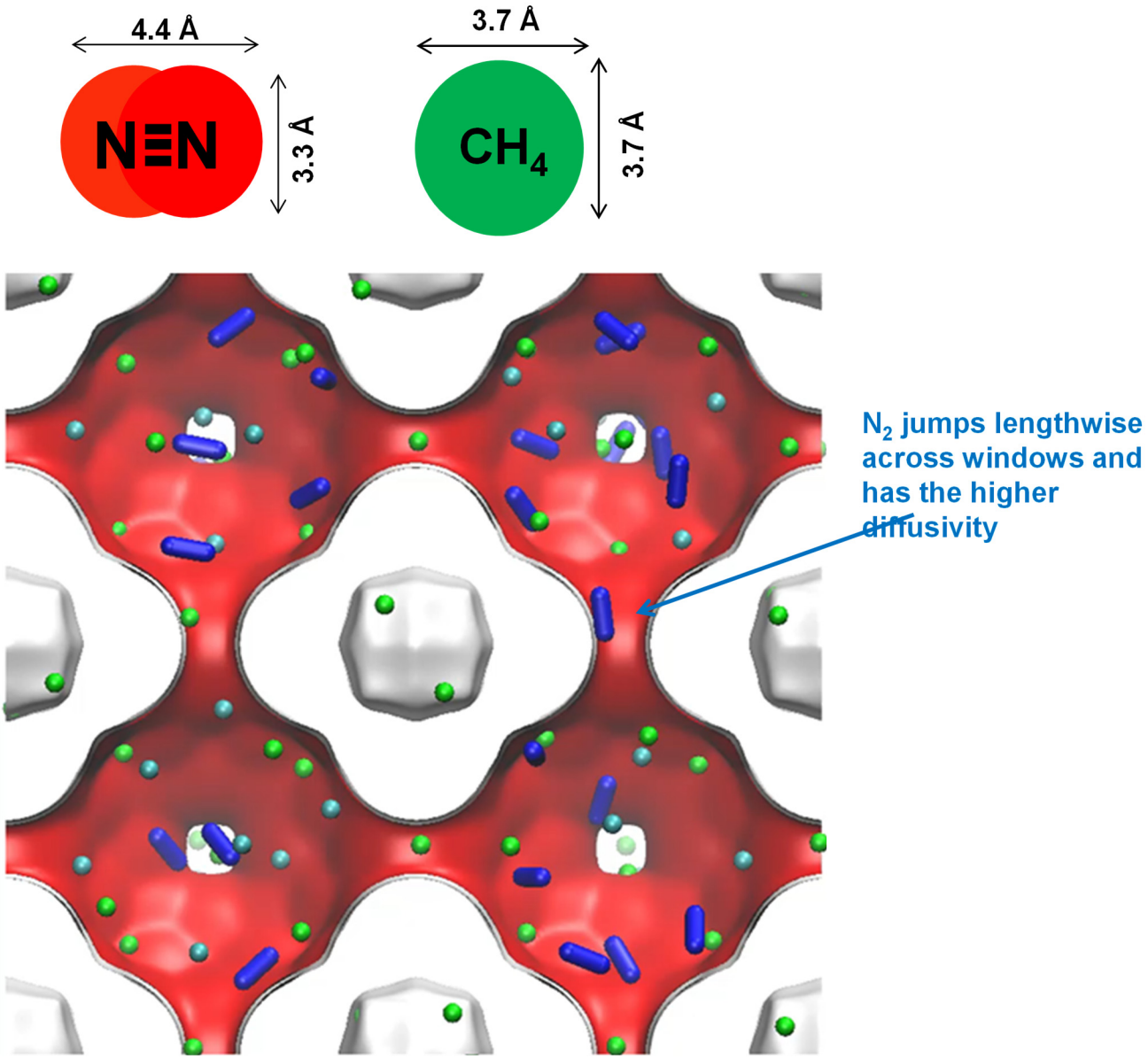

Figure S40. Computational snapshot showing that N_2 jumps lengthwise across the 4 Å windows of LTA-4A zeolite.

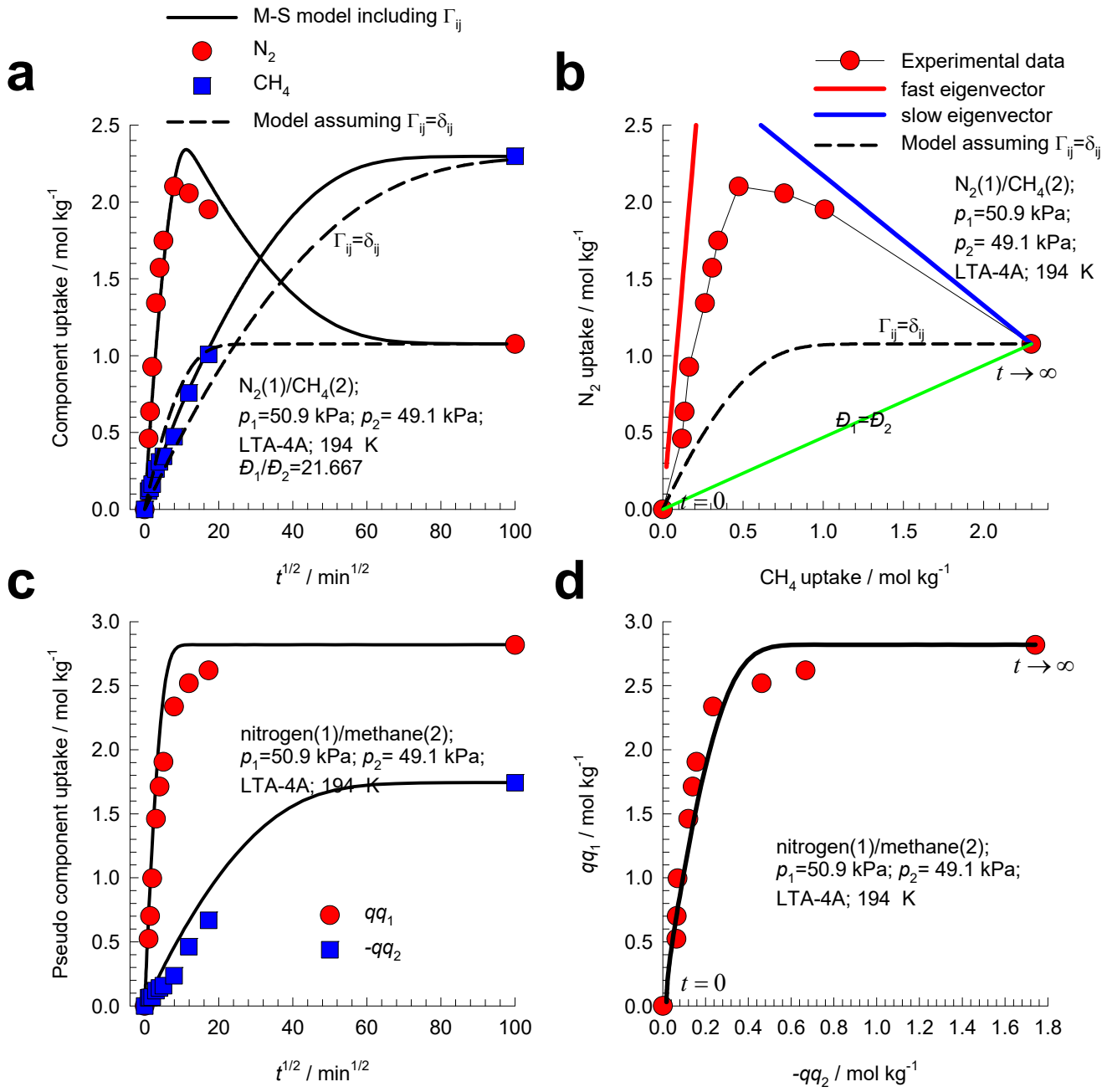

Figure S41. (a) Experimental data of Habgood[17] on transient uptakes of $N_2(1)/CH_4(2)$ mixture within LTA-4A crystals, exposed to binary gas mixtures at partial pressures p_1 =50.9 kPa; p_2 = 49.1 kPa. The unary isotherms are provided in Table S8. (b) Equilibration trajectories plotted in composition space. (c) Transient equilibration of pseudo component loadings. (d) Pseudo component loading plotted in composition space.

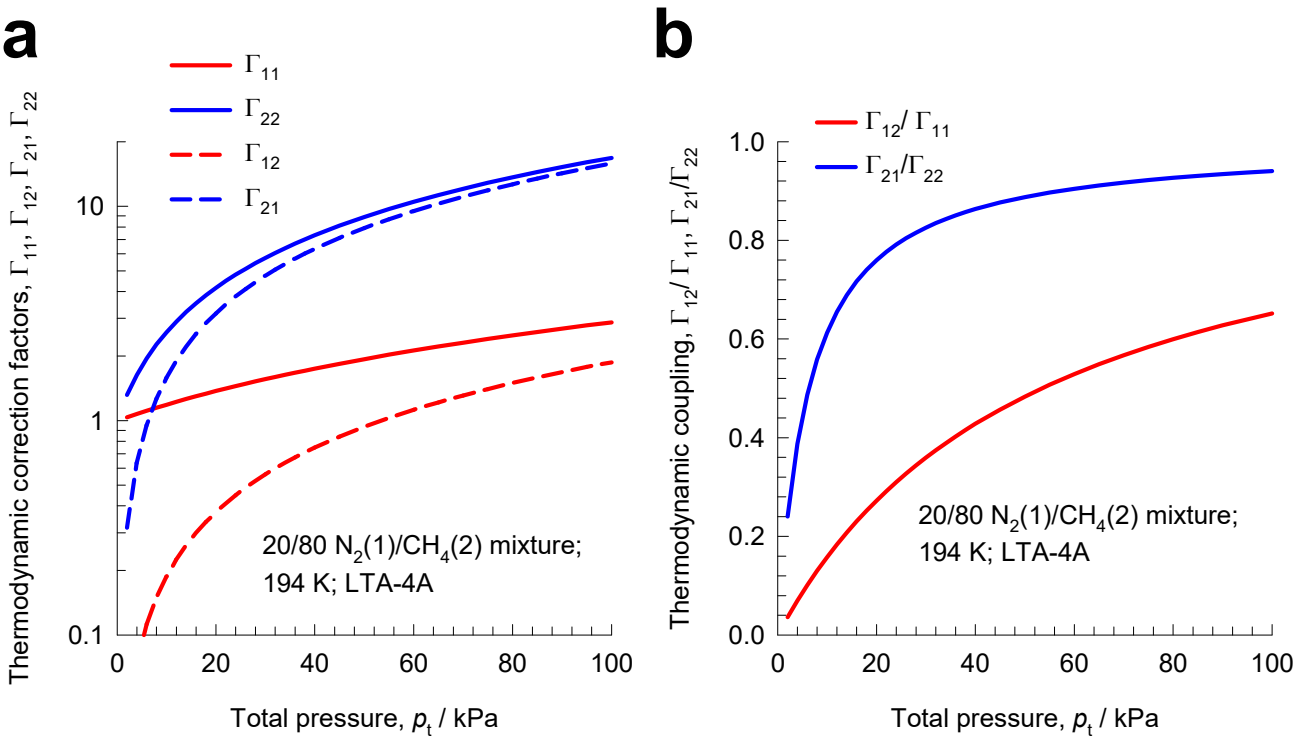

Figure S42. (a) Elements of the matrix of thermodynamic correction factors Γ_{ij} as a function of total bulk gas pressure, p_t, calculated using the mixed-gas Langmuir model for 20/80 $N_2(1)/CH_4(2)$ mixtures adsorption in LTA-4A zeolite at 194 K. (b) Calculations of the ratios Γ_{12}/Γ_{11}, Γ_{21}/Γ_{22} as a function of total bulk gas pressure, p_t,

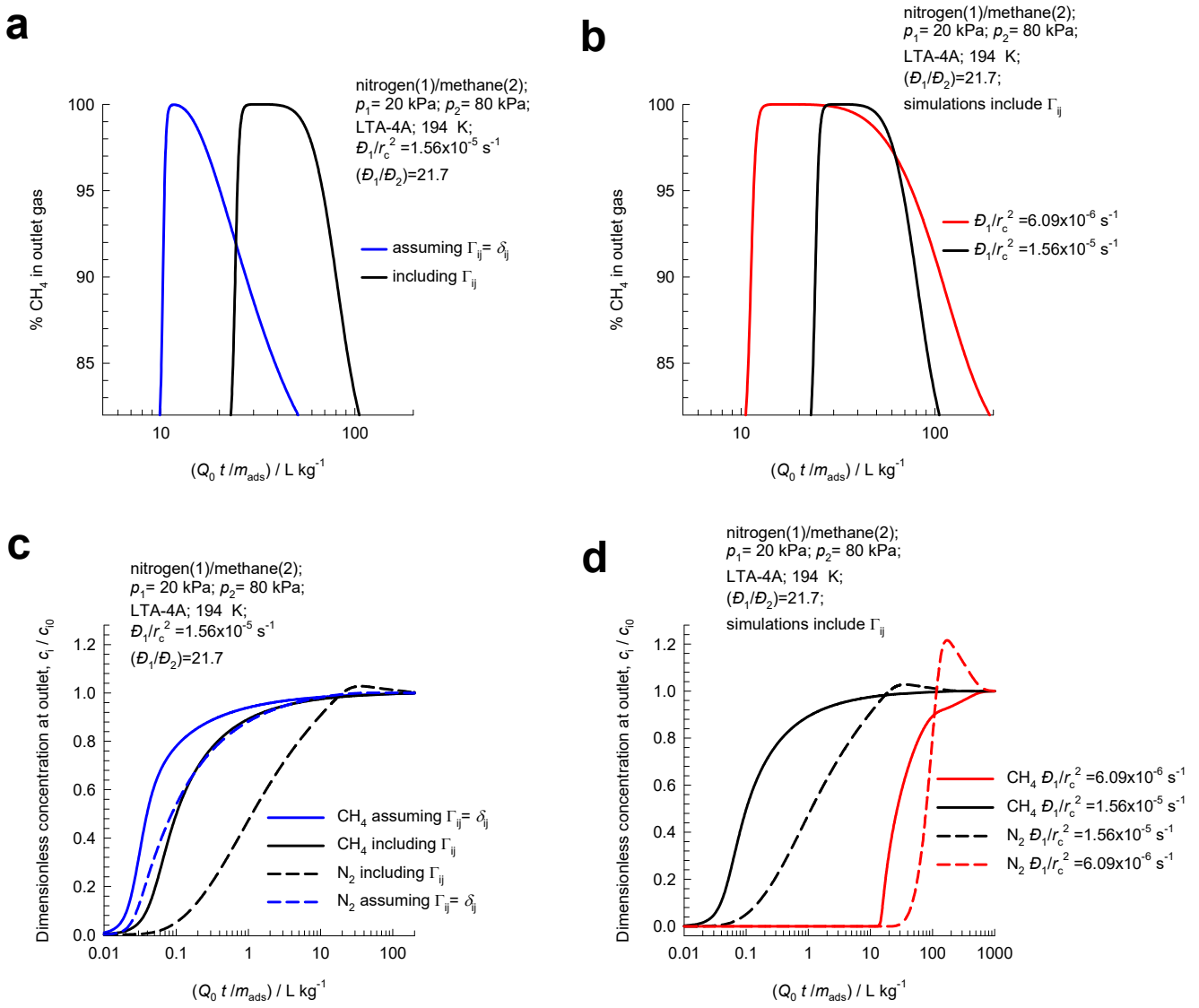

Figure S43. (a, b) Transient breakthrough of 20/80 N_2(1)/CH_4(2) mixture in fixed bed adsorber packed with LTA-4A crystals operating at 194 K, and total pressure p_t = 100 kPa. The *y*-axis is the % CH_4 at the adsorber outlet. The *x*-axis is $Q_0 t/m_{ads}$, where Q_0 is the volumetric flow rate of the gas mixture at the inlet to the fixed bed at actual temperature and pressure conditions. The black lines are simulations based on eq (S21). The blue lines are the simulations based on eq (S22) in which the thermodynamic correction factors are assumed to be described by $\Gamma_{ij} = \delta_{ij}$, the Kronecker delta. In (a) we maintain $Đ_1/r_c^2 = 1.56\times10^{-5}$ s^{-1}; $Đ_1/Đ_2 = 21.7$. In (b) the two simulations (black and red lines) include thermodynamic coupling, and maintain the ratio $Đ_1/Đ_2 = 21.7$; the black and red lines represent

two different severities of diffusional influences $Đ_1/r_c^2 = 1.56\times10^{-5}$ s^{-1}; $Đ_1/r_c^2 = 6.09\times10^{-6}$ s^{-1}. In Figure S43c,d the same sets of data in Figure S43a,b are plotted using the dimensionless concentrations in the gas phase exiting the adsorber, c_i/c_{i0}, as *y*-axes.

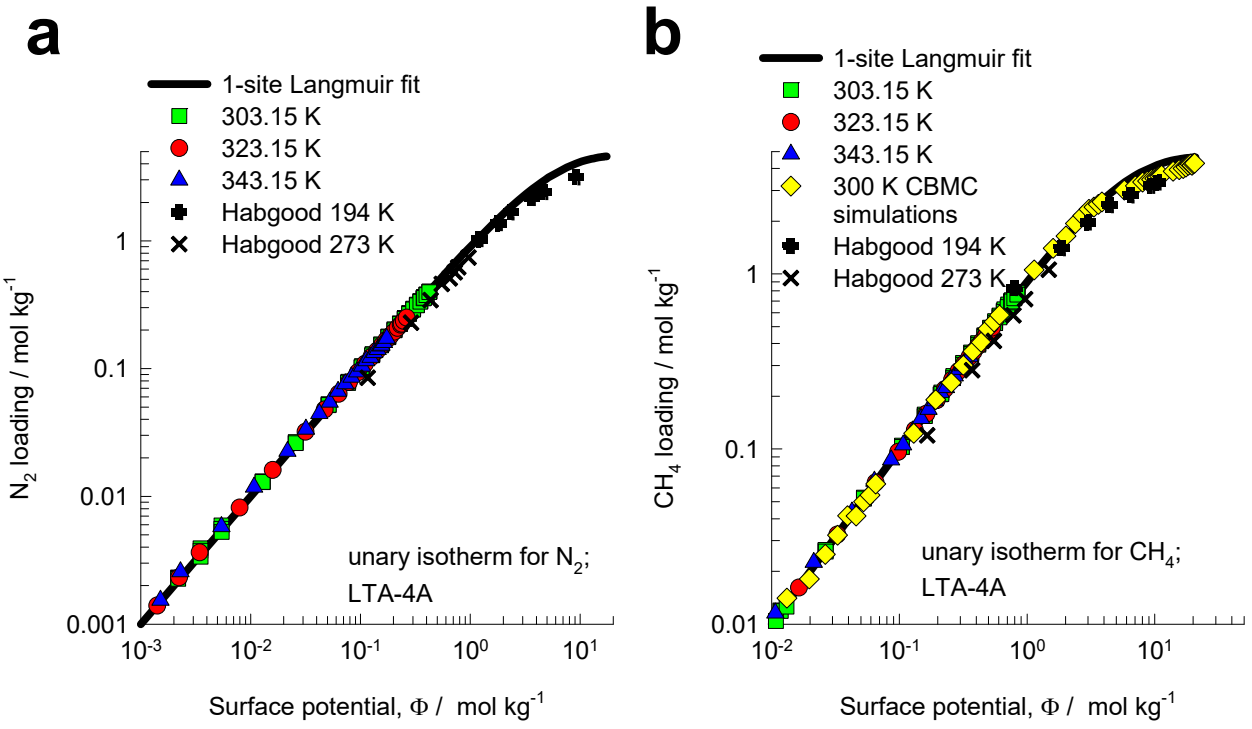

Figure S44. 1-site temperature-dependent Langmuir parameter fits for N_2 and CH_4 in LTA-4A zeolite using the parameters in Table S9. The component loadings are plotted as function of the surface potential Φ ; for details of the concept of surface potential refer to Krishna and van Baten.[84]

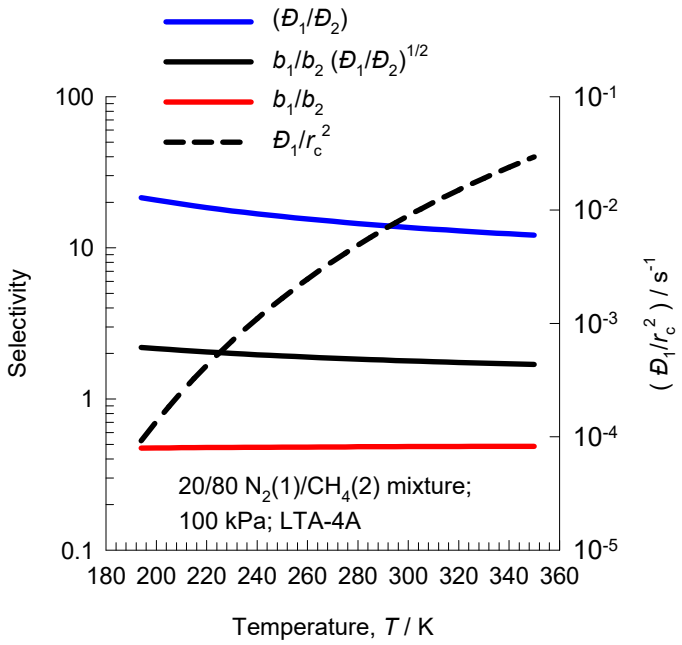

Figure S45. Plot of adsorption selectivity, $\frac{b_1}{b_2}$, diffusion selectivity, $\frac{Đ_1}{Đ_2}$, and kinetic selectivity, $\frac{b_1}{b_2}\sqrt{\frac{Đ_1}{Đ_2}}$ as function of the temperature, *T*, for LTA-4A zeolite. Also plotted on the right *y*-axes are the values of $Đ_1/r_c^2$.

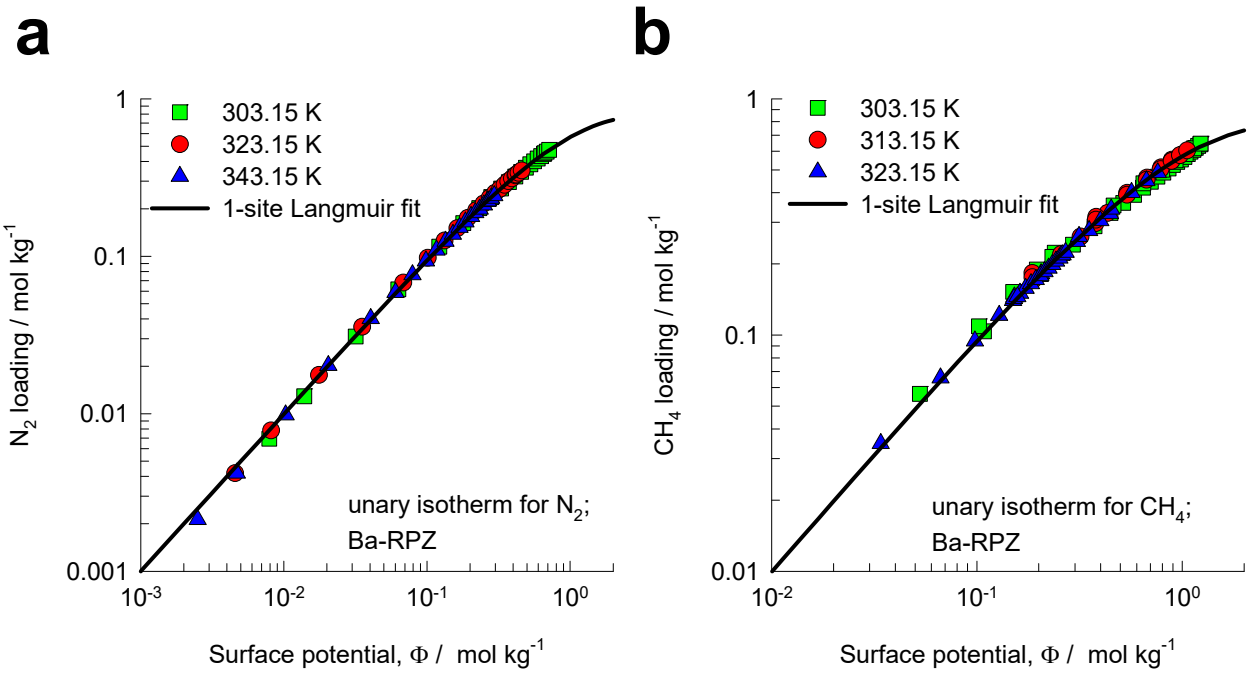

Figure S46. 1-site temperature-dependent Langmuir parameter fits for N_2 and CH_4 in Ba-RPZ using the parameters in Table S10. The component loadings are plotted as function of the surface potential Φ ; for details of the concept of surface potential refer to Krishna and van Baten.[84]

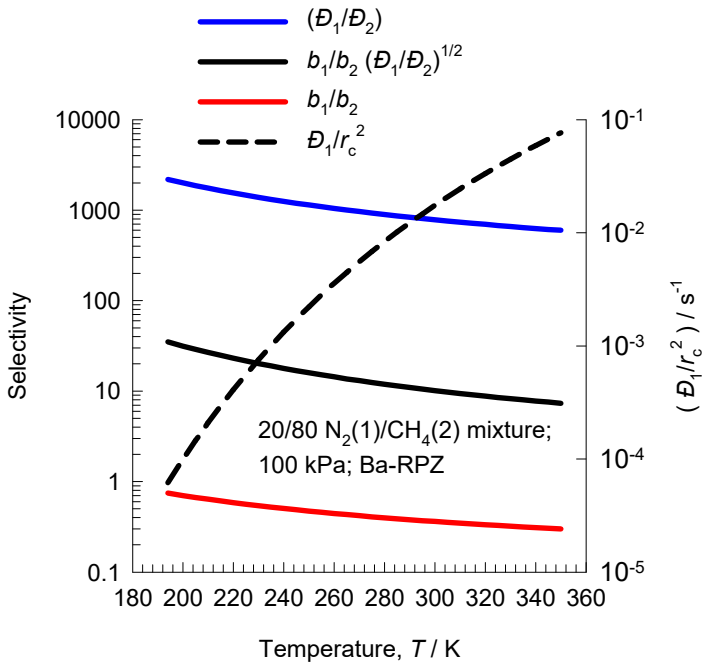

Figure S47. Plot of adsorption selectivity, $\frac{b_1}{b_2}$, diffusion selectivity, $\frac{Đ_1}{Đ_2}$, and kinetic selectivity, $\frac{b_1}{b_2}\sqrt{\frac{Đ_1}{Đ_2}}$ as function of the temperature, *T*, for Ba-RPZ. Also plotted on the right *y*-axes are the values of $Đ_1/r_c^2$.

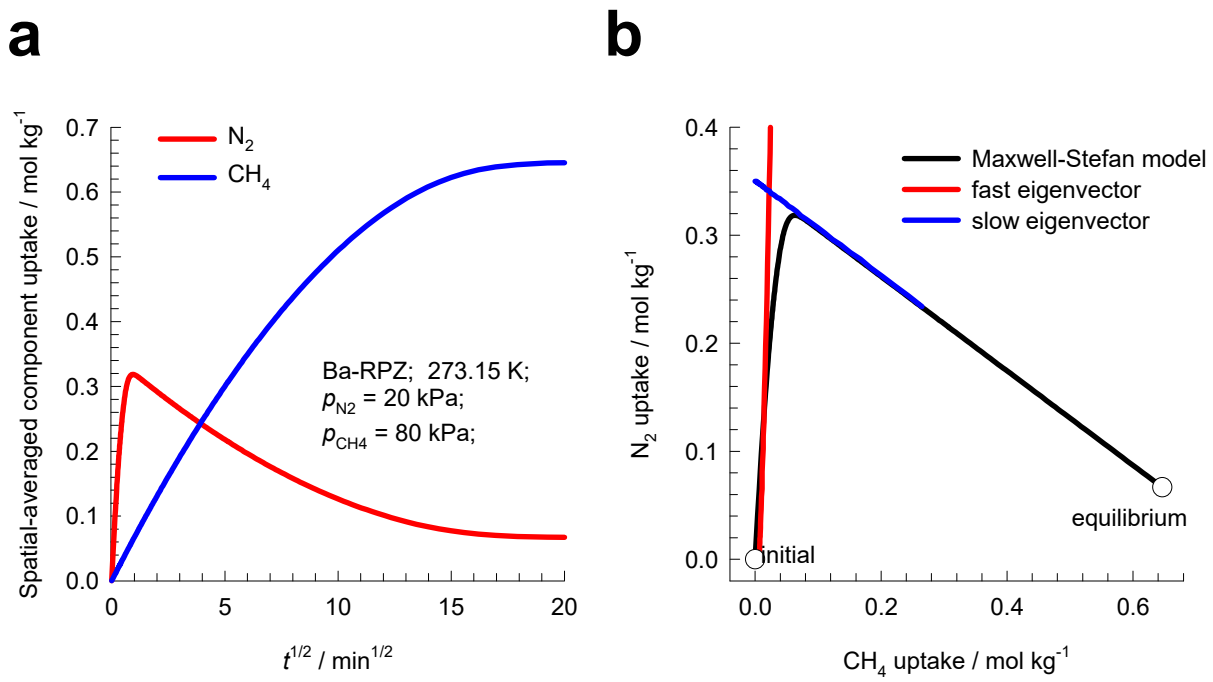

Figure S48. (a) Transient uptake of 20/80 N_2(1)/CH_4(2) mixture in Ba-RPZ crystals operating at 273 K, and total pressure p_t = 100 kPa. (b) The component loadings plotted in composition space. The red and blue lines are the fast and slow eigenvectors.

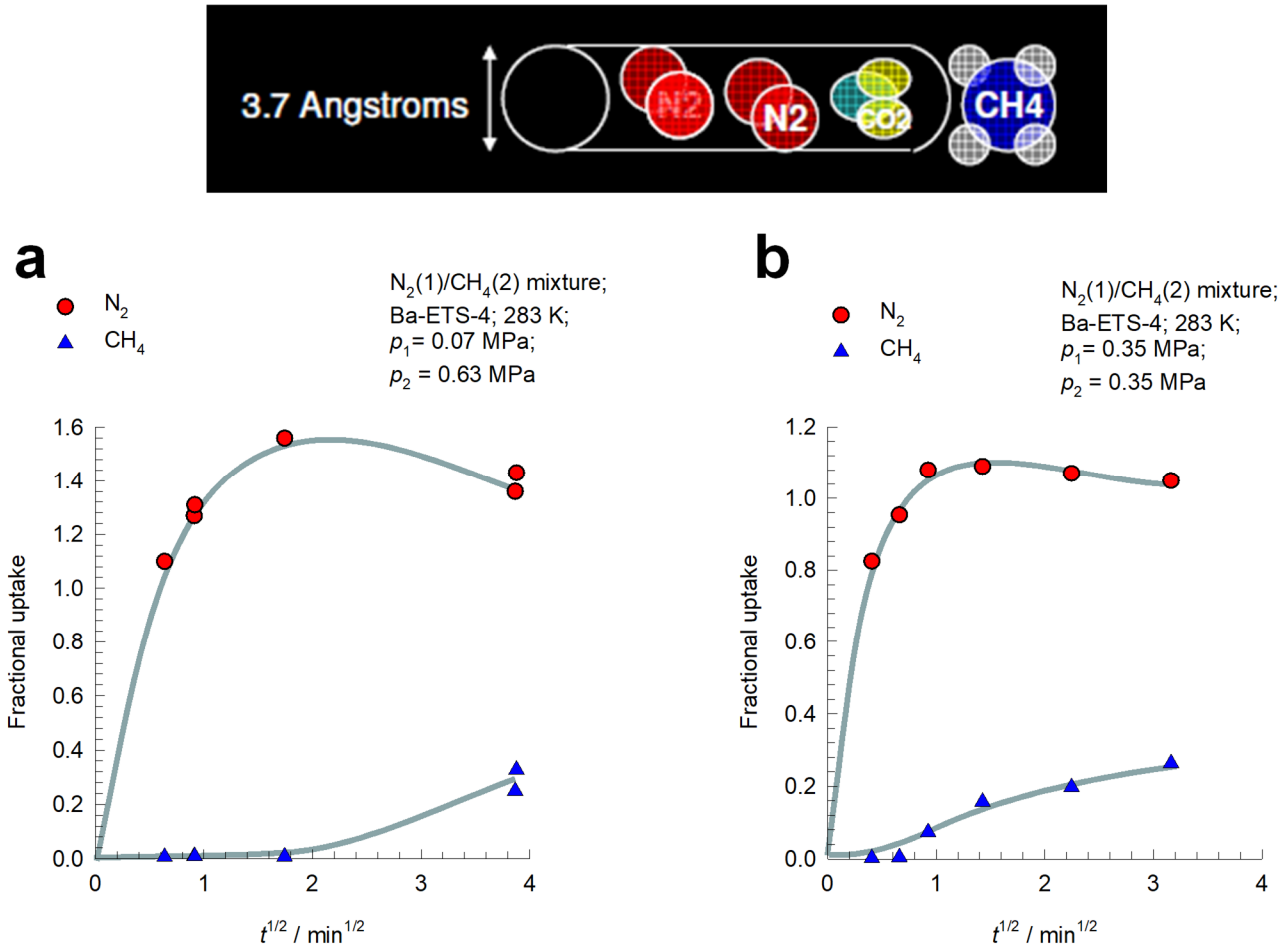

Figure S49. (a, b) The transient uptake data of Majumdar et al.[88] for Ba-ETS-4 for (a) 10/90, and (b) 50/50 mixtures in Ba-ETS-4 at 283 K and 0.7 MPa. Note that the *y*-axes are plotted in terms of fractional uptake.

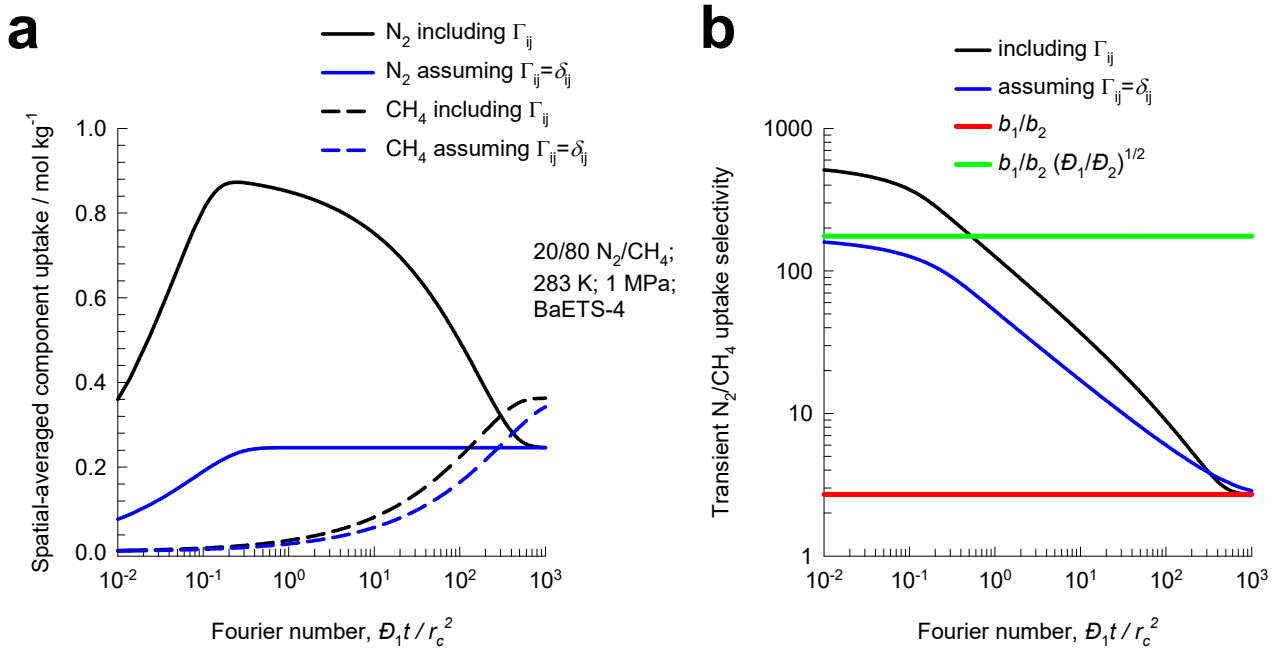

Figure S50. (a, b) Transient uptake of 20/80 N_2(1)/CH_4(2) mixture inside crystallite of Ba-ETS-4. The surrounding bulk gas mixture is at 283 K, and total pressure p_t = 1 MPa. The *x*-axes represent the Fourier number $Đ_1 t/r_c^2$. The black lines are simulations based on eq (S21). The blue lines are the simulations based on eq (S22) in which the thermodynamic correction factors are assumed to be described by $\Gamma_{ij} = \delta_{ij}$, the Kronecker delta.

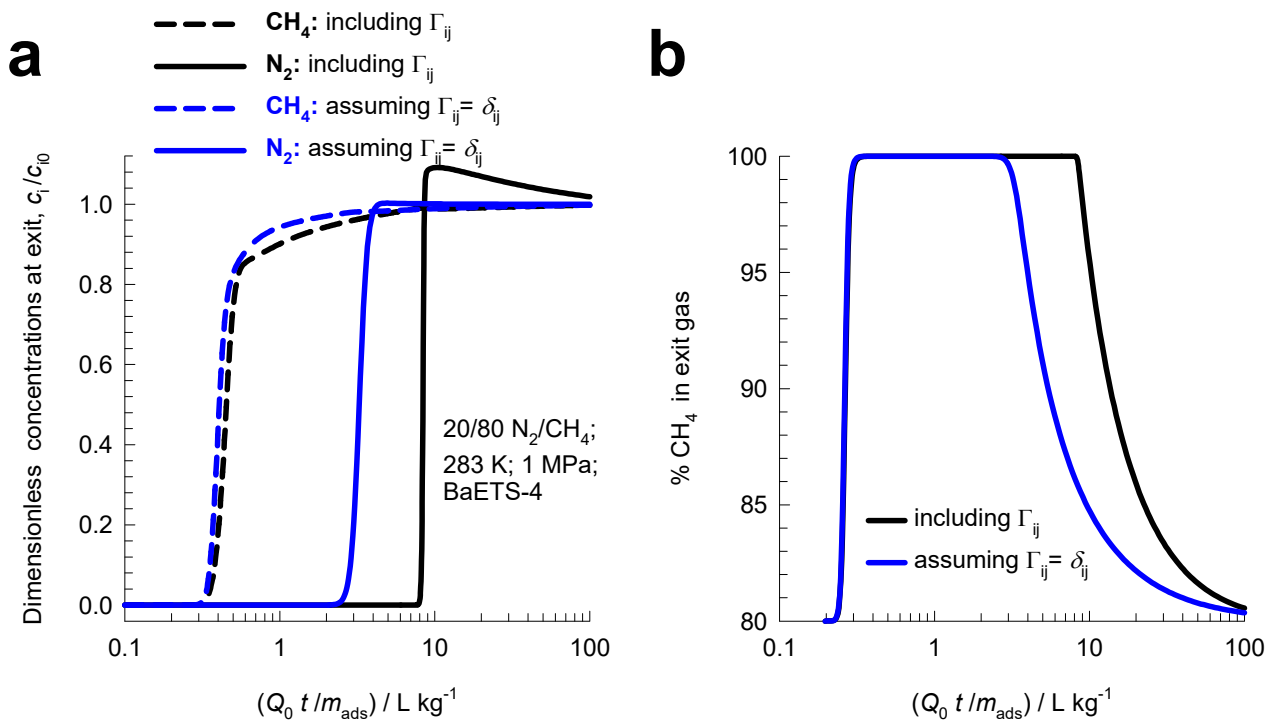

Figure S51. (a, b) Ttransient breakthroughs of 20/80 N_2(1)/CH_4(2) mixture in fixed bed adsorber packed with Ba-ETS-4, operating at 283 K, and total pressure p_t = 1 MPa. The *x*-axes are $Q_0 t/m_{ads}$, where Q_0 is the volumetric flow rate of the gas mixture at the inlet to the fixed bed at actual temperature and pressure conditions. The *y*-axis in (b) is the % CH_4 at the adsorber outlet. The black lines are simulations based on eq (S21). The blue lines are the simulations based on eq (S22) in which the thermodynamic correction factors are assumed to be described by $\Gamma_{ij} = \delta_{ij}$, the Kronecker delta.

9 Separation of O_2/N_2 mixtures

The separation of air to produce N_2 and O_2 of high purities is one of the most important industrial processes that uses pressure swing adsorption technology.[18, 93] The process technologies are geared to either production of purified O_2 or purified N_2. Cryogenic distillation has been the common technologies for this separation, but adsorptive separations offer energy efficient alternatives. Purified O_2 is required for a wide variety of applications that include portable adsorption units for medical applications and in space vehicles. Nitrogen is required in applications where it is desired or necessary to exclude oxygen. Typical industrial applications include preservation of fruit and produce during trucking, the blanketing of fuel tanks of fighter aircraft, the inerting of reactors in a number of pharmaceutical processes, laser cutting. N_2 is required for use in laboratory analytical equipment such as GC, LC, LCMS, FTIR, ICP, and in glove boxes.

For production of purified O_2, cation-exchanged zeolites LTA-5A (also called 5A or NaCaA zeolite containing 96 Si, 96 Al, 32 Na^+, 32 Ca^{++} per unit cell; Si/Al=1), NaX (also called 13 X zeolite, containing 106 Si, 86 Al, 86 Na^+ per unit cell; Si/Al=1.23), CaX, LiX, and LiLSX (= low silica LiX zeolite) and can be used as selective adsorbents.[93-97] The larger permanent quadrupole of N_2 compared to that of O_2 is responsible for the stronger adsorption strength of N_2 on these zeolites.[96] Both O_2, and N_2 have similar polarizabilities and magnetic susceptibilies. However, the quadrupole moment of N_2 is about 4 times that of O_2. The Skarstrom cycle can be used, with modifications such as the introduction of a pressure equalization step, for production of enriched O_2 using say LiLSX zeolite. The different steps (stages) in the operation of a single bed for producing oxygen in small-scale units are shown in Figure S52, that has been adapted from Ruthven and Farooq.[98] Desorption of the preferentially adsorbed nitrogen is achieved by pressure reduction followed by purging with a fraction of the oxygen product to

remove the nitrogen from the interstices of the bed. Further details are available in the excellent texts of Ruthven et al.[18], and Yang.[91, 99]

For production of purified N_2 from air, a different strategy is often employed that rely on diffusion selectivity.[20, 100] Diffusion-selective separation are achieved with Carbon Molecular Sieve (CMS), and LTA-4A zeolite. Diffusion limitations manifest in LTA-4A because the window regions are partially blocked by the cations; see pore landscape in Figure S53. The same basic Skarstrom cycle can be used, with the kinetically selective 4A zeolite or carbon molecular sieve adsorbent, in a nitrogen production process. However, in such a system purging with nitrogen to remove the faster diffusing oxygen from the bed is undesirable since, as well as wasting product, a certain fraction of the slowly diffusing nitrogen will be adsorbed, thus reducing the capacity for oxygen during the next adsorption step. At the end of the counter-current blowdown step (see Figure S54), the adsorbent contains both oxygen (fast diffusing) and nitrogen (slow diffusing). Thus if the bed is simply closed at one end and left for a period of time the oxygen will diffuse out first followed by the nitrogen so the system is, in effect, self purging. [18, 98]

Watch **PSA for Air Separations** on YouTube

https://www.youtube.com/@rajamanikrishna250/videos

9.1 Transient uptake of O_2/N_2 mixtures in LTA-4A

Figure S55 presents the simulations of transient uptake of $O_2(1)/N_2(2)$ mixture in LTA-4A zeolite at 298 K and total pressure of 600 kPa. The partial pressures of the components in the bulk gas phase are p_1 = 126 kPa, p_2 = 474 kPa. The continuous solid lines are Maxwell-Stefan model simulations based on Eq (S20), that accounts for thermodynamic coupling. The O_2 overshoot signals uphill diffusion.[12,41] The dashed lines are the simulations based on Eq (S22), in which the thermodynamic correction factors are assumed to be described by $\Gamma_{ij} = \delta_{ij}$, the Kronecker delta; in this scenario there is no O_2 overshoot. The conclusion to be drawn is that the O_2 overshoot is engendered by thermodynamic coupling effects.

9.2 List of Tables for Separation of O2/N2 mixtures

Table S12. 1-site Langmuir parameters for O_2 and N_2 in LTA-4A zeolite at 298 K. These isotherm data are taken from Farooq et al.[20, 100] These data are for RS-10, a modified version of LTA-4A that affords higher diffusion selectivity in favor of O_2.

	q_{sat} mol kg^{-1}	b Pa^{-1}
O_2	1.91	5.65×10^{-7}
N_2	1.91	1.13×10^{-6}

On the basis of the information provided in Table 3 of Farooq et al.[20]

The crystal framework density $\rho = 1100$ kg m^{-3}

The Maxwell-Stefan diffusivities are

$Đ_1/r_c^2 = 2.75\times10^{-2}$ s^{-1}; . $Đ_2/r_c^2$. $= 7.5\times10^{-4}$ s^{-1}; $Đ_1/Đ_2 = 36.7$.

9.3 List of Figures for Separation of O2/N2 mixtures

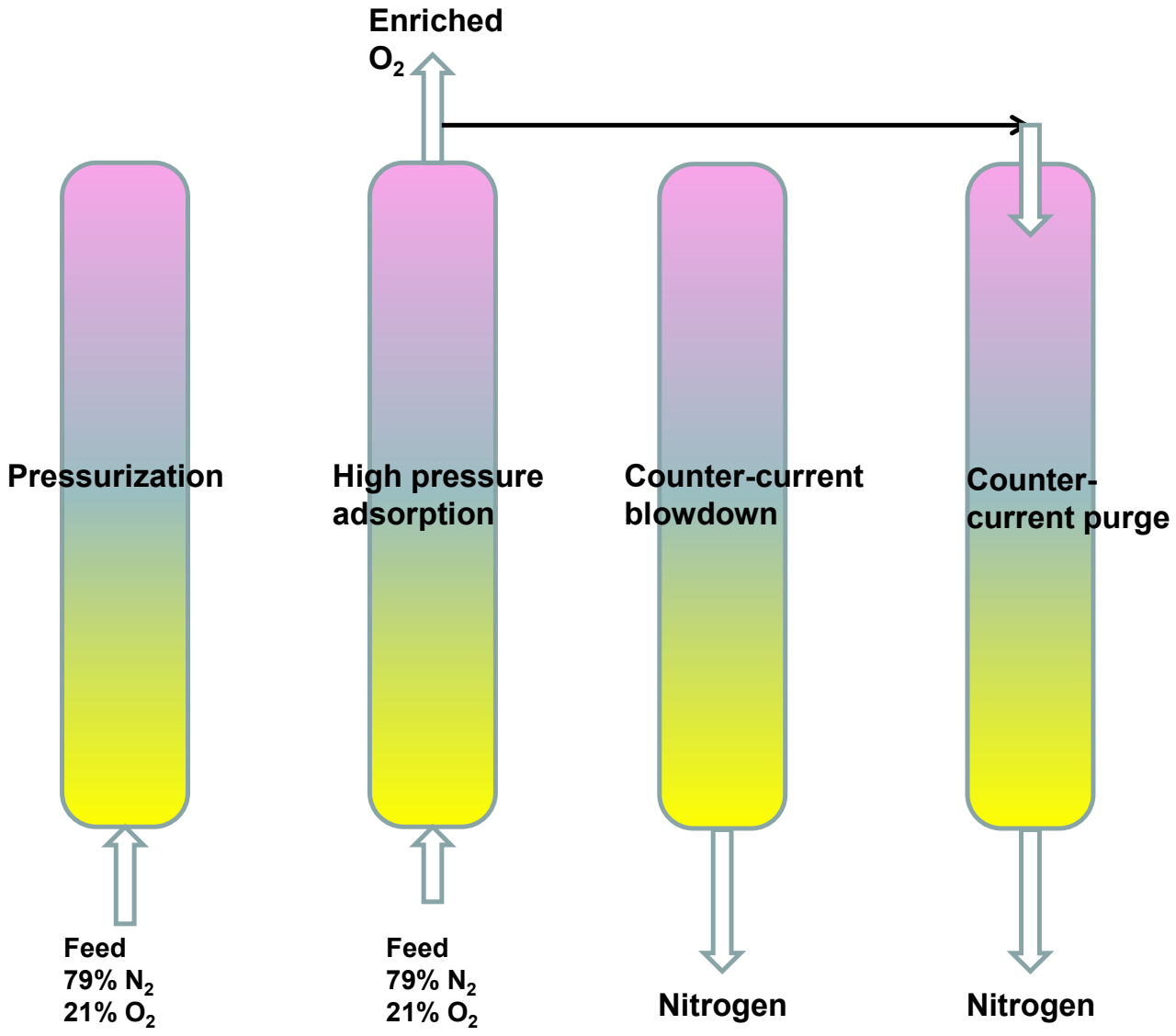

Figure S52. Different steps in the production of purified O_2 using an adsorbent such as LiLSX. The scheme shows the sequence of processing of a single bed in a multi-bed PSA scheme. Adapted from Ruthven and Farooq.[98]

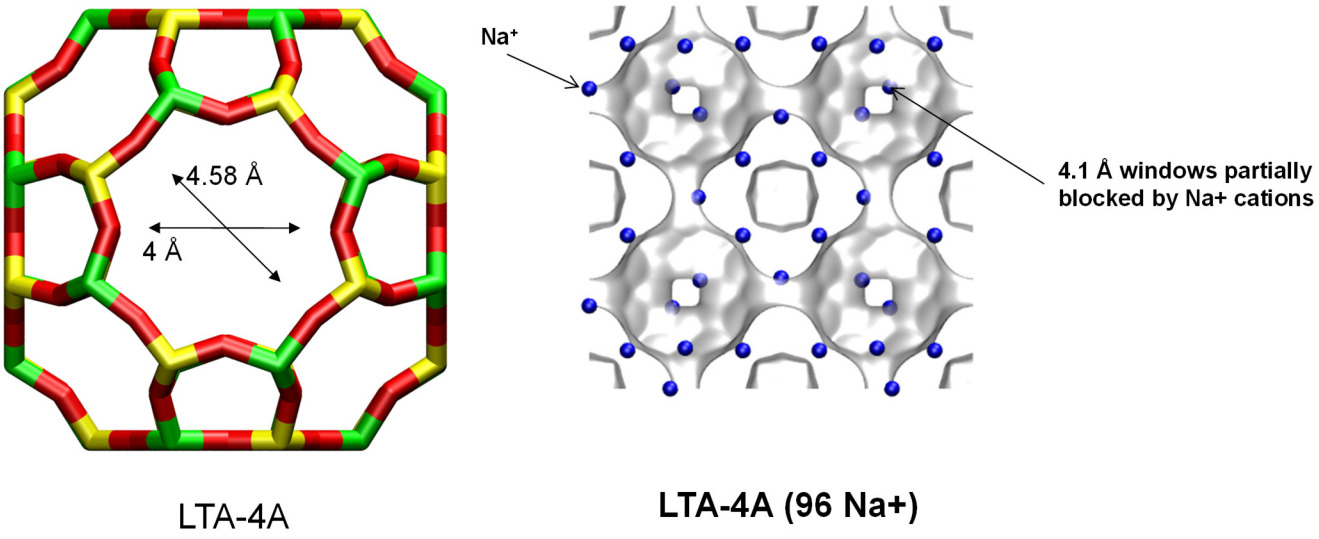

Figure S53. Partial blocking of the windows of LTA-4A zeolite.

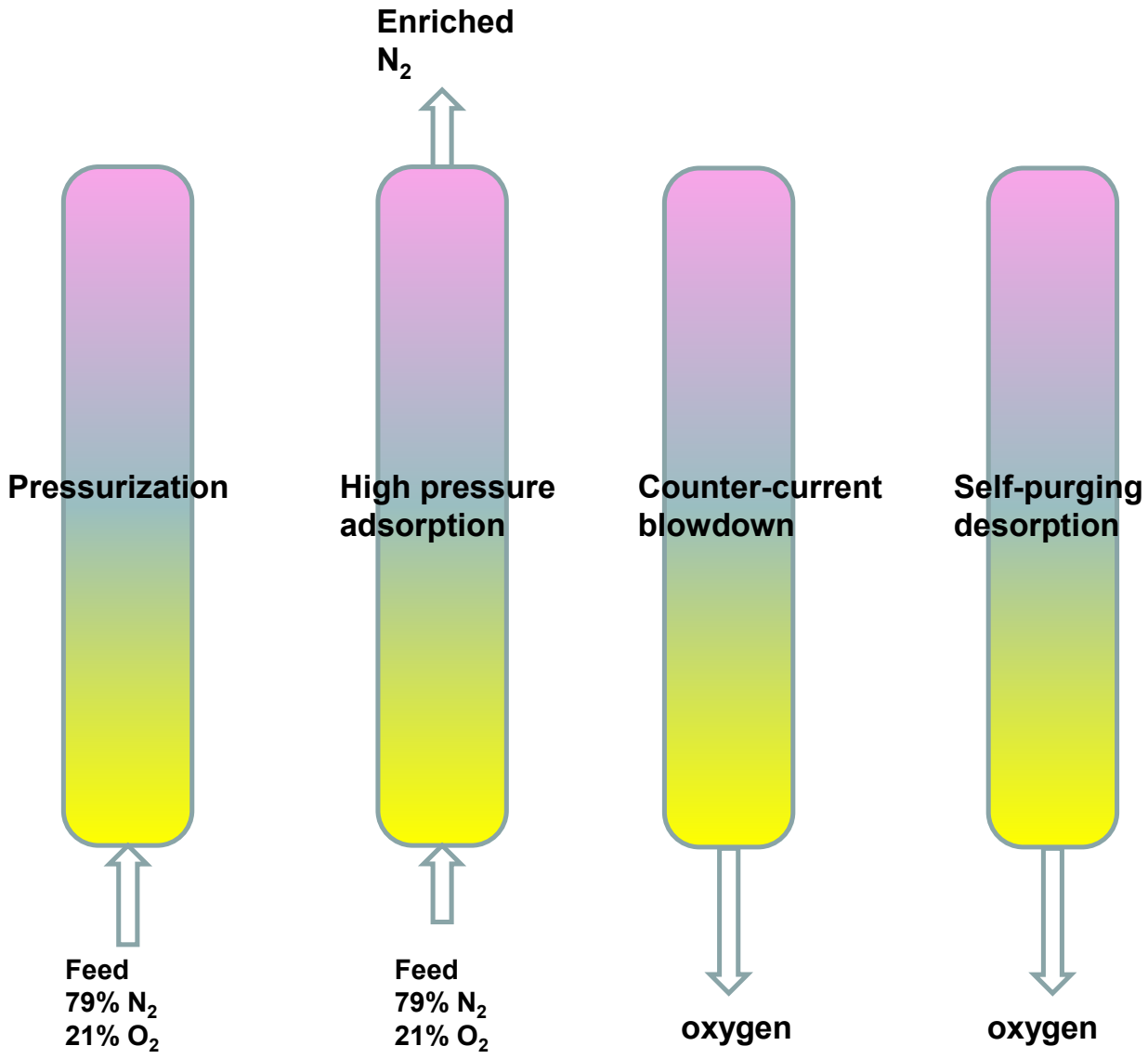

Figure S54. Different steps in the production of purified N_2 using an adsorbent such as LTA-4A, that relies on kinetic selectivity. The scheme shows the sequence of processing of a single bed in a multi-bed PSA scheme. Adapted from Ruthven and Farooq.[98]

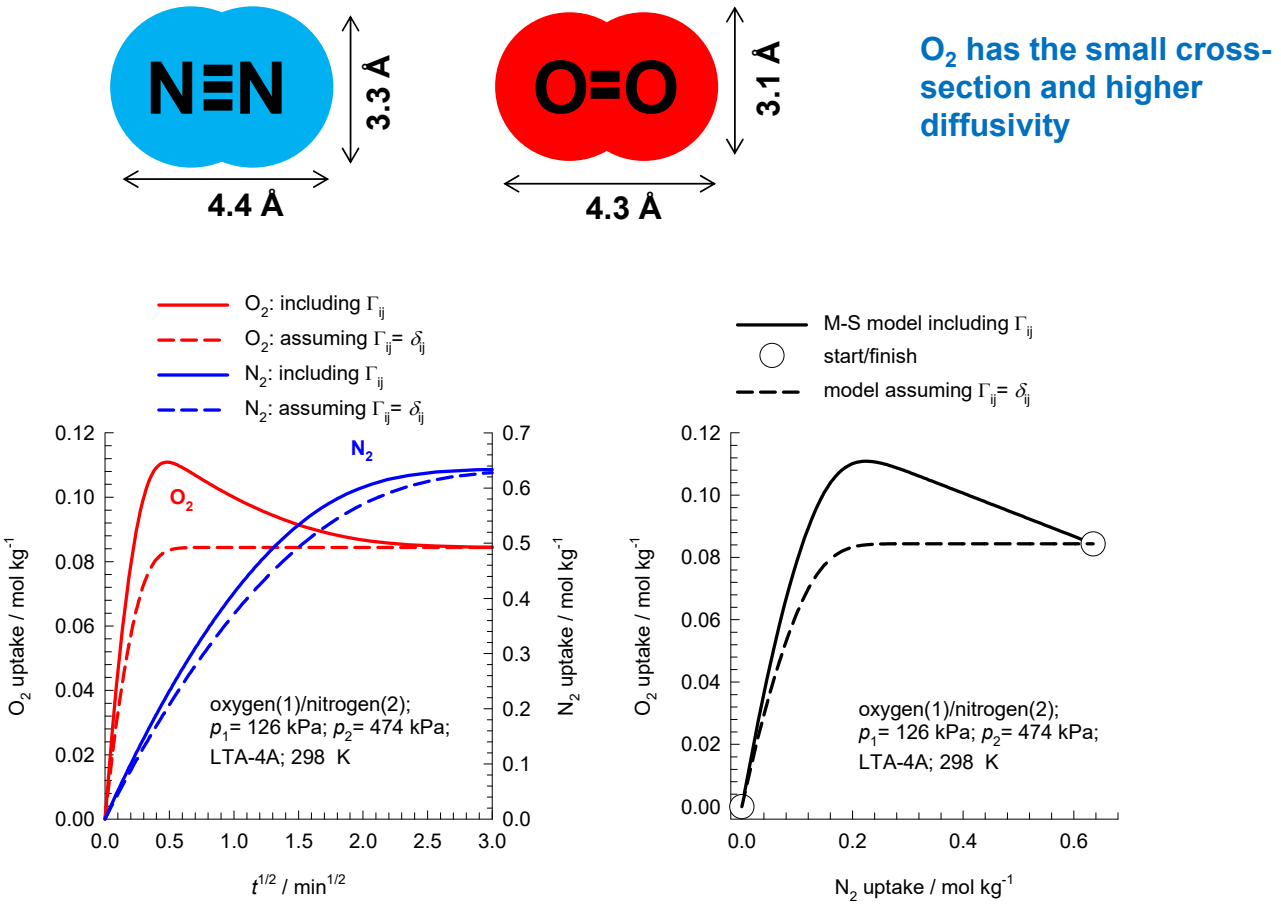

Figure S55. Transient uptake of $O_2(1)/N_2(2)$ mixture in LTA-4A zeolite at 298 K and total pressure of 600 kPa. The partial pressures of the components in the bulk gas phase are p_1 = 126 kPa, p_2 = 474 kPa. The unary isotherms are provided in Table S12. The continuous solid lines are Maxwell-Stefan model simulations based on eq (S20). The dashed lines are the simulations based on eq (S22), in which the thermodynamic correction factors are assumed to be described by $\Gamma_{ij} = \delta_{ij}$, the Kronecker delta. The Maxwell-Stefan diffusivities used in the simulations are: $Đ_1/r_c^2 = 2.75\times10^{-2}$ s^{-1}; $Đ_2/r_c^2 = 7.5\times10^{-4}$ s^{-1}; $Đ_1/Đ_2 = 36.7$.

10 C_3H_6/C_3H_8 separations

For production of alkene feedstocks of 99.95%+ purity required for polymerization reactors, cryogenic distillation columns operated at high pressures and high reflux ratios are commonly employed for large scale separations of C_2H_4/C_2H_6, and C_3H_6/C_3H_8 mixtures. Many MOF developments have targeted alkene/alkane separations with the objective of eventually supplanting the energy-intensive distillation technologies.[85, 101-106] Each of the unsaturated alkenes C_2H_4, and C_3H_6 possesses a π-bond, and the preferential adsorption of the alkene from the corresponding alkane with the same number of C atoms can be achieved by choosing zeolitic adsorbents with extra-framework cations (e.g. LTA-4A, LTA-5A,[107-109] and NaX (= 13X) zeolites[107, 110]), or MOFs with unsaturated "open" metal sites[101, 111] (e.g. M_2(dobdc)[101, 111] [M = Mg, Mn, Co, Ni, Zn, Fe; $dobdc^{4-}$ = 2,5- dioxido-1,4-benzenedicarboxylate], M_2(*m*-dobdc) [112] [M = Mn, Fe, Co, Ni; *m*-$dobdc^{4-}$ = 4,6-dioxido-1,3-benzenedicarboxylate] and CuBTC[113]). An alternative is employ NbOFFIVE-1-Ni (= KAUST-7) [102] or Co-gallate,[114] that almost completely exclude the saturated alkane from the pores due to diffusional limitations.

Watch presentation titled **Alkene/Alkane Separations with MOFs** on YouTube

https://www.youtube.com/@rajamanikrishna250/videos

Figure S56 compares the experimental data on transient breakthroughs for separation of C_3H_6/C_3H_8 mixtures in a fixed bed adsorber packed with: KAUST-7,[102] Co-Gallate,[114] LTA-5A,[102] and Ni_2(dobdc).[115] The dimensionless concentrations at the exit of the fixed bed, c_i/c_{i0}, are plotted as a function of $Q_0 t/m_{ads}$, where Q_0 is the volumetric flow rate of the gas mixture at the inlet to the fixed bed, expressed in L s^{-1}, at STP conditions. Though LTA-5A and Ni_2(dobdc) have significantly higher C_3H_6 uptake capacities, these materials also adsorb significant amounts of saturated alkane. In the vacuum blowdown step, the presence of the saturated alkanes in the void spaces of the bed is a detrimental factor in the achievement of the desired high-purity C_3H_6 product.

To attain higher C_3H_6 purities that are required for polymerization feedstocks, we need to operate with multiple beds involving five different steps, as schematized in Figure S57, [21, 108, 110, 116] consisting of

(i) Pressurization with C_3H_6/C_3H_8 feed mixture

(ii) High pressure adsorption separation with withdrawal of purified C_3H_8

(iii) Co-current purge with a portion of the product C_3H_6

(iv) Co-current blowdown, and

(v) Counter-current vacuum blowdown

The recovery of high purity C_3H_6 product in the final vacuum blowdown step is expected to be enhanced if C_3H_8 is (almost) excluded during the high pressure adsorption cycle. Near-total exclusion of C_3H_8 is achievable by kinetically based separations using cage-type zeolites with 8-ring windows. Due to the small cross-section of the propene molecule (see Figure S58), kinetic separations, selective to propene, are possible using all-silica CHA zeolite (all-silica CHA zeolite, also named SiCHA, consists of cages of volume 316 $Å^3$, separated by 3.8 Å × 4.2 Å 8-ring windows; the pore landscapes and structural details of CHA zeolite are provided in Figure S20, and Figure S21.[21, 117-119]

Ruthven and Reyes[119] compare the ratio of diffusivities of propene to that of propene in CHA with the corresponding values in DDR; see Figure S59. Their data show that CHA is the more effective sieve.

It is to be noted for LTA-4A zeolite,[107, 108] both mixture adsorption and diffusion favor propene, whereas with all-silica CHA zeolite, the adsorption equilibrium is in favor of propane, whereas diffusion favors propene.

In order to appreciate the significance of thermodynamic coupling, Figure S60 presents the calculations of the thermodynamic correction factors Γ_{ij}. We note that at a total pressure of 200 kPa, the cross-coefficients are about 75-90% of the magnitudes of the diagonal elements, indicating that coupling effects cannot be ignored.

Figure S61a,b shows the simulations of transient uptake of 50/50 $C_3H_6(1)/C_3H_8(2)$ mixtures within crystals of all-silica CHA at 353 K.

The elements of the $[\Gamma]$ are $\begin{bmatrix} \Gamma_{11} & \Gamma_{12} \\ \Gamma_{21} & \Gamma_{22} \end{bmatrix} = \begin{bmatrix} 2.5 & 1.5 \\ 4 & 5 \end{bmatrix}$. The Fick diffusivity matrix is calculated to be

$$\frac{\begin{bmatrix} D_{11} & D_{12} \\ D_{21} & D_{22} \end{bmatrix}}{r_c^2} = \begin{bmatrix} 4250 & 2550 \\ 1.36 & 1.7 \end{bmatrix} \times 10^{-7} \quad \text{s}^{-1}.$$

The spatial averaged component loadings are plotted as a function of $\sqrt{t}$. The bulk gas mixture is at a total pressure of 100 kPa. The solid black lines are simulations based on eq (S10); the Maxwell-Stefan diffusivities are $Đ_1/r_c^2 = 1.7\times10^{-4}$ s^{-1}; $Đ_1/Đ_2 = 5000$. The more mobile C_3H_6 exhibits a pronounced overshoot in its approach to thermodynamic equilibrium. The attainment of supraequilibrium loadings during the initial stages of transience signals the phenomenon of uphill diffusion, and enhanced separation. The dashed lines are simulations based on eq (S11), in which the thermodynamic correction factors are assumed to be described by $\Gamma_{ij} = \delta_{ij}$. in which the thermodynamic correction factors are assumed to be described by $\Gamma_{ij} = \delta_{ij}$, the Kronecker delta. In this scenario, no C_3H_6 overshoot is observed indicating that thermodynamic coupling effects are the root cause of uphill diffusion.

Figure S61b plots the equilibration trajectories for C_3H_6(1), and C_3H_8(2). If thermodynamic coupling effects are ignored, both C_3H_6, and C_3H_8 display monotonous equilibration characteristics.

ZIF-8 has a cage-window SOD (sodalite) topology (see pore landscape in Figure S62). The crystallographic size of the windows of ZIF-8 are 3.3 Å, but the windows are flexible. Due to subtle differences in bond lengths and bond angles, the diffusivity of C_3H_6 (1) is significantly higher than that of C_3H_8 (2); Li et al.[120] report the value of the ratio $Đ_1/Đ_2$ = 125 based on the data on pure component uptakes. In ZIF-8, the adsorption strength of the saturated propane is higher than that of propene. From the experimental isotherm data of Li et al.,[120] the ratio of single-site Langmuir parameter b_2/b_1 = 1.07 at 303 K. From a practical standpoint, it is of interest to know under what set of conditions transient overshoots can be expected to occur. To get some insights into this question, we investigated binary C_3H_6(1)/C_3H_8(2) mixture uptake in ZIF-8. The windows of ZIF-8 have a dimension of about 3.3 Å.

Due to subtle differences in bond lengths and bond angles (see Figure S62), the diffusivity of C_3H_6 is higher than that of C_3H_8.

Figure S62 presents simulations of transient uptake of C_3H_6(1)/C_3H_8(2) mixture within crystals of ZIF-8, taking $Đ_1/Đ_2$ =125. The more mobile propene exhibits a sharp overshoot in the uptake for simulations in which thermodynamic coupling is properly accounted for. If thermodynamic coupling effects are ignored, both C_3H_6, and C_3H_8 display monotonous equilibration characteristics.

10.1 List of Tables for C3H6/C3H8 separations

Table S13. 1-site Langmuir parameters for C_3H_6, and C_3H_8 in all-silica CHA zeolite at 353 K. These isotherm data are taken from Table 4 of Khalighi et al.[21]

	$\frac{q_{sat}}{\text{mol kg}^{-1}}$	$\frac{b}{\text{Pa}^{-1}}$
C_3H_6	2.9	3×10^{-5}
C_3H_8	2.9	8×10^{-5}

On the basis of the information provided in Table 4 of Khalighi et al.,[21] the Maxwell-Stefan diffusivities are $Đ_1/r_c^2 = 1.7\times10^{-4}$ s^{-1}; $Đ_2/r_c^2 = 3.4\times10^{-8}$ s^{-1}; $Đ_1/Đ_2 = 5000$.

Table S14. 1-site Langmuir parameters for propene and propane in ZIF-8.[121] The *T*-dependent parameters are obtained by fitting the combined sets of pure component isotherm data of Li et al.[120] and Böhme et al.[122] determined for a variety of temperatures in the range 273 K to 408 K.

$$q = q_{sat}\frac{bp}{1+bp}; \quad b_A = b_0 \exp\left(\frac{E}{RT}\right)$$

	$\frac{q_{sat}}{\text{mol kg}^{-1}}$	$\frac{b_0}{\text{Pa}^{-1}}$	$\frac{E}{\text{kJ mol}^{-1}}$
propene	5.2	4.57×10^{-11}	33.9
propane	5.2	1.39×10^{-10}	31.3

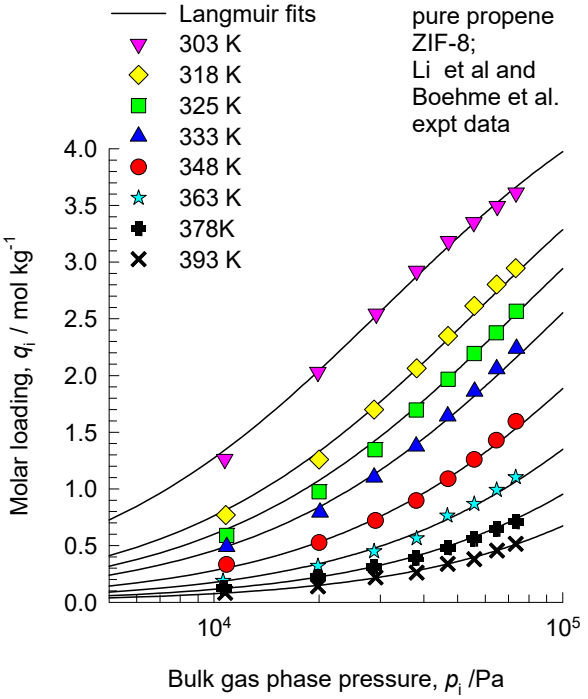

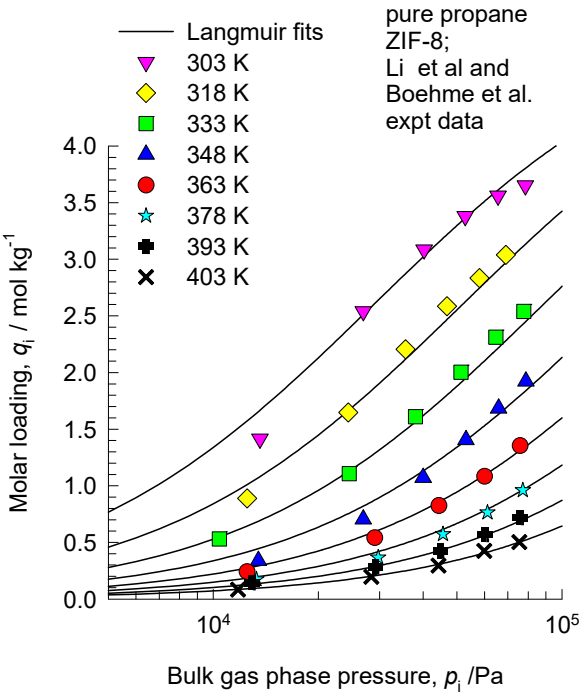

10.2 List of Figures for C3H6/C3H8 separations

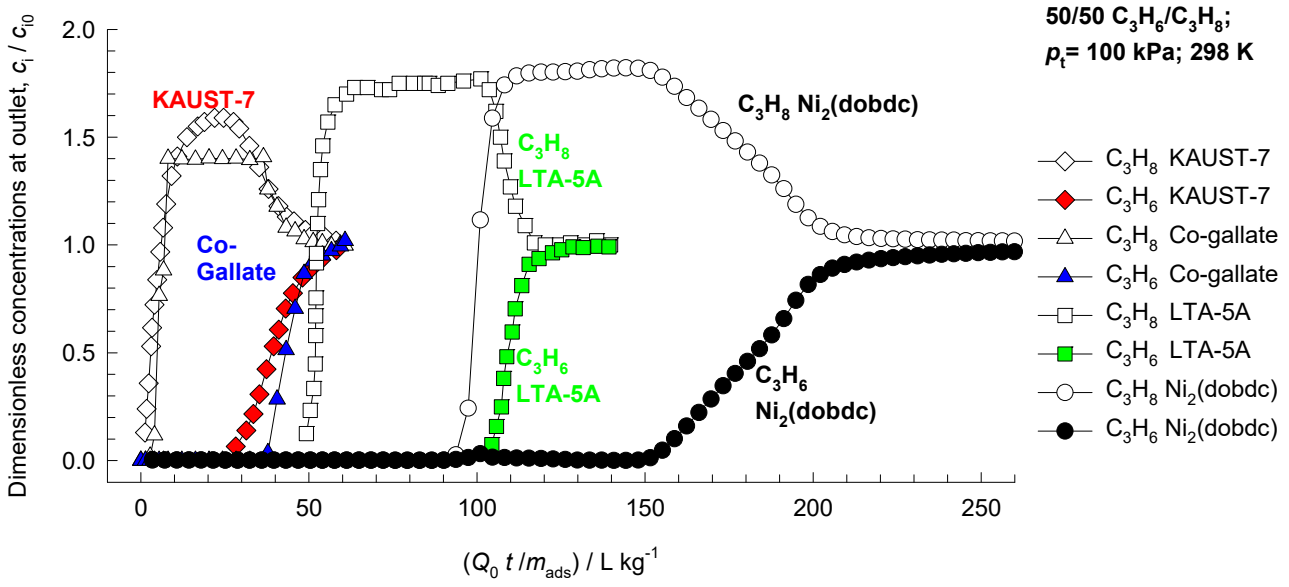

Figure S56. Experimental data on transient breakthroughs for separation of 50/50 C_3H_6/C_3H_8 mixtures in a fixed bed adsorber packed with: KAUST-7,[102] Co-Gallate,[114] LTA-5A zeolite,[102] and Ni_2(dobdc).[115] The dimensionless concentrations at the exit of the fixed bed, c_i/c_{i0}, (open symbols = C_3H_8; filled symbols = C_3H_6) are plotted as a function of $Q_0 t/m_{ads}$, where Q_0 is the volumetric flow rate of the gas mixture at the inlet to the fixed bed, expressed in L s^{-1}, at STP conditions.

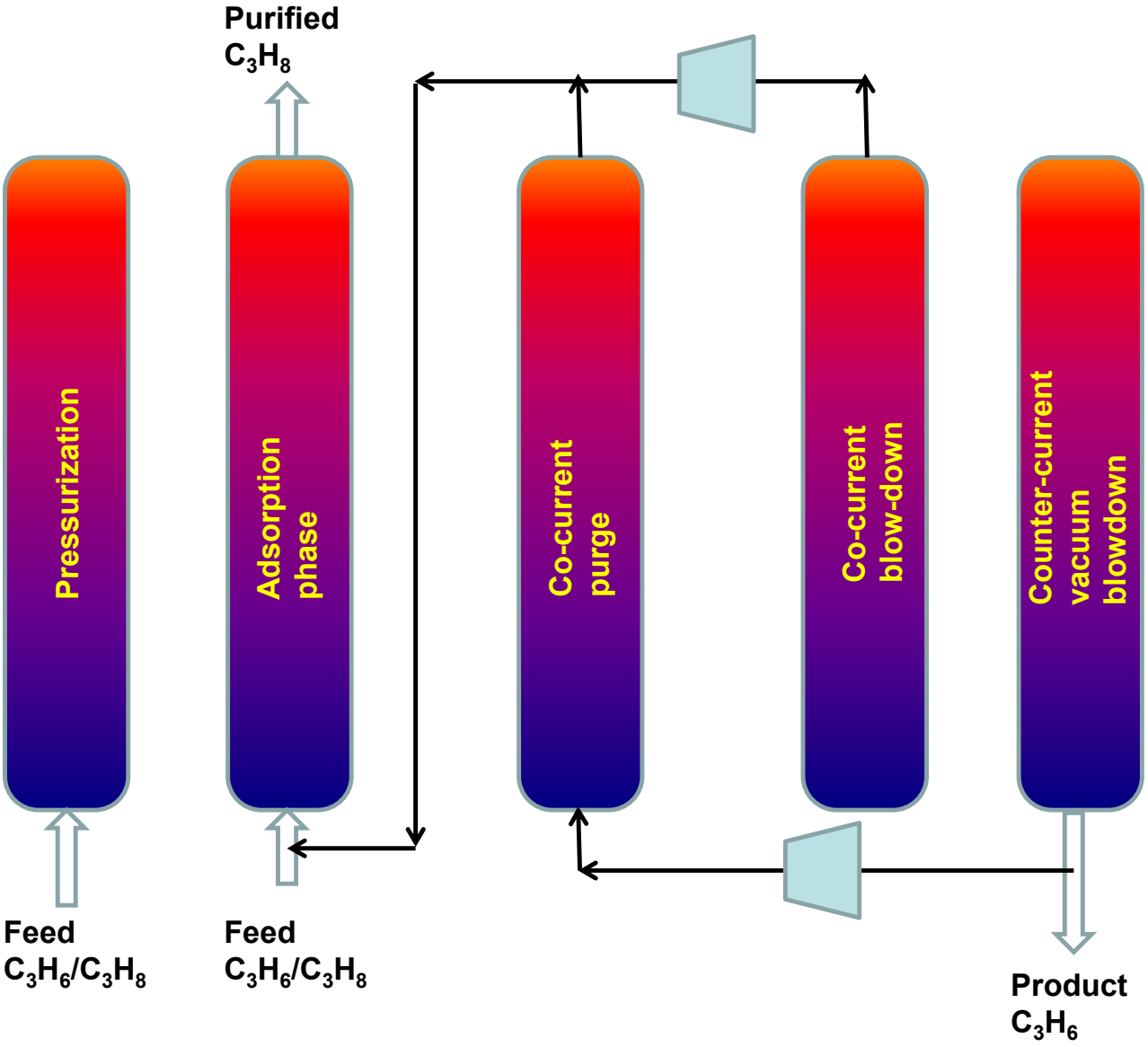

Figure S57. Five-step PSA process for separating C_3H_6/C_3H_8 mixtures.[108, 110, 116]

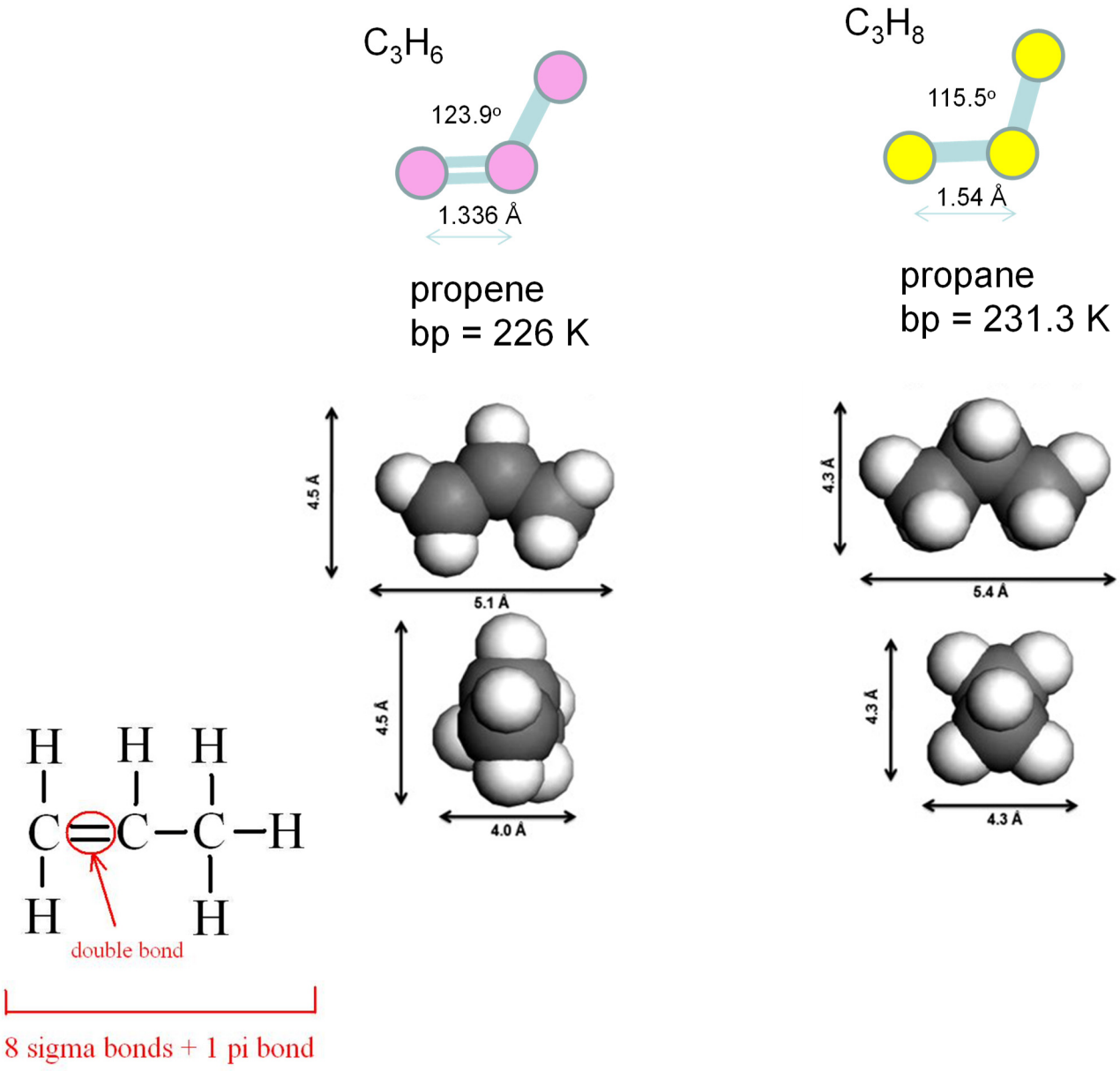

Figure S58. Molecular dimensions of C_3H_6 and C_3H_8, culled from the literature.[123]

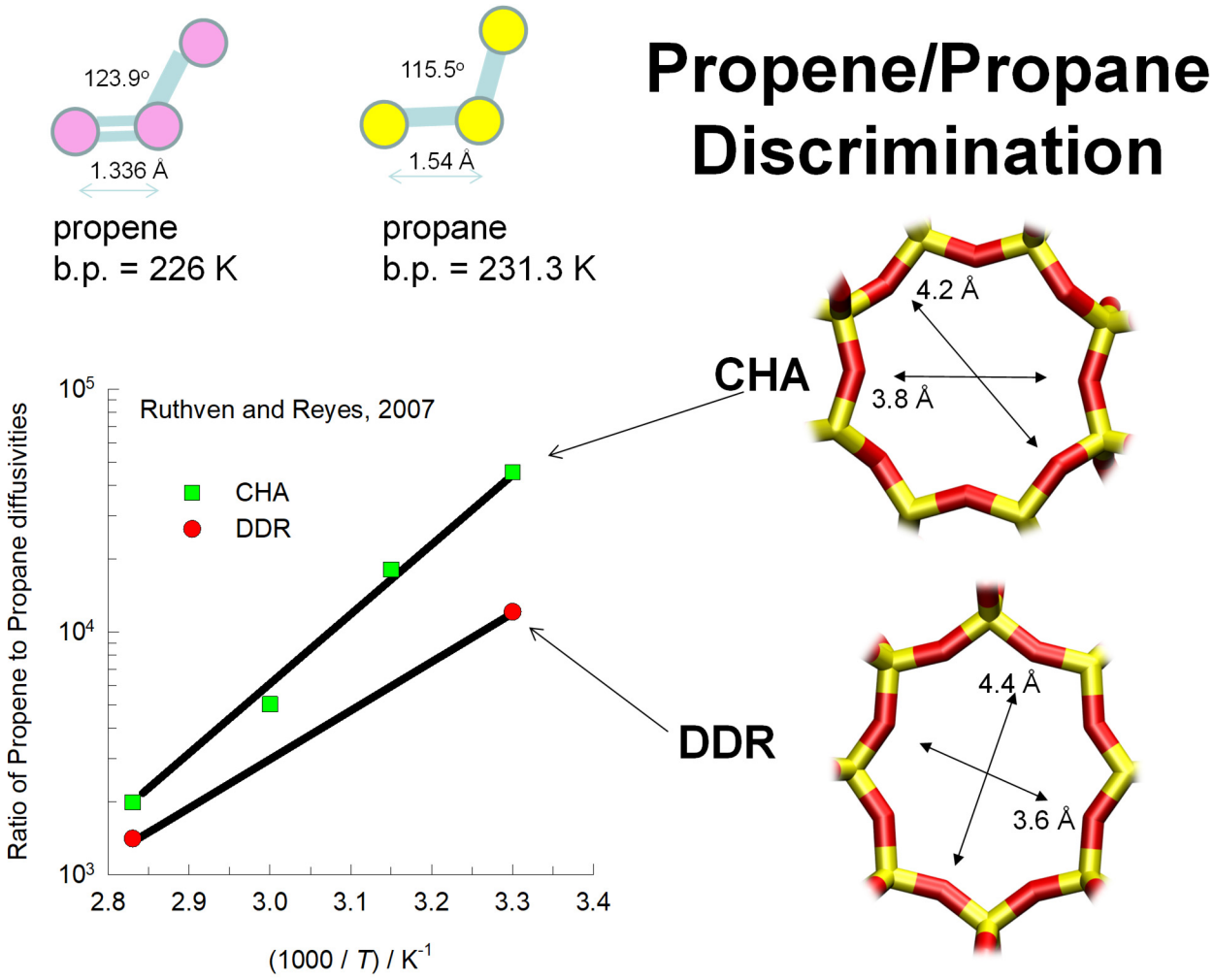

Figure S59. Data of Ruthven and Reyes[119] for the ratio of diffusivities of propene to that of propane in all-silica CHA and DDR zeolites.

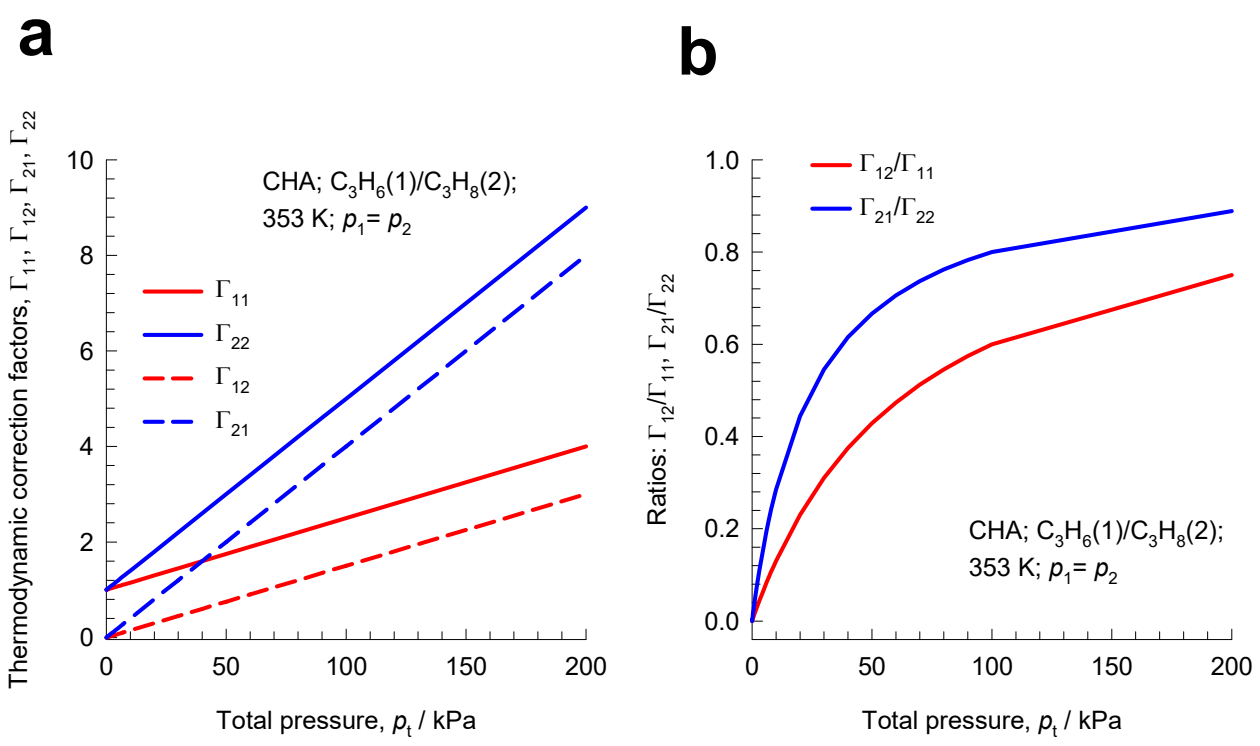

Figure S60. (a) Calculations of the elements of the matrix of thermodynamic factors for 50/50 $C_3H_6(1)/C_3H_8(2)$ mixture adsorption within crystals of all-silica CHA at 353 K (b) Ratios of the off-diagonal elements to the diagonal elements of the matrix of thermodynamic factors.

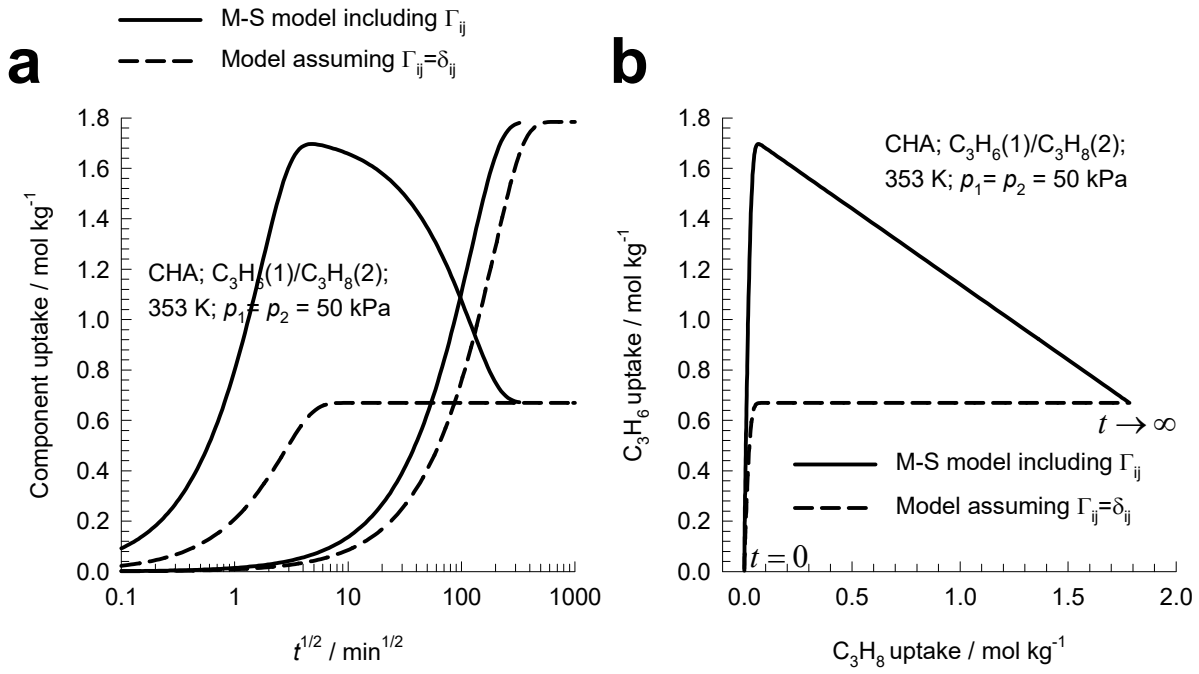

Figure S61. (a) Simulations of transient uptake of 50/50 $C_3H_6(1)/C_3H_8(2)$ mixtures within crystals of all-silica CHA at 353 K, and total pressure of 100 kPa. The solid black lines are simulations based on eq (S10), the dashed black lines are simulations based on eq (S11), in which the thermodynamic correction factors are assumed to be described by $\Gamma_{ij} = \delta_{ij}$. (b) Equilibration trajectories. The unary isotherms and diffusivity data are provided in Table S13.

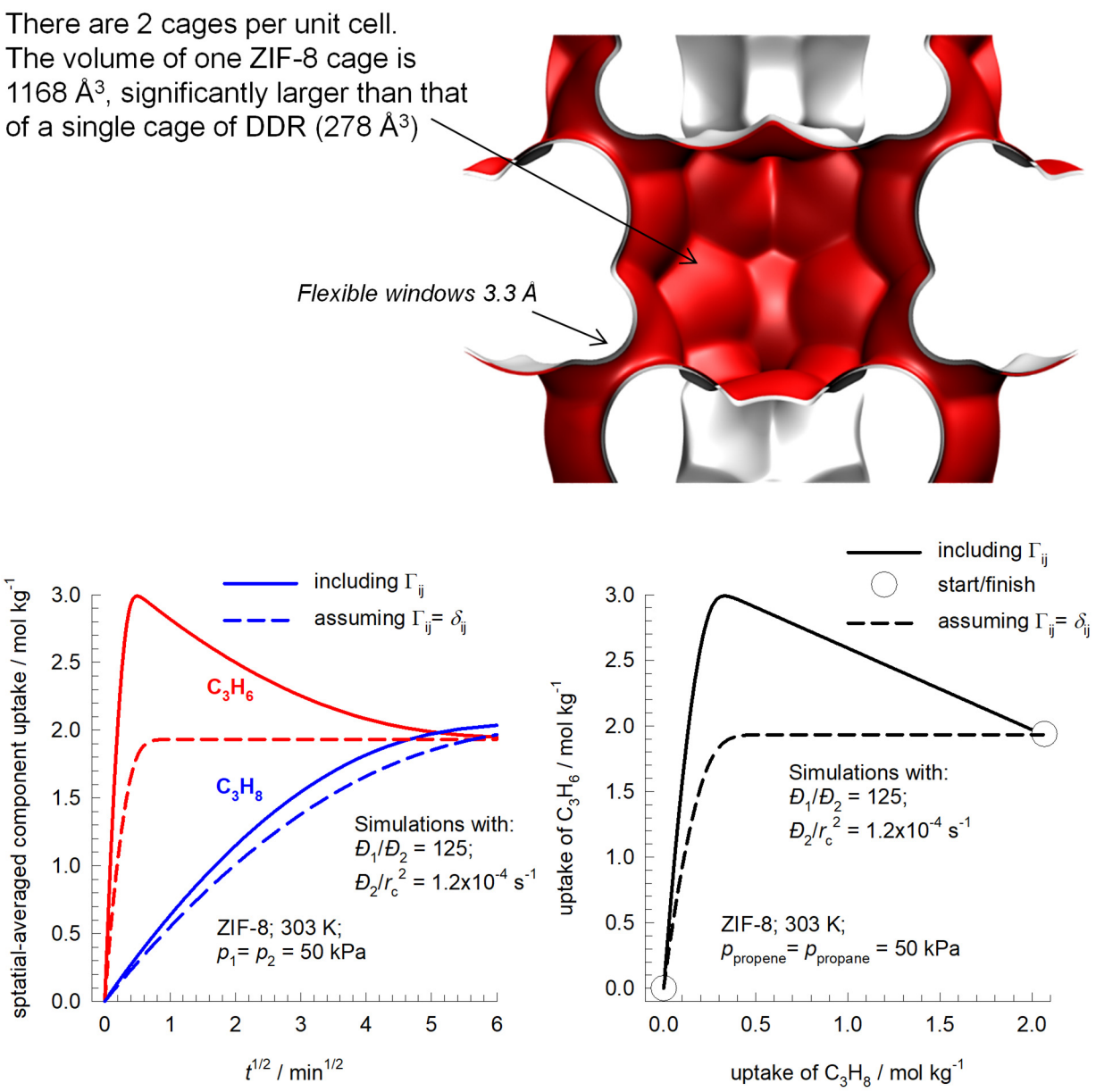

Figure S62. Simulations of transient uptake of C_3H_6(1)/C_3H_8(2) mixtures within crystals of ZIF-8 at 303 K. The simulations use the isotherm parameters specified in Table S14, along with $Đ_1/r_c^2$ = 1.5×10^{-2} s^{-1}; $Đ_2/r_c^2$ = 1.2×10^{-4} s^{-1}; $Đ_1/Đ_2$ = 125; ratio of single-site Langmuir parameter b_2/b_1 = 1.07. The black lines are simulations based on eq (S10), the blue lines are simulations based on eq (S11), in which the thermodynamic correction factors are assumed to be described by $\Gamma_{ij} = \delta_{ij}$.

11 Synergistic separation of C_3H_4/C_3H_6 mixtures

The selective capture of propyne from propene is important in the context of preparing polymer-grade propene feedstocks. Jiang et al.[124] report the efficacy of SIFSIX-Cu-TPA (also named as ZNU-2-Si) for this separation task. A particularly interesting feature is that this MOF is that the separations display synergism between adsorption and diffusion. To highlight this synergism Figure S63a compares the experimental data for transient breakthroughs for separation of 10/90 C_3H_4/C_3H_6 mixtures in a fixed bed adsorber packed with SIFSIX-Cu-TPA (also named as ZNU-2-Si), with transient breakthrough simulations in which the intra-crystalline diffusional influences are ignored. We note that the experimental data displays superior separations in terms of productivities of purified C_3H_6 as compared to simulations ignoring diffusional influences.

Jiang et al.[124] provide evidence to show that adsorption-diffusion synergy is the reason for the superior separations with SIFSIX-Cu-TPA. In order to demonstrate this adsorption-diffusion synergy, Figure S63b presents a comparison to two sets of simulations of transient breakthroughs. The continuous solid black lines are the transient breakthrough simulations in which the intra-crystalline diffusional influences are ignored. The continuous red lines are the simulations including intra-crystalline diffusional influences, taking $Đ_1/Đ_2 = 10; Đ_1/r_c^2 = 2.5\times10^{-3}$ s^{-1}; $Đ_2/r_c^2 = 2.5\times10^{-4}$ s^{-1}. In this case, both adsorption and diffusion favor the selective capture of C_3H_4. During the early stages of the transience, a larger amount of purified C_3H_6 is recoverable. This is also demonstrated in the experiments reported by Jiang et al.[124] Our simulations including synergistic diffusional influences are in qualitative agreement with the experimental breakthroughs. If the fixed bed adsorber is allowed to equilibrate, both simulations shown in Figure S63b will result in the same component loadings in the adsorbed phase. The component loadings remaining in the adsorbent are C_3H_4 = 4.26 mol kg^{-1}, C_3H_6 = 2.38 mol kg^{-1}. The corresponding loadings calculated from IAST for the feed mixture are: C_3H_4 = 4.39

mol kg^{-1}, C_3H_6 = 2.4 mol kg^{-1}. The differences in the breakthrough characteristics influences the productivity of purified C_3H_6 that is recovered prior to bed equilibration.

11.1 List of Tables for Synergistic separation of C3H4/C3H6 mixtures

Table S15. Dual-site Langmuir-Freundlich fits for C_3H_4, and C_3H_6 in SIFSIX-Cu-TPA (=ZNU-2-Si).

$$q = \frac{q_{sat,A} b_A p^{\nu A}}{1 + b_A p^{\nu A}} + \frac{q_{sat,B} b_B p^{\nu B}}{1 + b_B p^{\nu B}}; \quad b_A = b_{A0} \exp\left(\frac{E_A}{RT}\right); \quad b_b = b_{B0} \exp\left(\frac{E_B}{RT}\right)$$

	Site A				Site B			
	$\frac{q_{A.sat}}{\text{mol kg}^{-1}}$	$\frac{b_{A,0}}{\text{Pa}^{-\nu_A}}$	$\frac{E_A}{\text{kJ mol}^{-1}}$	ν_A	$\frac{q_{B.sat}}{\text{mol kg}^{-1}}$	$\frac{b_{B,0}}{\text{Pa}^{-\nu_B}}$	$\frac{E_B}{\text{kJ mol}^{-1}}$	ν_B
C_3H_4	6.42	6.614E-14	55.4	1.28	2.8	4.036E-13	44	1
C_3H_6	5.2	4.575E-13	44.3	1.26	1.65	2.132E-15	54.2	1

11.2 List of Figures for Synergistic separation of C3H4/C3H6 mixtures

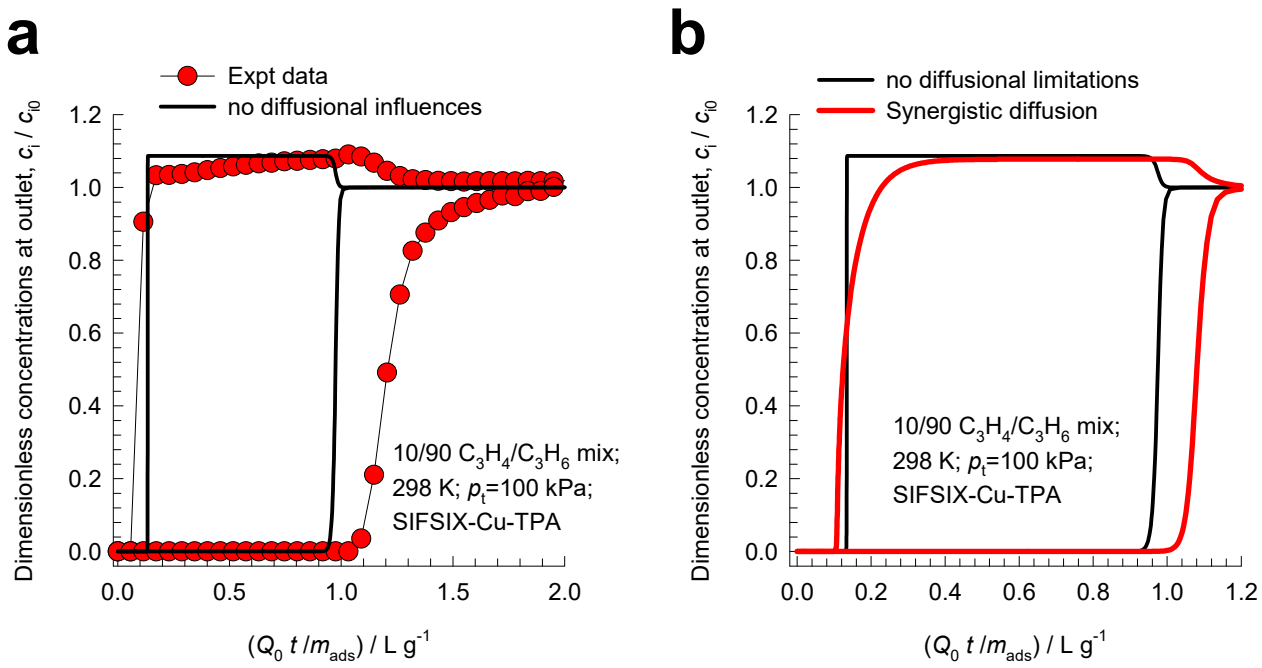

Figure S63. (a, b) Experimental data for transient breakthroughs for separation of 10/90 C_3H_4/C_3H_6 mixtures in a fixed bed adsorber packed with SIFSIX-Cu-TPA (also named as ZNU-2-Si), operating at a temperature of 298 K and at a total pressure of 100 kPa. The continuous solid black lines are the transient breakthrough simulations in which the intra-crystalline diffusional influences are ignored. The continuous red lines are the simulations including intra-crystalline diffusional influences, taking $Đ_1/Đ_2=10; Đ_1/r_c^2=2.5\times10^{-3}$ s^{-1}; $Đ_2/r_c^2=2.5\times10^{-4}$ s^{-1}. The unary isotherm data are provided in Table S15.

12 Uphill diffusion of mixtures of aromatics in H-ZSM-5

The experimental data of Niessen and Karge[125, 126] for transient uptake of benzene(1)/ethylbenzene(2), and benzene(1)/*p*-xylene(2) mixtures in H-ZSM-5 show overshoots in the benzene uptake; see Figure S64a,b. The detailed analysis of these data is available in our previous publication.[6]

12.1 List of Figures for Uphill diffusion of mixtures of aromatics in H-ZSM-5

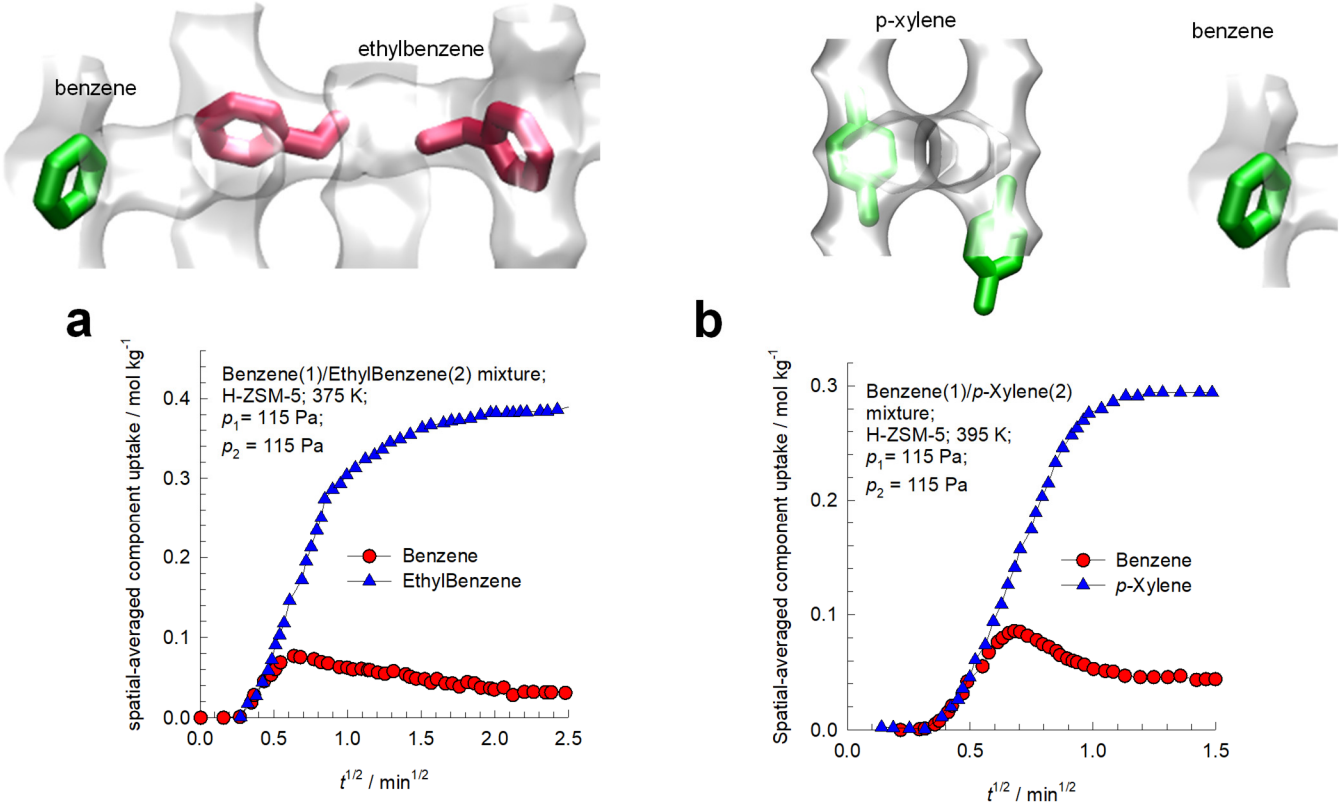

Figure S64. Experimental data of Niessen and Karge[125, 126] for uptake of (a) benzene(1)/ethylbenzene(2) and (b) benzene(1)/*p*-xylene(2) mixtures in H-ZSM-5.

13 Nomenclature

Latin alphabet

b_i	Langmuir parameter, Pa^{-1}
$[B]$	matrix of inverse M-S coefficients, m^{-2} s
c_i	molar concentration of species *i*, mol m^{-3}
c_t	total molar concentration in mixture, mol m^{-3}
c_{i0}	molar concentration of species *i* in fluid mixture at inlet to adsorber, mol m^{-3}
$Đ_i$	Maxwell-Stefan diffusivity for molecule-wall interaction, m^2 s^{-1}
$Đ_{ij}$	M-S exchange coefficient for *n*-component mixture, m^2 s^{-1}
$Đ_{12}$	M-S exchange coefficient for binary mixture, m^2 s^{-1}
$[D]$	Fick diffusivity matrix, m^2 s^{-1}
f_i	partial fugacity of species *i*, Pa
m_{ads}	mass of adsorbent packed in fixed bed, kg
n	number of species in the mixture, dimensionless
L	length of packed bed adsorber, m
N_i	molar flux of species *i* with respect to framework, mol m^{-2} s^{-1}
p_i	partial pressure of species *i* in mixture, Pa
p_t	total system pressure, Pa
q_i	component molar loading of species *i*, mol kg^{-1}
$q_{i,sat}$	molar loading of species *i* at saturation, mol kg^{-1}
q_t	total molar loading in mixture, mol kg^{-1}
$\bar{q}_i(t)$	radial-averaged component loading of species *i*, mol kg^{-1}
Q_0	volumetric flow rate of gas mixture entering fixed bed, m^3 s^{-1}
r	radial direction coordinate, m

r_c radius of crystallite, m

R gas constant, 8.314 J mol^{-1} K^{-1}

t time, s

T absolute temperature, K

u_i velocity of motion of adsorbate species *i* with respect to the framework material, m s^{-1}

u superficial gas velocity in packed bed, m s^{-1}

v interstitial gas velocity in packed bed, m s^{-1}

x_i mole fraction of species *i* in adsorbed phase, dimensionless

z distance along the adsorber, m

Greek alphabet

Γ_{ij} thermodynamic factors, dimensionless

$[\Gamma]$ matrix of thermodynamic factors, dimensionless

δ_{ij} Kronecker delta, dimensionless

ε voidage of packed bed, dimensionless

λ_i eigenvalues of Fick diffusivity matrix $[D]$, m^2 s^{-1}

θ_i fractional occupancy of component *i*, dimensionless

θ_t fractional occupancy of adsorbed mixture, dimensionless

θ_V fractional vacancy, dimensionless

$[\Lambda]$ matrix of Maxwell-Stefan diffusivities, m^2 s^{-1}

μ_i molar chemical potential, J mol^{-1}

ν Freundlich exponent, dimensionless

ρ framework density, kg m^{-3}

Subscripts

i	referring to component *i*
t	referring to total mixture
sat	referring to saturation conditions

14 References

(1) Krishna, R. Describing the Diffusion of Guest Molecules inside Porous Structures. *J. Phys. Chem. C* **2009**, *113*, 19756-19781. https://doi.org/10.1021/jp906879d.

(2) Krishna, R. Diffusion in Porous Crystalline Materials. *Chem. Soc. Rev.* **2012**, *41*, 3099-3118. https://doi.org/10.1039/C2CS15284C.

(3) Krishna, R. Using the Maxwell-Stefan formulation for Highlighting the Influence of Interspecies (1-2) Friction on Binary Mixture Permeation across Microporous and Polymeric Membranes. *J. Membr. Sci.* **2017**, *540*, 261-276. https://doi.org/10.1016/j.memsci.2017.06.062.

(4) Krishna, R. The Maxwell-Stefan Description of Mixture Diffusion in Nanoporous Crystalline Materials. *Microporous Mesoporous Mater.* **2014**, *185*, 30-50. https://doi.org/10.1016/j.micromeso.2013.10.026.

(5) Krishna, R.; van Baten, J. M. Maxwell-Stefan modeling of slowing-down effects in mixed gas permeation across porous membranes. *J. Membr. Sci.* **2011**, *383*, 289-300. https://doi.org/10.1016/j.memsci.2011.08.067.

(6) Krishna, R. Tracing the Origins of Transient Overshoots for Binary Mixture Diffusion in Microporous Crystalline Materials. *Phys. Chem. Chem. Phys.* **2016**, *18*, 15482-15495. https://doi.org/10.1039/C6CP00132G.

(7) Myers, A. L.; Prausnitz, J. M. Thermodynamics of Mixed Gas Adsorption. *A.I.Ch.E.J.* **1965**, *11*, 121-130.

(8) Krishna, R.; van Baten, J. M. Investigating the Influence of Diffusional Coupling on Mixture Permeation across Porous Membranes *J. Membr. Sci.* **2013**, *430*, 113-128.

(9) Krishna, R.; Baur, R. Modelling Issues in Zeolite Based Separation Processes. *Sep. Purif. Technol.* **2003**, *33*, 213-254.

(10) Krishna, R.; van Baten, J. M. Diffusion of alkane mixtures in zeolites. Validating the Maxwell-Stefan formulation using MD simulations. *J. Phys. Chem. B* **2005**, *109*, 6386-6396.

(11) Krishna, R.; van Baten, J. M. Influence of segregated adsorption on mixture diffusion in DDR zeolite. *Chem. Phys. Lett.* **2007**, *446*, 344-349.

(12) Krishna, R.; van Baten, J. M. Insights into diffusion of gases in zeolites gained from molecular dynamics simulations. *Microporous Mesoporous Mater.* **2008**, *109*, 91-108.

(13) Krishna, R.; van Baten, J. M. Segregation effects in adsorption of CO_2 containing mixtures and their consequences for separation selectivities in cage-type zeolites. *Sep. Purif. Technol.* **2008**, *61*, 414-423. https://doi.org/10.1016/j.seppur.2007.12.003.

(14) Krishna, R.; van Baten, J. M. Onsager coefficients for binary mixture diffusion in nanopores. *Chem. Eng. Sci.* **2008**, *63*, 3120-3140.

(15) Krishna, R.; van Baten, J. M. Describing Mixture Diffusion in Microporous Materials under Conditions of Pore Saturation. *J. Phys. Chem. C* **2010**, *114*, 11557-11563.

(16) Krishna, R.; van Baten, J. M. A molecular dynamics investigation of the diffusion characteristics of cavity-type zeolites with 8-ring windows. *Microporous Mesoporous Mater.* **2011**, *137*, 83-91. https://doi.org/10.1016/j.micromeso.2010.08.026.

(17) Habgood, H. W. The Kinetics of Molecular Sieve Action. Sorption of Nitrogen-Methane Mixtures by Linde Molecular Sieve 4A. *Canad. J. Chem.* **1958**, *36*, 1384-1397. https://doi.org/10.1139/v58-204.

(18) Ruthven, D. M.; Farooq, S.; Knaebel, K. S. *Pressure swing adsorption*. VCH Publishers: New York, 1994.

(19) Farooq, S.; Ruthven, D. M. Numerical-Simulation of a Kinetically Controlled Pressure Swing Adsorption Bulk Separation Process Based on a Diffusion-Model. *Chem. Eng. Sci.* **1991**, *46*, 2213-2224.

(20) Farooq, S.; Rathor, M. N.; Hidajat, K. A Predictive Model for a Kinetically Controlled Pressure Swing Adsorption Separation Process. *Chem. Eng. Sci.* **1993**, *48*, 4129-4141.

(21) Khalighi, M.; Chen, Y. F.; Farooq, S.; Karimi, I. A.; Jiang, J. W. Propylene/Propane Separation Using SiCHA. *Ind. Eng. Chem. Res.* **2013**, *52*, 3877-3892. https://doi.org/10.1021/ie3026955.

(22) Siperstein, F. R.; Myers, A. L. Mixed-Gas Adsorption. *A.I.Ch.E.J.* **2001**, *47*, 1141-1159.

(23) Streb, A.; Mazzotti, M. Adsorption for efficient low carbon hydrogen production: part 1—adsorption equilibrium and breakthrough studies for $H_2/CO_2/CH_4$ on zeolite 13X. *Adsorption* **2021**, *27*, 541-558. https://doi.org/10.1007/s10450-021-00306-y.

(24) Krishna, R.; Van Baten, J. M. Using Molecular Simulations to Unravel the Benefits of Characterizing Mixture Permeation in Microporous Membranes in Terms of the Spreading Pressure. *ACS Omega* **2020**, *5*, 32769−32780. https://dx.doi.org/10.1021/acsomega.0c05269.

(25) Krishna, R.; Van Baten, J. M. Elucidation of Selectivity Reversals for Binary Mixture Adsorption in Microporous Adsorbents. *ACS Omega* **2020**, *5*, 9031-9040. https://doi.org/10.1021/acsomega.0c01051.

(26) Krishna, R.; Van Baten, J. M. Using Molecular Simulations for Elucidation of Thermodynamic Non-Idealities in Adsorption of CO_2-containing Mixtures in NaX Zeolite. *ACS Omega* **2020**, *5*, 20535-20542. https://doi.org/10.1021/acsomega.0c02730.

(27) Krishna, R.; Van Baten, J. M. Water/Alcohol Mixture Adsorption in Hydrophobic Materials: Enhanced Water Ingress caused by Hydrogen Bonding. *ACS Omega* **2020**, *5*, 28393-28402. https://doi.org/10.1021/acsomega.0c04491.

(28) Krishna, R.; Van Baten, J. M. Investigating the Non-idealities in Adsorption of CO_2-bearing Mixtures in Cation-exchanged Zeolites. *Sep. Purif. Technol.* **2018**, *206*, 208-217. https://doi.org/10.1016/j.seppur.2018.06.009.

(29) Kooijman, H. A.; Taylor, R. A dynamic nonequilibrium model of tray distillation columns. *A.I.Ch.E.J.* **1995**, *41*, 1852-1863.

(30) Michelsen, M. An efficient general purpose method of integration of stiff ordinary differential equations. *A.I.Ch.E.J.* **1976**, *22*, 594-597.

(31) Bulirsch, R.; Stoer, J. Numerical treatment of ordinary differential equations by extrapolation methods. *Numer. Math.* **1966**, *8*, 1-14.

(32) Krishna, R.; Baur, R. Diffusion, Adsorption and Reaction in Zeolites: Modelling and Numerical Issues. http://krishna.amsterchem.com/zeolite/, University of Amsterdam, Amsterdam, 1 January 2015.

(33) Krishna, R.; van Baten, J. M. Investigating the potential of MgMOF-74 membranes for CO_2 capture. *J. Membr. Sci.* **2011**, *377*, 249-260.

(34) He, Y.; Krishna, R.; Chen, B. Metal-Organic Frameworks with Potential for Energy-Efficient Adsorptive Separation of Light Hydrocarbons. *Energy Environ. Sci.* **2012**, *5*, 9107-9120.

(35) Geddes, R. L. Local efficiencies of bubble-plate fractionators. *Trans. Am. Inst. Chem. Engrs.* **1946**, *42*, 79-105.

(36) Taylor, R.; Krishna, R. *Multicomponent mass transfer*. John Wiley: New York, 1993.

(37) Krishna, R. Screening Metal-Organic Frameworks for Mixture Separations in Fixed-Bed Adsorbers using a Combined Selectivity/Capacity Metric. *RSC Adv.* **2017**, *7*, 35724-35737. https://doi.org/10.1039/C7RA07363A.

(38) Krishna, R. Methodologies for Evaluation of Metal-Organic Frameworks in Separation Applications. *RSC Adv.* **2015**, *5*, 52269-52295. https://doi.org/10.1039/C5RA07830J.

(39) Krishna, R. Metrics for Evaluation and Screening of Metal-Organic Frameworks for Applications in Mixture Separations. *ACS Omega* **2020**, *5*, 16987−17004. https://doi.org/10.1021/acsomega.0c02218.

(40) Herm, Z. R.; Wiers, B. M.; Van Baten, J. M.; Hudson, M. R.; Zajdel, P.; Brown, C. M.; Maschiocchi, N.; Krishna, R.; Long, J. R. Separation of Hexane Isomers in a Metal-Organic Framework with Triangular Channels *Science* **2013**, *340*, 960-964. https://www.science.org/doi/10.1126/science.1234071.

(41) Krishna, R.; van Baten, J. M. Screening of zeolite adsorbents for separation of hexane isomers: A molecular simulation study. *Sep. Purif. Technol.* **2007**, *55*, 246-255. https://doi.org/10.1016/j.seppur.2006.12.011.

(42) Dubbeldam, D.; Krishna, R.; Calero, S.; Yazaydın, A. Ö. Computer-Assisted Screening of Ordered Crystalline Nanoporous Adsorbents for Separation of Alkane Isomers. *Angew. Chem. Int. Ed.* **2012**, *51*, 11867-11871. https://doi.org/10.1002/anie.201205040.

(43) Dandekar, H. W.; Funk, G. A.; Gillespie, R. D.; Zinnen, H. A.; McGonegal, C. P.; Kojima, M.; Hobbs, S. H., Process for alkane isomerization using reactive chromatography. UOP, Des Plaines, Illinois, USA., *U.S. Pat.*, US 5763730, 1999.

(44) Dandekar, H. W.; Funk, G. A.; Zinnen, H. A., Process for separating and recovering multimethyl-branched alkanes. UOP LLC, Des Plaines, Illinois, USA., *U.S. Pat.*, US 6069289, 2000.

(45) Carr, R. W.; Dandekar, H. W. *Adsorption with reaction*. Reactive Separation Processes; 2nd, Edited by S. Kulprathipanja, 115-154, Taylor & Francis: New York, USA, 2001.(

(46) Krishna, R.; Smit, B.; Calero, S. Entropy effects during sorption of alkanes in zeolites. *Chem. Soc. Rev.* **2002**, *31*, 185-194.

(47) Vlugt, T. J. H.; Zhu, W.; Kapteijn, F.; Moulijn, J. A.; Smit, B.; Krishna, R. Adsorption of linear and branched alkanes in the silicalite-1. *J. Am. Chem. Soc.* **1998**, *120*, 5599-5600.

(48) Vlugt, T. J. H.; Krishna, R.; Smit, B. Molecular Simulations of Adsorption Isotherms for Linear and Branched Alkanes and Their Mixtures in Silicalite. *J. Phys. Chem. B* **1999**, *103*, 1102-1118.

(49) Schenk, M.; Vidal, S. L.; Vlugt, T. J. H.; Smit, B.; Krishna, R. Separation of alkane isomers by exploiting entropy effects during adsorption on silicalite-1: A configurational-bias Monte Carlo simulation study. *Langmuir* **2001**, *17*, 1558-1570.

(50) Titze, T.; Chmelik, C.; Kärger, J.; van Baten, J. M.; Krishna, R. Uncommon Synergy Between Adsorption and Diffusion of Hexane Isomer Mixtures in MFI Zeolite Induced by Configurational Entropy Effects *J. Phys. Chem. C* **2014**, *118*, 2660-2665. https://doi.org/10.1021/jp412526t.

(51) Krishna, R. Highlighting the Influence of Thermodynamic Coupling on Kinetic Separations with Microporous Crystalline Materials. *ACS Omega* **2019**, *4*, 3409-3419. https://doi.org/10.1021/acsomega.8b03480.

(52) Schuring, D.; Jansen, A. P. J.; van Santen, R. A. Concentration and chainlength dependence of the diffusivity of alkanes in zeolites studied with MD simulations. *J. Phys. Chem. B* **2000**, *104*, 941-948.

(53) Krishna, R.; van Baten, J. M. Diffusion of Hydrocarbon Mixtures in MFI Zeolite: Influence of Intersection Blocking. *Chem. Eng. J.* **2008**, *140*, 614-620.

(54) Cavalcante, C. L.; Ruthven, D. M. Adsorption of Branched and Cyclic Paraffins in Silicalite .2. Kinetics. *Ind. Eng. Chem. Res.* **1995**, *34*, 185-191.

(55) Jolimaître, E.; Tayakout-Fayolle, M.; Jallut, C.; Ragil, K. Determination of mass transfer and thermodynamic properties of branched paraffins in silicalite by inverse chromatography technique. *Ind. Eng. Chem. Res.* **2001**, *40*, 914-926.

(56) Krishna, R.; van Baten, J. M. In silico screening of metal-organic frameworks in separation applications. *Phys. Chem. Chem. Phys.* **2011**, *13*, 10593-10616. https://doi.org/10.1039/C1CP20282K.

(57) Krishna, R. Maxwell-Stefan Modelling of Mixture Desorption Kinetics in Microporous Crystalline Materials. *Sep. Purif. Technol.* **2019**, *229*, 115790. https://doi.org/10.1016/j.seppur.2019.115790.

(58) Calero, S.; Smit, B.; Krishna, R. Configurational entropy effects during sorption of hexane isomers in silicalite. *J. Catal.* **2001**, *202*, 395-401.

(59) Krishna, R.; van Baten, J. M. Entropy-based Separation of Linear Chain Molecules by Exploiting Differences in the Saturation Capacities in Cage-type Zeolites. *Sep. Purif. Technol.* **2011**, *76*, 325-330. https://doi.org/10.1016/j.seppur.2010.10.023.

(60) Remy, T.; Saint-Remi, J. C.; Singh, R.; Webley, P. A.; Baron, G. V.; Denayer, J. F. M. Adsorption and Separation of C1-C8 Alcohols on SAPO-34. *J. Phys. Chem. C* **2011**, *115*, 8117-8125.

(61) Saint-Remi, J. C.; Baron, G. V.; Denayer, J. F. M. Non-Uniform Chain Length Dependent Diffusion of Short 1-Alcohols in SAPO-34 in Liquid Phase. *J. Phys. Chem. C* **2013**, *117*, 9758-9765.

(62) Matsuda, R.; Kitaura, R.; Kitagawa, S.; Kubota, Y.; Belosludov, R. V.; Kobayashi, T. C.; Sakamoto, H.; Chiba, T.; Takata, M.; Kawazoe, Y.; Mita, Y. Highly controlled acetylene accommodation in a metal–organic microporous material. *Nature* **2005**, *436*, 238-241.

(63) Fischer, M.; Hoffmann, F.; Fröba, M. New Microporous Materials for Acetylene Storage and C_2H_2/CO_2 Separation: Insights from Molecular Simulations. *ChemPhysChem* **2010**, *11*, 2220-2229.

(64) Li, P.; He, Y.; Zhao, Y.; Weng, L.; Wang, H.; Krishna, R.; Wu, H.; Zhou, W.; O'Keeffe, M.; Han, Y.; Chen, B. A Rod-Packing Microporous Hydrogen-Bonded Organic Framework for Highly Selective Separation of C_2H_2/CO_2 at Room Temperature. *Angew. Chem. Int. Ed.* **2015**, *54*, 574-577.

(65) Chen, K.-J.; Scott, H. S.; Madden, D. G.; Pham, T.; Kumar, A.; Bajpai, A.; Lusi, M.; Forrest, K. A.; Space, B.; Perry IV, J. J.; Zaworotko, M. J. Benchmark C_2H_2/CO_2 and CO_2/C_2H_2 Separation by Two Closely Related Hybrid Ultramicroporous Materials. *Chem* **2016**, *1*, 753-765. https://dx.doi.org/10.1016/j.chempr.2016.10.009.

(66) Jiang, M.; Cui, X.; Yang, L.; Yang, Q.; Zhang, Z.; Yang, Y.; Xing, H. A thermostable anion-pillared metal-organic framework for C_2H_2/C_2H_4 and C_2H_2/CO_2 separations. *Chem. Eng. J.* **2018**, *352*, 803-810. https://doi.org/10.1016/j.cej.2018.07.104.

(67) Luo, F.; Yan, C.; Dang, L.; Krishna, R.; Zhou, W.; Wu, H.; Dong, X.; Han, Y.; Hu, T.-L.; O'Keeffe, M.; Wang, L.; Luo, M.; Lin, R.-B.; Chen, B. UTSA-74: A MOF-74 Isomer with Two Accessible Binding Sites per Metal Center for Highly Selective Gas Separation. *J. Am. Chem. Soc.* **2016**, *138*, 5678-5684.

(68) Ye, Y.; Ma, Z.; Lin, R.-B.; Krishna, R.; Zhou, W.; Lin, Q.; Zhang, Z.; Xiang, S.; Chen, B. Pore Space Partition within a Metal-Organic Framework for Highly Efficient C_2H_2/CO_2 Separation. *J. Am. Chem. Soc.* **2019**, *141*, 4130-4136. https://doi.org/10.1021/jacs.9b00232.

(69) Gao, J.; Qian, X.; Lin, R.-B.; Krishna, R.; Wu, H.; Zhou, W.; Chen, B. Mixed Metal-Organic Framework with Multiple Binding Sites for Efficient C_2H_2/CO_2 Separation. *Angew. Chem. Int. Ed.* **2020**, *59*, 4396-4400. https://doi.org/10.1002/anie.202000323.

(70) Zhang, Y.; Hu, J.; Krishna, R.; Wang, L.; Yang, L.; Cui, X.; Duttwyler, S.; Xing, H. Rational design of microporous MOFs with anionic boron cluster functionality and cooperative dihydrogen binding sites for highly selective capture of acetylene. *Angew. Chem. Int. Ed.* **2020**, *59*, 17664-17669. https://doi.org/10.1002/anie.202007681.

(71) Yang, L.; Yan, L.; Wang, Y.; Liu, Z.; He, J.; Fu, Q.; Liu, D.; Gu, X.; Dai, P.; Li, L.; Zhao, X. Adsorption Site Selective Occupation Strategy within a Metal–Organic Framework for Highly Efficient Sieving Acetylene from Carbon Dioxide. *Angew. Chem. Int. Ed.* **2021**, *60*, 4580-4574. https://doi.org/10.1002/anie.202013965.

(72) Wang, L.; Sun, W.; Zhang, Y.; Xu, N.; Krishna, R.; Hu, J.; Jiang, Y.; He, Y.; Xing, H. Interpenetration symmetry control within ultramicroporous robust boron cluster hybrid MOFs for benchmark purification of acetylene from carbon dioxide. *Angew. Chem. Int. Ed.* **2021**, *xx*, xx. https://doi.org/10.1002/anie.202107963.

(73) Zhang, L.; Jiang, K.; Yang, L.; Li, L.; Hu, E.; Yang, L.; Shao, K.; Xing, H.; Cui, Y.; Yang, Y.; Li, B.; Chen, B.; Qian, G. Benchmark C_2H_2/CO_2 Separation in an Ultramicroporous Metal–Organic Framework via Copper(I)-Alkynyl Chemistry. *Angew. Chem. Int. Ed.* **2021**, *60*, 15995-16002. https://doi.org/10.1002/anie.202102810.

(74) Cui, J.; Qiu, Z.; Yang, L.; Zhang, Z.; Cui, X.; Xing, H. Kinetic-Sieving of Carbon Dioxide from Acetylene through a Novel Sulfonic Ultramicroporous Material. *Angew. Chem. Int. Ed.* **2022**, *61*, e202208756. https://doi.org/10.1002/anie.202208756.

(75) Zhang, Z.; Peh, S. B.; Krishna, R.; Kang, C.; Chai, K.; Wang, Y.; Shi, D.; Zhao, D. Optimal Pore Chemistry in An Ultramicroporous Metal-Organic Framework for Benchmark Inverse CO_2/C_2H_2 Separation. *Angew. Chem. Int. Ed.* **2021**, *60*, 17198–17204. https://doi.org/10.1002/anie.202106769.

(76) He, C.; Zhang, P.; Wang, Y.; Zhang, Y.; Hu, T.; Li, L.; Li, J. Thermodynamic and kinetic synergetic separation of CO_2/C_2H_2 in an ultramicroporous metal-organic framework. *Sep. Purif. Technol.* **2023**, *304*, 122318. https://doi.org/10.1016/j.seppur.2022.122318.

(77) Binder, T.; Lauerer, A.; Chmelik, C.; Haase, J.; Kärger, J.; Ruthven, D. M. Micro-imaging of transient intracrystalline concentration profiles during two-component uptake of light hydrocarbon - carbon dioxide mixtures by DDR-type zeolites. *Ind. Eng. Chem. Res.* **2015**, *54*, 8997-9004. https://doi.org/10.1021/acs.iecr.5b02163.

(78) Lauerer, A.; Binder, T.; Chmelik, C.; Miersemann, E.; Haase, J.; Ruthven, D. M.; Kärger, J. Uphill Diffusion and Overshooting in the Adsorption of Binary Mixtures in Nanoporous Solids. *Nat. Commun.* **2015**, *6*, 7697. http://dx.doi.org/doi:10.1038/ncomms8697.

(79) Binder, T. *Mass Transport in Nanoporous Materials: New Insights from Micro-Imaging by Interference Microscopy*. Ph.D. Dissertation, Universität Leipzig, Leipzig, 2013.

(80) Krishna, R. Diffusing Uphill with James Clerk Maxwell and Josef Stefan. *Chem. Eng. Sci.* **2019**, *195*, 851-880. https://doi.org/10.1016/j.ces.2018.10.032.

(81) Lastari, F.; Pareek, V.; Trebble, M.; Tade, M. O.; Chinn, D.; Tsai, N. C.; Chan, K. I. Extractive Distillation for CO_2–Ethane Azeotrope Separation. *Chem. Eng. Process.* **2012**, *52*, 155-161. https://doi.org/10.1016/j.cep.2011.10.001.

(82) Ribeiro, C. P.; Freeman, B. D.; Paul, D. R. Pure- and Mixed-Gas Carbon Dioxide/Ethane Permeability and Diffusivity in a Cross-linked Poly(ethylene oxide) Copolymer. *J. Membr. Sci.* **2011**, *377*, 110-123.

(83) Krishna, R. Describing Mixture Permeation across Polymeric Membranes by a Combination of Maxwell-Stefan and Flory-Huggins Models. *Polymer* **2016**, *103*, 124-131.

(84) Krishna, R.; van Baten, J. M. Using the Spreading Pressure to Inter-Relate the Characteristics of Unary, Binary and Ternary Mixture Permeation across Microporous Membranes. *J. Membr. Sci.* **2022**, *643*, 120049. https://doi.org/10.1016/j.memsci.2021.120049.

(85) Lin, R.-B.; Li, L.; Zhou, H.-L.; Wu, H.; He, C.; Li, S.; Krishna, R.; Li, J.; Zhou, W.; Chen, B. Molecular Sieving of Ethylene from Ethane using a Rigid Metal-Organic Framework. *Nature Materials* **2018**, *17*, 1128-1133. http://dx.doi.org/10.1038/s41563-018-0206-2.

(86) Bhadra, S. J.; Farooq, S. Separation of Methane Nitrogen Mixture by Pressure Swing Adsorption for Natural Gas Upgrading. *Ind. Eng. Chem. Res.* **2011**, *50*, 14030-14045.

(87) Tagliabue, M.; Farrusseng, D.; Valencia, S.; Aguado, S.; Ravon, U.; Rizzo, C.; Corma, A.; Mirodatos, C. Natural gas treating by selective adsorption: Material science and chemical engineering interplay. *Chem. Eng. J.* **2009**, *155*, 553-566.

(88) Majumdar, B.; Bhadra, S. J.; Marathe, R. P.; Farooq, S. Adsorption and Diffusion of Methane and Nitrogen in Barium Exchanged ETS-4. *Ind. Eng. Chem. Res.* **2011**, *50*, 3021-3034. https://doi.org/10.1021/ie1014124.

(89) Wilkins, N. S.; Sawada, J. A.; Rajendran, A. Diffusion of CH_4 and N_2 in Barium-Exchanged Reduced Pore Zorite (Ba-RPZ) and Zeolite 4A. *Ind. Eng. Chem. Res.* **2021**, *60*, 10777-10790. https://doi.org/10.1021/acs.iecr.1c01714.

(90) Jayaraman, A.; Hernandez-Maldonado, A. J.; Yang, R. T.; Chinn, D.; Munson, C. L.; Mohr, D. H. Clinoptilolites for Nitrogen/Methane Separation. *Chem. Eng. Sci.* **2004**, *59*, 2407-2417.

(91) Yang, R. T. *Adsorbents: Fundamentals and Applications*. John Wiley & Sons, Inc.: Hoboken, New Jersey, 2003.

(92) Bhadra, S. J. *Methane-Nitrogen Separation by Pressure Swing Adsorption*. Ph.D. Dissertation, National University of Singapore, Singapore, 2007.

(93) Farooq, S.; Ruthven, D. M.; Boniface, H. A. Numerical-Simulation of a Pressure Swing Adsorption Oxygen Unit. *Chem. Eng. Sci.* **1989**, *44*, 2809-2816.

(94) Rama Rao, V.; Farooq, S.; Krantz, W. B. Design of a Two-Step Pulsed Pressure-Swing Adsorption-Based Oxygen Concentrator. *A.I.Ch.E.J.* **2010**, *56*, 354-370.

(95) Rama Rao, V. *Adsorption based portable oxygen concentrator for personal medical applications*. Ph.D. Dissertation, National University of Singapore, Singapore, 2011.

(96) Sircar, S.; Myers, A. L. *Gas Separation by Zeolites, Chapter 22*. Handbook of Zeolite Science and Technology; Edited by S.M. Auerbach, K.A. Carrado and P.K. Dutta, 1063-1104, Marcel Dekker: New York, 2003.(

(97) Ritter, J. A. Development of Pressure Swing Adsorption Technology for Spaceflight Oxygen Concentrators. http://www.dsls.usra.edu/meetings/hrp2010/pdf/Friday/Ritter.pdf, NASA Human Research Program, Houston, 2010.

(98) Ruthven, D. M.; Farooq, S. Air Separation by Pressure Swing Adsorption. *Gas Sep. Purif.* **1990**, *4*, 141-148.

(99) Yang, R. T. *Gas separation by adsorption processes*. Butterworth: Boston, 1987.

(100) Farooq, S. Sorption and Diffusion of Oxygen and Nitrogen in Molecular- Sieve RS-10. *Gas Sep. Purif.* **1995**, *9*, 205-212.

(101) Bloch, E. D.; Queen, W. L.; Krishna, R.; Zadrozny, J. M.; Brown, C. M.; Long, J. R. Hydrocarbon Separations in a Metal-Organic Framework with Open Iron(II) Coordination Sites. *Science* **2012**, *335*, 1606-1610. https://doi.org/10.1126/science.1217544.

(102) Cadiau, A.; Adil, K.; Bhatt, P. M.; Belmabkhout, Y.; Eddaoudi, M. A Metal-Organic Framework–Based Splitter for Separating Propylene from Propane. *Science* **2016**, *353*, 137-140. https://doi.org/10.1126/science.aaf6323.

(103) Yang, H.; Wang, Y.; Krishna, R.; Jia, X.; Wang, Y.; Hong, A. N.; Dang, C.; Castillo, H. E.; Bu, X.; Feng, P. Pore-Space-Partition-Enabled Exceptional Ethane Uptake and Ethane-Selective Ethane−Ethylene Separation. *J. Am. Chem. Soc.* **2020**, *142*, 2222-2227. https://doi.org/10.1021/jacs.9b12924.

(104) Bao, Z.; Wang, J.; Zhang, Z.; Xing, H.; Yang, Q.; Yang, Y.; Wu, H.; Krishna, R.; Zhou, W.; Chen, B.; Ren, Q. Molecular Sieving of Ethane from Ethylene through the molecular Cross-section Size Differentiation in Gallate-based Metal-Organic Frameworks. *Angew. Chem. Int. Ed.* **2018**, *57*, 16020-16025. https://doi.org/10.1002/anie.201808716.

(105) Li, L.; Lin, R.-B.; Krishna, R.; Li, H.; Xiang, S.; Wu, H.; Li, J.; Zhou, W.; Chen, B. Ethane/ethylene Separation in a Metal-Organic Framework with Iron-Peroxo Sites. *Science* **2018**, *362*, 443-446. https://doi.org/10.1126/science.aat0586.

(106) Zhang, X.; Li, L.; Wang, J.-X.; Wen, H.-M.; Krishna, R.; Wu, H.; Zhou, W.; Chen, Z.-N.; Li, B.; Qian, G.; Chen, B. Selective Ethane/Ethylene Separation in a Robust Microporous Hydrogen-Bonded Organic Framework. *J. Am. Chem. Soc.* **2020**, *142*, 633-640. https://doi.org/10.1021/jacs.9b07807.

(107) Da Silva, F. A.; Rodrigues, A. E. Vacuum swing adsorption for propylene/propane separation with 4A zeolite. *Ind. Eng. Chem. Res.* **2001**, *40*, 5758-5774.

(108) Grande, C. A.; Poplow, F.; Rodrigues, A. E. Vacuum pressure swing adsorption to produce polymer-grade polypropylene. *Separ. Sci. Technol.* **2010**, *45*, 1252-1259.

(109) Divekar, S.; Nanoti, A.; Dasgupta, S.; Aarti; Chauhan, R.; Gupta, P.; Garg, M. O.; Singh, S. P.; Mishra, I. M. Adsorption Equilibria of Propylene and Propane on Zeolites and Prediction of Their Binary Adsorption with the Ideal Adsorbed Solution Theory. *J. Chem. Eng. Data* **2016**, *61*, 2629-2637.

(110) Da Silva, F. A.; Rodrigues, A. E. PropylenePropane Separation by Vacuum Swing Adsorption Using 13X Zeolite. *A.I.Ch.E.J.* **2001**, *47*, 341-357.

(111) Geier, S. J.; Mason, J. A.; Bloch, E. D.; Queen, W. L.; Hudson, M. R.; Brown, C. M.; Long, J. R. Selective adsorption of ethylene over ethane and propylene over propane in the metal–organic frameworks M_2(dobdc) (M = Mg, Mn, Fe, Co, Ni, Zn). *Chem. Sci.* **2013**, *4*, 2054-2061.

(112) Bachman, J. E.; Reed, D. A.; Kapelewski, M. T.; Chachra, G.; Jonnavittula, D.; Radaelli, G.; Long, J. R. Enabling alternative ethylene production through its selective adsorption in the metal–organic framework Mn_2(*m*-dobdc). *Energy Environ. Sci.* **2018**, *11*, 2423-2431. http://dx.doi.org/doi:10.1039/c8ee01332b.

(113) Yoon, J. W.; Jang, I. T.; Lee, K.-Y.; Hwang, Y. K.; Chang, J.-S. Adsorptive Separation of Propylene and Propane on a Porous Metal-Organic Framework, Copper Trimesate. *Bull. Korean Chem. Soc.* **2010**, *31*, 220-223.

(114) Liang, B.; Zhang, X.; Xie, Y.; R.-B., L.; Krishna, R.; Cui, H.; Li, Z.; Shi, Y.; Wu, H.; Zhou, W.; Chen, B. An Ultramicroporous Metal–Organic Framework for High Sieving Separation of Propylene from Propane. *J. Am. Chem. Soc.* **2020**, *142*, 17995-17801. https://doi.org/10.1021/jacs.0c09466.

(115) Chen, D.-L.; Shang, H.; Zhu, W.; Krishna, R. Transient Breakthroughs of CO_2/CH_4 and C_3H_6/C_3H_8 Mixtures in Fixed Beds packed with Ni-MOF-74. *Chem. Eng. Sci.* **2014**, *117*, 407-415. https://doi.org/10.1016/j.ces.2014.07.008.

(116) Khalighi, M.; Karimi, I. A.; Farooq, S. Comparing SiCHA and 4A Zeolite for Propylene/Propane Separation using a Surrogate-Based Simulation/Optimization Approach. *Ind. Eng. Chem. Res.* **2014**, *53*, 16973-16983.

(117) Olson, D. H.; Camblor, M. A.; Vallaescusa, L. A.; Kuehl, G. H. Light hydrocarbon sorption properties of pure silica Si-CHA and ITQ-3 and high silica ZSM-58. *Microporous Mesoporous Mater.* **2004**, *67*, 27-33.

(118) Hedin, N.; DeMartin, G. J.; Roth, W. J.; Strohmaier, K. G.; Reyes, S. C. PFG NMR self-diffusion of small hydrocarbons in high silica DDR, CHA and LTA structures. *Microporous Mesoporous Mater.* **2008**, *109*, 327-334.

(119) Ruthven, D. M.; Reyes, S. C. Adsorptive separation of light olefins from paraffins. *Microporous Mesoporous Mater.* **2007**, *104*, 59-66.

(120) Li, K.; Olson, D. H.; Seidel, J.; Emge, T. J.; Gong, H.; Zeng, H.; Li, J. Zeolitic Imidazolate Frameworks for Kinetic Separation of Propane and Propene. *J. Am. Chem. Soc.* **2009**, *131*, 10368-10369.

(121) Krishna, R. Evaluation of Procedures for Estimation of the Isosteric Heat of Adsorption in Microporous Materials. *Chem. Eng. Sci.* **2015**, *123*, 191-196.

(122) Böhme, U.; Barth, B.; Paula, C.; Kuhnt, A.; Schwieger, W.; Mundstock, A.; Caro, J.; Hartmann, M. Ethene/Ethane and Propene/Propane Separation via the Olefin and Paraffin Selective Metal−Organic Framework Adsorbents CPO-27 and ZIF-8. *Langmuir* **2013**, *29*, 8592-8600.

(123) Chng, M. L.; Xiao, Y.; Chung, T.-S.; Toriida, M.; Tamai, S. Enhanced propylene/propane separation by carbonaceous membrane derived from poly (aryl ether ketone)/2,6-bis(4-azidobenzylidene)-4-methyl-cyclohexanone interpenetrating network. *Carbon* **2009**, *47*, 1857-1866.

(124) Jiang, Y.; Wang, L.; Yan, T.; Hu, J.; Sun, W.; Krishna, R.; Wang, D.; Gu, Z.; Liu, D.; Cui, X.; Xing, H.; Zhang, Y. Insights into thermodynamic-kinetic synergistic separation of propyne/propylene in anion pillared cage MOFs with entropy-enthalpy balanced adsorption sites. *Chemical Science* **2023**, *14*, 289-309. https://doi.org/10.1039/D2SC05742E.

(125) Niessen, W.; Karge, H. G. Diffusion of *p*-xylene in Single and Binary Systems Investigated by FTIR Spectroscopy. *Microporous Mater.* **1993**, *1*, 1-8.

(126) Karge, H. G. Infrared Spectroscopic Investigation of Diffusion, Co-diffusion and Counter-diffusion of Hydrocarbon Molecules in Zeolites. *C.R. Chimie* **2005**, *8*, 303-319.